Transverse target spin asymmetries in exclusive vector meson muoproduction

Katharina Schmidt

Physikalisches Institut
Albert-Ludwigs-Universität Freiburg

Transverse target spin asymmetries in exclusive vector meson muoproduction

Dissertation
zur
Erlangung des Doktorgrades
der
Fakultät für Mathematik und Physik
der
Albert-Ludwigs-Universität
Freiburg im Breisgau

vorgelegt von
Katharina Schmidt
aus
Frankfurt am Main

Freiburg, Juni 2014

Dekan:	Prof. Dr. Michael Růžička
Leiter der Arbeit:	Prof. Dr. Horst Fischer
Referent:	Prof. Dr. Horst Fischer
Korreferent:	
Tag der Verkündigung des Prüfungsergebnisses:	

Teile dieser Arbeit wurden in folgenden Fachzeitschriften veröffentlicht:

K. Schmidt, proceedings of "Sixth International Conference on Quarks and Nuclear Physics" PoS(QNP2012)044.

C. Adolph *et al.*, Nucl. Phys. B **865** (2012) 1 [arXiv:1207.4301 [hep-ex]].

K. Schmidt, proceedings of "XXI International Workshop on Deep-Inelastic Scattering and Related Subjects" PoS(DIS2013)223.

C. Adolph *et al.*, Phys. Lett. B **731** (2014) 19 [arXiv:1310.1454 [hep-ex]].

Contents

List of Figures

List of Tables

1. Introduction

The first experiment to understand the internal structure of matter was performed in 1911 by Ernest Rutherford, who explored atoms by scattering α particles on a gold foil [1]. He proposed that the positive charge is concentrated in the center of the atom, nowadays recognised as the nucleus, and surrounded by a cloud of electrons. The nucleus consists of protons and neutrons (nucleons), which are bound together by the strong nuclear force. At a fundamental level, this interaction is described by Quantum Chromodynamics (QCD). In particular, QCD characterises the interactions between partons, all of them being particles that carry colour charges and build up colourless hadrons (baryons and mesons).

Since protons and neutrons are the only stable baryons and build up all atomic nuclei, their decoding and detailed description is of particular importance. Our current understanding of the structure of protons and neutrons, and the cohesive forces, is mainly the result of measurements using particle accelerators during the last decades. In particular, lepton nucleon scattering is a powerful tool to investigate the internal structure of the nucleons. The reason is the point-like nature of leptons and the fact that they interact mainly through the electromagnetic force, which is described by an extremely precise theory, the Quantum Electro-Dynamics (QED). A large body of experimental data could be explained with QCD, despite the fact that the fundamental particles – quarks and gluons – were so far never observed as isolated states.

The strength of an interaction is determined by the corresponding coupling constant. An important property of QCD is the dependence of the strength of the strong coupling constant α_s on the space-time distance of quarks and gluons. It gets smaller for shorter distances which can be probed, for example, in high-energy experiments. This observation is known as asymptotic freedom and allows the usage of perturbation theory (pQCD) in high energy experiments. In the low-energy range, the coupling constant is large and no exact analytical tool is available.

Nucleons are such non-perturbative objects. They are complex systems, which consists of three valence quarks as well as sea quarks and gluons. A considerable understanding of nucleons has already been achieved by combining the experimental

results with powerful theoretical models. However, the question how the spin of the nucleon is made up by the angular momenta of its constituents still has not been solved entirely.

Experimental information about the spin structure of the nucleon is obtained by scattering polarised high-energy charged leptons on targets containing polarised protons or light nuclei containing neutrons. In 1987, the European Muon Collaboration (EMC) carried out an experiment at the Conseil Européen pour la Recherche Nucléaire (CERN) and found out that only a marginal part of the proton spin is carried by its valence quarks. This finding is known as the "Spin crisis" [2] and was the starting point of several experiments. The years which followed were dedicated to the study of the nucleon spin carried by gluons and sea quarks. One possible decomposition of the nucleon spin was derived by Jaffe and Manohar [3]. Characteristic is the fact that all terms of this decomposition have a probabilistic interpretation as parton densities in the helicity basis. It can be written as:

$$\frac{1}{2}\hbar = J_z = \frac{1}{2}\Delta\Sigma + \Delta G + \mathcal{L} \tag{1.1}$$

Here, J_z is the z component of the total angular momentum J, the contribution of the quarks and anti-quarks to the spin of the nucleon is denoted by $\frac{1}{2}\Delta\Sigma$ and ΔG is the intrinsic gluon spin contribution. The total orbital angular momentum of all partons is denoted $\mathcal{L}$. A full understanding of the nucleon spin is only possible if the orbital angular momenta of quarks, anti-quarks and gluons are included. Unfortunately, such angular momenta are not directly accessible in experiments.

A comprehensive theoretical picture of the nucleon might be given by a phase-space distribution of quarks and gluons. In classical physics this is given by the position and momentum information of the particle. In quantum mechanics the Heisenberg uncertainty principle is valid. Hence, position and momentum of a particle can not be determined simultaneously. Nonetheless, it is possible to introduce quantum phase space distributions, i.e. the Wigner distribution. They are not experimentally accessible. Nevertheless, Wigner distributions reduce to distributions which are accessible in experiments, for instance, Generalized Parton Distributions (GPDs).

In the decomposition of Ji [4], the total angular momentum of the nucleon is written as the sum of the total angular momenta of the quarks/anti-quarks q, denoted by J_q, and the total angular momenta of the gluons J_g and can be obtained through the equation

$$\sum_q J_q + J_g = J_z = \frac{1}{2}\hbar. \tag{1.2}$$

where both quantities, J_q and J_g, are connected to GPDs via Ji's sum rule.

These GPDs can be constrained via the measurement of Hard Exclusive Meson Production (HEMP), as well as Deep Virtual Compton Scattering (DVCS). For exclusive production of mesons by longitudinally polarised photons the factorisation theorem is valid [5, 6] and allows for a separation of the amplitude into a hard part, described by perturbative QCD, and a soft part. This non-perturbative part consist of two long-distance parts: the structure of the nucleon which is parametrised by the GPDs, and the structure of the produced meson which is described by the distribution amplitude (DA).

This thesis is dedicated to the analysis of the transverse target spin azimuthal asymmetries in hard exclusive production of ρ^0 mesons. Such asymmetries are physical observables, which are sensitive to GPDs. The measurement was performed at the COmmon Muon Proton Apparatus for Structure and Spectroscopy (COMPASS) by scattering 160 GeV/c muons off transversely polarised deuterons and protons. The COMPASS experiment is a fixed-target experiment situated at the Super Proton Synchrotron (SPS) M2 beam line at CERN. In the years 2002-2004 data was collected with a transversely polarised ^{6}LiD target and in the years 2007 and 2010 with a transversely polarised NH_3 target, where the scattering centers are protons and deuterons, respectively. The experimental setup allows the evaluation of single-spin and double-spin asymmetries.

In this thesis the data of the year 2010, taken during the PhD phase, is analysed. Additionally, the data taken in the years 2003, 2004 and 2007 are analysed/reanalysed. For the first time, all five single-spin and three double-spin asymmetries accessible with a longitudinally polarised beam and a transversely polarised NH_3 target are extracted. For the low statistic ^{6}LiD data the leading-twist asymmetry $A_{\mathrm{UT}}^{\sin(\phi-\phi_S)}$ is extracted. Altogether, this thesis is the first complete analysis of exclusive ρ^0 mesons of all available data taken with transversely polarised ^{6}LiD and NH_3 targets at COMPASS. In the near future, there will be no more data available for such processes in the kinematic domain of COMPASS.

The thesis is organised as follows: The second chapter is dedicated to the theoretical background of the field of study, starting with a brief overview of the general formulation of deep inelastic scattering, followed by a summary of the study of the nucleon spin structure. In Sec. 2.3, the focus is on exclusive meson production and the relevant cross section is introduced. The theory chapter is closed with an introduction to GPDs. Chapter 3 contains an overview of the COMPASS spectrometer, with emphasis on the detector elements needed for this analysis. Chapter 4 describes the selection of exclusive ρ^0 mesons, whereas Chapter 5 is dedicated to the discussion of the background estimation method. Finally, in Chapter 6 the evaluation of asymmetries is explained. It starts with introducing the basic concept of asymmetry extraction followed by a presentation of the applied fit methods. In Chapter 7 the asymmetries for the NH_3 target are discussed. Sec. 7.1 focuses on the extraction of background uncorrected asymmetries. The background corrected asymmetries are presented after the discussion of the influence of non-exclusive events. The chapter closes with studies of the systematic uncertainties and a comparison of $A_{\mathrm{UT}}^{\sin(\phi-\phi_S)}$ extracted with one-dimensional and two-dimensional methods. In Chapter 8 the asymmetries for the ^{6}LiD target are discussed. Finally, Chapter 9 provides a summary of the results and a comparison with theoretical model calculations. The thesis finishes with Chapter 10 where a conclusion and an outlook is given.

2. Theory

This chapter starts with introducing the main concepts of deep inelastic scattering as it is the basis of the field of study. This is followed by a historical description of the understanding of the spin structure of the nucleon in Sec. 2.2. Recent reviews, addressing the measurements as well as the theoretical concepts to decode the spin structure of the nucleon can be found in Refs. [7, 8]. Section 2.3 is dedicated to the formal derivation of the cross section, which is mainly based on what is presented in Refs. [9, 10]. Additional details can be found in Refs. [11, 12]. In Sec. 2.4, the concept of Generalized Parton Distributions (GPDs) is introduced and their main properties are discussed. Finally, experimental constraints for GPDs are summarised in Sec. 2.6 and concepts for modelling GPDs are introduced in Sec. 2.5.

2.1 Deep Inelastic Scattering

At first, the relevant kinematic variables to describe deep inelastic scattering will be introduced. A summary of the most important kinematic variables used in this thesis is listed in Tab. 2.1. In this chapter $\hbar = c = 1$ is used.

Deep ($Q^2 \gg M^2$) inelastic ($W^2 \gg M^2$) scattering is an extensively studied process. It allows us to learn about the structure of nucleons, as well as testing underlying theories. The most up-to-date knowledge about the high-energy spin structure of the nucleon comes from polarised deep inelastic scattering (DIS) experiments, where a high-energy charged lepton beam is scattered on a nucleon target. In polarised deep inelastic scattering the lepton beam is usually longitudinally polarised and the nucleon target may be either longitudinally or transversely polarised. The analysis presented in this thesis is done on a data sample taken with a transversely polarised target, so the emphasis is placed on the theory related to transversely polarised fixed targets.

Table 2.1: Important variables.

$k = (E, \vec{k})$	Four-momentum-vector of the incident muon
$k' = (E', \vec{k'})$	Four-momentum-vector of the scattered muon
p	Four-momentum-vector of the target nucleon
$q = k - k'$	Four-momentum-vector of the virtual photon
E	Energy of the incident lepton
E'	Energy of the scattered lepton
M	Mass of the target nucleon
m	Mass of the incoming lepton
θ	Scattering angle of the scattered lepton
$Q^2 = -q^2 \stackrel{\text{lab}}{=} EE' \sin^2(\frac{\theta}{2})$	Invariant negative mass squared of the virtual photon
$W = \sqrt{(p+q)^2}$ $\stackrel{\text{lab}}{=} M^2 + 2M\nu - Q^2$	Total energy in the $\gamma^* - N$ system
$s_{cm} = (k+p)^2$	Squared invariant center of mass energy
$\nu = \frac{p \cdot q}{M} \stackrel{\text{lab}}{=} E - E'$	Energy of the virtual photon
$y = \frac{p \cdot q}{p \cdot k} \stackrel{\text{lab}}{=} \frac{\nu}{E}$	Fractional energy of the virtual photon
$x_{Bj} = \frac{Q^2}{2p \cdot q} \stackrel{\text{lab}}{=} \frac{Q^2}{2M\nu}$	Bjorken scaling variable
s	Spin of the lepton
S	Spin of the target nucleon
λ	Helicity of the lepton
H	Helicity of the target nucleon

First, the most generic process:

$$lN \to l'X, \tag{2.1}$$

will be discussed. Here, l is the incoming lepton which scatters off the target nucleon N. The scattered lepton is denoted by l'. In inclusive deep inelastic scattering, only the energy and direction of the scattered lepton are measured with a detector. The undetected hadronic system is denoted by X. The incoming lepton interacts with the nucleon in the target through the exchange of a virtual photon. In Fig. 2.1 a schematic picture of the process of Eq. 2.1 is shown, where one-photon exchange is assumed[1]. The effects beyond one-photon exchange are suppressed with at least $\frac{1}{\alpha_{em}}$. The weak interaction can be neglected because the center-of-mass energy at COMPASS $\sqrt{s} \approx 17.4\,\text{GeV}$ is much smaller than the Z^0 mass. Under the assumption of the validity of the Bjorken limit:

$$\nu, Q \to \infty, \text{ with } x_{Bj} = \frac{Q^2}{2M\nu} \text{ fixed}, \tag{2.2}$$

the total cross section can be written in terms of the leptonic tensor $L_{\mu\nu}$ and the hadronic tensor $W^{\mu\nu}$:

$$\sigma_{\text{DIS}} \sim L_{\mu\nu} W^{\mu\nu}, \tag{2.3}$$

where Q^2, x_{Bj}, ν and M are introduced in Tab. 2.1. The leptonic tensor contains the information on the emission of the virtual photon by the incoming lepton and can be calculated explicitly in QED. It is composed of a spin-independent part $L^{(S)}_{\mu\nu}(k, k')$ that is symmetric in $\mu\nu$ and a spin-dependent part $L^{(A)}_{\mu\nu}(k, s, k')$ that is antisymmetric in $\mu\nu$ [18]:

$$L_{\mu\nu} = L^{(S)}_{\mu\nu}(k, k') + \mathrm{i} L^{(A)}_{\mu\nu}(k, s, k'), \tag{2.4}$$

where the spin of the incoming lepton is denoted by s.

The hadronic tensor includes the description of the structure of the nucleon. In contrast to $L^{\mu\nu}$, the hadronic tensor $W^{\mu\nu}$ cannot be calculated from first principles as it contains crucial information involving non-perturbative effects of QCD (see Sec. 2.1.2). Still, it is possible to specify the tensor structure, allowed by the underlying principles, for instances Lorentz symmetry, parity invariance and time reversal. Usually in experiments spin-$\frac{1}{2}$ targets are used. In this case $W^{\mu\nu}$ depends on the nucleon spin in the initial and final state denoted by S and S'. Like the leptonic tensor, the hadronic tensor can be separated into a symmetric and an anti-symmetric part [18]:

$$W^{\mu\nu} = W^{\mu\nu(S)}(P, q) + \mathrm{i} W^{\mu\nu(A)}(P, S, q), \tag{2.5}$$

where only the anti-symmetric part depends on the spin of the initial nucleon S. Since the contraction of a symmetric and an antisymmetric tensor cancels, the cross

[1] Multi-photon exchange might explain (some) inconsistencies in measurements of electric and magnetic form factors in elastic scattering [13]. Beside the beam-charge asymmetry in inclusive DIS, which arises from the one-photon and two-photon exchange amplitude, a non-zero transverse-target single-spin asymmetry $A_{\text{UT}}^{\sin\phi_S}$ in inclusive DIS is an indication for the existence of two-photon exchange [14]. For the former, an earlier measurement of Brookhaven National Laboratory [15] and a measurement from EMC [16] were consistent with zero. The latter was measured at HERMES [17].

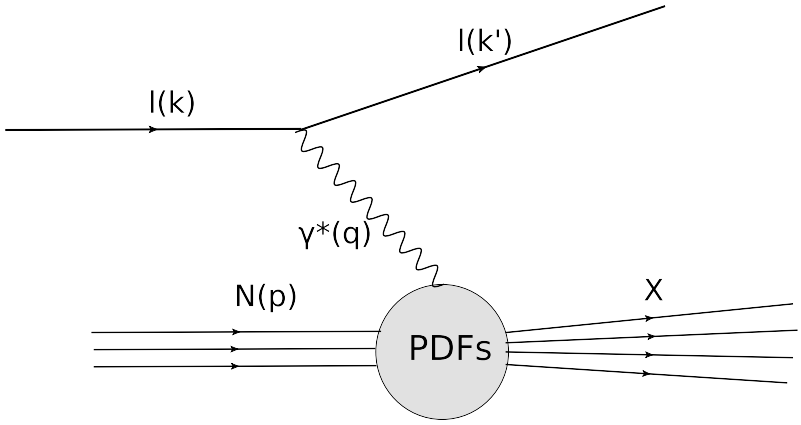

Figure 2.1: Schematic picture of deep inelastic scattering. The four-momentum-vectors of the particles involved are given in parentheses. The Parton Distribution Functions (PDFs) encode the long-distances physics due to the partonic substructure of the nucleon. They will be introduced later in this section.

section is separated into an unpolarised and a polarised part, where only the latter depends on the spins of the incoming lepton and the target nucleon. This strict separation is only true for spin-$\frac{1}{2}$ targets. The hadronic tensor can be formulated in terms of four structure functions F_1, F_2, g_1 and g_2. They parametrise the structure of the target as seen by the virtual photon and have to be determined by experiments.

The symmetric part of the hadronic tensor is parametrised by the structure functions F_1 and F_2 and F_2 can be measured in experiments using an unpolarised beam and an unpolarised target. The anti-symmetric part of the hadronic tensor is parametrised by g_1 and g_2. Their measurement requires both a polarised target and a polarised beam. The dimensionless structure functions F_1, F_2, g_1 and g_2 depend on the variables ${x_{Bj}}^2$ and Q^2, For brevity this dependence is omitted in the following.

The unpolarised part of the cross section for scattering a lepton on a spin-$\frac{1}{2}$ target can be written as [18][3]:

$$\frac{d^2\sigma}{dx_{Bj}dy} = \frac{4\pi\alpha_{em}^2}{Q^2 x_{Bj} y}\left[x_{Bj}y^2F_1 + (1 - y - \frac{x_{Bj}^2 y^2 M^2}{Q^2})F_2\right]. \tag{2.6}$$

The structure function F_1 and F_2 have been measured over a wide range of x_{Bj} and Q^2 using different target material. The present status of the measurement of F_2^p is shown in Fig. 2.2. Experimentally it is observed that over a wide range the structure functions F_i, with $i \in \{1, 2\}$, do not depend on Q^2:

$$F_i(x_{Bj}, Q^2) \to F_i(x_{Bj}). \tag{2.7}$$

[2]In theoretical context, often the symbol x rather than x_{Bj} is used for the measured quantity. However, in DIS processes x is identified with the Bjorken variable x_{Bj}.

[3]Often experiments give the cross section, $\frac{d^2\sigma}{dE'd\Omega}$, as a function of the final lepton energy E' and the solid angle Ω of the scattered lepton. Using the Jacobian matrix the cross section can be converted to a cross section as a function of x_{Bj} and y or x_{Bj} and Q^2.

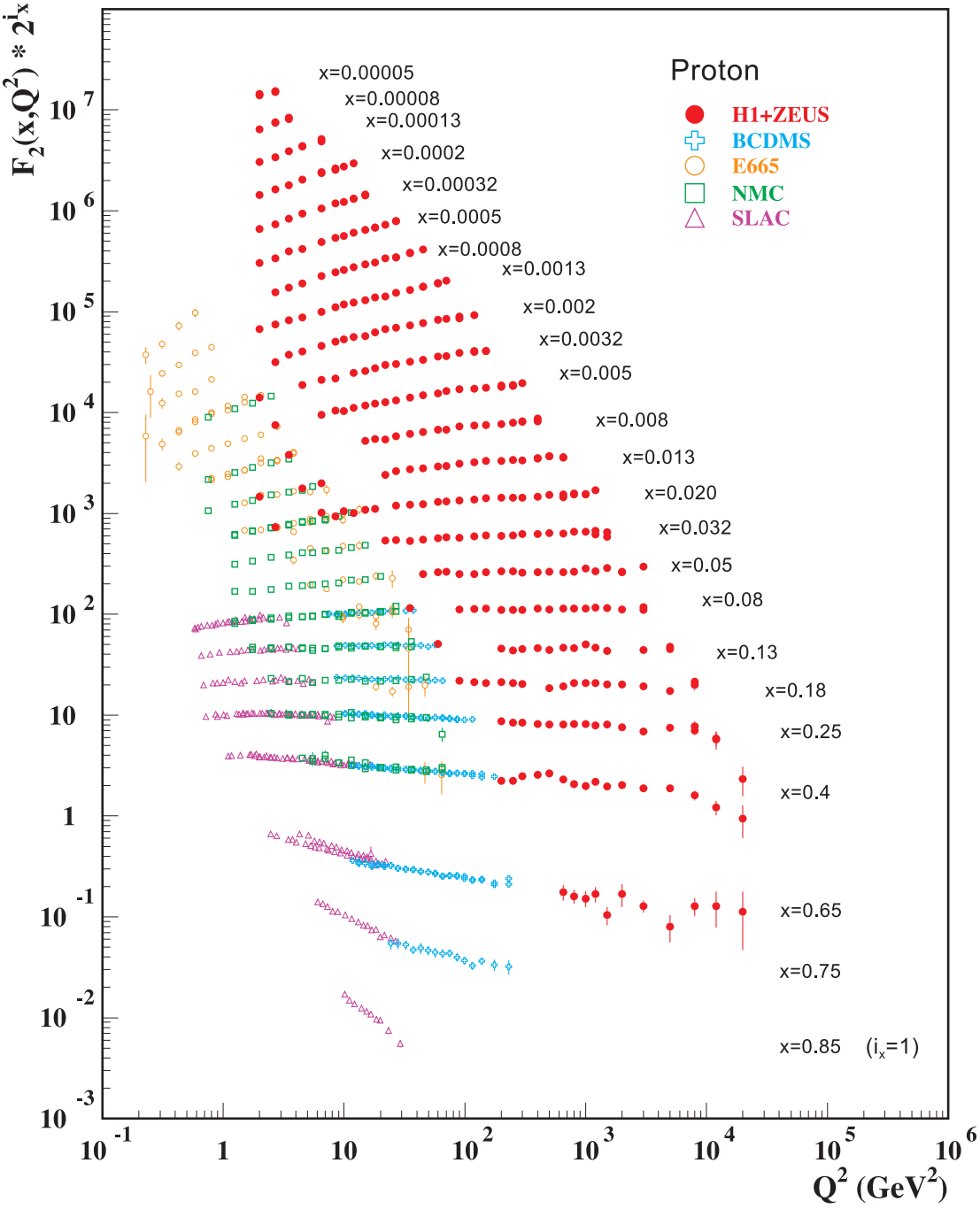

Figure 2.2: Results for the proton structure function F_2^p versus Q^2 measured at different experiments [19]. The data is shown in bins of fixed x_{Bj}. Note that F_2^p has been multiplied by 2^{i_x}, where i_x is the number of the x_{Bj} bin, ranging from $i_x = 1$ ($x_{Bj} = 0.85$) to $i_x = 24$ ($x_{Bj} = 0.00005$).

This is known as Bjorken scaling. It was predicted by James Bjorken in 1968 [20] and confirmed at SLAC National Accelerator Laboratory (SLAC) [21]. It is a consequence of the point-like nature of the partons (see Sec. 2.1.2). The Callan-Gross-relation:

$$F_2(x_{Bj}) = 2x_{Bj}F_1(x_{Bj}), \tag{2.8}$$

is well-established in experiments, and, as a consequence, gives a hint to the spin-$\frac{1}{2}$ nature of quarks.

The structure functions g_1 and g_2 can be probed either with a longitudinally polarised target or a transversely polarised target. If the incoming lepton is polarised anti-parallel the beam direction (-) and the target nucleon is either polarised parallel or anti-parallel (+ or -) to the beam direction the cross section difference reads [18]:

$$\begin{aligned}\frac{d^3\sigma^{-+}}{dx_{Bj}dyd\phi} - \frac{d^3\sigma^{--}}{dx_{Bj}dyd\phi} &= \frac{4\alpha_{em}^2}{Q^2}\Big[\left(2 - y - \frac{2M^2x_{Bj}^2y^2}{Q^2}\right)g_1 \\ &- \frac{4M^2x_{Bj}^2y}{Q^2}g_2\Big].\end{aligned} \tag{2.9}$$

The azimuthal angle between the lepton scattering plane and the spin plane defined by $\vec{k}$ and the target Spin $\vec{S}$ is denoted by ϕ. In measurements performed with a longitudinally polarised target, the dominant contribution comes from g_1, whereas g_2 is suppressed. In experiments the measured quantity is connected to the double-spin asymmetry A_1:

$$A_1 = \frac{g_1 - \gamma^2 g_2}{F_1}. \tag{2.10}$$

where γ is defined as:

$$\gamma = \frac{2Mx_{Bj}}{Q}. \tag{2.11}$$

The target nucleon can be polarised perpendicular to the beam direction as well ($\uparrow$, $\downarrow$). Then the cross section difference reads [18]:

$$\frac{d^3\sigma^{-\uparrow}}{dx_{Bj}dyd\phi} - \frac{d^3\sigma^{-\downarrow}}{dx_{Bj}dyd\phi} = \frac{8\alpha_{em}^2}{Q^2}\gamma\sqrt{1 - y - \gamma^2\frac{y^2}{4}}\left[\frac{y}{2}g_1 + g_2\right]\cos\phi. \tag{2.12}$$

Here, the whole cross section is suppressed although $g_1(x_{Bj}, Q^2)$ and $g_2(x_{Bj}, Q^2)$ contribute at the same order and appear in combinations. Therefore the measurement with and transversely polarised target can be used to determine g_2, once g_1 has been measured with a longitudinally polarised target. A present status of the measurement of g_1^p can be fount in Ref. [22] and is shown in Fig. 2.3. A recent result for the proton structure function g_2^p can be found in Ref. [23] and is presented in Fig. 2.4.

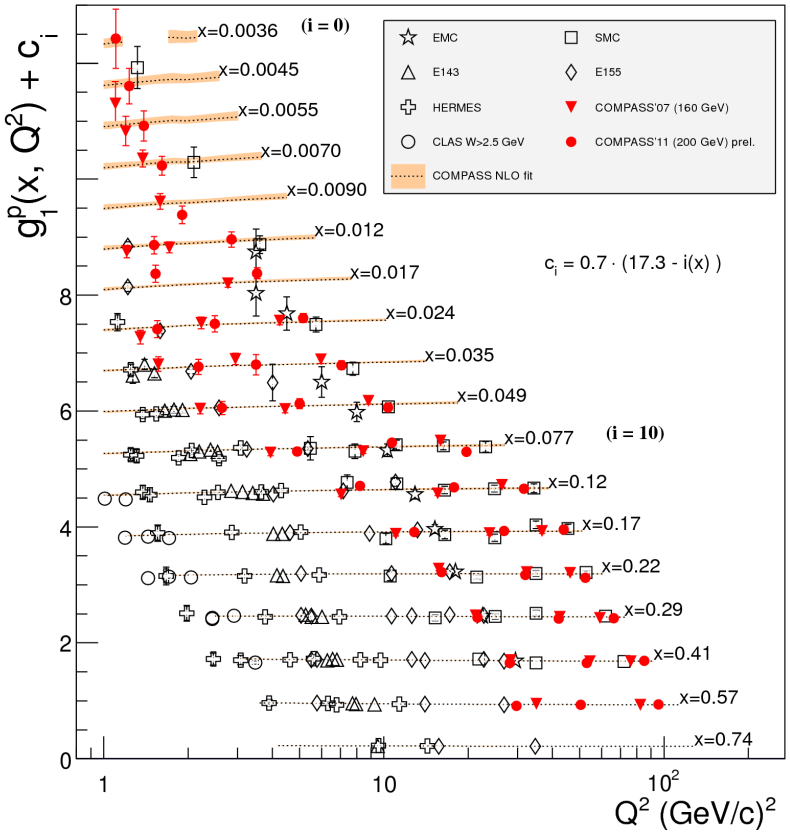

Figure 2.3: World data for the proton structure function g_1^p versus Q^2 for several values of x_{Bj}. Plot from Ref.[22].

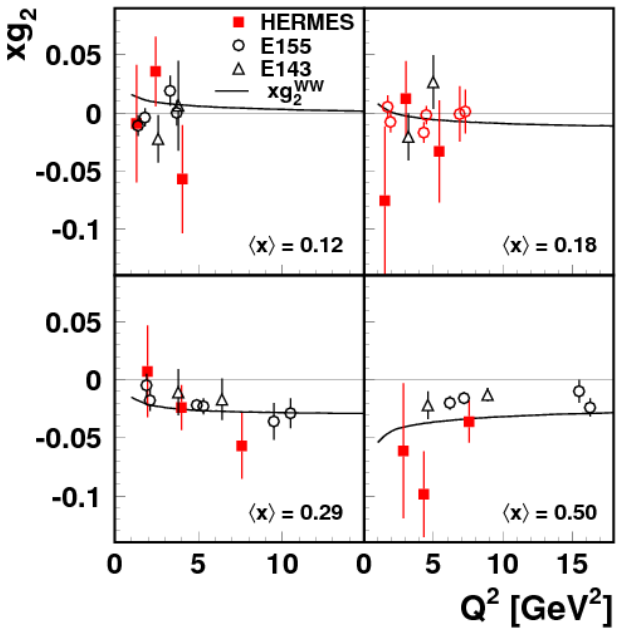

Figure 2.4: Results for the proton structure function $x_{Bj}g_2^p$ versus Q^2 measured at HERMES, E155 and E143 for selected values of x_{Bj}. Plot from Ref. [23].

2.1.1 Polarisation & Helicity

In general, the helicity of a particle is defined as the projection of its spin onto its momentum direction. If the spin is parallel (anti-parallel) to the momentum direction the helicity is 1 (-1). In this case the particle is usually called longitudinally polarised. Whereas if the spin and the momentum vector are perpendicular the helicity is zero and the particle is called transversely polarised. Note that for the photon, for historic reasons, the notation is usually contrary. A real photon can have the three helicity states denoted by -1, 0, or 1, thereby $\lambda = -1, 1$ is called transversely polarised and $\lambda = 0$ longitudinally polarised.

2.1.2 The Parton Model & Factorisation

The parton model was introduced at the end of the 1960s [24] and could explain the observed Bjorken scaling. In the infinite-momentum-frame, the nucleon can be described as an object consisting of almost collinearly moving quasi-real partons which are point-like spin-$\frac{1}{2}$ particles. Then the DIS process can be described as the sum of a scattering from the virtual photon with one parton. Each parton q is characterised by the momentum distribution $q(x_{Bj})$, where, in this context, x_{Bj} is the longitudinal momentum fraction of quark with respect to the nucleon momentum. Therefore, the momentum distribution $q(x_{Bj})$ multiplied by the differential momentum fraction dx_{Bj} gives the probability to find the parton q, which carries the fractional momentum x_{Bj} in the range $[x_{Bj}; x_{Bj} + dx_{Bj}]$. The charged partons can be identified with the quarks, the constituents of the nucleon.

A polarised spin-$\frac{1}{2}$ nucleon can be fully described by three fundamental parton distributions:

$$q(x_{Bj}) = q^{+}(x_{Bj}) + q^{-}(x_{Bj}), \tag{2.13}$$

$$\Delta q(x_{Bj}) = q^{+}(x_{Bj}) - q^{-}(x_{Bj}), \tag{2.14}$$

$$\Delta_T q(x_{Bj}) = q^{\uparrow}(x_{Bj}) - q^{\downarrow}(x_{Bj}). \tag{2.15}$$

The quantity $\Delta q(x_{Bj})$ is known as the helicity distribution, whereas the distributions $q^{+}(x_{Bj})$ ($q^{-}(x_{Bj})$) represent the probabilities that the parton helicity is parallel, $+$, (anti-parallel, $-$) to the spin of the nucleon. The transversity distribution $\Delta_T q(x_{Bj})$ describes the number density of partons with parallel polarisation minus the number density of partons with anti-parallel polarisation, in a transversely polarised nucleon.

In the limit $Q^2 \to \infty$, the coupling constant of the strong interaction denoted by α_S is decreasing. This property of QCD is known as asymptotic freedom and was observed by Gross & Wilczek and Politzer. In this range perturbative technics (pQCD) can be applied to compute the interaction[4]. Therefore, the lepton parton scattering mentioned above can be calculated in pQCD whereas the long-distance physics describing the parton in the nucleon is encoded in the Parton Distribution Functions (PDFs).

[4] In contrast, at low Q^2 quarks occur only in bound states. This is known as confinement. Then instead of pQCD phenomenological models have to be used.

The total cross section of the DIS process is given as a convolution of a hard partonic sub-process, and the parton distribution functions, PDFs. Schematically this convolution reads:

$$d\sigma = [\text{partonic cross section}] \otimes [\text{PDFs}]. \tag{2.16}$$

In the parton model, the structure functions can be expressed in terms of the PDFs as:

$$\begin{aligned} F_1(x_{Bj}, Q^2) &= \frac{1}{2} \sum_f e_f^2 q_f(x_{Bj}), \\ F_2(x_{Bj}, Q^2) &= x_{Bj} \sum_f e_f^2 q_f(x_{Bj}), \\ g_1(x_{Bj}, Q^2) &= \frac{1}{2} \sum_f e_f^2 \Delta q_f(x_{Bj}), \\ g_2(x_{Bj}, Q^2) &= 0. \end{aligned} \tag{2.17}$$

The sum runs over all quark and anti-quark flavors and e_f is the charge of the quark or anti-quark q. Hence, in the parton model, a simple interpretation of the structure functions exists. Whereas F_1 can be interpreted as the probability to scatter on a quark in the nucleon with momentum fraction x_{Bj}, g_1 is the differences in probabilities for scattering off a quark in the nucleon with momentum fraction x_{Bj} and parton helicity parallel and anti-parallel to the spin of the nucleon. There is no such interpretation of g_2. It is not possible to access the transversity distribution $\Delta_T q(x_{Bj})$ in inclusive DIS. This distribution includes a helicity flip of the struck quark, which can not be realised in leading-order DIS.

In contrast to structure functions, which are measurable in experiments, PDFs have to be parametrised using experimental data. Nevertheless, PDFs are universal quantities. Once measured for one process, they can be used to predict the cross sections for other processes. A typical parametrisation is presented in Fig. 2.5.

Note that in the parton model the structure functions scale, i.e. they are independent of Q^2. Precise measurements confirmed that in QCD this scaling is broken proportional to $\alpha_S \log Q^2$. These logarithmic scaling violations occur because quarks and gluons interact and outgoing quarks can radiate gluons. This behaviour can not be explained within the simple parton model and requires a QCD-improved parton model. In pQCD the cross sections are expanded in powers of the coupling constant α_S, where the terms are known as leading order (LO), next-to-to leading order (NLO), etc. At higher orders of pQCD loop corrections corresponding to hard radiative correction have to be considered. The division between the radiation of hard gluons, which are included in the partonic cross section, and the soft gluons, which are absorbed into the parton density, is defined by the factorisation scale μ_F^2. Thus in the QCD-improved parton model the quantities q, Δq and $\Delta_T q$ depend on μ_F^2. For brevity this dependence is omitted in the following. Note that in a QCD-improved parton model the structure function g_2 differs from zero [19].

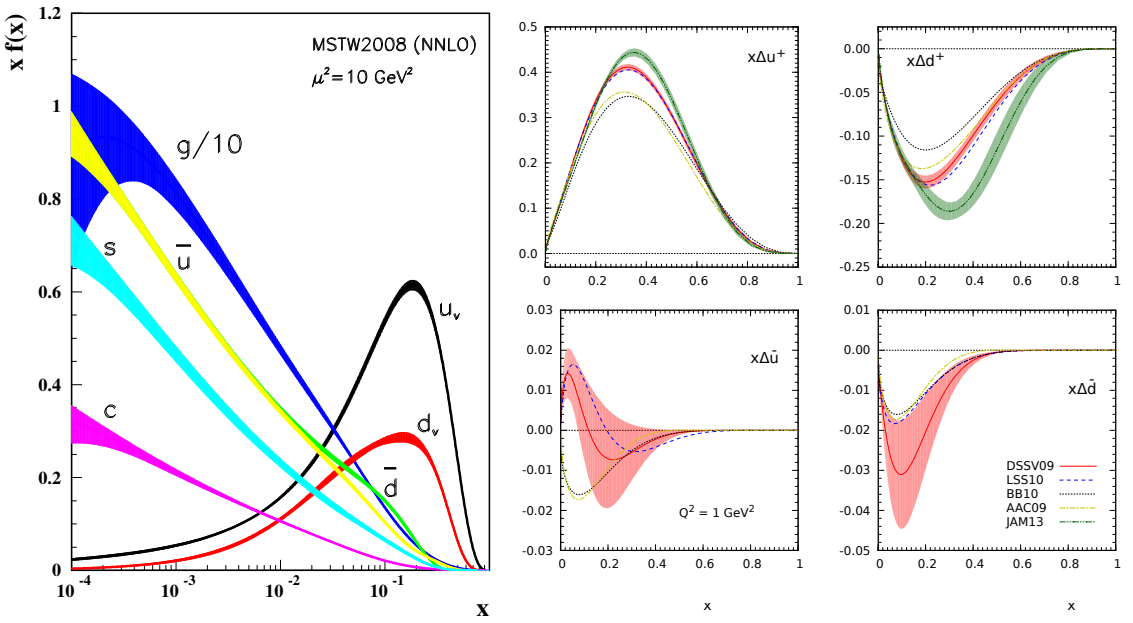

Figure 2.5: Left-hand panel: Distributions of x times the unpolarised parton distributions, here denoted by $f(x)$ (where $f = u_v, d_v, \bar{u}, \bar{d}, s, c, g$) using the NNLO MSTW2008 parametrisation [19]. Right-hand panels: Comparison of helicity distributions $x\Delta u^+ = x(\Delta u + \Delta\bar{u})$, $x\Delta d^+ = x(\Delta d + \Delta\bar{d})$, $x\Delta\bar{u}$ and $x\Delta\bar{d}$ for different parametrisations [25]. Details of the parametrisations are available in the references.

The parton distribution functions can be written in terms of operators[5] on the light-cone[6] [26, 27]:

$$
\begin{aligned}
q(x) &= \int \frac{dz^-}{4\pi} e^{ixp^+z^-} \left\langle p|\bar{\psi}_q(0)(0)\gamma^+\psi_q(z)|p\right\rangle \Big|_{z^+=z_\perp=0}, \\
\Delta q(x) &= \int \frac{dz^-}{4\pi} e^{ixp^+z^-} \left\langle pS_L|\bar{\psi}_q(0)\gamma^+\gamma_5\psi_q(z)|pS_L\right\rangle \Big|_{z^+=z_\perp=0}, \\
\Delta_T q(x) &= \int \frac{dz^-}{4\pi} e^{ixp^+z^-} \left\langle pS_T|\bar{\psi}_q(0)\gamma^+\gamma^1\gamma_5\psi_q(z)|pS_T\right\rangle \Big|_{z^+=z_\perp=0},
\end{aligned}
\tag{2.18}
$$

where ψ is the quark field of flavor q, p represents the initial and final nucleon momenta, x is the momentum fraction of the quark and S_L (S_T) is the longitudinal (transverse) nucleon spin projection. The operators in Eq. 2.18 contains currents which are constructed as a combination of Γ matrices and Dirac fields, i.e. $\bar{\psi}\Gamma\psi$. Depending on the Γ matrices, where $\Gamma \in \{\mathbb{1}, \gamma_5, \gamma^\mu, \gamma^\mu\gamma_5, \sigma^{\mu\nu}\}$, the constructed currents are scalar, pseudo-scalar, vector, axial or tensor currents. In Eq. 2.18 the space-time coordinates z of the initial and final quarks are different. Thus the operator is non-local, but the momenta of initial and final nucleon are identical. Hence the operator is diagonal.

[5] All operators are defined using the light-cone-gauge.

[6] Light-cone-coordinates are summarised in Appendix A.

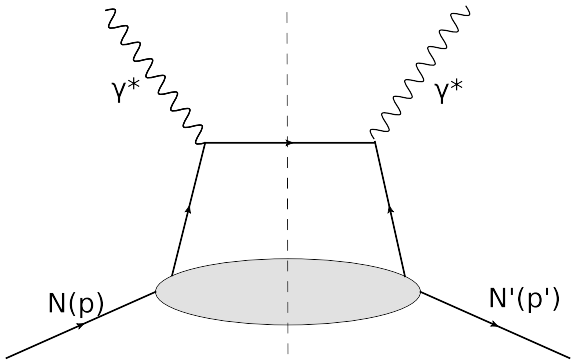

Figure 2.6: Hand-bag diagram.

It is possible to expand the operators[7] in terms of $(1/Q)^{\tau-2}$, where τ is known as twist and is connected to the dimension d in mass units minus spin s of the operators. For $\tau = 2$ only the $\ln Q^2$ appears. Thus leading twist is twist two.

2.1.3 Optical Theorem

The process $\gamma^* p \to X$ is described by the cross section [28]:

$$\sigma^{\gamma^* p \to X} \propto \frac{\alpha_{em}}{K} \epsilon^{\mu *} W_{\mu\nu} \epsilon^{\nu}, \tag{2.19}$$

where K is the virtual-photon flux factor and ϵ^{ν} is the virtual-photon polarisation vector. The virtual photon has the momentum $q = (q^0, 0, 0, q^3)$ with the three possible polarisation states ϵ^{μ}: ϵ^{μ}_{+}, ϵ^{μ}_{-} and ϵ^{μ}_{0}, which correspond to the helicities +, -, and 0, respectively. The diagram describing this process is similar to the diagram of the forward[8] Compton scattering amplitude $T_{\mu\nu}$, which describes the reaction $\gamma^* p \to \gamma^* p$. Therefore the optical theorem can be derived:

$$W_{\mu\nu} \propto \operatorname{Im} T_{\mu\nu}. \tag{2.20}$$

It relates the hadronic tensor that appears in the cross section of inclusive deep inelastic scattering to the imaginary part of the forward scattering amplitude for the Compton process which describes the absorption and emission of a virtual photon by the nucleon. The latter is illustrated with the 'hand-bag' diagram in Fig. 2.6. Hence the evaluation of the forward Compton scattering amplitude in pQCD allows for conclusions regarding the hadronic tensor $W_{\mu\nu}$.

The forward Compton amplitude can be expanded in terms of helicity amplitudes $\mathcal{M}_{h'H',hH}$ [28]. Here, h (h') denotes the initial (final) photon helicity and H (H') denotes the initial (final) nucleon helicity. For a spin-$\frac{1}{2}$ target four independent helicity amplitudes exist. They can be chosen to be:

$$\mathcal{M}_{++,+-}, \qquad \mathcal{M}_{+-,+-}, \qquad \mathcal{M}_{0+,0+}, \qquad \mathcal{M}_{0+,+-}. \tag{2.21}$$

They are connected to four independent structure functions. Therefore, it is possible to express the structure functions in terms of combinations of helicity amplitudes. The single helicity flip amplitude $\mathcal{M}_{0+,+-}$ is suppressed by a factor of M/Q relative to the diagonal helicity amplitudes.

[7] Operator Product expansion (OPE)

[8] The term forward expresses the fact that the initial and the final states are equal.

2.2 The Spin Structure of the Nucleon

A central question towards a more complete understanding of the structure of nucleons is how the nucleon spin is distributed amongst its constituents. In the early 1980's, a longitudinally polarised electron beam was scattered of a longitudinally polarised proton (butanol) target at SLAC [29]. The setup allowed for the measurement of g_1 down to $x_{Bj} = 0.1$. These measurements were consistent with the relativistic parton model, which predicts that $\approx 60\%$ of the nucleon spin is carried by the quarks. Some years later the European Muon Collaboration (EMC) at CERN[9] extended the measurement down to $x_{Bj} = 0.01$. In this experiment longitudinally polarised muons were scattered of a longitudinally polarised proton (NH_3) target [30]. The measurements lead to the conclusion that the contribution of the quarks to the spin of the proton is significantly smaller. In the following years, a variety of experiments were built up to confirm this result. In particular, they were dedicated to measure the spin contributions separately carried by the valence and sea quarks and by the gluons.

The experiments can be divided into fixed target experiments with electron or muon beams and Collider experiments. The muon beam experiments were performed at CERN. They started with the EMC Collaboration, followed by the Spin Muon Collaboration (SMC) and, finally, were continued at the COMPASS[10] experiment. They have a high energy beam between 100 GeV and 270 GeV but the beam has a limited intensity. Therefore, they need a large solid target to achieve a reasonable luminosity. The electron beam experiments were performed at SLAC, Deutsche Elektronen-Synchrotron (DESY) and Jefferson Lab (JLAB). They have a higher beam intensity and, consequently, only need relatively small targets to reach a high statistical accuracy. Polarised proton-proton collisions were performed at the Relativistic Heavy Ion Collider (RHIC) in Brookhaven. Mainly the three experiments – PHENIX[11], STAR[12] and BRAHMS[13] – contribute to the decoding of the spin of the nucleon.

One possible decomposition of the nucleon spin was derived by Jaffe and Manohar [3]. Characteristically is the fact that all terms of this decomposition have a probabilistic interpretation as parton densities in the helicity basis, where the spin is quantised along the axis in the direction of motion of the particle. It can be written as:

$$\frac{1}{2} = J_z = \frac{1}{2}\Delta\Sigma + \Delta g + \mathcal{L}. \tag{2.22}$$

Here, J_z is the z component of the total angular momentum J and the total quark contribution to the nucleon spin is denoted by $\frac{1}{2}\Delta\Sigma$, while Δg is the intrinsic gluon spin contribution. The orbital angular momentum is named $\mathcal{L}$. The measurement of $g_1^{p,n}(x_{Bj}, Q^2)$ allows for the constraint of:

$$\Gamma_1^{p,n} = \int_0^1 dx_{Bj} g_1^{p,n}(x_{Bj}, Q^2) = \frac{1}{2}\sum_f e_f^2 \Delta q_f, \tag{2.23}$$

[9] Conseil Européen pour la Recherche Nucléaire

[10] COmmon Muon Proton Apparatus for Structure and Spectroscopy

[11] Pioneering High Energy Nuclear Interaction eXperiment

[12] Solenoidal TrAcker at RHIC

[13] Broad RAnge Hadron Magnetic Spectrometers

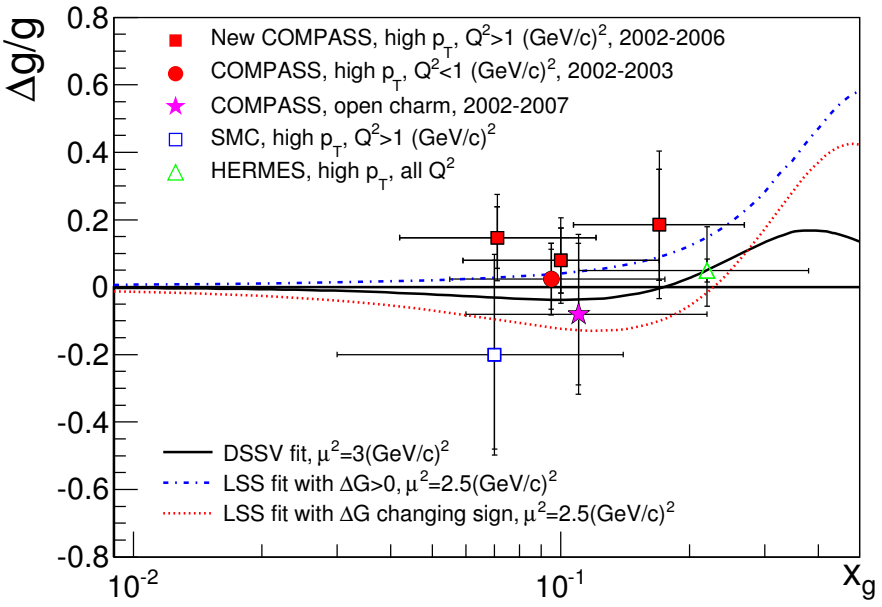

Figure 2.7: Experimental results and NLO fits for the gluon polarisation $\Delta g/g$ in the nucleon [31]. The experimental results and the model calculations shown in the figure are explained therein.

where the sum runs over all quark flavors in the proton p or neutron n and the helicity distribution consists of contributions from quarks q and anti-quarks $\bar{q}$:

$$\Delta q_f = \int_0^1 \left[q_f^+(x) - q_f^-(x) + \bar{q}_f^+(x) - \bar{q}_f^-(x) \right] dx. \tag{2.24}$$

The precision of $\Gamma_1^{p,n}$ is limited by the fact that it is impossible to measure the complete range $0 < x_{Bj} < 1$, therefore the evaluation of $\Gamma_1^{p,n}$ always includes assumptions for the unmeasured range. Moreover, Q^2 and x_{Bj} are strongly correlated in the experiment. So each measured point $g_1^p(x_{Bj}, Q^2)$ corresponds to a different value of Q^2. Note that the expression for $\Gamma_1^{p,n}$ in Eq. 2.23 is only valid in the naive parton model. Under the assumption of the validity of the naive parton model the study of $g_1^{p,n}(x_{Bj}, Q^2)$ and, among other results, the evaluation of Eq. 2.23 enables the determination of the flavor-singlet combination :

$$\Delta\Sigma \equiv (\Delta u + \Delta\bar{u}) + (\Delta d + \Delta\bar{d}) + (\Delta s + \Delta\bar{s}). \tag{2.25}$$

The various experimental results lead to the conclusion that $\Delta\Sigma$ is approximately 30%, where the contribution from the sea quarks $(\Delta s + \Delta\bar{s})$ is measured in DIS to be comparable with zero.

The gluon spin contribution Δg is accessible in experiments. COMPASS has been designed to measure Δg via the study of the photon-gluon fusion. This process can be selected by requiring charmed mesons or high p_T charged hadron pairs in the final state. Additionally, Δg was evaluated at HERMES and through polarised proton collisions at RHIC. The results are presented in Fig. 2.7. The COMPASS [31, 32] and RHIC [33, 34] measurements suggest that the spin contribution from the gluons

is not sufficient to resolve the difference between the small value of $\Delta\Sigma$ and the constituent quark model predictions.

The final challenge is the determination of the orbital angular momentum $\mathcal{L}$. Up to now, it is not known how to direct measure the orbital angular momenta of quarks and gluons. The formalism of generalized parton distributions (GPDs) allows to extract certain information about the quark angular momentum since the GPD E is related to the total angular momentum of the quarks J^q and gluons J^g via Ji's sum rule:

$$J^q = \frac{1}{2}\int_{-1}^{+1} dx x \left[H^q(x,\xi,\Delta^2=0) + E^q(x,\xi,\Delta^2=0)\right],$$
$$J^g = \frac{1}{2}\int_{-1}^{+1} dx \left[H^g(x,\xi,\Delta^2=0) + E^g(x,\xi,\Delta^2=0)\right]. \quad (2.26)$$

The used variables are listed in Tab. 2.2. The total quark contribution to the nucleon spin can be obtained, in principle, by extrapolating Eq. 2.26 to $t = 0$. Experimentally, GPDs can be probed via hard exclusive production of mesons (HEMP) or photons (DVCS) [35, 36]. While the HEMP process is discussed in the next section, GPDs are introduced in Sec. 2.4.

2.3 Exclusive Meson Production

Hard exclusive meson production includes the production of vector mesons as ρ^0, $\rho^\pm$, ω, ϕ and J/ψ, as well as pseudo-scalar mesons as π^0,$\pi^\pm$, $K^\pm$ and η. A schematic picture is presented in Fig. 2.8. This thesis is dedicated to the measurement of the ρ^0 meson. The ρ^0 meson is the lightest vector meson and, therefore, has the highest production cross section depicted in Fig. 2.9. The ρ^0 meson decays after the mean lifetime of $c\tau = 1.3\,\text{fm}$, with a branching ratio of almost 100% into a $\pi^+\pi^-$ pair. The pions themselves have a mean lifetime of $c\tau = 7.8$ m and can be detected in the spectrometer.

2.3.1 Factorisation Theorem

The factorisation of the amplitude of the scattering process into a short-distance and a long-distance part is not only valid for DIS processes, as introduced in Sec. 2.1.2. It can be translated into a more general case, where a finite momentum transfer to the target exists, for instance Deep Virtual Compton Scattering (DVCS) [38]. The factorisation is proven in the general Bjorken limit where, in addition to Eq. 2.2, W is large and the invariant momentum transfer t remains fixed. The long-distance part is then encoded in GPDs[14]. Schematically, this can be illustrated by:

$$d\sigma = [\text{partonic amplitude}] \otimes [\text{GPD}]. \quad (2.27)$$

For exclusive meson production, the factorisation approach is valid for reactions induced by longitudinally polarised virtual photons and is illustrated schematically in Fig. 2.10. In the particular case of the production of longitudinally polarised

[14]The properties of GPDs will be discussed in Sec. 2.4

Table 2.2: Important variables in HEMP.

$v = (E_{\rho^0}, \vec{v})$	Four-momentum-vector of ρ^0 meson
E_{ρ^0}	Energy of the ρ^0 meson
$M_{\pi\pi} = \sqrt{(v^2)}$	Invariant mass of the reconstructed ρ^0 meson
$M_x^2 = (p + q - v)^2$	Missing mass squared of the undetected system
p_T^2	Transverse momentum squared of the vector meson with respect to the virtual photon direction
$t = (p - p')^2 = (q - v)^2$ $= -\Delta^2$	Square of the four-momentum transfer to the target nucleon
t_0	Lower bound of the total four-momentum transfer
$t' = t - t_0$	Measure of the transverse four-momentum transfer
$\xi = x_{Bj} \frac{1+\frac{\Delta^2}{2Q^2}}{2-x_{Bj}+x_{Bj}\frac{\Delta^2}{Q^2}}$ $\approx \frac{x_{Bj}}{2-x_{Bj}}$	Skewness variable
$E_{\text{miss}} = \nu - E_{\rho^0} + \frac{t}{2M}$ $= \frac{(p+q-v)^2-p^2}{2 \cdot M_P}$	Missing energy of the undetected system
$z = \frac{p \cdot v}{p \cdot q} \overset{\text{lab}}{=} \frac{E_{\rho^0}}{\nu}$	Fractional energy of the ρ^0 meson

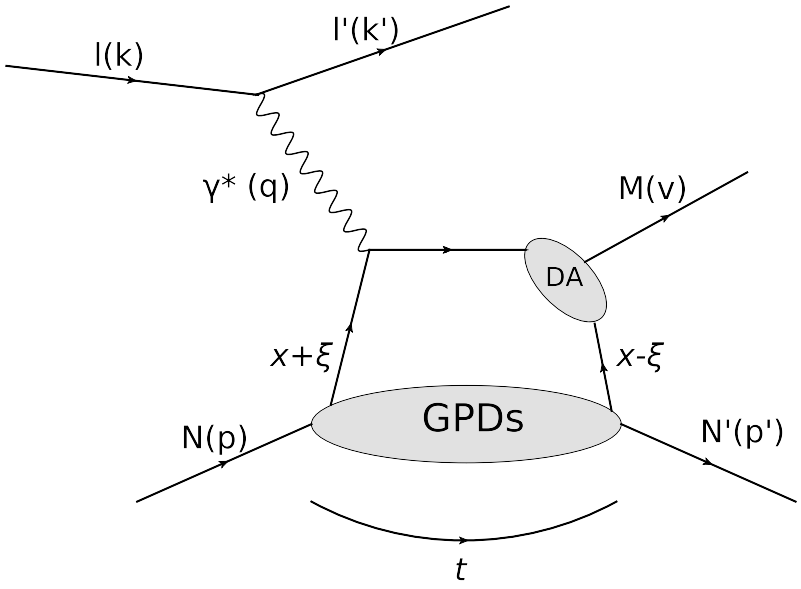

Figure 2.8: Schematic picture of hard exclusive meson production of the meson M. The four-vectors of the particles involved are given in parentheses. The Generalized Parton Distribution Functions (GPDs) and the meson Distribution Amplitude (DA) encode the long-distances physics due to the partonic sub-structure of the nucleon and the meson, respectively. They will be introduced later in this section.

ρ^0 mesons, induced by longitudinal polarised virtual photons the factorisation theorem is proven [5, 6]. The cross section for transversely polarised virtual photons is predicted to be smaller by a factor of $1/Q^2$ compared to that for longitudinally polarised ones.

The hard exclusive meson production (HEMP) is one possible process to probe GPDs. According to the quark content of the meson in the final state, the process is sensitive to different combinations of quark GPDs. Additionally, if the meson quantum numbers permit, the GPDs for gluons enter at the same order of α_S as those for quarks. However, a second non-perturbative quantity enters the process, which is known as meson distribution amplitude (DA). The DA describes the coupling of the meson to the $q\bar{q}$ pairs or gluons in the hard scattering process. As well as the PDFs, the GPDs and the DA depend on the factorization scale μ_F^2. The transformation of the virtual photon into the meson requires a finite momentum transfer t from the initial to the final proton. In an appropriate frame where both protons move fast this transfer has to be in direction of the initial proton. This is often referred as longitudinally momentum transfer.

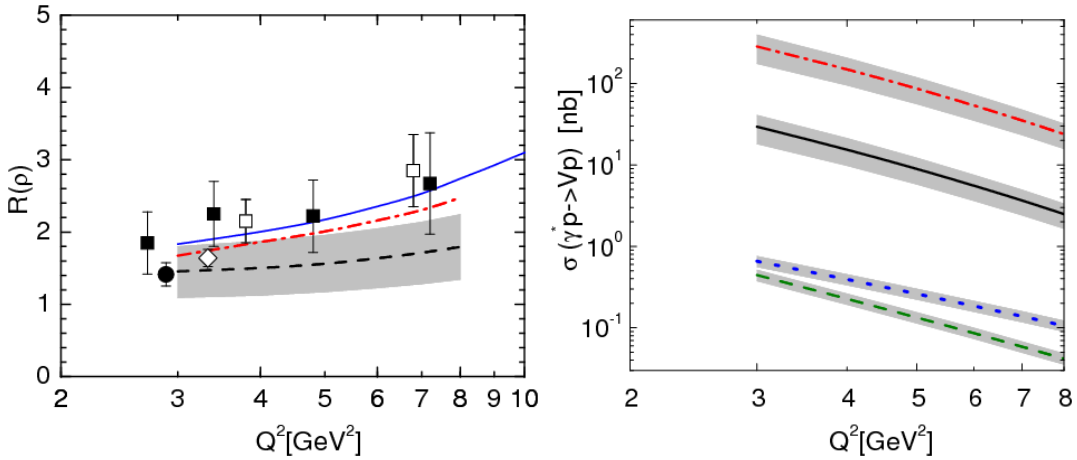

Figure 2.9: Left-hand panel: The ratio of longitudinal and transverse cross sections for ρ^0 production. Predictions for HERA (blue solid line), COMPASS (red dashed-dotted line) and Hermes (black dashed line) [37]. Right-hand panel: Model calculations of the integrated cross sections for vector meson production at W=10 GeV. Predictions for ρ^0 (red dotted-dashed line), ω (black solid line), ρ^+ (blue dotted line) and K^{*0} (green dashed line) [37].

2.3.2 Cross Section

In this section the cross section for the exclusive production of ρ^0 mesons is discussed. In this process a lepton l is scattered on a nucleon N, where in the final state the recoiled nucleon N', the scattered lepton l' and the ρ^0 meson are present:

$$lN \rightarrow l'\rho^0 N'. \tag{2.28}$$

The ρ^0 meson is detected via its decay particles π^+ and π^-. The reaction of Eq. 2.28 can be described in terms of the virtual photoproduction process:

$$\gamma^* N \rightarrow \rho^0 N'. \tag{2.29}$$

The angles ϕ and ϕ_S are defined according to the Trento conventions [40]. The azimuthal angle between the lepton scattering plane and the production plane defined by the virtual photon and the produced meson is denoted by ϕ, whereas ϕ_S is the azimuthal angle of the target spin vector around the direction of the virtual photon with respect to the lepton scattering plane (see Fig. 2.11). The target spin vector S is defined as:

$$\vec{S} = \begin{pmatrix} S_T \cos(\phi - \phi_S) \\ S_T \sin(\phi - \phi_S) \\ S_L \end{pmatrix}. \tag{2.30}$$

where S_L and S_T indicates the longitudinal and transverse polarisation component of the target nucleon relative to the virtual photon direction.

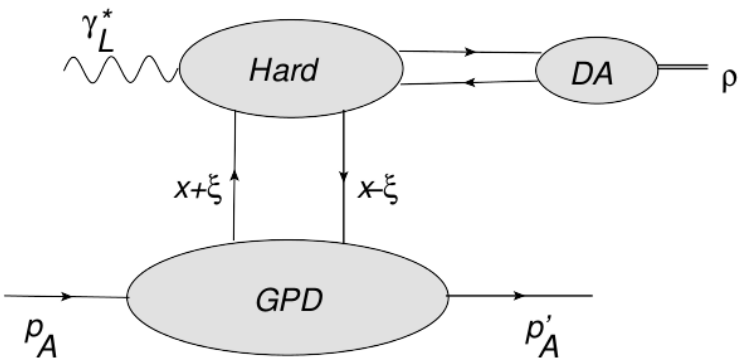

Figure 2.10: Schematic picture of the factorisation of hard exclusive meson production [39].

The cross section is derived in the target rest frame, according to Ref. [9]. As in DIS, the differential cross section for polarised scattering via a virtual photon can be expressed in terms of $L^{\nu\mu}$ and $W_{\mu\nu}$, the leptonic and hadronic tensors:

$$d\sigma(lN \to l\rho^0 X) \propto L^{\nu\mu} W_{\mu\nu} \frac{d^3k'}{2E} \frac{d^3v}{2E_\rho}, \tag{2.31}$$

with a proportionality factor depending on x_{Bj}, y and Q^2 which is not explicitly shown here. As mentioned above the leptonic tensor can be calculated in QED. As shown in Ref. [10], the leptonic tensor $L^{\nu\mu}$ can be expressed as a linear combination in terms of $\varepsilon_n^\nu \varepsilon_m^{\mu *}$:

$$L^{\nu\mu} = k'^\nu k^\mu + k^\nu k'^\mu - (k' \cdot k)\, g^{\nu\mu} + i P_\ell\, \epsilon^{\nu\mu\alpha\beta} q_\alpha k_\beta, \tag{2.32}$$

with:

$$g^{\nu\mu} = (\varepsilon^\nu \cdot \varepsilon^\mu), \tag{2.33}$$

$$\varepsilon^{\nu\mu\alpha\beta} = \det(\varepsilon^\nu, \varepsilon^\mu, \varepsilon^\alpha, \varepsilon^\beta). \tag{2.34}$$

and ε denotes the ratio of longitudinal and transverse photon-flux and is defined as:

$$\varepsilon = \frac{1 - y - \frac{1}{4}y^2\gamma^2}{1 - y + \frac{1}{2}y^2 + \frac{1}{4}y^2\gamma^2}\,, \tag{2.35}$$

with γ defined in Eq. 2.11. Here, terms depending on m_μ^2/Q^2 are neglected, where m_μ denotes the mass of the incoming lepton. In Eq. 2.32, the convention $\epsilon_{0123} = 1$ is used.

The polarisation of the exchanged virtual photon is fully described by the leptonic tensor. The polarisation vector ϵ^μ for a virtual photon is defined according to Ref. [9] in a right-handed coordinate system as:

$$\epsilon_0^\mu = \frac{1}{Q\sqrt{1+\gamma^2}} \left(q^\mu + \frac{Q^2}{p \cdot q}\, p^\mu \right), \tag{2.36}$$

$$\epsilon_{\pm 1} = \mp \frac{1}{\sqrt{2}(\epsilon_1 \pm \mathrm{i}\epsilon_2)} = \frac{1}{\sqrt{2}}\,(0, \mp 1, \mathrm{i}, 0). \tag{2.37}$$

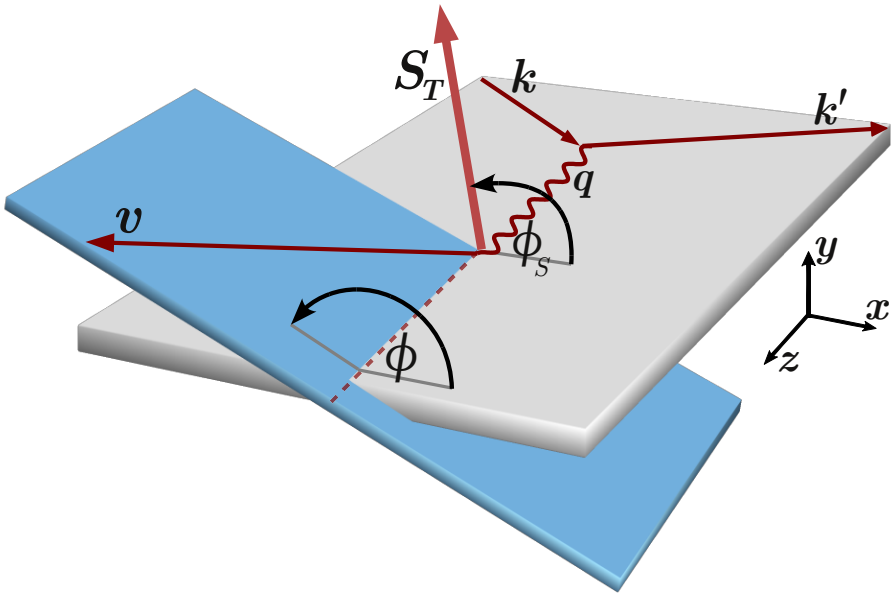

Figure 2.11: Definition of the angles ϕ and ϕ_s. Here k, k', q and v represent three-momentum vectors of the incident and the scattered muon, the virtual photon and the meson. The symbol S_T denotes the component of the target spin vector perpendicular to the virtual-photon direction.

The polarisation vector for positive and negative helicity is obtained as a combination of transversely polarised virtual photons, denoted by:

$$\epsilon_1 = \begin{pmatrix} 0 \\ 1 \\ 0 \\ 0 \end{pmatrix} \qquad \epsilon_2 = \begin{pmatrix} 0 \\ 0 \\ 1 \\ 0 \end{pmatrix}. \tag{2.38}$$

Eq. 2.36 describes longitudinally polarised virtual photons whereas Eq. 2.37 is valid for transversely polarised virtual photons.

The hadronic tensor is given by:

$$W_{\mu\nu} = \sum_{ij} \rho_{ji} \sum_{X} \delta^{(4)}(p' + v - p - q) \sum_{\text{spins}} \langle N(i)|J_\mu(0)|\rho^0 X\rangle \langle \rho^0 X|J_\nu(0)|N(j)\rangle, \tag{2.39}$$

where J_μ is the electromagnetic current and ρ_{ji} the spin density matrix. In general the spin orientation of an ensemble with particles with spin j can be characterised by a $(2j+1) \times (2j+1)$ matrix, known as the spin density matrix; for a spin-1/2 nucleon, the matrix can be written as:

$$\rho_{ji} = \frac{1}{2}\left[\delta_{ji} + \vec{S}\cdot\vec{\sigma}_{ji}\right] = \frac{1}{2}\begin{pmatrix} 1+S_L & S_T e^{-i(\phi-\phi_S)} \\ S_T e^{i(\phi-\phi_S)} & 1-S_L \end{pmatrix}, \tag{2.40}$$

where $\vec{\sigma}$ contains the three Pauli matrices and $\vec{S}$ is the nucleon spin vector. In Eq. 2.39, the $\sum_X$ denotes the integral over the momenta of all hadrons in the final state X. There are further sums $\sum_{ij}$ over target spin states $i, j = \pm\frac{1}{2}$ and $\sum_{\text{spins}}$

over all polarisations in the hadronic final state $\rho^0 X$. The contraction $L^{\nu\mu}W_{\mu\nu}$ can then be written in terms of the following quantities:

$$\sigma_{mn} = \sum_{ij} \rho_{ji}\, \sigma^{ij}_{mn} \propto \int dM_X^2\, (\epsilon^{\mu *}_m W_{\mu\nu}\, \epsilon^{\nu}_n), \tag{2.41}$$

where the proportionality factor, depending on x_{Bj} and Q^2, is chosen such that σ_{mm} is the $\gamma^* N$ cross section for photon helicity m. In Eq. 2.41 we have integrated over the invariant mass M_X^2 of the system X.

Finally, the cross section for exclusive ρ^0 muoproduction, $\mu N \to \mu' \rho^0 N'$, on a transversely polarised target reads [9][15]:

$$\begin{aligned}
&\left[\frac{\alpha_{\rm em}}{8\pi^3}\,\frac{y^2}{1-\varepsilon}\,\frac{1-x_{Bj}}{x_{Bj}}\,\frac{1}{Q^2}\right]^{-1} \frac{d\sigma}{dx_{Bj}\,dQ^2\,d\phi\,d\phi_S dt} \\
&= \frac{1}{2}\Big(\sigma^{++}_{++} + \sigma^{--}_{++}\Big) + \varepsilon\sigma^{++}_{00} - \varepsilon\cos(2\phi)\,{\rm Re}\,\sigma^{++}_{+-} - \sqrt{\varepsilon(1+\varepsilon)}\,\cos\phi\,{\rm Re}\,(\sigma^{++}_{+0} + \sigma^{--}_{+0}) \\
&\quad - P_\ell\,\sqrt{\varepsilon(1-\varepsilon)}\,\sin\phi\,{\rm Im}\,(\sigma^{++}_{+0} + \sigma^{--}_{+0}) \\
&\quad - S_T\left[\sin(\phi-\phi_S)\,{\rm Im}\,(\sigma^{+-}_{++} + \varepsilon\sigma^{+-}_{00}) + \frac{\varepsilon}{2}\sin(\phi+\phi_S)\,{\rm Im}\,\sigma^{+-}_{+-} + \frac{\varepsilon}{2}\sin(3\phi-\phi_S)\,{\rm Im}\,\sigma^{-+}_{+-}\right. \\
&\qquad \left. + \sqrt{\varepsilon(1+\varepsilon)}\,\sin\phi_S\,{\rm Im}\,\sigma^{+-}_{+0} + \sqrt{\varepsilon(1+\varepsilon)}\,\sin(2\phi-\phi_S)\,{\rm Im}\,\sigma^{-+}_{+0}\right] \\
&\quad + S_T P_\ell\left[\sqrt{1-\varepsilon^2}\,\cos(\phi-\phi_S)\,{\rm Re}\,\sigma^{+-}_{++}\right. \\
&\qquad \left. - \sqrt{\varepsilon(1-\varepsilon)}\,\cos\phi_S\,{\rm Re}\,\sigma^{+-}_{+0} - \sqrt{\varepsilon(1-\varepsilon)}\,\cos(2\phi-\phi_S)\,{\rm Re}\,\sigma^{-+}_{+0}\right].
\end{aligned} \tag{2.42}$$

The symbols $\sigma^{\nu\lambda}_{\mu\sigma}$ in Eq. 2.42 stand for polarised photoabsorption cross sections or interference terms, which are given as products of helicity amplitudes $\mathcal{M}$:

$$\sigma^{\nu\lambda}_{\mu\sigma} = \sum \mathcal{M}^*_{\mu'\nu',\mu\nu}\mathcal{M}_{\mu'\nu',\sigma\lambda}, \tag{2.43}$$

where the sum runs over $\mu' = 0, \pm 1$ and $\nu' = \pm 1/2$. The helicity amplitude labels appear in the following order: vector meson (μ'), final state proton (ν'), photon (μ or σ), initial state proton (ν or λ). For brevity, the helicities -1, -1/2, 0, 1/2, 1 are labelled by only their signs or zero. In general, $\sigma^{\nu\lambda}_{mn}$ depends on the kinematic variables x_{Bj} and Q^2, whereas the dependence on ε and ϕ is contained in $L^{\nu\mu}$ and the dependence on S_T, S_L and ϕ_S in ρ_{ji}. From hermiticity and parity invariance the following relations can be derived: $\sigma_{nm} = \sigma^*_{mn}$ and

$$\sigma^{ji}_{nm} = (\sigma^{\nu\lambda}_{mn})^*, \qquad \sigma^{-i-j}_{-m-n} = (-1)^{m-n-i+j}\,\sigma^{\nu\lambda}_{mn}. \tag{2.44}$$

[15] Note that the t-dependence of the cross section is indicated explicitly here and the definition of $\sigma^{\nu\lambda}_{\mu\sigma}$ given by Eq. 2.43 slightly differs from that in Ref. [9].

They imply that σ_{00}^{+-}, σ_{+-}^{+-} and σ_{+-}^{-+} are purely imaginary, whereas other interference terms have both real and imaginary parts. The structure functions can be obtained as combinations of the photoabsorption cross sections and interference terms as shown in Appendix B. The unpolarised cross section reads:

$$\sigma_0 = \sigma_{\mathrm{T}} + \varepsilon\sigma_{\mathrm{L}} = \frac{1}{2}(\sigma_{++}^{++} + \sigma_{++}^{--}) + \varepsilon\sigma_{00}^{+-}. \tag{2.45}$$

The S_T dependent part of Eq. 2.42 contains eight different azimuthal modulations: five sine modulations for the case of an unpolarised beam and three cosine modulations for the case of a longitudinally polarised beam. Each of the eight azimuthal modulations of the cross section in Eq. 2.42 give rise to a cross section asymmetry. It is defined as the ratio of the respective cross section or interference term to the unpolarised cross section σ_0:

$$\begin{aligned}
A_{\mathrm{UT}}^{\sin(\phi-\phi_s)} &= -\frac{\mathrm{Im}(\sigma_{++}^{+-} + \varepsilon\,\sigma_{00}^{+-})}{\sigma_0} & A_{\mathrm{LT}}^{\cos(\phi-\phi_S)} &= \frac{\mathrm{Re}\,\sigma_{++}^{+-}}{\sigma_0} \\
A_{\mathrm{UT}}^{\sin(\phi+\phi_s)} &= -\frac{\mathrm{Im}\,\sigma_{+-}^{+-}}{\sigma_0} & A_{\mathrm{LT}}^{\cos(\phi_s)} &= -\frac{\mathrm{Re}\,\sigma_{+0}^{+-}}{\sigma_0} \\
A_{\mathrm{UT}}^{\sin(3\phi-\phi_s)} &= -\frac{\mathrm{Im}\,\sigma_{+-}^{-+}}{\sigma_0} & A_{\mathrm{LT}}^{\cos(2\phi-\phi_s)} &= -\frac{\mathrm{Re}\,\sigma_{+0}^{-+}}{\sigma_0} \\
A_{\mathrm{UT}}^{\sin(\phi_s)} &= -\frac{\mathrm{Im}\,\sigma_{+0}^{+-}}{\sigma_0} & & \\
A_{\mathrm{UT}}^{\sin(2\phi-\phi_s)} &= -\frac{\mathrm{Im}\,\sigma_{+0}^{-+}}{\sigma_0}. & &
\end{aligned} \tag{2.46}$$

Here, the unpolarised (longitudinally polarised) beam is denoted by U (L) and the transverse target polarisation by T. The asymmetries in Eq. 2.46 are accessible in experiments where a longitudinally polarised lepton beam is scattered of a transversely polarised target, and the dependence on ϕ and ϕ_S is measured. Usually, in an experiment, the target is transversely polarised with respect to the direction of the lepton beam and the polarisation value is denoted by P_T. However, in Eq. 2.42, the target polarisation is transversely with respect to the direction of the virtual photon, which is denoted by S_T. In the kinematic region of COMPASS the effect due to the transition from S_T to P_T is small and Eq. 2.42 is used. A more detailed discussion of the transition is given in Sec. 7.4.

The factorization theorem shows that the leading transitions in the large Q^2 limit have both the virtual photon and the produced meson longitudinally polarised, all other transitions being suppressed by at least one power of $1/Q$. The only leading-twist observables are the longitudinal cross section σ_{00}^{++} and the interference term σ_{00}^{+-} . The only asymmetry containing a leading-twist term is $A_{\mathrm{UT}}^{\sin(\phi-\phi_S)}$where the leading-twist (higher-twist) term σ_{00}^{+-} (σ_{++}^{+-}) describes longitudinal ρ^0 production by longitudinal (transverse) photons [9]:

$$\begin{aligned}
\frac{\alpha_{\mathrm{em}}}{Q^6}\,\frac{x_{Bj}^2}{1-x_{Bj}}\,\frac{d\sigma_{00}^{++}}{dt} &= (1-\xi^2)\,|\mathcal{H}_{\rho^0}|^2 - \left(\xi^2 + \frac{t}{4M_p^2}\right)|\mathcal{E}_{\rho^0}|^2 - 2\xi^2\,\mathrm{Re}\,(\mathcal{E}_{\rho^0}^{*}\mathcal{H}_{\rho^0}), \\
\frac{\alpha_{\mathrm{em}}}{Q^6}\,\frac{x_{Bj}^2}{1-x_{Bj}}\,\mathrm{Im}\,\frac{d\sigma_{00}^{+-}}{dt} &= -\sqrt{1-\xi^2}\,\frac{\sqrt{-t'}}{M_p}\,\mathrm{Im}\,(\mathcal{E}_{\rho^0}^{*}\mathcal{H}_{\rho^0}).
\end{aligned} \tag{2.47}$$

The skewness variable ξ will be introduced in the next section, as well as $t' = t - t_0$ which will be discussed therein. The quantity $\mathcal{E}_{\rho^0}$ can be decomposed in [41]:

$$\mathcal{E}_{\rho^0} = \frac{1}{\sqrt{2}}(\frac{2}{3}\mathcal{E}^u + \frac{1}{3}\mathcal{E}^d + \frac{3}{4}\mathcal{E}^g). \tag{2.48}$$

The decomposition in Eq. 2.48 dependence on the measured meson in the final state. For instance for the ϕ meson it changes to:

$$\mathcal{E}_{\phi} = \frac{1}{\sqrt{2}}(\frac{1}{3}\mathcal{E}^s + \frac{1}{4}\mathcal{E}^g). \tag{2.49}$$

The quantities $\mathcal{E}^q$, $\mathcal{E}^g$ are integrals over the GPDs E^q, E^g in convolution with hard scattering kernels. Similar equations are valid for $\mathcal{H}$. The GPDs will be discussed in the next section.

2.4 Generalized Parton Distribution

The concept of Generalized Parton Distribution is introduced in Ref. [42]. Several reviews exist, see for instance Refs. [43, 44]. Here, we will mainly follow the extensive reviews in Refs. [45, 27, 36].

2.4.1 Properties of GPDs

In addition to the logarithmic Q^2 dependence, the GPDs depend on the three kinematic variable x, ξ and t, respectively, which are discussed individually in the following. An important difference, in comparison to ordinary PDFs, is the presence of a non-vanishing four-momentum transfer between the initial and final state proton, which is denoted with t. This includes that the momentum fraction carried by the struck parton in the nucleon differs between the initial and final states. The longitudinal momentum fraction, with respect to the average momentum of the initial and final state nucleon $(x+\xi)P^\mu$ and $(x-\xi)P^\mu$ is:

$$(x+\xi)P = \frac{x+\xi}{1+\xi} \qquad (x-\xi)P = \frac{x-\xi}{1-\xi}. \tag{2.50}$$

Here, x represents the average of the momentum fraction of the struck parton and the so-called skewness parameter ξ quantifies the deviation from the average of the momentum fraction before and after the hard scattering process. In DIS processes, the momentum fraction x carried by the struck parton is identified with the Bjorken variable x_{Bj}. This is not the case in exclusive processes, where x is an internal variable that is integrated over in a convolution of the given GPD with a kernel, that describes the hard virtual-photon quark interaction, and can assume values between -1 and 1. Therefore only ξ and t are experimentally accessible. For $Q^2 \gg M^2$ the relation [9]:

$$\xi \simeq \frac{x_{Bj}}{2 - x_{Bj}} > 0, \tag{2.51}$$

is valid. Hence the ξ coverage of a measurement is related to the coverage in x_{Bj} via Eq. 2.51. Additionally, non-vanishing values of ξ imply a lower bound of the total momentum transfer [9]:

$$|t| > |t_0| = \frac{4\xi^2 M^2}{1-\xi^2}. \tag{2.52}$$

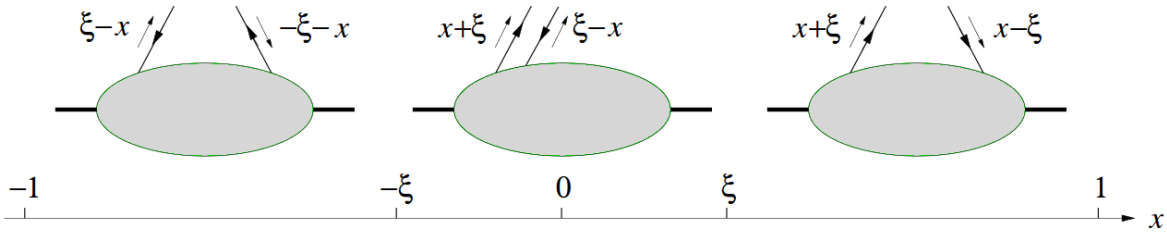

Figure 2.12: Schematic picture of the parton interpretation in different x ranges (Figure adapted from Ref. [45]).

Depending on the sign of the quantity $x \pm \xi$, the corresponding parton is interpreted as quark or anti-quark. As illustrated in Fig. 2.12, three different ranges have to be distinguished. For $x > \xi$ ($x < \xi$), the GPD is the amplitude to take a (anti-)quark of momentum $(-)x + \xi$ out of the proton and reinsert a (anti-)quark of momentum $(-)x - \xi$ into the proton to reform the recoiling proton. In this range, the GPD is a generalisation of the usual PDFs, defined in Eq. 2.18, and can be studied in DIS or SIDIS. In the remaining range $-\xi < x < \xi$, the GPD depicts taking out or inserting a $q\bar{q}$ pair with momentum $\pm x + \xi$.

As mentioned above and illustrated in Fig. 2.8 and Eq. 2.50, the momenta of the parton and the proton in the initial and the final state are not the same anymore. Therefore, GPDs do not correspond to squared amplitudes and can not be interpreted as probabilities. Instead, they parametrise the interference between amplitudes. The finite momentum transfer between the proton in the initial and final state is a very important attribute of GPDs. It leads to further interesting consequences in the interpretation of these objects. On the one hand, the momentum transfer can have a small transverse component. This encodes information about the transverse structure of the target and will be discussed in Sec. 2.4.1.2 in further detail. On the other hand, the finite momentum transfer allows for a change of the angular momentum of the corresponding parton. We will return to this aspect in Sec. 2.4.2. The exclusive meson production can be described by four parton helicity conserving GPDs, called $H(x,\xi,t)$, $E(x,\xi,t)$, $\tilde{H}(x,\xi,t)$ and $\tilde{E}(x,\xi,t)$ and four parton helicity flip GPDs, denoted by $H_T(x,\xi,t)$, $E_T(x,\xi,t)$, $\tilde{H}_T(x,\xi,t)$ and $\tilde{E}_T(x,\xi,t)$. The GPDs can be defined through non-forward matrix elements of quark and gluon operators with the general structure $\left\langle p'S'|\bar{\psi}(-\frac{1}{2}z)\mathcal{O}\psi(\frac{1}{2}z)|pS\right\rangle$, with $\mathcal{O} \in \{\gamma^+, \gamma^+\gamma^5, i\sigma^{+-}\}$. The spatial coordinate z of the quark and the momentum coordinates p of the nucleon are written in terms of light-cone-coordinates (Appendix A). The complete parametrisation can be found in Ref. [45]. Other parametrisations of GPDs exist, for instance see Refs. [46, 5, 47].

The parton helicity conserving GPDs have been studied for several years. The GPDs H and $\tilde{H}$ describe nucleon helicity non-flip matrix elements, while E and $\tilde{E}$ describe nucleon helicity flip matrix elements. Their properties are summarised in Fig. 2.13. For illustration, a model parametrisation for $H^u(x,\xi,0)$ is presented in Fig. 2.14.

The parton helicity flip GPDs, also called transversity GPDs, have been discussed recently [49, 50]. They were introduced in Refs. [51, 52]. Again, we have four

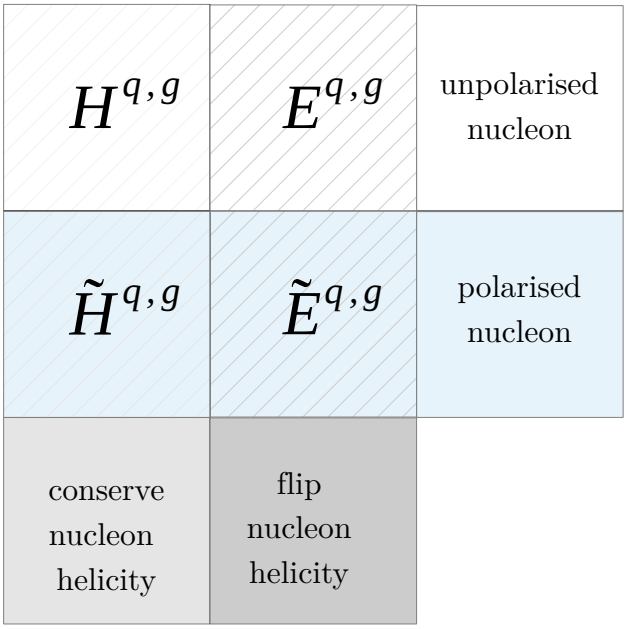

Figure 2.13: Interpretation of the GPDs H, E, $\tilde{H}$ and $\tilde{E}$ at the nucleon level.

different GPDs: H_T, E_T, $\tilde{H}_T$ and $\tilde{E}_T$. These distributions are off-diagonal in the parton helicity basis. But, they become diagonal if one changes the basis from eigenstates of helicity to eigenstates of transversity [53, 45]. For many processes, the quark transversity GPDs only play a minor role. The reason is that they require a helicity flip between the emitted and reabsorbed quark. The interaction of light quarks with gluons or photons conserve helicity. Hence the helicity flip has to be compensated by the utilisation of a higher-twist meson wave function [54].

2.4.1.1 Limiting Cases

In the forward limit, where $\xi = t = 0$,and $p = p'$, the hadrons have equal helicities in the initial and final state, The quark GPDs H^q and $\tilde{H}^q$, are related to the common parton distributions for quarks in unpolarised or polarised DIS [45]:

$$H^q(x,0,0) = \begin{cases} q(x), & \text{for } x > 0 \\ -\bar{q}(-x), & \text{for } x < 0 \end{cases} \tag{2.53}$$

$$\tilde{H}^q(x,0,0) = \begin{cases} \Delta q(x), & \text{for } x > 0 \\ -\Delta\bar{q}(-x), & \text{for } x < 0 \end{cases} \tag{2.54}$$

$$H_T^q(x,0,0) = \begin{cases} \Delta_T q(x), & \text{for } x > 0 \\ -\Delta_T\bar{q}(-x), & \text{for } x < 0. \end{cases} \tag{2.55}$$

A similar equality can be derived for the gluon GPDs H^g and $\tilde{H}^g$:

$$H^g(x,0,0) = xg(x), \quad \text{for } x > 0 \tag{2.56}$$

$$\tilde{H}^g(x,0,0) = x\Delta g(x), \quad \text{for } x > 0, \tag{2.57}$$

and the relations for $x < 0$. In this limit, $x \to x_{Bj}$ also applies. The GPDs E and $\tilde{E}$ do not have such analogues. The definition of these GPDs includes a multiplicative

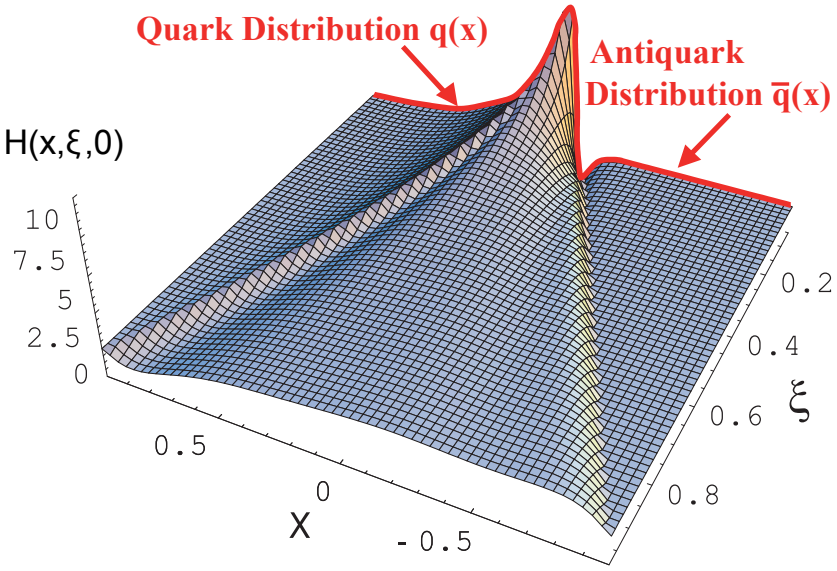

Figure 2.14: Model calculation for $H^u(x,\xi,0)$ [48]. The red line at $\xi = 0$ corresponds to the normal PDFs (Picture form Ref. [7]).

factor $\Delta = \sqrt{-t}$. Therefore, they are only accessible in exclusive reactions, with a finite momentum transverse to the target, and they vanish in the forward limit.

The Dirac and Pauli form factors, F_1 and F_2, of the proton are defined as matrix elements of the local electromagnetic current:

$$\sum_q e_q \left\langle p'S'|\bar{\psi}_q(0)\gamma_\mu\psi_q(0)|pS\right\rangle, \tag{2.58}$$

$$= F_1(t)\bar{u}(p',S')\gamma_\mu u(p,S) + F_2(t)\bar{u}(p',S')\frac{i\sigma_{\mu\alpha}\Delta^\alpha}{2M}u(p,S).$$

These operators are local because the initial and final quarks are created or annihilated at the same space-time point and they are non-diagonal since the initial and final nucleons have different momenta. Form factors provide a static two-dimensional picture of the nucleon although they do not contain information about the dynamical motion of the constituents as this would require knowledge of the momentum space distribution. The first moments of the GPDs, which are obtained by integrating over x, lead to the same matrix elements. Therefore, the parton helicity conserving GPDs are related to the nucleon form-factors by:

$$\int_{-1}^{1} dx H(x,\xi,t) = F_1(t), \tag{2.59}$$

$$\int_{-1}^{1} dx E(x,\xi,t) = F_2(t), \tag{2.60}$$

$$\int_{-1}^{1} dx \tilde{H}(x,\xi,t) = G_A(t), \tag{2.61}$$

$$\int_{-1}^{1} dx \tilde{E}(x,\xi,t) = G_P(t), \tag{2.62}$$

where the dependence on ξ drops out after integration over x. Here, F_1 and F_2 are again the Dirac and Pauli form-factors of the nucleon, and G_A and G_P are the axial and pseudo-scalar form-factors, respectively. They only depend on the four-momentum transfer t. Furthermore, the elastic form factors do not depend on the factorisation scale anymore as the local electromagnetic current is conserved and the elastic form factors are physical observables, in contrast to GPDs or PDFs.

2.4.1.2 Impact Parameter Interpretation

The fact that the ordinary PDFs, as well as the form factors, can be derived from GPDs as limiting cases, points to the situation that both, momentum and space position of the quarks, are encoded in GPDs. First, we introduce the transverse locations of partons denoted with b. Then, a Fourier transform of GPDs with respect to the momentum transfer in the transverse direction is built, which is known as impact parameter distribution [55, 56, 57]:

$$q(x, |b|) = \int \frac{d^2\Delta}{(2\pi)^2} e^{-i\Delta_\perp \cdot b} H^q(x, \xi = 0, t = -\Delta^2). \tag{2.63}$$

Here, the case, $\xi = 0$ is discussed although a generalisation to $\xi \neq 0$ is possible. In this representation, the parton has a definite longitudinal momentum fraction x_i and a definite transverse location b_i. It can be shown that $q(x, b)$ has a density interpretation in the infinite momentum frame [55]. Often GPDs are said to provide a three-dimensional picture of the nucleon. This interpretation can be traced back to the fact that the impact parameter b represents the two-dimensional coordinate in transverse space of the probed parton relative to the center-of-momentum B^*:

$$B^* = \sum_i x_i b_i, \tag{2.64}$$

where x_i contains the longitudinally momentum fraction of the parton. In Fig. 2.15 the impact-parameter representation for three different values of x is illustrated.

Also for the other GPDs a Fourier transformation, as shown in Eq. 2.63 is possible. Whereas H^q is related to the impact parameter distribution of unpolarised quarks in an unpolarised nucleon, $\tilde{H}^q$ is related to the distribution of longitudinally polarised quarks in a longitudinally polarised nucleon and E^q is related to the distortion of the unpolarised quark distribution in the transverse plane when the nucleon has transverse polarisation.

2.4.2 GPDs and Spin

As already mentioned above, the GPDs $E^q(x, \xi, t)$ and $\tilde{E}^q(x, \xi, t)$ describe reactions with nucleon helicity flip; while the quark helicity is conserved. This can happen only if quarks carry orbital angular momentum. Thus these GPDs also contain information about the orbital angular momenta carried by quarks. The total angular momentum J is the sum of the total angular momenta of the quarks q, denoted by J^q, and the total angular momentum of the gluons, J^g, and can be obtained through the equation:

$$\sum_q J^q + J^g = J_z = \frac{1}{2}. \tag{2.65}$$

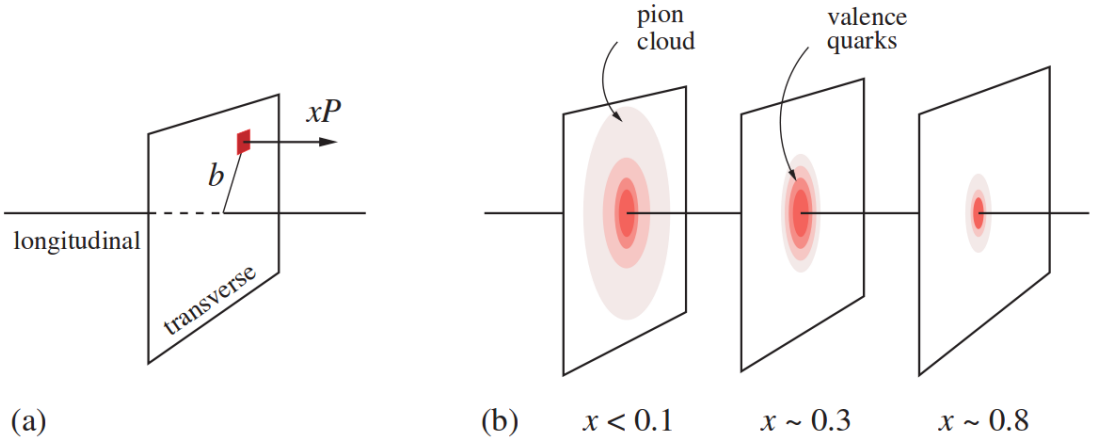

Figure 2.15: Schematic picture of the nucleon tomography. The Fourier transform of the GPD describes the simultaneous distribution of quarks with respect to longitudinal momentum, xP, and transverse position, b, in the infinite momentum frame (a). It produces a $1+2$ dimensional tomographic picture of the quark structure of the nucleon. Here, shown exemplarily for three different x values [58].

The total angular momentum J is uniquely defined. However, this is not the case if the total angular momentum of an interacting multi-constituent system is decomposed into the contributions from its constituents. Furthermore, the decomposition depends on the gauge used. Therefore, several possible spin decompositions of the nucleon spin exist, each of them having its advantages and disadvantages. Beside the decomposition proposed by Jaffe and Manohar presented in Eq. 1.1, another well known decomposition was introduced by Ji [4] and results in:

$$\vec{J} = \sum_q \left(\vec{S}^q + \vec{L}^q \right) + \vec{J}^g. \tag{2.66}$$

This decomposition is gauge invariant and all three terms can be calculated in the lattice gauge theory. The expectation values $\vec{S}^q$ and $\vec{J}^q$ can be accessed experimentally, and $\vec{J}$ can, at least in principle, be accessed in HEMP. The main drawback of this decomposition is that only the term $\vec{S}$ has, for the z-quantization axis, an interpretation as number densities. In contrast, in Eq. 1.1, each of the terms have such a partonic interpretation. A summary of several decompositions, including the Jaffe-Manohar decomposition and Ji decomposition and the decompositions from Belinfante, Chen et al. and Wakamatsu can be found in Ref. [59].

It is possible to calculate moments of GPDs on the lattice. For instance, this can be used to evaluate J^u and J^d. A recent lattice calculation [60] gives:

$$J^u = 0.22 \pm 0.02, \tag{2.67}$$

$$J^d = 0.00 \pm 0.02, \tag{2.68}$$

at $m_\pi \approx 350\,\text{MeV}$, with $L_u \approx -L_d \approx 20 - 30\%$ of the protons spin $\frac{1}{2}$. These values of the total angular momentum contributions are close to the asymptotic values predicted by QCD evolution. A model-dependent constraints on u-quark total angular momentum J^u vs. d-quark total angular momentum J^d is shown in Fig. 2.16.

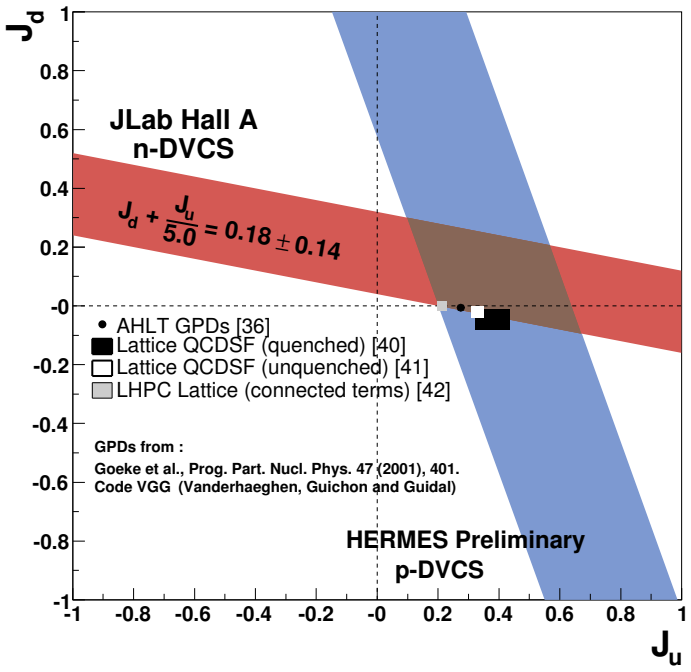

Figure 2.16: Model-dependent constraints on u-quark total angular momentum J^u vs. d-quark total angular momentum J^d [61].

2.5 Experimental Constraints for GPDs

GPDs are only accessible in exclusive reactions with a finite momentum transverse to the target. Experimentally, the measurement of exclusive processes is very challenging. The reasons are that the cross sections are rather small and the verification of the exclusivity of the reaction is required. Therefore, especially for those GPDs without a forward limit measurable in unpolarised or polarised DIS (see Sec. 2.4.1.1), only a limited number of experimental data is available to provide constraints for GPDs. A summary of the current status can be found in Tab. 2.3. An additional difficulty arises because the GPDs typically appear in the physical observables, for example $A_{\mathrm{UT}}^{\sin(\phi-\phi_S)}$, in a convolution with hard scattering amplitudes, and can not be extracted directly from the measured data.

2.6 From Asymmetries to GPDs

This work is dedicated to the evaluation of transverse single-spin and double-spin asymmetries in exclusive ρ^0 production on a NH_3 and ^{6}LiD target. These asymmetries can be used to constrain GPDs. Presently only model-dependent extractions of GPDs are known. After a short introduction to the principles of GPD modelling in Sec. 2.6.1, the model from Goloskokov and Kroll (GK model) is presented in Sec. 2.6.2.

Table 2.3: Summary of experimental and theoretical constraints for different GPDs [62].

GPDs	constraints for valence quarks		constraints for gluons and sea quarks	
	experimental	theoretical	experimental	theoretical
H	ρ^0, ϕ cross section	PDFs, Dirac form factor	ρ^0, ϕ cross sections	PDFs
$\tilde{H}$	π^+ data	Polarised PDFs, Axial form factor	$A_{\mathrm{LL}}(\rho^0)$	Polarised PDFs
E	$A_{\mathrm{UT}}^{\sin(\phi-\phi_S)}(\rho^0,\phi)$	Pauli form factor	-	Sum rule of 2nd moments
$\tilde{E}$	π^+ data	Pseudo-scalar form factor	-	-
H_T, E_T	π^+ data, $A_{\mathrm{UT}}^{\sin\phi_S}(\rho^0)$	transversity PDFs	-	-

2.6.1 Modelling GPDs

There are several reviews on GPDs available which also address the modelling of GPDs (see, for instance, Ref. [27]) and provide a good overview of the different concepts. GPD models are based on the ordinary parton densities that are used as input or as a boundary condition. Additionally, an ansatz for the t and ξ dependence is required. Finally, the modelled GPDs have to satisfy the positivity bounds, the polynomiality and the limiting cases which are summarised in Sec. 2.4. Polynomiality implies that the n-th moment of one GPD $F(x,\xi,t)$, $\int_{-1}^{1} dx x^n F(x,\xi,t))$ is described by polynom of order n or $n+1$ in ξ. Mainly there are two approaches, the double-distribution (DD) [63] and the dual representation [64, 65].

The DD representation is widely used and is based on a factorisation of the GPD into a GPD in the forward limit, a ξ dependent term and a factor that generates the t-dependence. However, since this factorisation assumption is not strictly valid, alternative approaches also exist. One of these alternatives is the dual representation, based on a partial wave expansion of the GPDs in the t channel.

2.6.2 The Model from Goloskokov and Kroll

This model is based on a phenomenological 'handbag' approach. The handbag approach is based on factorization of the process amplitudes in the hard sub-process, and soft hadronic matrix elements parametrised in terms of GPDs. Here, GPDs are parametrised using the DD factorisation [66].

Recently the transversity GPDs were included in the model [49], which was motivated by measurements of the HERMES Collaboration. The HERMES Collaboration extracted single-spin asymmetries as a function of t, x_{Bj} and Q^2 for exclusive produced π^+ mesons. The measurement was performed by scattering positrons or electrons with 27.6 GeV/c on a transversely polarised hydrogen target. Most of the

asymmetries were found to be small, except $A_{\mathrm{UT}}^{\sin\phi_S}$ which was found to be large and positive [67]. It was observed that the asymmetry $A_{\mathrm{UT}}^{\sin\phi_S}$ does not vanish for $t \to 0$. These findings could not be explained, in terms of the model of Goloskokov and Kroll, with the GPDs $\tilde{H}$ and $\tilde{E}$ alone. But the extension of the model by including the transversity GPDs has shown promising results [49, 50] in explaining this observation. This phenomenological approach can also be applied in a very similar way to ρ^0 production.

The model of Goloskokov and Kroll includes both longitudinally-photon contributions as well as transverse-photon contributions, which are expressed in terms of helicity amplitudes as introduced in Sec. 2.1.3. Up to now no rigorous treatment is available in pQCD to calculate the moments from helicity amplitudes if transverse-photon contributions are involved. The presently best suited ansatz to include these contributions is the phenomenological 'handbag' approach, based on $k_\perp$-factorisation. In this model, the meson distribution amplitude introduced in Sec. 2.3 is replaced by twist-3 meson wave functions parametrised according to Ref. [54]. Therefore, this approach allows to go beyond leading twist and includes the transversity GPDs mentioned in Sec. 2.4.

The GPDs are parametrised via [66, 68, 62]:

$$F^i(x.\xi,t) = \int_{-1}^{1} du \int_{-1+|u|}^{1-|u|} dv \delta(u+\xi v - x) f^i(u,\eta,t) + D_i \Theta(\xi^2 - x^2), \tag{2.69}$$

where the last part in the equation is the D-term [69], which arises from the polynomiality conditions. Here, the GPD is written as a convolution of the zero-skewness GPD and a weight function:

$$f_i(u,\eta,t) = F^i(u,\xi=0,t) w_i(u,\eta), \tag{2.70}$$

The weight function generates the ξ dependence and is written as:

$$w_i(u,v,t) = \frac{\Gamma(2n_i+2)}{2^{2n_i+1}\Gamma^2(n_i+1)} \frac{[(1-|u|)^2 - v^2)]^{n_i}}{(1-|u|)^{2n_i+1}}. \tag{2.71}$$

Here, $n = 1$ is valid for valence quarks, whereas $n = 2$ is used for sea quarks and gluons. The zero-skewness GPD consists of the quark GPD in the forward limit multiplied with a term which generates the t dependence:

$$F^i(u,\xi=0,t) = F^i(u,\xi=0,t=0) e^{p_{fi}(u)t}, \tag{2.72}$$

where $p_{fi}(u)$ is the profile function [62]. For the forward limits $F^i(u,\xi=0,t=0)$ of the quark GPDs H, $\tilde{H}$ and H_T the parton distributions, helicity distributions and transversity distributions, respectively, determined in DIS and SIDIS measurements, are used. The parametrisation of the forward limits of the other GPDs is much more involved since limits from measurements are not existing. Thus they are parametrised via:

$$F^i(u,\xi=0,t=0) = c_i u^{\alpha_i} (1-u)^{\beta_i}, \tag{2.73}$$

and the parameters c_i, α_i and β_i are constrained by lattice calculations and from fits to data. A description of the parametrisation of the gluon GPDs can be found in Ref. [66].

Table 2.4: Summary of possible transitions in exclusive ρ^0 production. The helicity amplitudes and the corresponding GPDs are given [62].

transition	helicity amplitudes	GPDs	chiral	
$\gamma_L^* \to \rho_L^0$	$\mathcal{M}_{0+,0+}$	H	even	dominant
	$\mathcal{M}_{0-,0+}$	E	even	dominant
$\gamma_T^* \to \rho_T^0$	$\mathcal{M}_{++,++}$	H	even	suppressed
	$\mathcal{M}_{+-,++}$	E	even	suppressed
$\gamma_T^* \to \rho_L^0$	$\mathcal{M}_{0-,++}$	H_T	odd	
	$\mathcal{M}_{0+,++}$	$\bar{E}_T$	odd	
$\gamma_L^* \to \rho_T^0$				suppressed, neglected
$\gamma_T^* \to \rho_{-T}^0$				suppressed, neglected

The possible transitions from the virtual-photon to the ρ^0 meson are listed in Tab. 2.4. A given transition can be written as a suitable combination of helicity amplitudes. Note that in the GK model all terms which are suppressed by at least $\sqrt{-t}/Q^2$ are neglected. The dominant $\gamma_L^* \to \rho_L^0$ transitions are described by the helicity amplitudes $\mathcal{M}_{0+,0+}$ and $\mathcal{M}_{0-,0+}$. The suppressed $\gamma_T^* \to \rho_T^0$ transitions are described by the helicity amplitudes $\mathcal{M}_{++,++}$ and $\mathcal{M}_{+-,++}$. Both amplitudes are related to H and E. The $\gamma_T^* \to \rho_L^0$ transitions are described by the amplitude $\mathcal{M}_{0-,++}$ and $\mathcal{M}_{0+,++}$. The first amplitude is related to the transversity GPD H_T, whereas the latter is related to combinations of transversity GPDs denoted by $\bar{E}_T$ [54], where:

$$\bar{E}_T = 2\tilde{H}_T + E_T. \tag{2.74}$$

These transitions can only be described if transversity GPDs are included in the model. The transitions $\gamma_L^* \to \rho_T^0$ and $\gamma_T^* \to \rho_{-T}^0$ are suppressed in the model calculations [70] and therefore neglected. This treatment is in agreement with experimental results. The helicity amplitudes describing the transitions are reappearing in some Spin Density Matrix Elements (SDMEs) that have been measured at HERMES [71] and H1 [72] and found to be small. The connection of the helicity amplitudes and the GPDs with the measured asymmetries in terms of the GK model will be discussed in Sec. 9.2.

3. The COMPASS Experiment

The COMPASS experiment is situated at the high intensity M2 beam line of the CERN SPS[1]. The main focus is on the investigation of the nucleon spin structure and the hadron spectroscopy. It is a fixed target experiment with a very flexible setup, which allows measurements with muon as well as hadron beams on unpolarised, longitudinally polarised or transverse polarised targets. The scattered muons and the produced particles are detected in the 50 m long two-stage spectrometer set-up downstream of the target. An artistic view of the COMPASS detector is shown in Fig. 3.1. A detailed description can be found in [73].

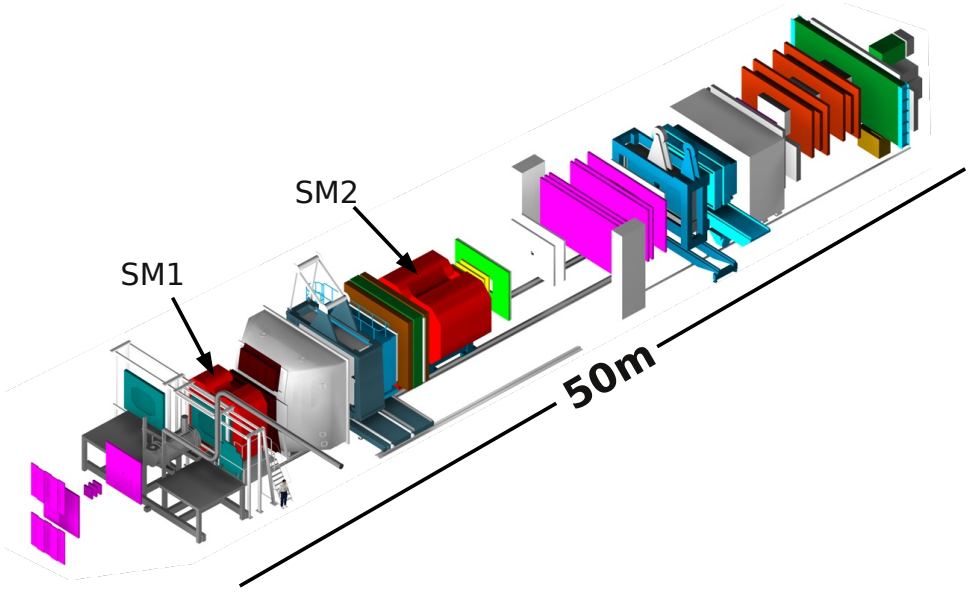

Figure 3.1: Artistic view of the COMPASS spectrometer. Picture adapted from Ref. [73]. The marking of the detector components can be found in Fig. 3.6.

[1]Super Proton Synchrotron

In this chapter mainly the setup of the year 2010 is described. Even so several years were used in the analysis, only significant differences are highlighted. Beside of the description of the beam line and the COMPASS spectrometer layout, the data acquisition and the trigger system as well as the data analysis chain are introduced.

3.1 The Beam Line

At COMPASS the hadron structure can be studied using muon as well as different hadron beams. A high intense primary proton beam is provided from the SPS at CERN. The protons are extracted during the so-called on-spill phase to the M2 beam line with an energy up to 450 GeV/c. The duration of each spill primarily depends on the number of experiments served by the SPS. The flux on the primary target is limited to 1.45 $\cdot 10^{13}$ protons during a 4.8 s extraction period and rises to 2.40 $\cdot 10^{13}$ protons if a 9.6 s long extraction is provided [75].

The measurements analysed in this thesis are performed using a tertiary μ^+ beam. The beam is produced by scattering the high intense primary proton beam on a Beryllium target (T6) with 500 mm thickness (Fig. 3.2). The secondary hadrons created in the interaction are mainly pions with a contamination of kaons of about 3.6%. A sizable fraction of these particles decay in a 650 m long tunnel in muons and neutrinos. The muons are selected by absorbing the remaining hadrons at the end of the decay tunnel with a hadron absorber. The momentum selection of the muons is done by magnetic collimation, with alternating focusing and defocusing quadrupole magnets. The remaining muons are focused and transported via a 400 m long beam line to the COMPASS experiment.

The muons produced in the decay process and used for the experiments can have a momentum from 60 GeV/c up to 190 GeV/c. They are naturally longitudinally polarised due to the parity violating nature of the weak decay. In the pion rest frame 100% of the muons are polarised. In the laboratory frame the average polarisation of the beam is a function of the pion and muon energy, given by E_π and E_μ:

$$P_{\mu^\pm} \approx \mp \frac{m_\pi^2 + (1 - 2\frac{E_{pi}}{E_\mu})m_\mu^2}{m_\pi^2 - m_\mu^2}, \tag{3.1}$$

where the sign of the polarisation is depending on the muon charge and is chosen to be negative for positive muons. The average muon polarisation as a function of the

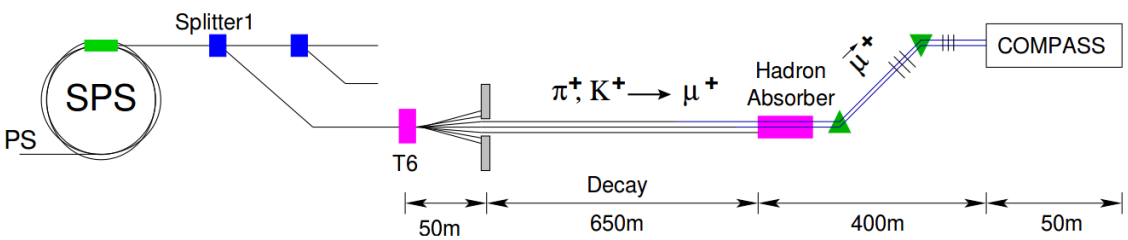

Figure 3.2: Generation of the μ^+ beam for the COMPASS experiment. The splitter magnets allow the sharing of the proton beam between different experimental halls. Picture adapted from Ref. [74].

muon momentum is presented on the left-hand side of Fig. 3.3. The selected muon momentum is a compromise between the reachable polarisation and total muon flux depicted on the right-hand side of Fig. 3.3. The used beam has a nominal momentum of 160 GeV/c with a spread of 5% and a longitudinal polarisation of $P_\ell \approx -0.8$. As mentioned above the spill length and the muon flux depend on the year. Up to 2007 the complete cycle lasts 16.8 s and the muons were extracted during a 4.8 s long spill with an intensity up to $2 \cdot 10^8$ μ/spill. In 2010 the data were taken at a mean intensity of $3.5 \cdot 10^8$ μ/spill, for an extraction length of about 9.6 s every 40 s.

On account of the considerable momentum spread and the broad diameter of the secondary beam it is very important to measure the momentum and the trajectory of every incoming muon. This is done with the Beam Momentum Station (BMS) which is situated around 100 m in front of the target. It consists of two scintillating fibre stations (BM05, BM06) and four scintillating hodoscopes (BM01-BM04) placed upstream and downstream of three bending dipole magnets (B6) and four quadruples (Q29-Q32). A schematic drawing of the BMS and the magnets is shown in Fig. 3.4. The measured precision is about $\delta p/p = 0.5\%$. Finally the beam is focused on the target, where the beam spot has the RMS width of about 0.8·0.8 cm^2.

3.2 The Polarised Target

The goal of the muon program of COMPASS is the measurement of cross section asymmetries. The corresponding observable is the asymmetry $A \propto P_T f \Delta\sigma$ where $\Delta\sigma$ is the cross section difference between two different spin configurations for the given process and P_T is the target polarisation. The measurement of such an observable is feasible if the selected target material is polarised to a high degree and both factors, P_T and f, are as large as possible to optimise the statistical significance of the measurements. The dilution factor f is calculated as the fraction of polarisable material weighted by the corresponding cross sections and depends on the analysed process. In the presented analysis the dilution factor is evaluated for incoherent exclusive ρ^0 production using the measured material composition and the nuclear dependence of the cross section.

While at a low enough temperature, the electron spin can be aligned in a strong magnetic field, only a negligible nuclear spin polarisation can be reached with the same conditions. At COMPASS the method of dynamic nuclear polarisation (DNP)

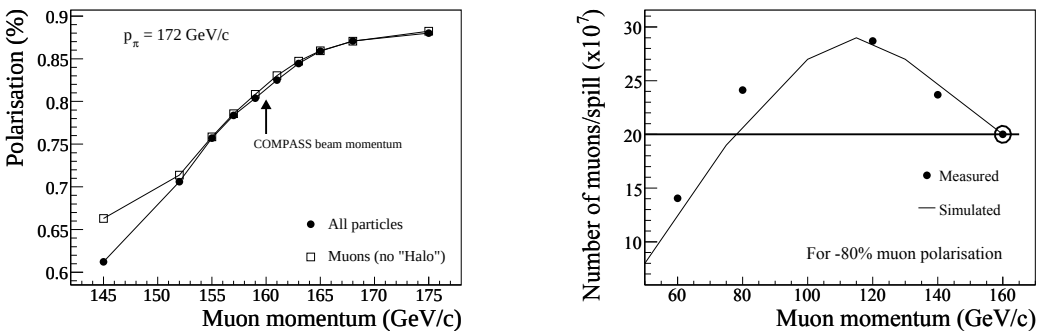

Figure 3.3: Muon momentum versus polarisation (left-hand side) and muon momentum versus total muon flux for a 4.8 s long spill (right-hand side) [73].

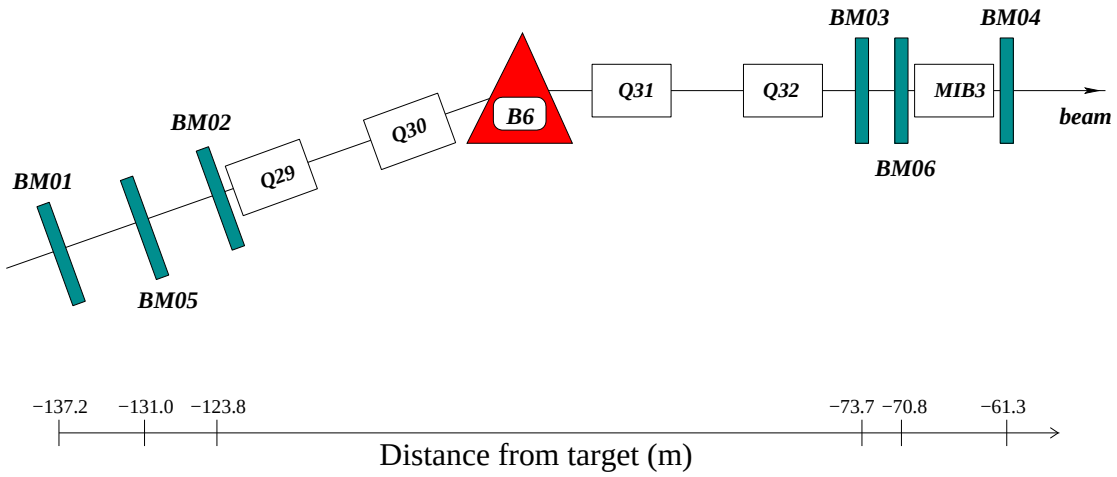

Figure 3.4: Layout of the BMS station [73].

is used to polarise the solid state targets [76]. This method demands for a material containing $\approx 10^{-5}$ of paramagnetic centres created by irradiation, a temperature below 1K and a strong and homogeneous magnetic field. These requirements are fulfilled by deuterated lithium (^{6}LiD) and the ammonia (NH_3), which have been chosen as target materials for polarised deuterons and protons, respectively. The polarisation of the unpaired electrons in the paramagnetic centres is almost 100% and is transferred to the nuclear spins of protons or deuterons by means of a microwave field.

The ammonia is contained in three cylindrical target cells with a diameter of 4 cm, placed one after another along the beam. The central cell is 60 cm long and the two outer ones are 30 cm long and 5 cm apart. The deuterated lithium target consist of only two cells, again placed one after another along the beam. Each of the cells has a diameter of 3 cm and a length of 60 cm with a 10 cm long gap in between. The spin directions in neighbouring cells are opposite. The target configuration allows for a simultaneous measurement of azimuthal asymmetries for the two opposite target spin directions in order to become independent of beam flux measurements. Systematic effects due to acceptance are reduced by reversing the spin directions on a weekly basis. With the three-cell configuration the acceptance for cells with opposite polarisation is more balanced, leading to a further reduction of systematic effects. From 2002 to 2004 the angular acceptance was 70 mrad at the upstream edge of the target. From 2006 onwards an upgraded target magnet with a new large-aperture solenoid was used. It provides an angular acceptance of 180 mrad for the upstream target edge resulting in an increased hadron acceptance.

A schematic picture of the target structure is presented in Fig. 3.5. The chosen target is located within a large aperture magnet with a dipole holding field of 0.5 T. A strong longitudinal magnetic solenoidal field of 2.5 T is generated by a superconducting magnet. It is used when polarising the target material. With a mixture of liquid ^{3}He and ^{4}He the target is cooled down to 50 mK. Ten NMR coils surrounding the target allow for a measurement of the target polarisation P_T, which typical amounts to $P_T = \approx 80\%$ or $P_T = \approx 50\%$ with an uncertainty of 3% and 5% for protons and deuterons, respectively. The dilutions factors are $f \approx 0.25$ and $f \approx 0.45$ for protons

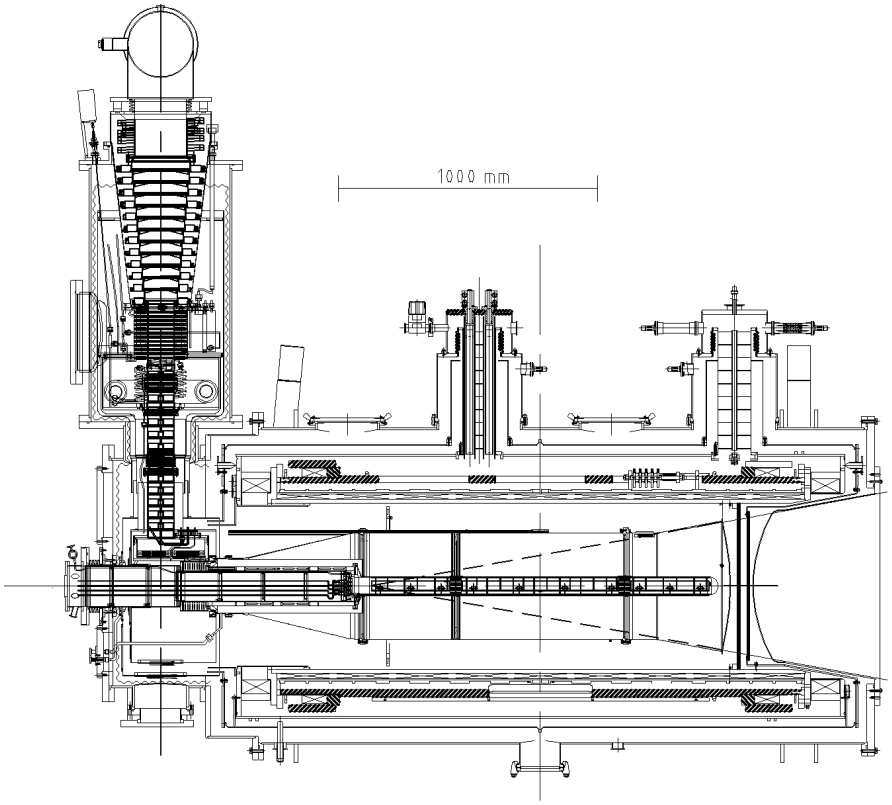

Figure 3.5: Side view of the COMPASS NH_3 polarised target (picture from Ref. [77]).

and deuterons [78]. A summary of the target compositions for the different years of data taking is presented in Tab. 3.1 and Tab. 3.2. The target cells are denoted, in the direction of the muon beam, with U (UP), C (CENTRAL) and D (DOWN). A schematic view of the naming scheme for the target cells is presented in Fig. 6.1.

3.3 The Spectrometer

3.3.1 Overview

The spectrometer consists of two stages. This allows the reconstruction of scattered muons and produced hadrons in a wide kinematic range. The Large Angle Spectrometer (LAS) starts directly behind the target region. It is built around a dipole magnet (SM1) with a field strength of 1.0 T and is designed to detect particles emitted under a large polar angle and particles with a low momentum. The Small Angle Spectrometer (SAS) is built around a second dipole magnet (SM2) with a field strength of 4.4 T. The SAS is used to measure high momentum particles emitted at angles smaller then 30 mrad with respect to the beam axis. The setup provides an excellent polar angle acceptance. Each stage has tracking detectors before and after the dipole magnet, hadronic and electromagnetic calorimeters and muon identification. In the first stage the RICH-1[2] detector allows to identify charged particles,

[2]RIng Imaging CHerenkov

Table 3.1: Target composition for 2007 [79] (upper part) and 2010 [80] (lower part).

	U [mol]	C [mol]	D [mol]
proton	25.903±0.141	55.663±0.282	28.439±0.141
deuteron	0.003±0.001	0.006±0.001	0.003±0.001
helium-3	0.547±0.070	1.026±0.120	0.502±0.070
helium-4	6.716±0.370	12.589±0.690	6.162±0.340
nitrogen-14	8.604±0.047	18.488±0.094	9.446±0.047
nitrogen-15	0.032±0.001	0.068±0.001	0.035±0.001
proton	27.32±0.282	54.374±0.564	33.16±0.282
deuteron	0.003±0.001	0.006±0.001	0.004±0.001
helium-3	0.308±0.038	0.619±0.077	0.247±0.030
helium-4	6.663±0.377	13.385±0.762	5.333±0.294
nitrogen-14	9.07±0.094	18.06±0.188	11.01±0.094
nitrogen-15	0.034±0.001	0.067±0.001	0.041±0.001

Table 3.2: Target composition for 2003 [81] (left-hand side) and 2004 [82] (right-hand side). The errors are presented if available in the publications.

	U [mol]	D [mol]	U [mol]	D [mol]
proton	0.11	0.11	0.105±0.010	0.108±0.010
deuteron	21.23	21.97	20.844±0.280	21.574±0.255
helium-3	0.9±0.3	0.9±0.3	0.669±0.171	0.647±0.163
helium-4	9.1±0.4	8.9±0.4	7.128±0.812	6.892±0.763
lithium-6	20.44	21.15	20.027±0.282	20.729±0.259
lithium-7	0.90	0.93	0.922±0.033	0.954±0.033

i.e. to separate between pions, kaons and protons. The top view of the COMPASS spectrometer is shown in Fig. 3.6.

The detector components will be described in the following section. For further information references to the publications of the different detector components will be given.

3.3.2 Tracking Detectors

A variety of types of tracking detectors are installed in the COMPASS spectrometer to handle best the expected particle flux, the needed spatial or time resolution and the required active region over the whole spectrometer. Additional the amount of material along the beam path has to remain a minimum in order to minimise multiple scattering and secondary interactions. The particle flux per unit transverse surface decreases by five orders of magnitude going from the region closest to the beam to the largest angles accepted by the spectrometer. Therefore the different types

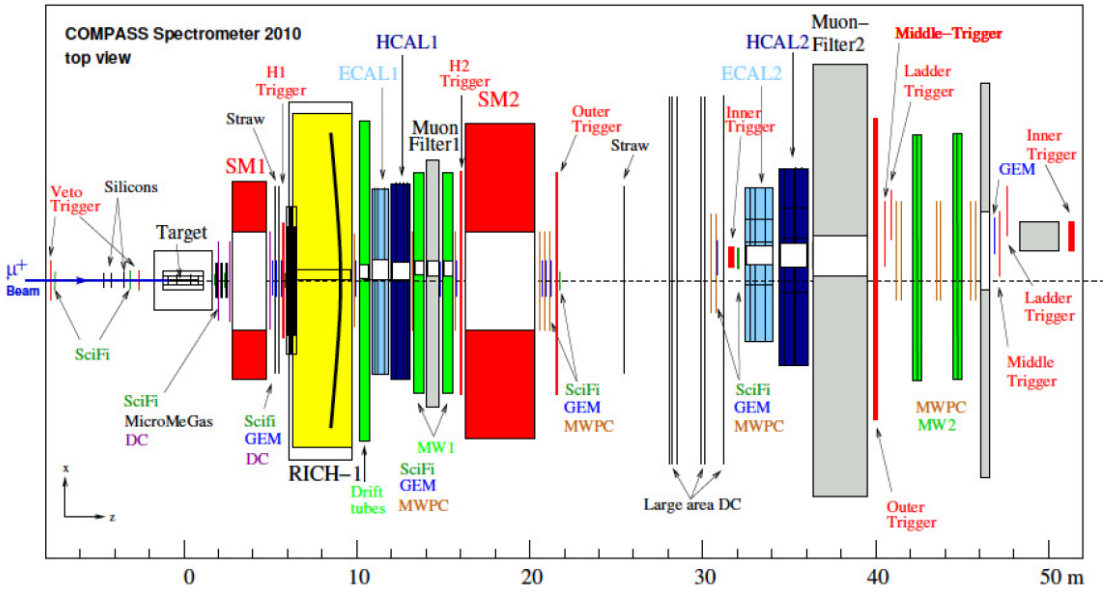

Figure 3.6: Top view of the COMPASS spectrometer in 2010 [83].

of tracking detectors used can be grouped in three classes: The Very Small Area Trackers (VSAT), which cover the beam region up to a radial distance of 2.5 cm - 3 cm, the Small Area Trackers (SAT), which cover the intermediate region at a radial distance of 2.5 cm to 40 cm and the Large Area Trackers (LAT) which cover the outermost regions.

Near the beam axis high particle rates up to $10^5\,\mathrm{mm^{-2}s^{-1}}$ occur [73]. The VSAT detectors have to be radiation hard and need to have a very good spatial resolution of 100-200 μm or a time resolution of up to 3 ns. This allows a precise vertex reconstruction and a good spatial resolution of the reconstructed tracks. Here, Scintillating fibres (SciFi) [84] and Silicon micro-strip detectors (SI) [85] are used. The SciFis are placed upstream and downstream of the target. They have an enormous rate capability of up to 5 MHz per fibre. They provide the tracking of the incoming and scattered muon as well as of all other charged reaction products very near of the centre of the primary beam. The SIs complement the tracking of the incoming beam trajectories.

Further from the centre as SAT detectors two types of gaseous detectors, the micromesh (MicroMega) detectors (MM) [86] and the Gaseous Electron Multiplier (GEM/GM) [87], are installed. The detectors have a region of about 3 cm in the central part which can be electrically deactivated, so that high momentum particles emitted under a small polar angle can fly to the SAS. The MMs have a typical space resolution of 70 μm and a time resolution better than 10 ns, where for the GEMs the space resolution is $\approx$ 50 μm and the time resolution $\approx$ 12 ns.

The LAT consist of three different designs: the planar drift chambers (DC) [73] and the large drift chambers W4-5 [73], the Straw Tube detectors (ST) [88] and the Multi-Wire Proportional Chambers (MWPC) [73, 89]. All detectors have active areas of several m^2.

3.3.3 Particle Identification

Muon Identification

The scattered muons are identified with the Muon Wall 1/2 (MW1/MW2) [73]. Both detector systems are located at the end of each spectrometer stage and consist of a hadron absorber called Muon Filter 1/2 (MF1/MF2) and several tracking detectors in front and behind the muon filters. Additionally the Muon Filter 3 (MF3) is placed in front of the hodoscope H5. The muon filters absorb all particles except the weak interacting muons. Therefore a particle is identified as a muon if its track can be reconstructed before and after the absorber. The Muon Wall MW1 is located at the end of LAS in front of SM2 and consist of a 60 cm thick iron absorber surrounded by gaseous wire detector called Mini Drift Tube (MDT). The MW2 consist of a 2.4 m thick concrete absorber followed by two Drift Tube stations and three MWPC stations.

Calorimeters

In each of the spectrometer stages an electromagnetic (ECAL1/ECAL2) followed by a hadronic calorimeter (HCAL1/HCAL2) are installed [90].

The aim of the ECALs is to measure the energy of electrons and photons. An electromagnetic shower is initiated if an electron or photon pass through the material. The electrons and positrons of the occurred shower emit Cherenkov radiation, where the intensity is proportional to the energy of the initial particle. Initially both ECALs consisted of lead glass modules. The ECAL1 has a size of $3.97 \times 2.86\,\mathrm{m}^2$ and is operational since 2006. The ECAL2 covers an area of $2.44 \times 1.83\,\mathrm{m}^2$. Before the run in 2008 it was partially upgraded. Near the beam axis, the lead glass GAMS modules were replaced by Shashlik sampling modules as they cope with a higher irradiation dose and provide an improved energy resolution.

Each hadron calorimeter is placed after the electromagnetic calorimeter and in front of the muon filter to measure the energy of the hadrons produced in the target and to participate in the triggering of inelastic muon scattering events. Additionally they can be used to identify muons which only deposit a characteristic small amount of energy in few detector cells. Both HCALs are sampling calorimeters with alternating iron converters and plastic scintillator plates. If a strong interacting particle passes through the iron it initiates a hadronic shower which produces a light signal in the scintillators. As for the ECALs, the sum of the signals is then proportional to the energy deposited by the hadron in the calorimeter.

The RICH-1 Detector

The LAS is equipped with a Ring Imaging CHerenkov detector (RICH-1) [91, 92] which allows for hadron identification. The RICH-1 is filled with the radiator gas C_4F_{10}. The index of refraction is $n = 1.0015$, at a temperature of 25°C and 1013 mbar pressure. If particles pass through this dielectric medium with a velocity βc larger as the speed of light c/n in this medium Cherenkov light is emitted under the characteristic angle:

$$\cos\Theta_C = \frac{1}{(\beta n)} = \frac{1}{n\sqrt{1+\frac{m^2}{p^2}}}, \tag{3.2}$$

with respect to the direction of motion. Here, m and p denote the mass and the momentum of the particle. Therefore, if Θ_C is measured the velocity of the particle can be determined. Additionally, if the momentum of the particle is known the corresponding mass can be calculated and thus the particle type can be identified.

The emitted Cherenkov photons are reflected and focused by two spherical mirror surfaces to the photo-detection areas outside the LAS spectrometer acceptance. The minimum momentum p_{ptr} for which Cherenkov photons get emitted depends on n and is received if Eq. 3.2 is evaluated for the limiting case $\cos\Theta_C = 1$:

$$p_{ptr} = \frac{m}{\sqrt{n^2 - 1}}. \tag{3.3}$$

The RICH-1 enables the identification of pions π, kaons K and protons P in a momentum range between $p_{min,\pi} = 2.5\,\mathrm{GeV}/c$, $p_{min,K} = 9\,\mathrm{GeV}/c$, $p_{min,P} = 17\,\mathrm{GeV}/c$ and $p_{max} \approx 50\,\mathrm{GeV}/c$. The RICH Wall, a large size tracking detector, is installed between the RICH-1 and the first electromagnetic calorimeter. It consists of eight alternating layers of Mini Drift Tubes (MDT) and converter layers made of stacks of steel and lead plates.

During the COMPASS upgrade in 2005 the RICH-1 detector was equipped with multi anode photo-multipliers in the central region and with new frontend readout electronics for the outer part to improve the particle identification.

3.4 The Trigger System

The aim of the trigger system is to select an interesting event candidate and activate the data recording. This has to happen with a decision time below 500 ns and a minimum dead time in a high rate environment. The trigger system [93] consists of different fast hodoscopes and two scintillating veto stations upstream of the target, mainly to select the scattered muon. To increase the trigger purity, in particular in the small Q^2 domain, the energy deposits in calorimeters complemented the trigger system. Three different classes of triggers exists:

- **Inclusive triggers** only require a scattered muon.
- **Semi-inclusive triggers** require a scattered muon and in addition a certain deposited amount of energy in at least one of the calorimeters ECAL1, HCAL1 or HCAL2.
- **Calorimeter trigger** only require a certain deposited energy in one of the calorimeters ECAL1, HCAL1 and HCAL2 where the required minimal deposited energy is higher as for the semi-inclusive trigger.

The triggering on muons which interact with the target is performed by demanding timed and spacial correlations of hits in pairs of hodoscopes. Two different trigger concepts are used, the so-called target pointing trigger and the so-called energy loss trigger. The target pointing trigger measures the scattering angle of the muon in a direction perpendicular to the bending plane of the dipole magnets SM1 and SM2. This is done by demanding a hit pattern in the hodoscopes which corresponds to

a track pointing towards the target. Thus requires horizontal scintillator strips. The energy loss triggers have vertical strips and use the fact that the muons which transferred some energy to the target nucleon get more deflected in the bending plane.

The setup allows to trigger on muons in two different kinematic ranges: the regime of deep inelastic scattering and the production of quasi-real photons. In the deep inelastic scattering range with $Q^2 > 0.5\,(\mathrm{GeV}/c)^2$ the information from the scattered muon is sufficient for triggering. It is extracted using the hodoscopes and the target pointing method. The quasi-real photon events with smaller four-momentum transfer occur under a very small scattering angle. Here the energy loss method is used. Additional also background events e.g. radiative events or low energy halo tracks have a small scattering angle. Therefore, the limited position accuracy of the track measurements of the incoming and outgoing muon will not allow to determine the vertex position with a satisfying precision. These events require additionally the information from the hadronic calorimeter. The elements of the muon trigger for the 2010 setup are distributed over the whole spectrometer as shown schematically in Fig. 3.7. They consist of four stations, the three semi-inclusive called inner (IT) (H4I, H5I), middle (MT) (H4M, H5M), ladder (LT) (H4L, H5L) and the inclusive outer (OT) (H3O, H4O), where each station is built up out of two scintillating hodoscopes. The kinematical coverage in y and Q^2 for the four hodoscope trigger subsystems and the calorimetric trigger is shown in Fig. 3.8.

In 2010 a new Large Angle Spectrometer Trigger (LAST) was set up. It consist of two additional hodoscopes H1 and H2, where H2 is composed of two halves (H2J and H2S). The H1 is situated in front of the RICH-1 where as H2 is located after the MF1 and MW1 modules. The goal of the LAST is the extension of the kinematic range towards higher Q^2. The trigger concept is similar to the OT the vertical target pointing. It replaces the pure calorimeter trigger (CT) in 2007. Additionally in 2007 the large Q^2 trigger was used. An analysis of the trigger performance in 2007 and 2010 can be found in Ref. [94].

Furthermore a veto system is installed. It prohibits muons not interacting with the target, so-called halo muons, from activating the data taking. It consist of two segmented scintillating counters in front of the target. They have a central hole of about 4 cm so it is not disturbing the beam. A third counter is installed 30 cm upstream of the target. It rejects the halo muons with a smaller slope.

3.5 Data Acquisition and Reconstruction

The data acquisition of the COMPASS experiment has to handle more than 250 000 detector channels with high trigger rates up to 100 kHz. The data is constantly digitised and buffered, where possible directly at the detector front-end electronics, in either dedicated ASICs[3] and/or sampling analog-to-digital (ADC) or time-to-digital (TDC) modules. The amplitudes or time information is transferred to the read-out modules named CATCH[4] and GeSiCA[5]. From 2010 onwards also GANDALF[6] [95]

[3] Application Specific Integrated Circuit

[4] Compass Accumulate, Transfer and Control Hardware

[5] Gem and Silicon Control and Acquisition

[6] Generic Advanced Numerical Device for Analytic and Logic Functions

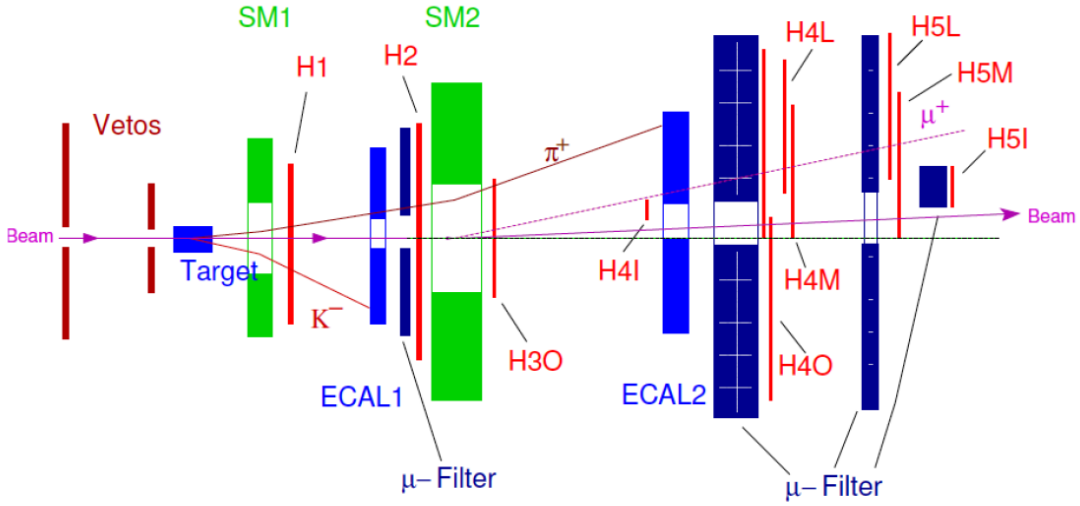

Figure 3.7: The trigger setup in 2010 [83].

modules are used. The synchronisation of the digitising and readout units is performed by the trigger control system (TCS). From the readout modules the data is transferred via optical S-LINK to the readout buffers and afterwards to the event builder. Schematically, the data flow is shown in Fig. 3.9.

The raw data contains all information about the recorded events and is stored on the Cern Advanced STORage manager (CASTOR). For data analysis it is processed by the reconstruction program CORAL[7]. In the first step the stored data are decoded, i.e. the information on the fired detector channel, either wire, pad, or cell, is extracted from the data and afterwards clustered, i.e. detector channels that are fired by the same particle are grouped together. Next, the tracks and vertices are reconstructed using a Kalman filter [96]. The information on tracks, vertices, clusters in the calorimeters and particle types (RICH likelihoods) are stored for every event in mDSTs[8]. A schematic view of the data reconstruction is presented in Fig. 3.10.

The data analysis is done with the PHysics Analysis Software Tools, PHAST [97]. It provides a summary of often used functions to access the information stored for every event and an environment for the development of physics analysis codes. It allows the analysis of COMPASS data on the level of mDST. The ROOT [98] framework can be used therein.

Additional in this thesis Monte-Carlo (MC) data generated by LEPTO [99] and PYTHIA [100] is used. After the generation the MC events are processed though COMGEANT, a program based on GEANT3 [101]. The GEANT[9] package is a collection of functions which allow to simulate the COMPASS spectrometer with predefined geometrical shapes. Also the response of the different detector types is simulated. It takes care of transporting the particles through the geometry and the

[7] COmpass Reconstruction and AnaLysis
[8] mini Data Summary Trees
[9] GEometry ANd TRacking

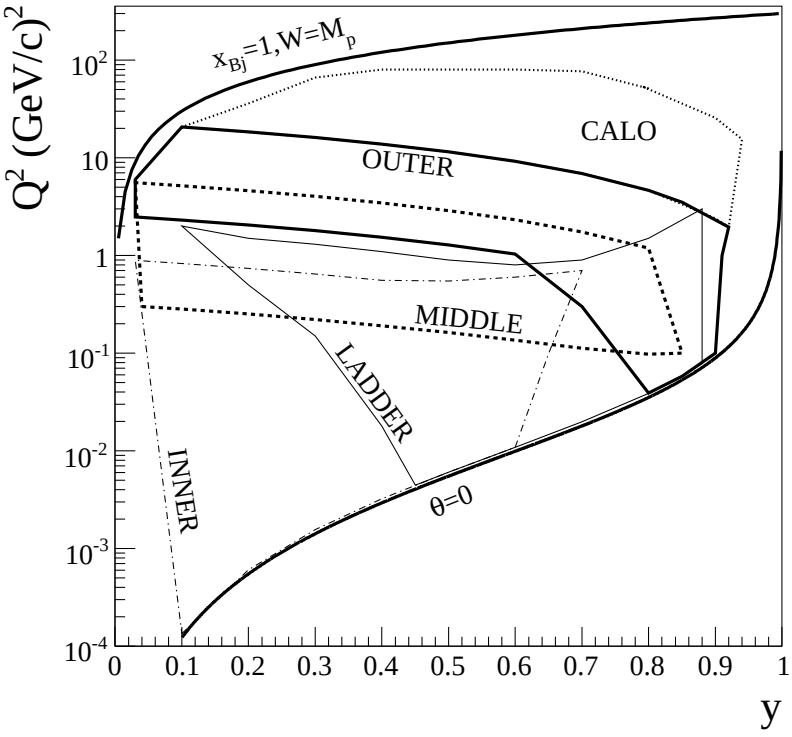

Figure 3.8: The kinematical coverage in y and Q^2 for the four hodoscope trigger subsystems and the calorimetric trigger [73].

varying material of the detectors, performing the different interaction of electromagnetic particles, hadrons and charged leptons. The MC events are also reconstructed with CORAL and can be analysed with PHAST.

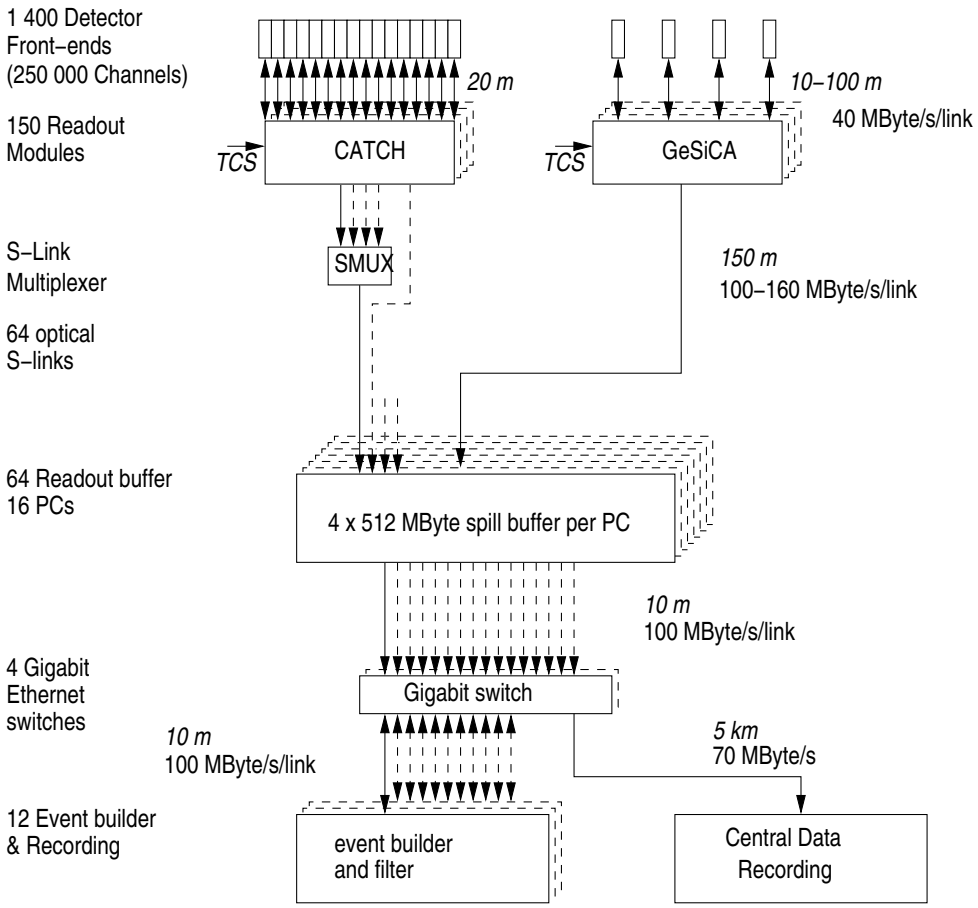

Figure 3.9: Architecture of the data acquisition [73].

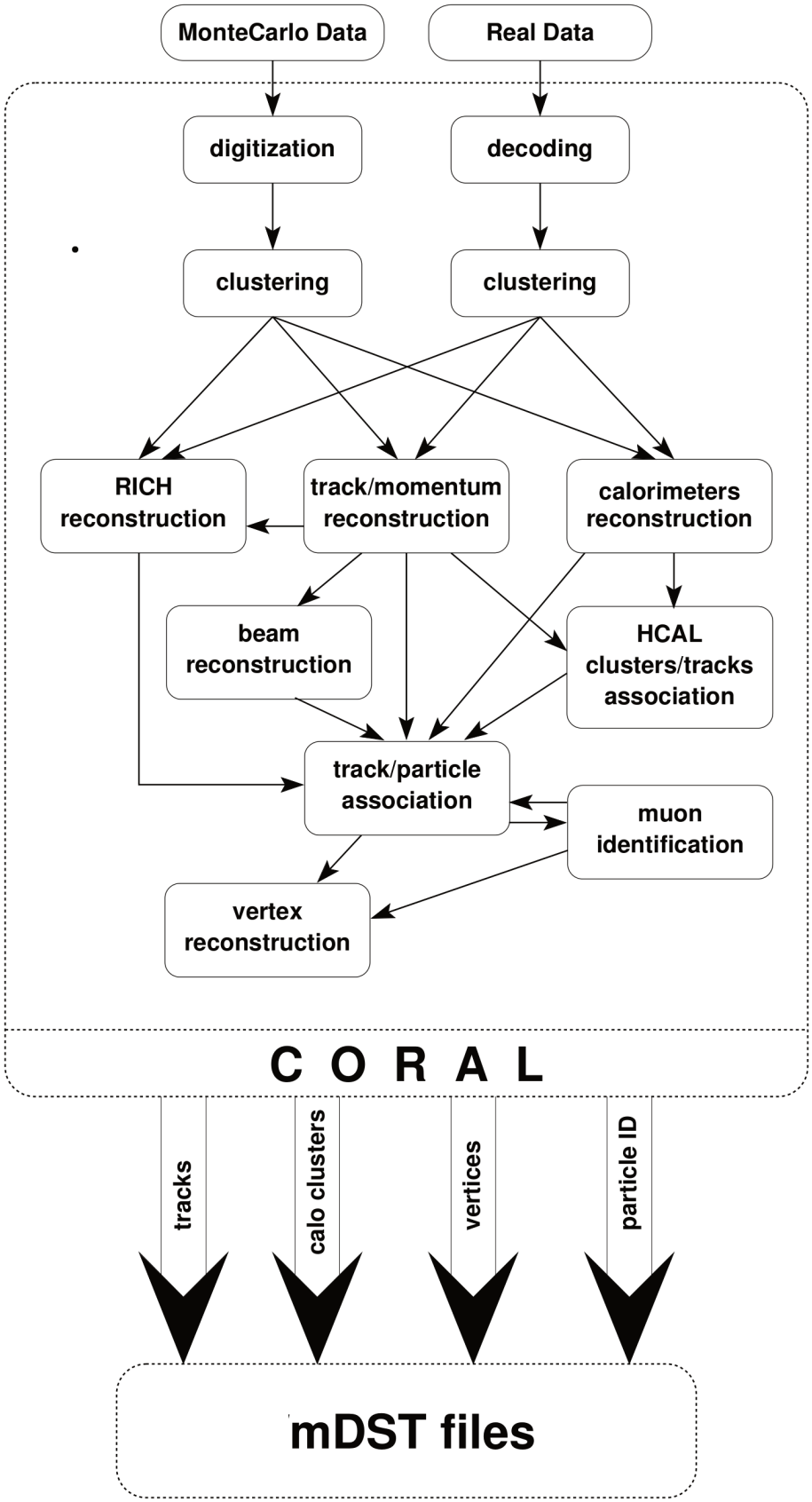

Figure 3.10: Reconstruction of data and MC [73].

4. Data Selection

In this thesis COMPASS data taken with transversely polarised targets is analysed. The measurements were performed during the years 2002-2004 (^{6}LiD target) and 2007 & 2010 (NH_3 target). In this section the reconstruction and selection of exclusive ρ^0 muoproduction events are described. Unless otherwise noted, identical cuts are used for the data taken with ^{6}LiD and NH_3 target. Before the various cuts are introduced, the underlying data sample is presented and the data quality checks at COMPASS are summarised.

4.1 Used Data

The data taking in COMPASS is organised in runs, where every run has a length of up to 200 spills. The length of the spills varies from year to year (Sec. 3). After processing the data, the important information of every event is stored in mDST files and can be analysed individually with PHAST and ROOT (Sec. 3.5). Before applying the user-defined cuts a pre-selection is done requiring a primary vertex[1] with at least one reconstructed outgoing muon and a photon virtuality $Q^2 > 1\,(\mathrm{GeV/c})^2$ for 2007 and $Q^2 > 0.7\,(\mathrm{GeV/c})^2$ for 2010 data. These cuts are mandatory for selecting deep inelastic scattering events and reduce the amount of data significantly. For 2003 and 2004 the analysis was started from a $Q^2 > 1\,(\mathrm{GeV}/c)^2$ sample.

Transversely Polarised NH_3

In 2007 the data taking at COMPASS was equally shared between a transversely polarised and a longitudinally polarised NH_3 target. With a transverse spin configuration 12 sub-periods were recorded, named with period 25-31 and 39-43, while in between data taking with a longitudinal target polarisation was performed. Each of the sub-periods has a length of about 5 days. The spin is reversed regularly, mostly after one or two sub-periods. In Tab. 4.1 the production slots of 2007 data, employed in this analysis, are listed. For the analysis the third production is used, which has the same alignment as the second production and the CORAL version 08-7-30-slc4.

[1] The primary vertex is defined as a vertex which contains a beam particle.

The used runs are summarised in Tab. 4.2. The three runs 62769, 62861 and 63807 could not be used in the analysis, since at the time of the analysis they were not accessible due to CASTOR problems. In 2007 a total number of $3 \cdot 10^{18}$ protons were delivered to the experimental hall, which corresponds to 440 TByte of data written to tape.

Table 4.1: Production slots used for 2007.

	W25	W26	W27	W28	W30	W31
slot	2-7	2-7	4-7	3-7	0-7	0-7
	W39	W40	W41	W42a	W42b	W43
slot	4-7	3-7	4-7	5-7	5-7	4-7

In 2010 the COMPASS data taking, which started in June and finished in November, was dedicated to the measurement with a transversely polarised NH_3 target. The data is split in 12 different periods, each consisting of two sub-periods with a length of about 5 days. Again, about every second sub-period the target polarisation is reversed. The periods are summarised in Tab. 4.2. The data is produced with the CORAL version 20101213. For nearly all periods slot 1 is used, except period W27. Here, slot 2 is used. In 2010 a total number of $36.6 \cdot 10^9$ events were collected and written on tape which corresponds to 1815.3 TByte of data.

Transversely Polarised ^{6}LiD

In total eight periods of data were collected with a deuterated lithium target (^{6}LiD), two periods in 2003 and four periods in 2004. They are summarised in 4.3.

Data taking was started at COMPASS in 2002. Already in the first year data with a transversely polarised deuterated ^{6}LiD target was recorded. This data has been analysed as well. The selection of exclusive ρ^0 events is based on a cut on the missing energy distribution E_{miss} as it will be introduced in Sec. 4.3.4.2. In the analyses of the 2002 data a significant shift in the E_{miss} distribution was observed. The E_{miss} shape is sensitive to the spectrometer setup as well as the alignment. A shift in this distribution might reflect instabilities in the data taking. Furthermore a not adequate E_{miss} shape leads to the selection of wrong ρ^0 candidates. Hence the 2002 measurement is excluded from the analysis, which leads to a reduction of the available deuteron data of 15%.

Combined Analysis of Several Years

The measurement with a ^{6}LiD target and NH_3 target were both done in two different years and additionally subdivided in several periods. Although the changes in the spectrometer setup between the periods are kept as small as possible, changes could not completely be prevented. In previous analyses at COMPASS the asymmetries were extracted on a period-wise basis, combining two sub-periods in which the data taking was performed under comparable conditions. The final asymmetries are calculated as the weighted sum of the period-wise extracted asymmetries.

Table 4.2: Overview of periods in 2007 and 2010. The left half of the table is dedicated to sub-periods where the target cells are polarised $+-+$, in the direction of the muon beam. For every sub-period the first and the last run is given. The right half of the table is dedicated to sub-periods where the target cells are polarised $-+-$, in the direction of the muon beam. Again, for every sub-period the first and the last run is given.

$+-+$	first run	last run	$-+-$	first run	last run
07W26	58267	58580	07W25	57992	58191
07W28	59225	59396	07W27	58844	59034
07W30	59966	60085	07W31	60147	60328
07W39	62747	62898	07W40	63013	63122
07W42a	63496	63608	07W41	63226	63354
07W42b	63610	63671	07W43	63754	63805
10W23b	85093	85164	10W23a	85026	85070
10W24a	85197	85301	10W24b	85362	85445
10W26b	85569	85638	10W26a	85468	85512
10W27a	85669	85713	10W27b	85771	85850
10W29a	86202	86323	10W29b	86355	86446
10W31b	86641	86703	10W31a	86462	86600
10W33a	86784	86945	10W33b	87024	87135
10W35b	87518	87619	10W35a	87354	87468
10W37a	87633	87711	10W37b	87780	87871
10W39b	88055	88204	10W39a/c	87902/88245	88013/88255
10W42b	88651	88767	10W42a	88512	88590
10W44a	88805	88933	10W44b	89046	89209

This thesis deals with the analysis of exclusive processes which are characterised by a small cross section and lower statistics. Additionally a subtraction of events from semi-inclusive processes is necessary, whereas the applied methods require a reasonable amount of statistics (Sec. 5). Thus the possibility of a combined analysis is studied, where all data of a certain target and spectrometer configuration enter the asymmetry calculation at once. Since the comparison of several distributions have shown a reasonable agreement of the various years a global analysis of the years 2003&2004 and 2007&2010 is performed. The differences on the level of asymmetries between the periods/years are studied in Sec. 7.1.3 and Sec. 8.1.1.2. Some differences are discussed in Sec. 4.3.6.

Table 4.3: Overview of periods in 2003 and 2004. The left half of the table is dedicated to sub-periods where the target cells are polarised $+-$, in the direction of the muon beam. For every sub-period the first and the last run is given. The right half of the table is dedicated to sub-periods where the target cells are polarised $-+$, in the direction of the muon beam. Again, for every sub-period the first and the last run is given.

$+-$	first run	last run	$-+$	first run	last run
03P1H	31192	31524	03P1G	30773	31123
04W33	38991	39168	04W34	39283	39545
04W36	39850	39987	04W35	39548	39780

4.2 Data Quality

After processing the data with CORAL (Sec. 3.5) quality checks are performed on the mDST level. They can be divided in bad spill analysis and bad run analysis. The bad spill analysis is performed by studying important variables like the average number of beam particles, the number of tracks per primary vertex, the number of primary vertices per event and the number of clusters in the hadronic calorimeter, normalised to the proton flux on the primary target, as a function of the spill number. Crucial for the decision if a spill is a bad spill is the number of neighbours within a box of x·RMS, where the required number of neighbours and x are depending on the studied variable and the year of data taking [102, 103, 104]. Additionally, if a single run has more than 80% bad spills, it is removed from the analysis.

The K^0 stability is checked on a run-by-run basis after applying the bad spill lists. The mean of the Gaussian distribution $m_{\pi^+\pi^-}$-$m_{K,lit}$, its width and the number of reconstructed K^0 per primary vertex is plotted as function of the run number. If a run deviates more than $3 \cdot \sigma$ from the mean this run is rejected. For the kinematic stability several kinematic variables are plotted as a function of the run number and their derivation from the mean is studied [102, 103, 104].

For the 2010 data taking the data quality checks are based on a two step process. In the first step the detector planes are monitored on a run-by-run basis to identify possible instabilities in the performance of the detectors [105]. Detector planes with varying efficiencies are excluded from the processing with CORAL. In a second step the above explained quality checks on the mDST level are applied.

The official badrun/badspill lists of 2010 [106] and 2007 [107] are applied to the event sample. In 2010 around 9% of the data is rejected. In 2007 the amount of runs removed from the analysis depends highly on the period and varies from 15% up to 50%. In total about 34% of the data is rejected. The higher fraction of rejected data in 2007 indicates a less stable operation of the experiment during data taking. Note that for the production of the 2007 data all runs with more than 10 spills have been produced. In contrast, in 2010 a two-step process is applied where unstable runs are already excluded from processing.

For the years 2003 and 2004 the mDSTs (Sec. 4.1) already include the quality checks. For 2004 data the momenta of all particles which crossed SM2 are rescaled using the PHAST function RescaleMom() to account for the lack of rescaling the magnetic field of SM2 in CORAL [108]. In 2007 events triggered by the pure ECAL1 trigger are rejected for the periods W27, W28, W39, W40, W41 and W42a due to instabilities of this pure calorimeter trigger.

4.3 Event Selection

4.3.1 Primary Vertex

The goal is the selection of exclusive produced ρ^0 mesons (Eq. 2.28). The initial state of the studied events is defined by one incoming muon which scatters off the target nucleon. The final state is build by the scattered muon, the recoiled proton, and the produced ρ^0 meson. The ρ^0 meson is a resonance with a lifetime of $c\tau \approx 1.3\,\text{fm}$ and decays with a branching ratio of almost 100% in $\pi^+\pi^-$. The ρ^0 particle itself can not be detected with the COMPASS spectrometer, same as the recoiled nucleon, which can not be detected due to the lack of a proton recoil detector. Hence the detected final state in the spectrometer consists of three reconstructed particles, the scattered muon and two hadrons with opposite charge, which are directly originating from the primary vertex.

If more then one primary vertex is reconstructed in one event the best primary vertex is defined as the one with the largest number of outgoing tracks. If several primary vertices have the same number of outgoing tracks the one with the best χ^2 of the vertex fit is tagged as best primary vertex. This definition seems to be not well adapted for exclusive events. Therefore the possible increase of ρ^0 candidates when including the additional primary vertices was tested and found to be negligible (≈ 0.5 %). Therefore only the best primary vertices of the events are selected for the analysis. To ensure their position inside one of the target cells the PHAST routine PaAlgo::InTarget() is used.

The z-positions of the target for 2007 and 2010 as well as for 2003 and 2004 agree exactly. In the xy-plane perpendicular to the beam axis the maximum difference is smaller than 0.4 cm for 2007 and 2010 and 0.2 cm for 2003 and 2004, respectively. The maximum allowed radial distance of the vertex from the target center is 1.3 cm for 2003&2004 data and 1.9 cm for 2007&2010 data. The values were chosen by taking into account the actual target position. The spatial distributions of the primary vertex are shown in Fig. 4.1 and Fig. 4.2. Clearly visible is the three (2007, 2010) and two (2003, 2004) cell structure of the COMPASS targets as introduced in Sec. 3.2. The uncertainties of the z-position determinations are presented in Fig. 4.3.

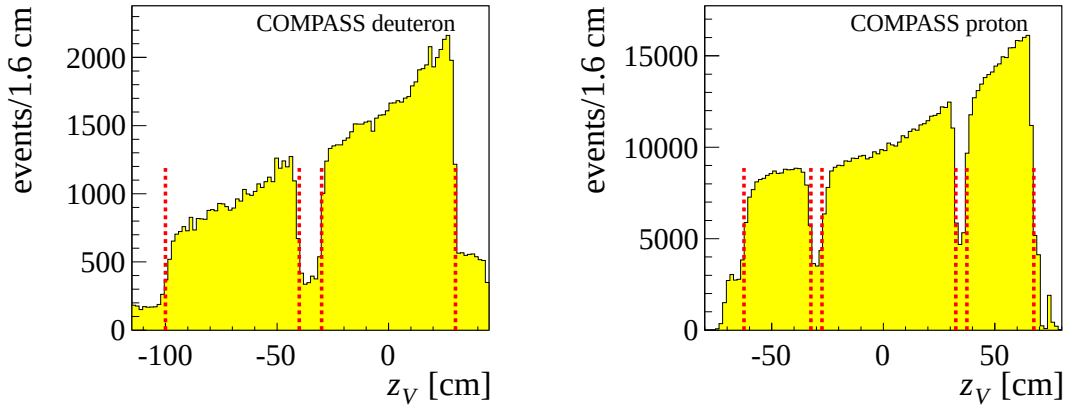

Figure 4.1: The spatial distributions of the primary vertex in z-direction for the 2003&2004 sample (left) and 2007&2010 sample (right). All cuts indicated in Tab. 4.5 are applied, except the cut on z_V.

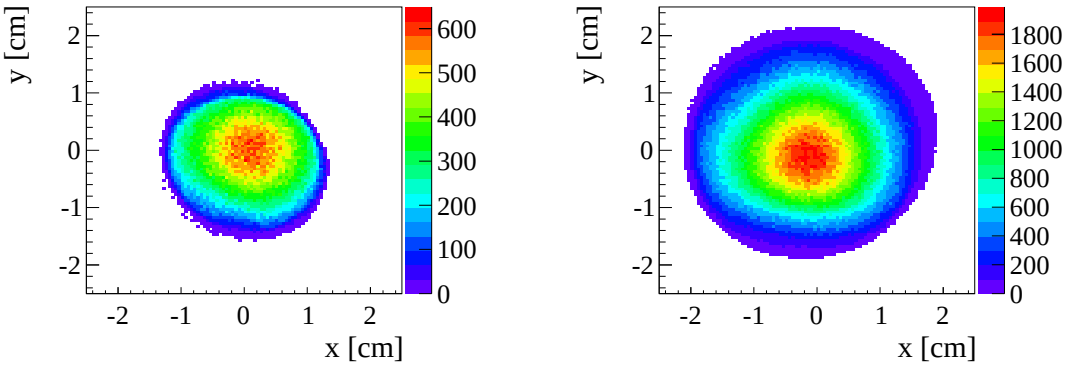

Figure 4.2: The spatial distributions of the primary vertex in the plane perpendicular to the beam axis for the 2003&2004 sample (left) and 2007&2010 sample (right). All cuts indicated in Tab. 4.5 are applied.

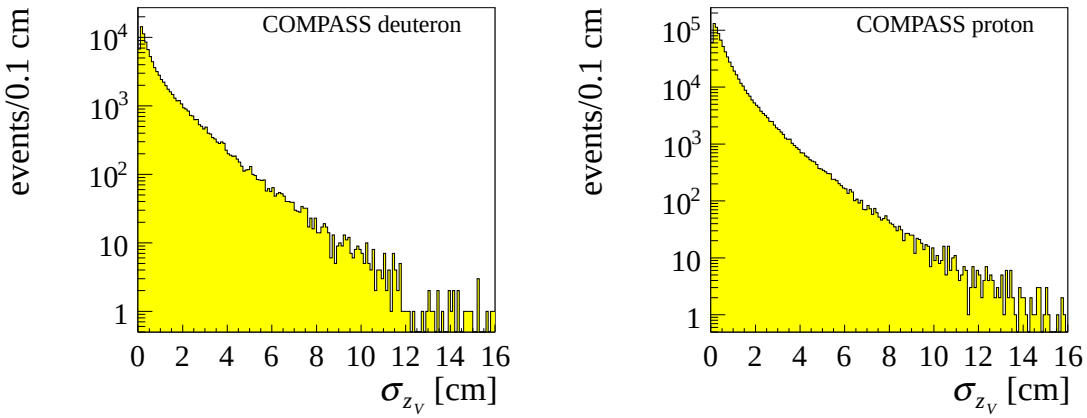

Figure 4.3: The distributions of the uncertainty of the primary vertex σ_{z_V} Z-position for the 2003&2004 sample (left) and 2007&2010 sample (right). All cuts indicated in Tab. 4.5 are applied.

4.3.2 Beam and Scattered Muon

In order to ensure a good fit quality of the track for both beam muon and outgoing muon, the reduced χ^2_{red} has to be smaller than 10. Moreover the beam momentum has to be in the range $140\,\mathrm{GeV}/c < p_\mu < 180\,\mathrm{GeV}/c$. Additionally the extrapolated track of the beam particle has to go through all existing target cells to equalise the flux through the target.

In the first and second production of 2007 data a large fraction of events ($\approx 20\%$) is observed, for which the assignment of momentum to the beam track is wrong. This leads for example to negative, kinematically forbidden, values of missing energy (see Sec. 4.3.4.2), visible as a tail with negative values in the distributions of this variable. The quality of the beam momentum reconstruction can be estimated using the likelihood of the back propagation algorithm LH_{back} [109], presented in Fig. 4.4. In this analysis events with bad beam tracks are suppressed by requiring $LH_{\mathrm{back}} > 0.005$. Additionally, in the 2010 data sample, LH_{back} assumes not defined numbers and non-physical values > 1. These values correspond to events where only two BMS planes have fired[2] (Fig. 4.5) and hence the likelihood is not well defined. The amount of such events is estimated to 1.4% of the 2007&2010 event sample. Those events have been rejected from the analysis requiring $LH_{\mathrm{back}} < 1$ and $N_{BMS} > 2$ [110]. The fraction of remaining events with bad beam momentum is estimated to be $\approx 5\,\%$. In 2003 and 2004 data the information from the back propagation algorithm is not available due to the old CORAL version used in the production (version 2004-08-05 for 2003 data and version 2004-11-17-slc3 for 2004 data). The fraction of events with bad beam tracks is estimated to be $\approx 7\,\%$.

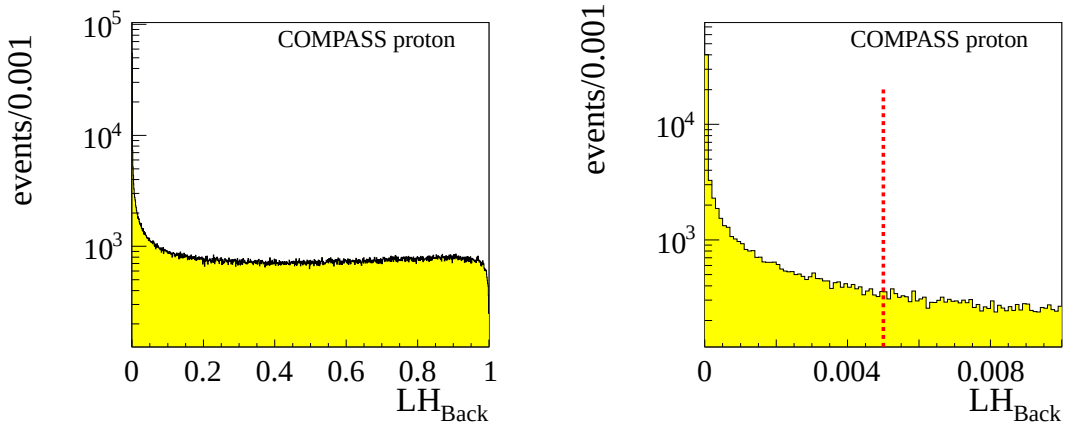

Figure 4.4: The distributions of the likelihood of the back propagation algorithm for the 2007&2010 sample. On the left-hand side the range $0.0 < LH_{\mathrm{Back}} < 1.0$ is shown, where on the right-hand side a zoom in $0.0 < LH_{\mathrm{Back}} < 0.01$ is presented. All cuts indicated in Tab. 4.5 are applied, except the cut on LH_{Back}.

[2]Note that in the here used algorithm of the beam momentum determination two of the six BMS stations (Sec. 3.4) are utilised as "rescue planes". Therefore the maximum number of activated BMS planes is four.

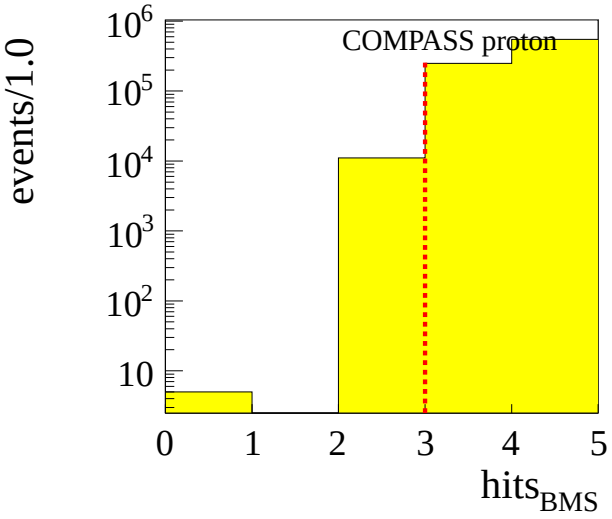

Figure 4.5: Number of participating BMS planes per beam particle for the 2007&2010 sample. All cuts indicated in Tab. 4.5 are applied, except the cut on the number of hits in the BMS.

The scattered muon is selected via the PHAST routine PaParticle::IsMuPrimCoral(), while the calculated penetration length of the μ' track, expressed in units of radiation lengths, has to exceed a minimum value, i.e. $X/X_0 > 30$. Recently the possibility to lower the cut to $X/X_0 > 15$ is discussed [111]. It incorporates muon candidates which traverse significantly less material. This change results in a gain $< 1\%$ of exclusive ρ^0 candidates and was not applied in this analysis. Events with more than one identified μ' are rejected. Also events with so called "recovered" muons are rejected. The recovering procedure is based on the hit information from the Muon Wall detectors. If one of the outgoing particles connected to the primary vertex causes more than four hits in MA01 and more than six hits in MA02, it is considered as a scattered muon. If the particle additionally fulfills the same requirements for χ^2_{red} and X/X_0 as the "tagged" μ', the particle is marked as a "recovered" muon and the event is rejected. Moreover, the event is rejected if the μ' track crosses the SM2 yoke, because then a correct reconstruction of the particle momentum is impossible. The distributions of the momentum of the incoming and scattered muon can be found in Fig. 4.6 and Fig. 4.7.

4.3.3 Kinematic Variables for Inclusive Scattering

The following kinematic cuts are employed to obtain a final data sample consisting of events in the deep inelastic scattering range. The variables for describing the inclusive scattering are calculated, using only the incoming and outgoing muon tracks. The negative square of the four-momentum of the virtual photon is restricted to $Q^2 > 1.0\,(\text{GeV/c})^2$ while the range of hadron resonances is excluded by applying a cut on the invariant mass of the final hadronic state $W > 5.0\,\text{GeV/c}^2$. Additionally y, the fractional energy of the virtual photon, is chosen in the range $0.1 < y < 0.9$, in order to remove events with large radiative corrections (large y) or poorly reconstructed kinematics (low y) (Fig. 4.8).

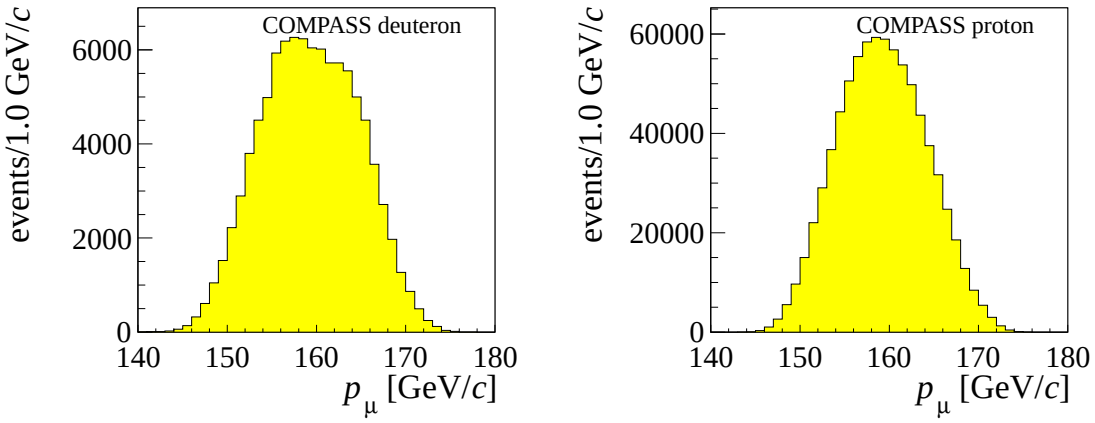

Figure 4.6: The beam momentum distributions for the 2003&2004 sample (left) and 2007&2010 sample (right). All cuts indicated in Tab. 4.5 are applied.

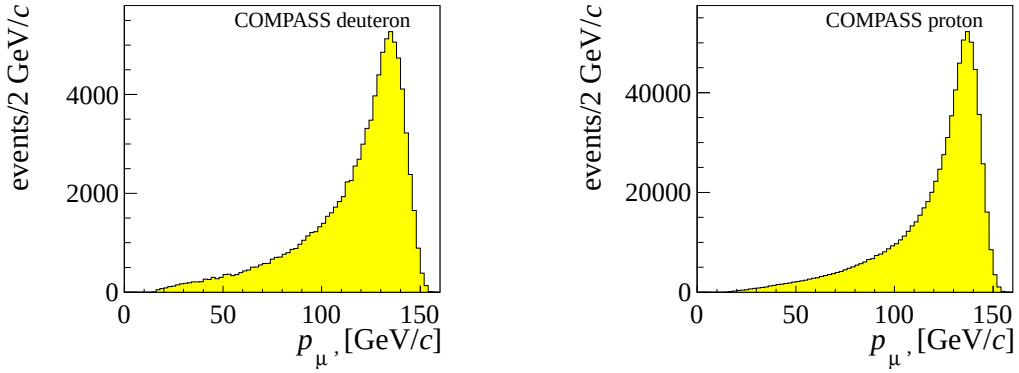

Figure 4.7: The scattered muon momentum distributions for the 2003&2004 sample (left) and 2007&2010 sample (right). All cuts indicated in Tab. 4.5 are applied.

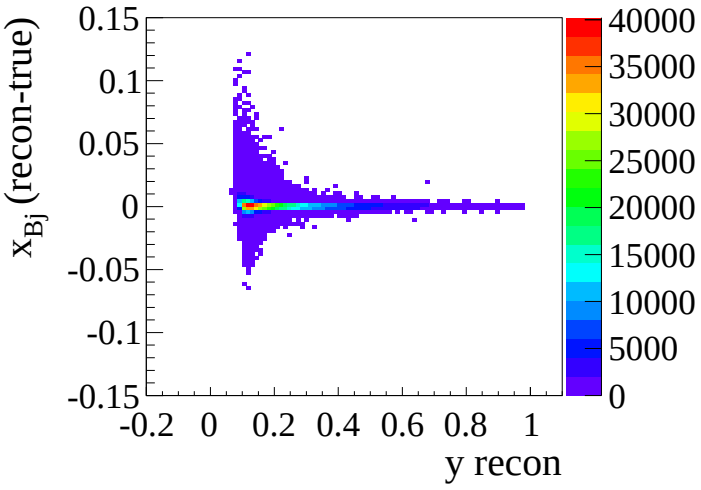

Figure 4.8: Difference of reconstructed and generated x_{Bj} as a function of the reconstructed y. The events are generated with PYTHIA. All cuts indicated in Tab. 4.5 are applied, except the cuts on y and W. To have a higher statistical precision the whole semi-inclusive sample is used.

Moreover the Bjorken scaling variable is limited to $0.003 < x_{Bj} < 0.35$. Some of the scattering variables are strongly correlated (Appendix C.1). The application of cuts even for correlated variables allows for the asymmetries extraction in a defined range (Sec. 6). The kinematic distributions are presented in Figs. 4.9, 4.10, 4.11 and 4.12. The shape of the distributions depends on the applied cuts, on the geometrical acceptance as well as the trigger system of the COMPASS experiment.

4.3.4 Meson Selection

The ρ^0 meson is reconstructed out of two oppositely charged hadrons. Similar to the requirements on the muon tracks, the tracks of the hadron candidates have to satisfy the condition $\chi^2_{red} < 10$. Moreover, hadron tracks have to start before z=350 cm and to stop after z=350 cm, which is the center of the SM1 and ensures that the momentum of the track can be measured precisely. Additionally the hadron track has to stop before the muon filter 2, which is situated at Z=3300 cm to prevent that muons are misidentified as hadrons. On the other hand, hadron tracks should not pass more than 10 radiation lengths. Finally the event is rejected if one of the hadron tracks crosses the yoke of SM2 or if the positive hadron could be a misidentified muon which goes through the hole of the absorber system.

4.3.4.1 Cut on Invariant Mass

A particle identification using the information from the RICH-1 detector (Sec. 3.3.3) is not done in the present analysis (see Sec. 4.3.5) and the invariant mass, $M_{\pi\pi}$, of the two hadrons is calculated always assuming pion masses for both particles. The cut on the two pion invariant mass is optimised in order to suppress non-resonant $\pi^+\pi^-$ production by applying the Ross-Stodolsky or Söding parametrisation [112]. The final invariant mass range is:

$$0.5\,\mathrm{GeV/c^2} < M_{\pi\pi} < 1.1\,\mathrm{GeV/c^2}\ .$$

As mentioned above all hadrons are considered as pions. The production of exclusive $\phi \to K^+K^-$ mesons is visible in the lower part of the invariant mass spectrum

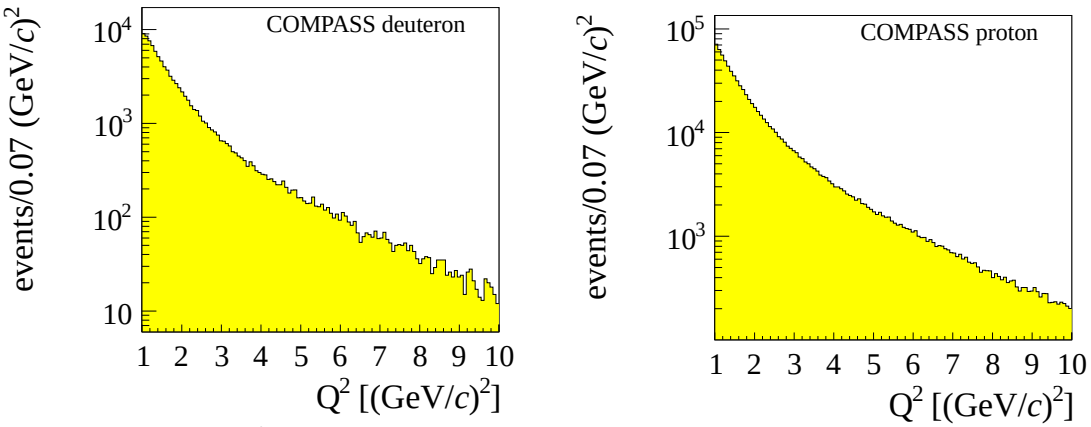

Figure 4.9: The Q^2 distributions for the 2003&2004 sample (left) and 2007&2010 sample (right). All cuts indicated in Tab. 4.5 are applied.

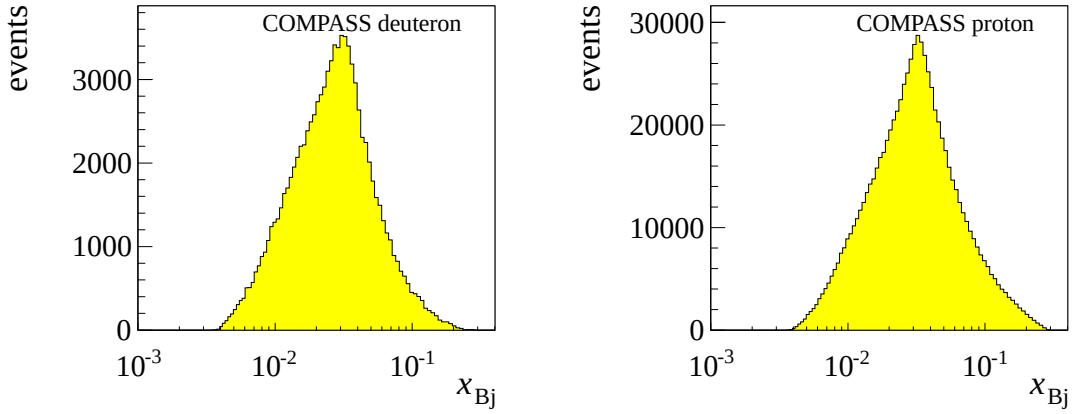

Figure 4.10: The x_{Bj} distributions for the 2003&2004 sample (left) and 2007&2010 sample (right). All cuts indicated in Tab. 4.5 are applied.

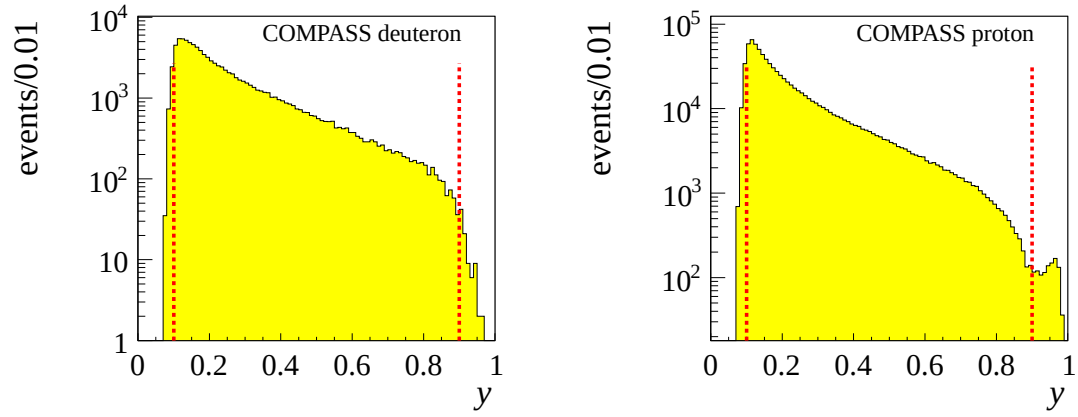

Figure 4.11: The y distributions for the 2003&2004 sample (left) and 2007&2010 sample (right). All cuts indicated in Tab. 4.5 are applied, except the cuts on y and W. The increase for $y > 0.9$, visible in the distribution for the 2007&2010 sample, can be traced back to hadron tracks which are accidentally assumed to be the scattered μ^+.

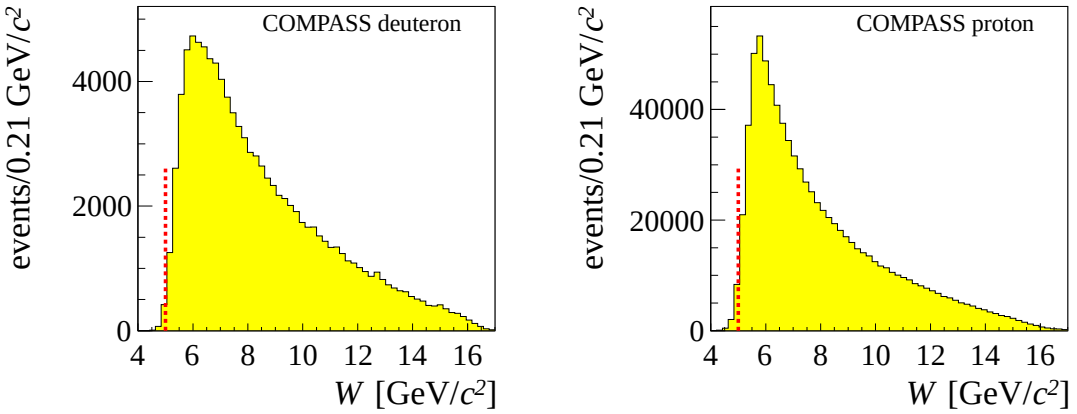

Figure 4.12: The W distributions for the 2003&2004 sample (left) and 2007&2010 sample (right). All cuts indicated in Tab. 4.5 are applied, except the cuts on y and W.

at around $0.35\,\mathrm{GeV}/c^2$. The resonance is suppressed by a cut on the invariant mass $M_{KK} > 1.04\,\mathrm{GeV/c^2}$, where M_{KK} is calculated assuming kaon masses for the two final state hadrons. The cut is chosen this way, that the reflection of M_{KK} disappears, although no ρ^0 candidate is rejected additionally. The $K^*(892)$ and $K^*(1430)$ resonances are much wider. They are located partially in the ρ^0 mass range. In the kinematic domain of COMPASS their cross sections are two orders of magnitude smaller than the cross section of the ρ^0 production [113], thus their contributions are negligible. The distributions of the invariant mass for 2003&2004 data (left) and 2007& 2010 data (right) are shown in Fig. 4.13.

4.3.4.2 Exclusivity and Incoherence

Exclusivity can be estimated using the missing energy variable defined as follows (Tab. 2.1):

$$
\begin{aligned}
E_{\mathrm{miss}} &= E_\mu - E_{\mu'} - E_{\rho^0} + E_P - E_{P'} && (4.1)\\
&= \frac{(p+q-v)^2 - p^2}{2\cdot M} && (4.2)\\
&= \frac{M_X^2 - M^2}{2M} && (4.3)\\
&= \nu - E_{\rho^0} + \frac{t}{2M}, && (4.4)
\end{aligned}
$$

where M is the proton mass, M_X the mass of the undetected recoiling system and p, q and v are the four-momentum vectors of the proton, the photon and the ρ^0 meson. The latter is reconstructed via its decay particles. The term $E_P - E_{P'} \overset{\mathrm{lab}}{=} \frac{t}{2M}$ on the RHS of Eq. 4.4 is equal to the kinetic energy of the recoiled proton. It is assumed to be small since the proton stays intact.

For scattering events where the recoiled proton stays intact and no additional particle is produced Eq. 4.2 should be equal to zero. Hence the non-exclusive background events can be suppressed requiring $E_{\mathrm{miss}} \approx 0$. Due to the experimental resolution, the reconstructed values of E_{miss} are smeared to a Gaussian distribution with a width of

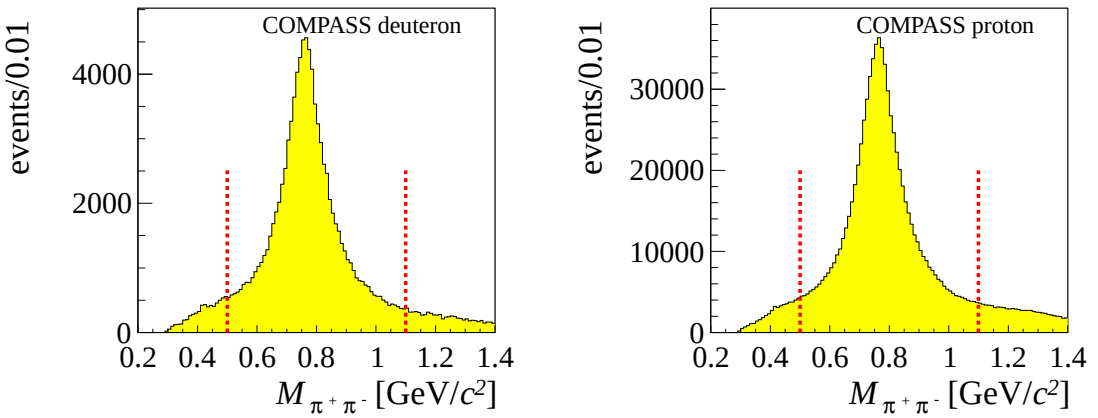

Figure 4.13: Invariant mass spectra $M_{\pi^+\pi^-}$ for the 2003&2004 sample (left) and 2007&2010 sample (right). All restrictions indicated in Tab. 4.5 are applied except the cut on $M_{\pi^+\pi^-}$.

about 1.24 GeV in 2003&2004, about 1.35 GeV in 2007 and about 1.25 GeV in 2010. Furthermore, the exclusive peak of the E_{miss} distributions is expected to be centred around zero. However, the analysis performed separately for each period indicates small changes of the position of the exclusive peak. The determination of these period-wise shifts in E_{miss} is done by fitting the signal and the background as described in Sec. 5.2.1, for each period individually. The procedure is done iteratively, since after each iteration the Monte-Carlo sample to estimate the semi-inclusive background has to be reweighted according to the shifted E_{miss} distribution. The procedure is repeated until the mean value of the signal Gaussian is within the errors well compatible with zero. The comparison of the extracted shift values of the 2007 and 2010 data taking shows a smaller and throughout negative shift for 2010, indicating a more stable data taking. This observation is in line with the results of the data quality checks presented in Sec. 4.2. In Tab. 4.4 the final shifts of E_{miss} for each period are listed. Using the period P1H as an example, the effect is illustrated, in Fig. 4.14, where the distributions before (left) and after (right) the shift of the E_{miss} values are shown.

Table 4.4: Applied shift to the missing energy E_{miss} distribution for each period separately.

$+-/+-+$	shift [GeV]	$-+/-+-$	shift [GeV]
P1H	−0.29	P1G	−0.13
04W33	−0.21	04W34	−0.04
04W36	−0.09	04W35	−0.07
07W26	0.13	07W25	0.10
07W28	0.05	07W27	0.04
07W30	−0.01	07W31	−0.07
07W39	−0.35	07W40	−0.29
07W42a	0.07	07W41	−0.22
07W42b	0.09	07W43	0.00
10W23b	−0.11	10W23a	−0.02
10W24a	−0.06	10W24b	0.00
10W26b	−0.12	10W26a	−0.09
10W27a	−0.11	10W27b	−0.15
10W29a	−0.13	10W29b	−0.16
10W31b	−0.16	10W31a	−0.12
10W33a	−0.12	10W33b	−0.13
10W35b	−0.10	10W35a	−0.08
10W37a	−0.10	10W37b	−0.15
10W39b	−0.06	10W39a/c	−0.06
10W42b	−0.05	10W42a	−0.13
10W44a	−0.14	10W44b	−0.14

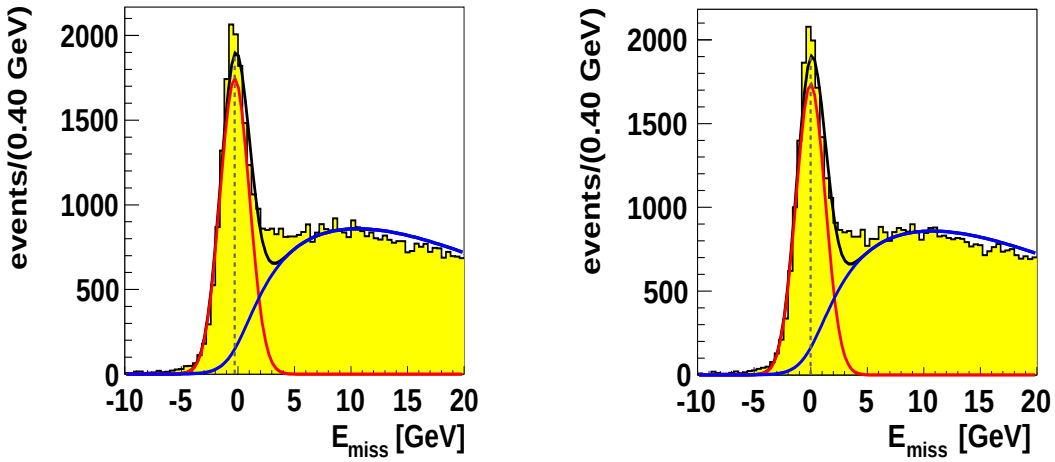

Figure 4.14: Fit of signal and background to the missing energy E_{miss} for P1H before shifting E_{miss} (left) and after (right). The vertical dashed line indicates the centre of the Gaussian. All cuts indicated in Tab. 4.5 are applied except the cut on E_{miss}.

Distributions of missing energy after corrections for the shifts and after all selections, except the cut on E_{miss}, are shown in Fig. 4.15 for 2003&2004 data (left) and for 2007&2010 data (right). For the final sample E_{miss} is limited to a range of $2 \cdot \sigma$:

$$\text{-}2.5\,\text{GeV} < E_{\text{miss}} < 2.5\,\text{GeV},$$

where σ is the width of the signal Gaussian. For further reduction of semi-inclusive background a cut on the energy of the ρ^0 meson, the cut $p_T^2 < 0.5\,(\text{GeV}/c)^2$ (see below) and the cut $Q^2 < 10\,\text{GeV}/c^2$ is used. The latter takes into account the different Q^2-dependences of semi-inclusive and exclusive cross sections. In Fig. 4.16 the correlation between the reconstructed ρ^0 energy E_ρ and missing energy E_{miss} is presented. The semi-inclusive background is significantly reduced with the cut:

$$E_\rho > 15\,\text{GeV}.$$

The fraction of incoherent ρ^0 production can be enhanced by a cut on the transverse momentum of the exclusively produced ρ^0 meson. In this analysis, the variable p_T^2 is used rather than t' for experimental reasons [114]. The p_T^2 variable is defined as the transverse component of the ρ^0 meson momentum vector with respect to the virtual photon direction. Distributions of p_T^2 are shown in Fig. 4.17. In order to reject events from coherent production on nuclei of the target material, a lower cut on p_T^2 is applied. Also an upper limit for this variable is chosen to further minimise non-exclusive background. The selected range for the 2003&2004 data is:

$$0.1\,(\text{GeV}/c)^2 < p_T^2 < 0.5\,(\text{GeV}/c)^2,$$

and for the 2007&2010 data it is:

$$0.05\,(\text{GeV}/c)^2 < p_T^2 < 0.5\,(\text{GeV}/c)^2.$$

The fits which constrain the used p_T^2 range can be found in [115, 114].

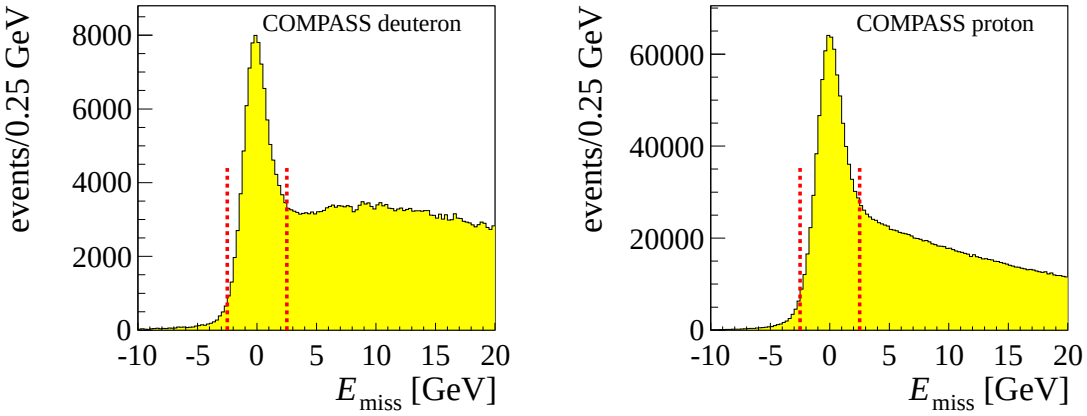

Figure 4.15: Distributions of the missing energy E_{miss} for the 2003&2004 sample (left) and 2007&2010 sample (right). All cuts indicated in Tab. 4.5 are applied except the cut on E_{miss}.

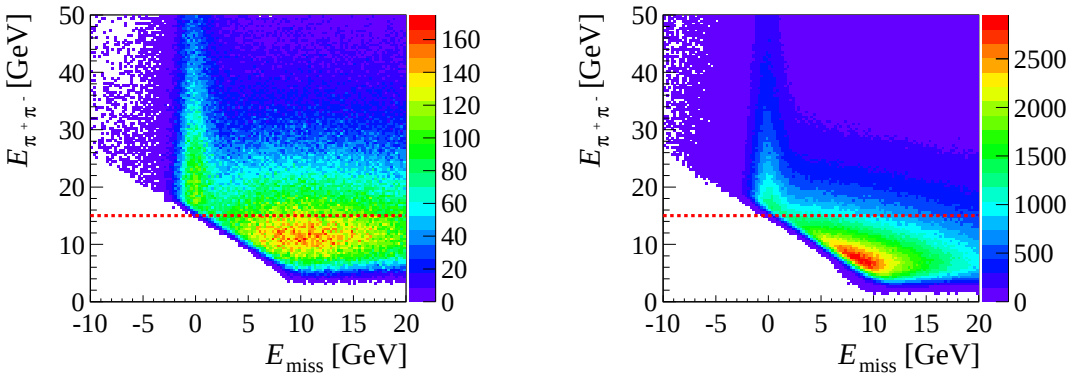

Figure 4.16: Correlation between E_{miss} and E_ρ for the 2003&2004 sample (left) and 2007&2010 sample (right). All restrictions indicated in Tab. 4.5 are applied except the cut on E_ρ and E_{miss}.

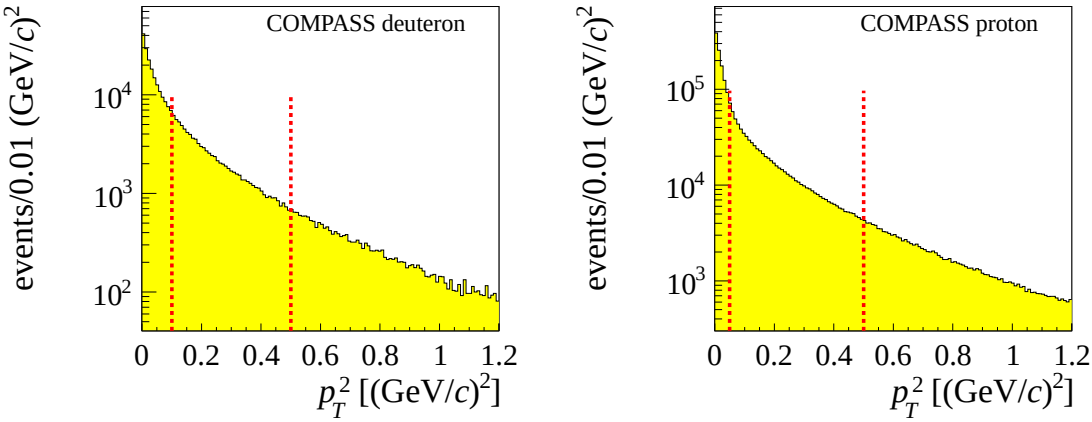

Figure 4.17: Distributions of p_T^2 for the 2003&2004 sample (left) and 2007&2010 sample (right). All restrictions indicated in Tab. 4.5 are applied except the cut on p_T^2.

4.3.5 Particle Identification

The RICH detector allows for particle identification and is included in the first stage of the COMPASS spectrometer as described in Sec. 3.3.3. In Fig. 4.18 the measured Cherenkov angle as a function of the particle momentum of the positive hadron p_{h^+} for all ρ^0 candidates is presented. Clearly visible are the contributions from pions, kaons and protons. In principle it is possible to restrict the used data sample to ρ^0 mesons, where both hadrons in the final state are identified as pions. However, the particle identification is limited to particle momenta smaller than $p_{max} < 50\,\mathrm{GeV}/c$. The minimal momentum threshold is calculated according to Eq. 3.3 individually for every event using the refractive index of the central RICH part. This limitation significantly reduces the available kinematic range and therefore also the statistics. Hence the possibility of using only ρ^0 candidates reconstructed out of two identified pions is discarded. However, the option of using the RICH detector as a veto is tested for the 2007&2010 data sample.

The particle identification algorithm relies on a likelihood function built for all photons associated to the particle in the region below 70 mrad. For each hadron the likelihood is computed for 5 hypothesis: pion, kaon, proton, electron and background. The latter corresponds to the hypothesis of the absence of a signal. The test on the electron hypothesis is only included if $\mathcal{L}_e > 1.8 \cdot \mathcal{L}_\pi$. One track is identified with a mass hypothesis if the corresponding likelihood is the highest. Moreover, the mis-identification probabilities are decreased adding a cut on the comparison to the second highest likelihood. The conditions of the RICH detector in 2007 and 2010 are the same, except that in 2010 the MWPC HV was lowered of 20 V in order to have a more stable behaviour. As the purity and efficiency in both years are compatible with each other the same likelihood cuts are used [116]. With these like-

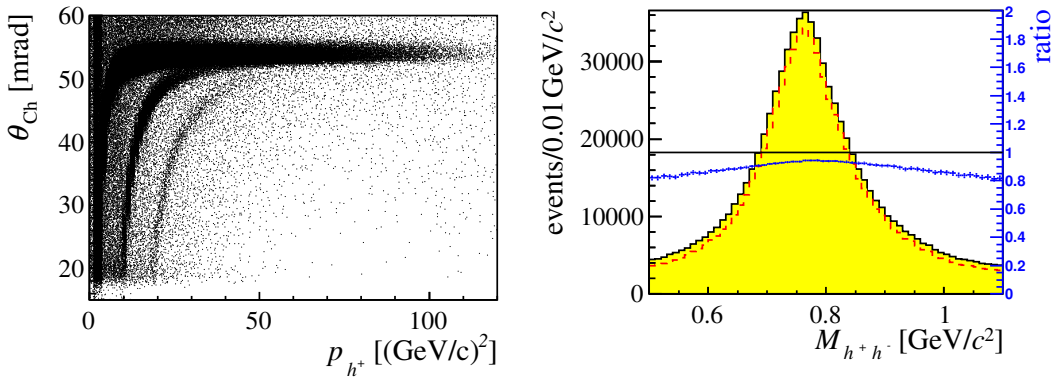

Figure 4.18: Left-hand side: The measured Cherenkov angle as a function of the particle momentum of the positive hadron p_{h^+} for the 2007&2010 sample. All cuts indicated in Tab. 4.5 are applied. Visible are contributions from pions (top band), kaons (middle band) and protons (bottom band). right-hand side: invariant mass distribution for all ρ^0 candidates recorded in 2007&2010 (yellow filled) and after applying RICH as a veto (red line). In blue the ratio is given where the corresponding scale is presented on the left-hand side of each histogram.

lihood cuts the purity of the pion identification is around 99% whereas the efficiency is depending on the hadron momentum and is $> 90\%$ for $p_\pi < 30\,\mathrm{GeV}/c$ [117].

The following likelihood cuts are used [116]: $\frac{\mathcal{L}_\pi}{\mathcal{L}_{2nd}} > 1.02$, $\frac{\mathcal{L}_K}{\mathcal{L}_{2nd}} > 1.08$ and the electron hypothesis is used if $\frac{\mathcal{L}_e}{\mathcal{L}_\pi} > 1.8$ and $\mathrm{p}_h < 8\,\mathrm{GeV/c}$. The RICH is used as a veto. Therefore all events are rejected where at least one of the hadrons in the final state is identified as a kaon, a proton or an electron. On the right-hand side of Fig. 4.18 the invariant mass distribution and in Fig. 4.19 the missing energy distribution for all ρ^0 candidates recorded in 2007&2010 (yellow filled) and after applying RICH as a veto (red line) are presented. The veto cut leads to a reduction of statistics of 9%, in detail:

one hadron is identified as	
kaon	7%
proton	1%
electron	1%
veto	9%

The shape of neither the ϕ distribution nor the ϕ_S distribution is changing due to the application of the veto cut. In Fig. 4.19 a reduction in the whole E_{miss} range is visible, with an expected increase at higher E_{miss} values. Still, the major part of semi-inclusive background is present. Therefore a semi-inclusive background estimation method, as it will be presented in Sec. 5, has to be applied. The usage of the RICH information brings the additional drawback that the outgoing hadrons are handled differently depending on their momenta. Hence the RICH was not used in the standard analysis. The RICH information is solely used for the study of systematic effects in Sec. 7.1.5.

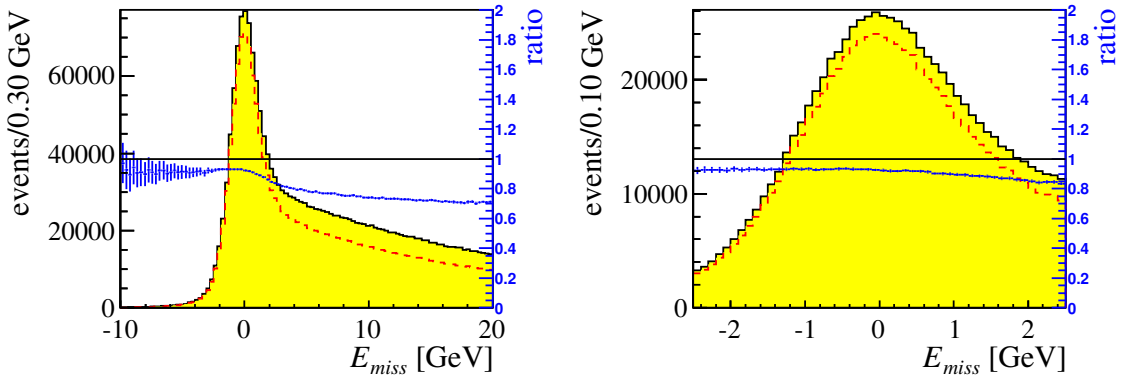

Figure 4.19: Missing energy distribution for all ρ^0 candidates recorded in 2007&2010 (yellow filled) and after applying RICH as a veto (red line). All cuts indicated in Tab. 4.5 are applied, except the cut on E_{miss} (left-hand side). In blue the ratio is given where the corresponding scale is presented on the right-hand side of each histogram.

4.3.6 Comparison of Data Taking Periods

In this thesis a combined analysis of the data taken in 2003&2004 and 2007&2010 is performed. This implies a fair agreement of the measured data taken in the different years. Various kinematic variables, the azimuthal angles ϕ and ϕ_S, the vertex position, $M_{\pi^+\pi^-}$, E_{miss}, p_T^2, the beam momentum p_μ and the momentum of the scattered muon $p_{\mu'}$ measured in 2003, 2004, 2007 and 2010 were compared. Although a different beam profile in 2007 and 2010 is observed, all other distributions are in a fair agreement. Especially the E_{miss} distribution in the background dominated range is very well compatible. Therefore the same Monte-Carlo as for the 2007 analysis is usable for the parametrisation of semi-inclusive background shape in 2010 (Sec. 5). In addition, a combined analysis may become possible.

During the first 5 periods in 2010 (W23-W29) the data was collected with Inner, Middle, Ladder, Outer and Calorimeter triggers. For the last 7 periods (W31-W44) the LAST trigger was included. The effect has been studied. The Q^2 and E_{miss} distribution is shown for W23-W29 (yellow histogram) and W31-W44 (blue line) in Fig. 4.20. The distributions agree well. The LAST trigger leads to an increase of high Q^2 events. This events are suppressed in the selected sample due to the cut $Q^2 < 10\,(\text{GeV}/c)^2$.

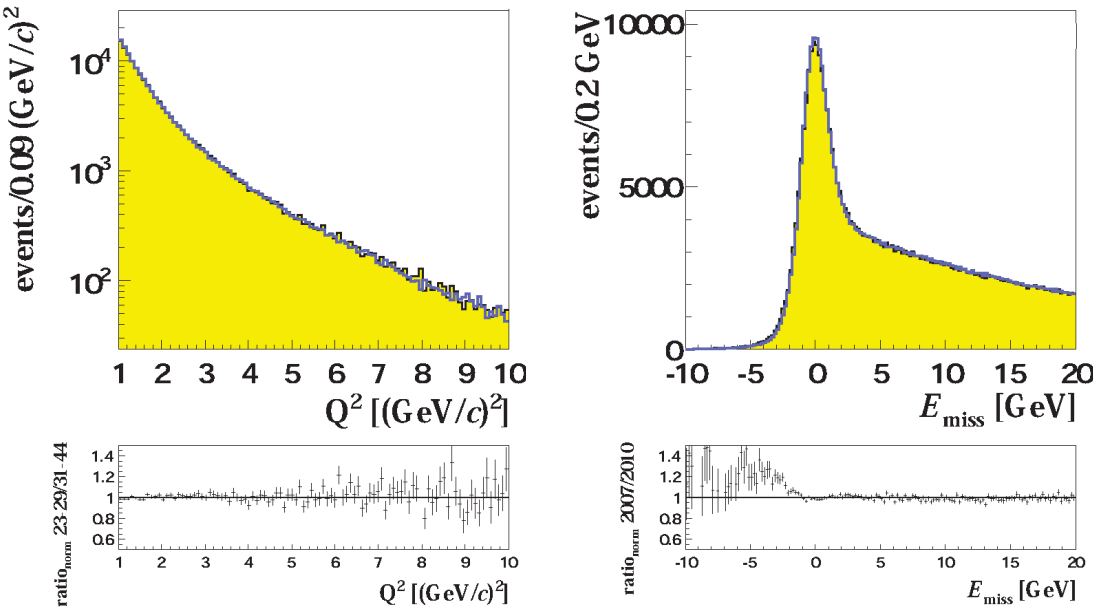

Figure 4.20: Comparison of W23-W29 (yellow histogram) and W31-W44 (blue line) for Q^2 and E_{miss}. The W31-W44 sample is normalised to the W23-W29 sample to allow for a better comparison.

4.4 Final Data Sample

In Tab. 4.5 all applied cuts are summarised. After the presented event selection we have in total 96646 ρ^0 candidates for 2003&2004 and 797134 for 2007&2010. (Tabs. 4.6 and 4.7). The mean values for the kinematic variables Q^2, x_{Bj}, y, W and p_T^2 are given in Tab. 4.8.

Table 4.5: Summary of all cuts.

topology	Best Primary Vertex reconstructed with 1 incident muon: μ 1 scattered muon: μ' 2 charged tracks with opposite charge: $h^+,\ h^-$
vertex in the target	PHAST routine PaAlgo::InTarget()
muon identification hadron identification	$X/X_0(\mu') > 30$ $X/X_0(h^+, h^-) < 10$
quality of the tracks	$\chi^2_{red} < 10$ for μ, μ', $h^+,\ h^-$ $z_{first}(h^+,h^-) < 350$ cm $350 < z_{last}(h^+,h^-) < 3300$ cm h^+, h^- and μ' do not cross SM2 yoke (PHAST routine) h^+ cannot be a muon (PHAST routine)
μ flux through all target cells beam momentum beam back propagation likelihood number of fired BMS planes	PHAST routine $140\,\mathrm{GeV}/c < p_\mu < 180\,\mathrm{GeV}/c$ $0.005 < LH_{\mathrm{back}} < 1$ (for 2007 and 2010) $N_{BMS} > 2$ (for 2007 and 2010)
domain of analysis	$1\,(\mathrm{GeV}/c)^2 < Q^2 < 10\,(\mathrm{GeV}/c)^2$ $W > 5\,\mathrm{GeV}/c^2$ $0.1 < y < 0.9$ $0.003 < x_{Bj} < 0.35$
production of ρ^0 meson	$0.5\,\mathrm{GeV/c^2} < M_{\pi^+\pi^-} < 1.1\,\mathrm{GeV}/c^2$ $M_{KK} > 1.04\,\mathrm{GeV/c^2}$
exclusivity	-2.5 GeV$< E_{\mathrm{miss}} < 2.5$ GeV
suppression of background	$E_{\pi^+\pi^-} > 15$ GeV $p_T^2 < 0.5\,(\mathrm{GeV}/c)^2$
suppression of coherent production	$\mathrm{p}_T^2 > 0.1\,(\mathrm{GeV/c})^2$ (for 2003&2004) $p_T^2 > 0.05\,(\mathrm{GeV}/c)^2$ (for 2007 and 2010)
quality of data	Pure ECAL1 trigger rejected for periods in 2007: W27, W28, W39, W40, W41, W42a

Table 4.6: Number of exclusive ρ^0 candidates for 2003&2004 after all cuts applied. The periods are sorted by the orientation of target polarisation.

+−	# Events	−+	# Events
03P1H	15861	03P1G	17725
04W33	14862	04W34	12648
04W36	13461	04W35	22089
all	44184		52462

Table 4.7: Number of exclusive ρ^0 candidates for 2007&2010 after all cuts applied. The periods are sorted by the orientation of target polarisation.

+ − +	# Events	− + −	# Events
07W26	20473	07W25	17495
07W28	21319	07W27	11560
07W30	22204	07W31	29826
07W39	33041	07W40	19552
07W42a	18788	07W41	23113
07W42b	9036	07W43	11285
10W23b	13293	10W23a	14751
10W24a	16853	10W24b	8049
10W26b	13702	10W26a	13872
10W27a	11809	10W27b	14668
10W29a	20151	10W29b	18357
10W31b	24554	10W31a	24053
10W33a	27374	10W33b	22333
10W35b	27683	10W35a	32364
10W37a	30034	10W37b	28186
10W39b	51212	10W39a/c	35948
10W42b	31881	10W42a	26309
10W44a	26122	10W44b	25884
	419529		377605

Table 4.8: Mean values for the most important kinematic variables.

Year	$\langle Q^2 \rangle$ [(GeV/c)^2]	$\langle x_{Bj} \rangle$	$\langle y \rangle$	$\langle W \rangle$ [GeV/c^2]	$\langle p_T^2 \rangle$ [(GeV/c)^2]
2003&2004	1.99	0.032	0.27	8.56	0.23
2007&2010	2.15	0.039	0.24	8.13	0.18

5. Background Estimation

In this chapter the estimation of non-exclusive events in the used sample is discussed. First the data in a non-exclusive range as well as semi-inclusive samples generated with Monte-Carlo (MC) are studied and compared to the exclusive ρ^0 candidates. Afterwards the used background estimation is introduced. The main focus is on the estimation of the semi-inclusive fraction of the background since this part is the most sizable. The chapter is closed with a discussion of additional contributions to the background.

5.1 Parametrisation of Semi-inclusive Background

The goal is to detect exclusively produced ρ^0 mesons. This implies that there are no additional particles in the final state except the produced ρ^0 meson and the proton. The exclusivity of the studied process is ensured by choosing a so-called exclusive range in the missing energy (Sec. 4.3.4.2), which was chosen to be $-2.5\,\mathrm{GeV} < E_{\mathrm{miss}} < 2.5\,\mathrm{GeV}$. This corresponds to $2 \cdot \sigma$, where σ is the resolution of the missing energy determination.

Due to the wide range, a large amount of ρ^0 mesons are produced in a semi-inclusive process where additional particles are generated in the final state. If, because of the limited acceptance of the spectrometer, these additional particles escape the detection, the corresponding event is detected by mistake as an exclusive event. The shape of the missing energy distribution shown in Fig. 4.15 indicates a sizable non-exclusive background in the selected range $-2.5 < E_{\mathrm{miss}} < 2.5$, which rises with increasing E_{miss} values.

Due to the conservation of momentum the transition of the virtual photon into the vector meson leads to a sizable recoil of the proton. Therefore the detection of the recoiled proton helps significantly to clean up the sample. The measurement of exclusive processes with an unpolarised liquid hydrogen target and such a recoiled proton detector is planned at COMPASS-II [83]. Pilot runs were performed in the years 2008, 2009 and 2012. In the past such a measurement was done, for instance at HERMES [118]. The measurement of the exclusive processes with a solid-state

transversely polarised target surrounded by a recoil proton detector at COMPASS is being discussed recently and is planned for the future (after 2018).

The presented data was recorded during the years 2003, 2004, 2007 and 2010. In these years the measurement was performed with a transversely polarised target, without the detection of the recoiled proton. Since we do not have the possibility to distinguish between pure exclusive events and misidentified non-exclusive events, a method to estimate the number of background events in the exclusive sample is needed. The estimation of the semi-inclusive background can be either based on measured data or on Monte-Carlo simulations. The goal is to have a precise estimation of the number of such events in the exclusive range as a function of important kinematic variables. This enables the correction of the ϕ, ϕ_S distributions which are used to extract the asymmetries.

A non-zero asymmetry of the semi-inclusive events could introduce a bias to the exclusive asymmetries. Hence, it is crucial for the analysis to study the asymmetries for non-exclusive produced ρ^0 mesons. This is done in Sec. 7.2. Furthermore, it is possible to correct the extracted values on the level of asymmetries. Here, background asymmetries are extracted from the data, for example applying all cuts except the cut on the missing energy and choosing a range in E_{miss} where only non-exclusive produced ρ^0 mesons are present. This approach is discussed in Sec. 7.3.

5.1.1 Exclusive Data vs. Semi-inclusive Data

At first, the possibility for a data-based estimation of the semi-inclusive background contribution is tested. The measured data sample includes semi-inclusive data from two sources: On the one hand, the high E_{miss} range; on the other hand, the like-sign sample.

Of particular interest are the events with a higher E_{miss} value. Their energy loss is so big that additional particles are certainly produced but escape the detection in the COMPASS spectrometer. These events are selected by applying the same restrictions as for the standard ρ^0 selection, but a different cut on E_{miss}. Here the missing energy range $7.0\,\text{GeV} < E_{\text{miss}} < 20.0\,\text{GeV}$ was chosen, with about the same amount of ρ^0 mesons as in the exclusive range. This range is well above the exclusive range, as well as the area where a further background contribution is present, known as diffractive dissociation, which is discussed in Sec. 5.4. As a consequence, the sample covers a different kinematic range, characterised by higher Q^2 and W with mean values $\langle Q^2 \rangle \approx 2.7\,(\text{GeV}/c)^2$ and $\langle W \rangle \approx 8.5\,\text{GeV}/c^2$, respectively, for the data sample of the years 2007&2010. Also the ϕ distributions of ρ^0 candidates with $-2.5\,\text{GeV} < E_{\text{miss}} < 2.5\,\text{GeV}$ and $7.0\,\text{GeV} < E_{\text{miss}} < 20.0\,\text{GeV}$ differ from each other as shown on the left-hand side of Fig. 5.1. But, the ϕ_S distributions presented on the right-hand side of Fig. 5.1 is not depending on E_{miss}. This observation also holds for the azimuthal modulations defined in Eq. 6.3. We will come back to this observation when estimating the amount of semi-inclusive background in Sec. 5.2.1[1].

Another semi-inclusive sample is a sample with like-sign hadrons, h^+h^+ or h^-h^-, in the final state. Due to the charge conservation of the strong interaction, further

[1]Even though the studies in this section are only presented for the 2007&2010 data sample, the conclusion is valid for the 2003&2004 sample too.

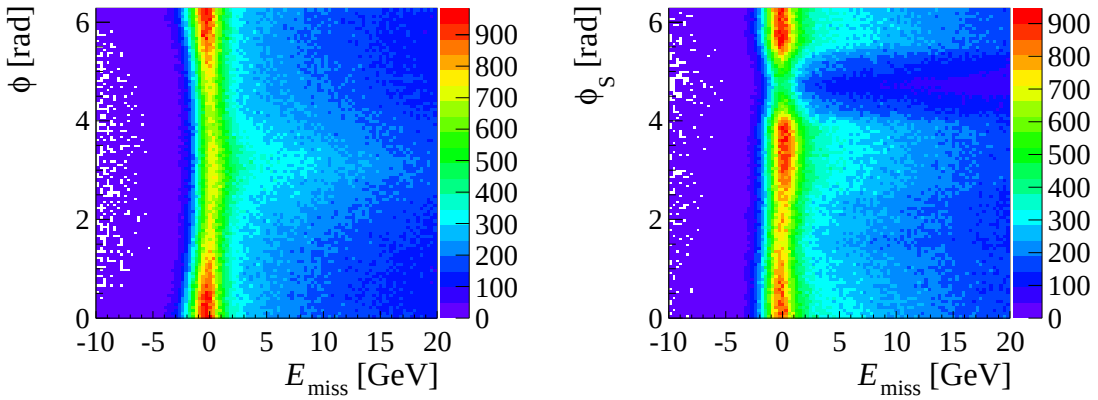

Figure 5.1: Correlation between E_{miss} and the angle ϕ (left-hand side) and the angle ϕ_S (right-hand side) for the 2007&2010 sample. All cuts indicated in Tab. 4.5 are applied, except the cut on E_{miss}.

particles are required to be produced in the formation process. Again the same restrictions are applied as for the standard ρ^0 selection, except the cut on the charge of the outgoing hadrons and an increase of the mass range:

$$0.475\,\text{GeV}/c^2 < M_{h^+h^-} < 1.775\,\text{GeV}/c^2,$$

to gain more statistics. As expected, the kinematic distributions of the exclusive and the like-sign sample differ significantly. The like-sign sample can be characterised by a flat decrease of the Q^2 distribution as shown in Fig. 5.2 and a steeper decrease of W. Unfortunately a direct parametrisation of the semi-inclusive background with the like-sign sample is not possible due to the different shape of the missing energy distribution for large E_{miss} values. A comparison of the missing energy of the standard ρ^0 sample and the like-sign sample is presented in Fig. 5.2.

5.1.2 Monte-Carlo vs. Data

For the determination of the background shapes, semi-inclusive Monte-Carlo samples are produced using the transverse setups of the spectrometer of the years 2004 and 2007. The generators LEPTO [99] and PYTHIA [100] were used with COMPASS tuning [31]. LEPTO is a pure semi-inclusive generator, whereas PYTHIA contains a large variety of processes, both semi-inclusive and exclusive ones. For the study of the background shape, the exclusive processes are rejected. The ρ^0 samples are selected applying the same cuts as for the real data. The cuts are summarised in Tab. 4.5.

However, as can be seen exemplary in Fig. 5.3, the shapes determined from Monte-Carlo do not agree well with the data. Moreover, the shapes of the E_{miss} distribution for the events generated with PYTHIA and LEPTO differ from each other. But, in general they raise and fall too steeply compared to the shape of the E_{miss} distribution of the real data. Furthermore, the more background is present, the less is the agreement between data and Monte-Carlo samples. This observation prevents us

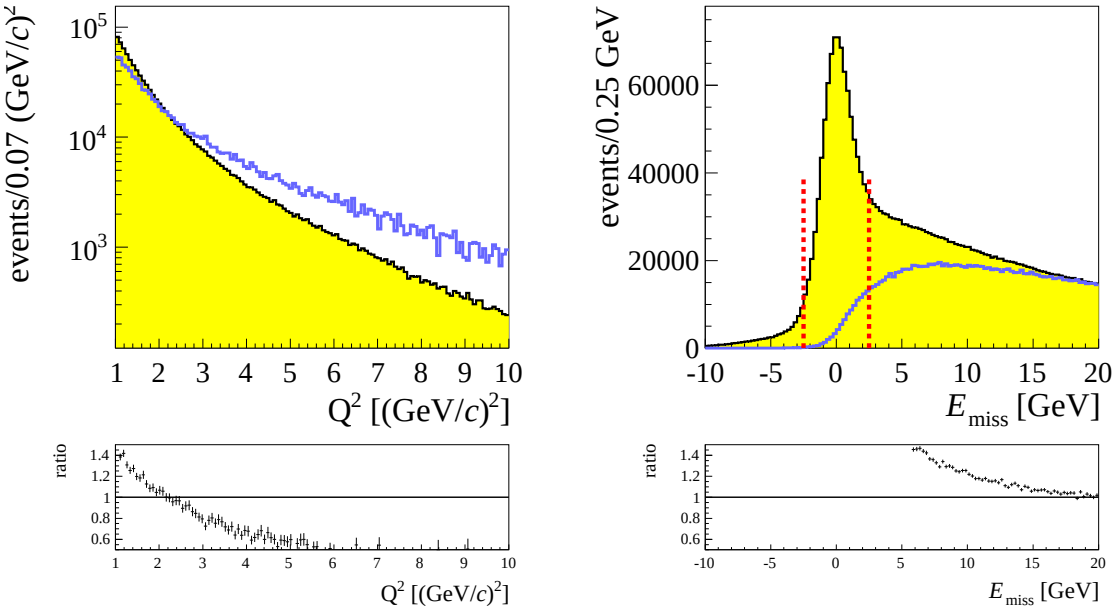

Figure 5.2: Comparison of the Q^2 distribution (left-hand side) and the E_{miss} distribution (right-hand side) for the exclusive ρ^0 sample (yellow histogram) and the like-sign two-hadron sample (blue line) for 2007&2010. All cuts indicated in Tab. 4.5 are applied, except the cut on E_{miss}.

from directly using the generated sample for a parametrisation of semi-inclusive background.

Therefore, neither the like-sign data sample nor the Monte-Carlo sample can be used to parametrised the semi-inclusive background directly. But the comparison of several kinematic distributions of the like-sign data sample, and a like-sign sample generated with LEPTO or PYTHIA Monte-Carlo shows a reasonable agreement. Hence, the like-sign samples are used to weight the unlike-sign Monte-Carlo sample as it will be described in the next section.

5.1.3 Weighting the Monte-Carlo

In order to improve the agreement between the Monte-Carlo and the measured data, the Monte-Carlo is weighted using the like-sign sample. The procedure is based on the observation that the comparison of the missing energy shape of the like-sign data sample and the like-sign Monte-Carlo sample shown in Fig. 5.4 results in the same trend, as well as observed for the ρ^0 sample presented in Fig. 5.3. For the years 2007&2010 a LEPTO as well as a PYTHIA Monte-Carlo sample is used, whereas for the years 2003&2004 only a LEPTO Monte-Carlo sample is utilised. The weights are calculated as a ratio out of the like-sign Monte-Carlo sample and the like-sign data sample. Firstly, a two-dimensional weighting in z and y is used. The variable z is chosen because it correlates with E_{miss} but avoids a direct weighting of the missing

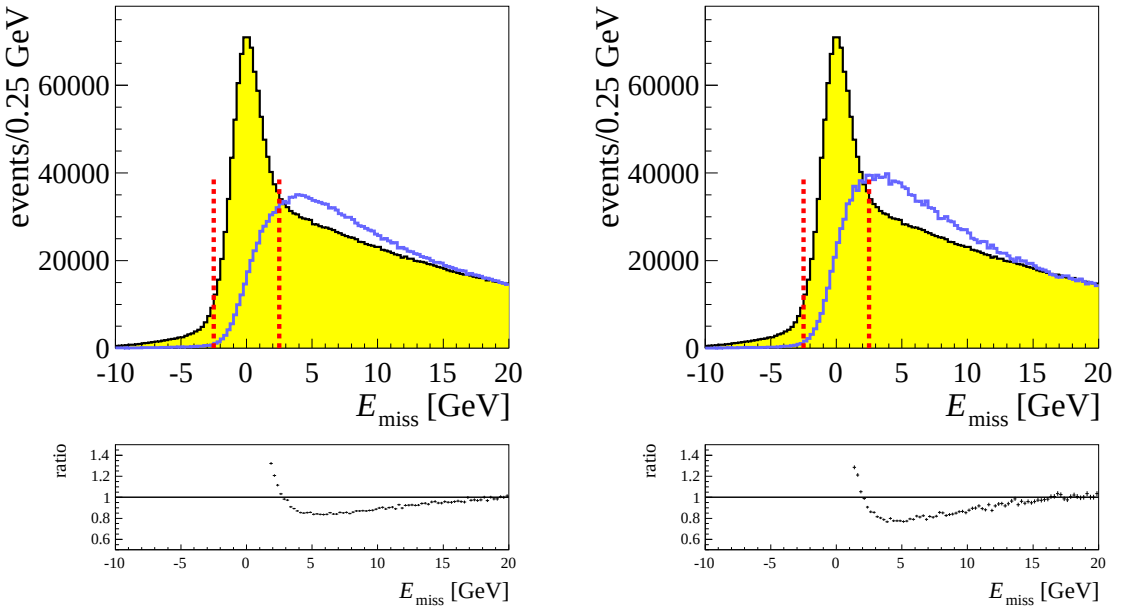

Figure 5.3: Comparison of the missing energy distribution from data (yellow histogram) and Monte-Carlo (blue line). On the left-hand side the Monte-Carlo sample generated with PYTHIA is shown whereas on the right-hand side the LEPTO sample is presented.

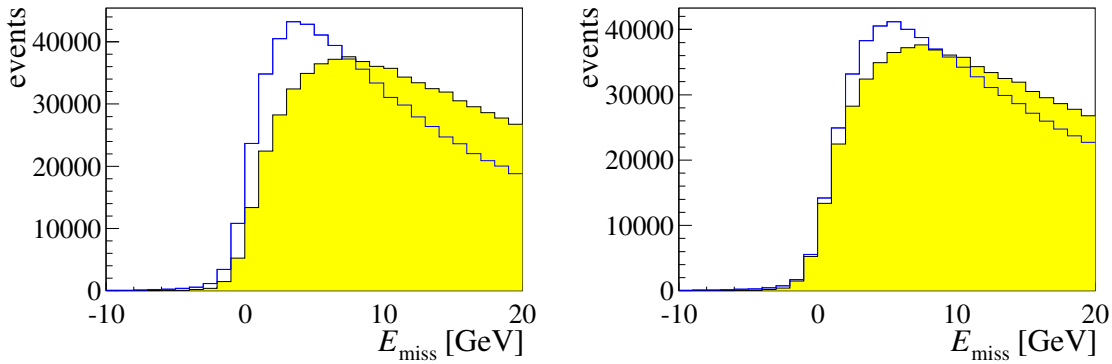

Figure 5.4: Missing energy distribution of the like-sign data for 2007&2010 (yellow filled histogram) and the like-sign LEPTO Monte-Carlo sample (left-hand side) and PYTHIA Monte-Carlo sample (right-hand side).

energy. Also y is taken because of its strong correlation with Q^2. The weights are calculated in every bin i as:

$$w_i(z,y) = \frac{N^{h^+h^+}_{\text{i,data}}(z,y) + N^{h^-h^-}_{\text{i,data}}(z,y)}{N^{h^+h^+}_{\text{i,MC}}(z,y) + N^{h^-h^-}_{\text{i,MC}}(z,y)}. \tag{5.1}$$

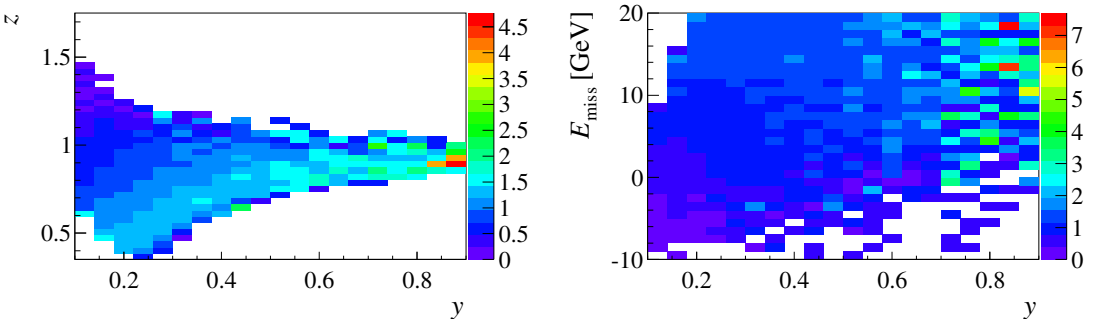

Figure 5.5: Two dimensional weights as a function of y and z (left-hand side) and y and E_{miss} (right-hand side) calculated from the like-sign sample of data and LEPTO Monte-Carlo for the 2007&2010 sample.

The result is shown on the left-hand side of Fig. 5.5 and can be compared to the two-dimensional weighting in E_{miss} and y where the weights are calculated in every bin i according to:

$$w_i(E_{\text{miss}}, y) = \frac{N^{h^+h^+}_{\text{i,data}}(E_{\text{miss}}, y) + N^{h^-h^-}_{\text{i,data}}(E_{\text{miss}}, y)}{N^{h^+h^+}_{\text{i,MC}}(E_{\text{miss}}, y) + N^{h^-h^-}_{\text{i,MC}}(E_{\text{miss}}, y)}. \tag{5.2}$$

These weights are presented on the right-hand side of Fig. 5.5.

A nice feature of the like-sign sample is that, due to charge conservation, it contains only pure background events. Hence the ρ^0 sample generated with Monte-Carlo can be weighted in the full E_{miss} range. Therefore a direct weighting of the E_{miss} distribution is possible. Finally a one-dimensional weighting is tested. The weights are simply calculated in every E_{miss} bin i as the ratio of numbers of like-sign events from data and Monte-Carlo as:

$$w_i(E_{\text{miss}}) = \frac{N^{h^+h^+}_{\text{i,data}}(E_{\text{miss}}) + N^{h^-h^-}_{\text{i,data}}(E_{\text{miss}})}{N^{h^+h^+}_{\text{i,MC}}(E_{\text{miss}}) + N^{h^-h^-}_{\text{i,MC}}(E_{\text{miss}})}. \tag{5.3}$$

They are presented in Fig. 5.6. All weighting procedures improve the agreement between the ρ^0 data and MC significantly. It was checked that the parametrisation of the shape of the missing energy distributions (Sec. 5.1.4) weighted with the different weights are well compatible with each other. The same observation applies on the level of asymmetries. As a standard method the weights calculated in Eq. 5.3 are used. What is remarkable is the linear increase of the weights calculated with the LEPTO sample. The approach is supported by the observation that the weights calculated for the ρ^0 sample and for the like-sign sample are comparable for large E_{miss}.

Note that all Monte-Carlo pictures in this thesis includes a smearing of the beam momenta. At first, it was observed that the weights for $E_{\text{miss}} < 2.5\,\text{GeV}$ are largely fluctuating between 2 and 5. This observation is cured by assigning false beam momenta randomly to 7% of the Monte-Carlo events [119]. The beam momenta are drawn randomly from a Gaussian distribution with a mean of $159.4\,\text{GeV}/c$ and a $\sigma = 5.2\,\text{GeV}/c$, representing the beam momentum distribution of Monte-Carlo. The reason might be that in real data false beam momenta are measured for a small

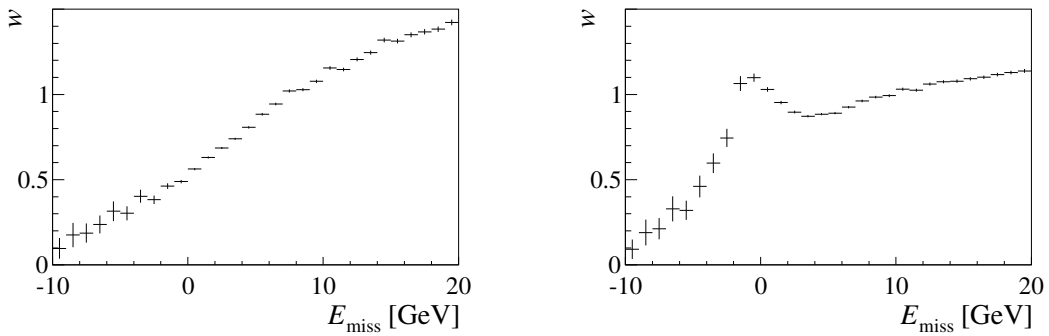

Figure 5.6: One dimensional weights as a function of E_{miss} calculated from the like-sign sample of data and LEPTO Monte-Carlo (left) and PYTHIA Monte-Carlo (right) for the 2007&2010 sample.

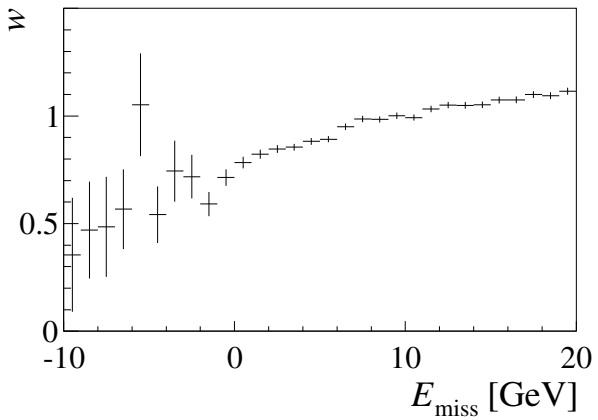

Figure 5.7: One dimensional weights as a function of E_{miss} calculated from the like-sign sample of data and LEPTO Monte-Carlo for the 2003&2004 sample.

fraction of events. In the Monte-Carlo simulation this uncertainty of the beam momentum reconstruction is not taken into account enough. The smearing is done for the deuteron as well as for the proton data. In Fig. 5.5 and Fig. 5.6 the weights obtained with this smeared Monte-Carlo are shown. As can be seen, they are now quite stable also for $E_{\text{miss}} < 2.5\,\text{GeV}$.

For the deuteron setup only a LEPTO MC sample was available. The weights are shown in Fig. 5.7. The trend is comparable with the proton sample, although for a small fraction of events the statistical fluctuations are significantly higher.

5.1.4 Parametrisation of E_{miss} Shape

In order to estimate the number of semi-inclusive events in the exclusive range, the shape of the missing energy distribution of the weighted semi-inclusive LEPTO Monte-Carlo sample is parametrised. For the 2007&2010 setup the parametrisation of the semi-inclusive E_{miss} shape is also done with the PYTHIA Monte-Carlo. The E_{miss} shapes of the samples generated with PYTHIA and LEPTO differ from each other as discussed in Sec. 5.1.2. Event though, this results in a slightly higher

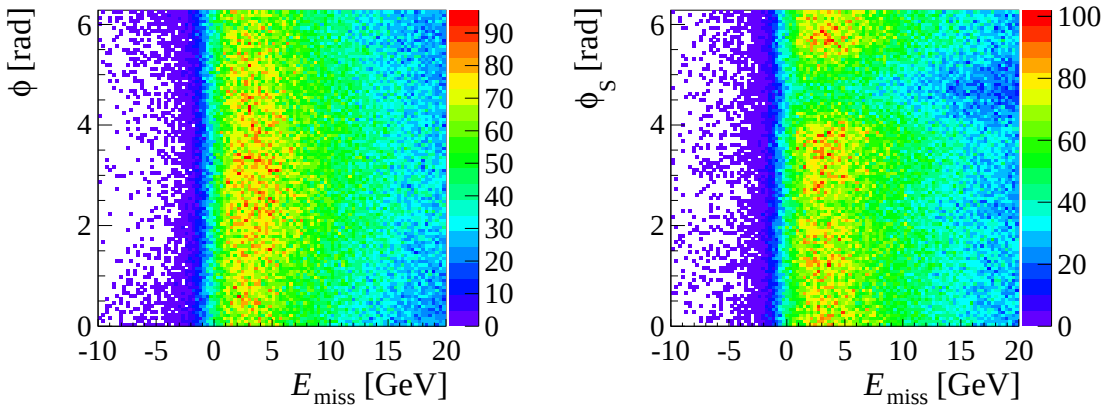

Figure 5.8: Correlation between E_{miss} and the angle ϕ (left-hand side) and the angle ϕ_S (right-hand side) for semi-inclusive events generated with LEPTO. All cuts indicated in Tab. 4.5 are applied, except the cut on E_{miss}.

amount of semi-inclusive events estimated with the LEPTO Monte-Carlo, the extracted asymmetries are well compatible. We will come back to this observation when we estimate the systematic uncertainty due to the background parametrisation in Sec. 7.5.4.1.

The Monte-Carlo sample is binned, as the real data, in x_{Bj}, Q^2 and p_T^2 for each target cell (Eq. 6.12). Based on the observation that the ϕ and ϕ_S distributions as well as the azimuthal modulations do not depend on the missing energy, as shown in Fig. 5.8 . Therefore no binning in the angles ϕ and ϕ_S is performed.

For each of the bins the Monte-Carlo E_{miss} distribution is fitted with the empirical function:

$$f(x)_{back} = A_{back} \cdot \left(1 + e^{\left(\frac{x-p_1}{p_2}\right)}\right)^{-0.2} \cdot \left(1 - \left(1 + e^{\left(\frac{x-p_3}{p_4}\right)}\right)^{-0.25}\right), \tag{5.4}$$

and the parameters p_1 to p_4 are evaluated. In principle the superscripts -0.25 and -0.2 can be take as an additional fit parameters. The fit results are compatible, although the fits get more unstable. Both the proton and the deuteron setup are fitted with the same function. Despite the different missing energy shapes of the setups this gives satisfying results. The results of the fits are presented in Fig. 5.9 for the proton setup and in Fig. 5.10 for the deuteron setup. The fit parameters for each bin as well as the reduced χ^2 of the fits, are given.

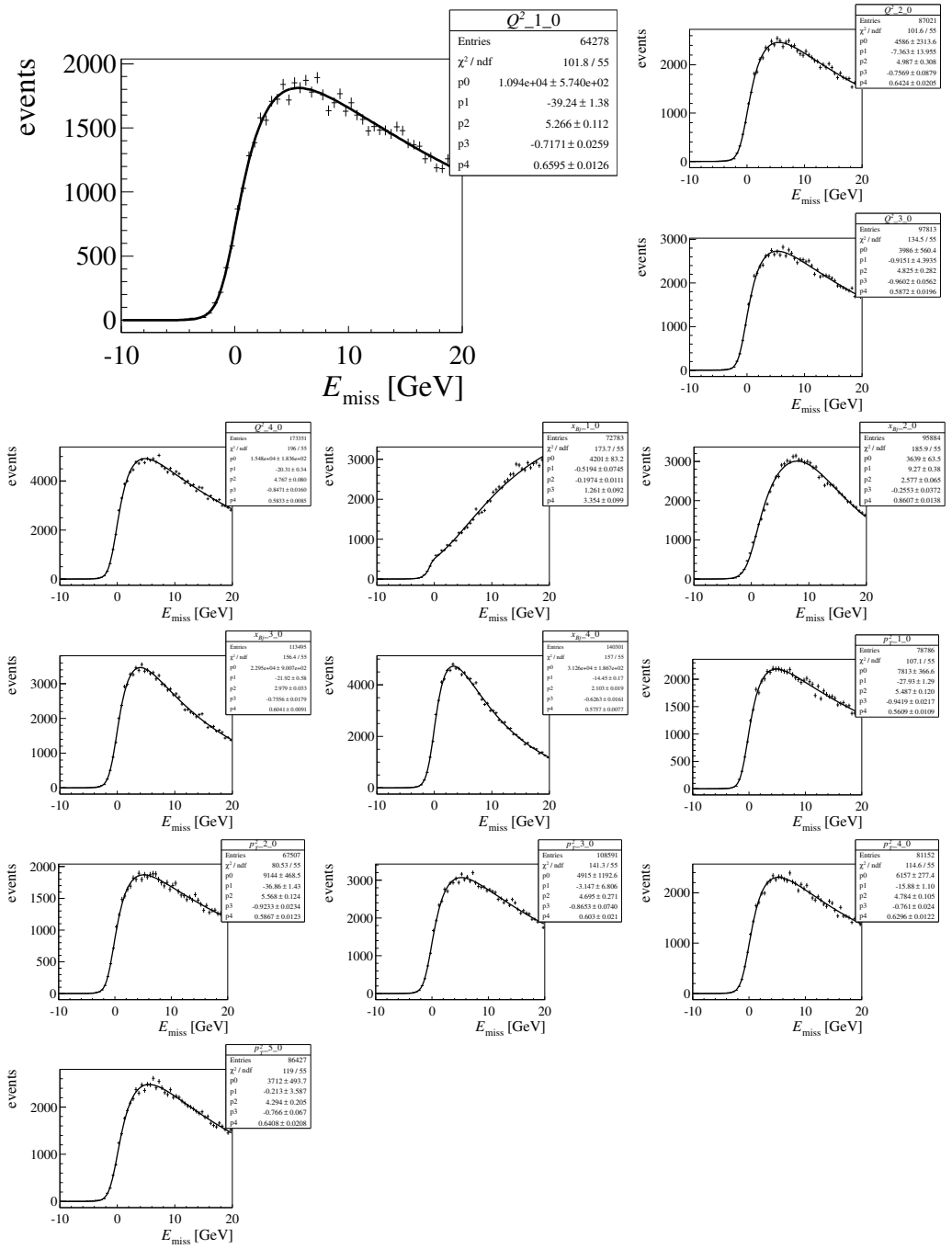

Figure 5.9: The E_{miss} distribution from LEPTO Monte-Carlo parametrised with Eq. 5.4 for the 2007&2010 sample. The four bins in Q^2 and x_{Bj} and the five bins in p_T^2 for the up plus down target cells are shown. The bins according to Eq. 6.12 are indicated by the first number in the histogram titles. The corresponding fits for the central target cell are presented in the Appendix C.2.

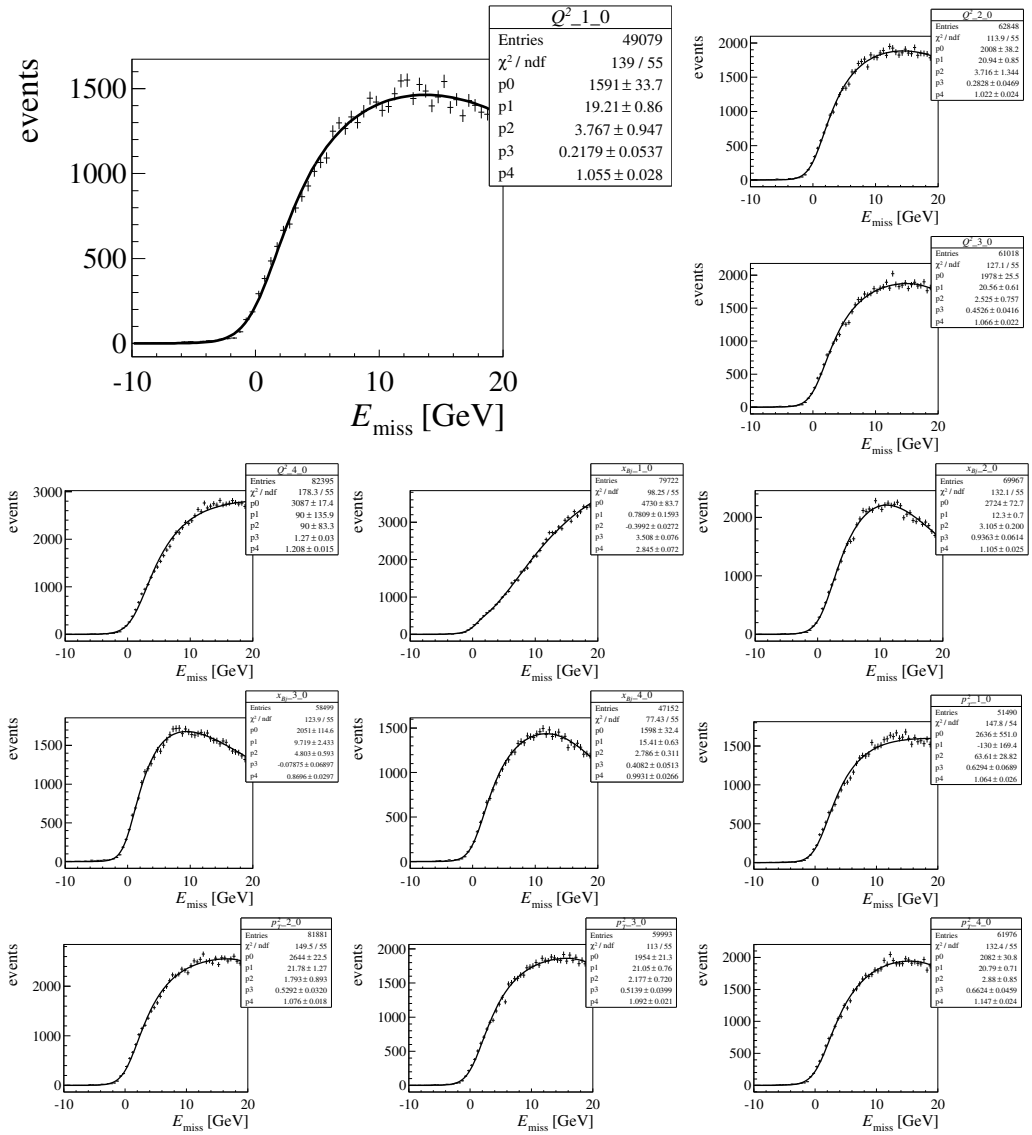

Figure 5.10: The E_{miss} distribution from LEPTO Monte-Carlo parametrised with Eq. 5.4 for the 2003&2004 sample. The four bins in Q^2 and x_{Bj} and the five bins in p_T^2 for the up target cell are shown. The bins according to Eq. 6.12 are indicated by the first number in the histogram titles. The corresponding fits for the down target cell are presented in the Appendix C.2.

5.2 Estimation of Semi-inclusive Background

5.2.1 Fit to Data

In order to correct for the remaining semi-inclusive background in the signal range, the E_{miss} shape of the background events is normalised to the data. This is done by performing a signal plus background fit, with a Gaussian function for the signal part and the semi-inclusive background shape fixed by Monte-Carlo as described above. Two different estimation methods are implemented.

For the first method the fits are done in every bin required for the asymmetry extraction, i.e the kinematic bins Q^2, x_{Bj}, and p_T^2, individually for each target cell and additionally for the two different spin orientations and will be denoted with k_1 in the following. For the second method, in addition, the Monte-Carlo data is binned in each azimuthal bin[2]. This is denoted with k_2.

Lets start with the discussion of the first approach. The fits are presented in Fig. 5.11 for the $+-+$ configuration in 2007&2010 and in Fig. 5.12 for the $+-$ configuration in 2003&2004. The corresponding fits for the $-+-$ and $-+$ configurations are shown in the Appendix C.2. Here, the normalisation constant A_{bgr} in Eq. 5.4 is denoted by p_3, where mean and σ of the Gaussian function are denoted by p_0 and p_1. The number of semi-inclusive events in bin k_1 is given by the integral of the background function, presented with a blue dashed line, in the exclusive range $-2.5\,\text{GeV} < E_{\text{miss}} < 2.5\,\text{GeV}$.

In order to arrive at background corrected (ϕ, ϕ_S) distributions, $N_{k_1}^{\text{sig}}(\phi, \phi_S)$, we consider the distributions measured in the signal range, $N_{k_1}^{\text{sig,raw}}(\phi, \phi_S)$, and the ones in the background range $7\,\text{GeV} < E_{\text{miss}} < 20\,\text{GeV}$, $N_{k_1}^{\text{back}}(\phi, \phi_S)$. These background distributions are extracted using the same binning i.e. for each kinematic bin in x_{Bj}, Q_2, and p_T^2 respectively, and for each target cell and each polarisation state individually. The distributions $N_{k_1}^{\text{back}}(\phi, \phi_S)$ is normalised to the number of ρ^0 events in the signal distribution $N_{k_1}^{\text{sig,raw}}(\phi, \phi_S)$. After that it is rescaled with the estimated amount of background events in the signal range and afterwards subtracted from the $N_{k_1}^{\text{sig,raw}}(\phi, \phi_S)$ distributions. The result is the background corrected distribution $N_{k_1}^{\text{sig}}(\phi, \phi_S)$.

In cases the statistics is sufficient the second method is used. The E_{miss} distribution is fitted for each kinematic bin x_{Bj}, Q_2 and p_T^2, for each target cell, each polarisation state and each angular bin, respectively and the number of semi-inclusive background is estimated. Note that the same Monte-Carlo shape is used as for the first method i.e. the missing energy shape is parametrised for all background events integrating over the azimuthal distributions. This shape is applied to the data, whereas the data is binned in the azimuthal distributions. This approach is supported by the observation that the ϕ and ϕ_S distributions as well as the azimuthal modulations do not depend on the missing energy (Sec. 5.1.4). This method has the advantage that it allows for a direct estimation of the number of background events in each

[2]Here, the expression "azimuthal bins" summarise different binnings. If a two-dimensional binning is applied it stands for bins in both ϕ and ϕ_S. On the other hand, if a one-dimensional binning is used it describes the binning directly in the azimuthal modulation introduced in Eq. 6.3. The different extraction methods of the asymmetries are discussed in Sec. 6.1.

bin. Therefore the azimuthal distribution $N_{k_2}^{\mathrm{sig,raw}}(\phi, \phi_S)$ can be corrected bin-by-bin without further assumptions on the ϕ, ϕ_S distributions of the background range. The result is the background corrected distribution $N_{k_2}^{\mathrm{sig}}(\phi, \phi_S)$.

The comparison of the shape of the missing energy distributions for the different target cells are shown in Fig 5.11, Fig 5.12 and Appendix C.2. In the signal range this results in a visible difference for the deuteron setup while the shapes for the proton setup are more stable. The observation can be explained with the different number of target cells. In 2003&2004, a two-cell target is used, where the cells have been polarised oppositely. On the contrary, in 2007&2010 a three cell target is used, where the outer cells are polarised in the same and the middle cell in the other direction. This setup leads to a more balanced acceptance. Additionally, the target magnet was renewed in 2006 (Sec. 3), which provides an increase of the angular acceptance to 180 mrad for the upstream target edge resulting in an increased hadron acceptance.

The total amount of semi-inclusive background in the signal range is 22% for the proton setup and 18% for the deuteron setup, where the numbers strongly depend on the corresponding kinematic bin and vary between 7% and 40% and 7% and 30%, respectively. Finally, the asymmetries are extracted using the $N_{k_1}^{\mathrm{sig}}(\phi, \phi_S)$ or $N_{k_2}^{\mathrm{sig}}(\phi, \phi_S)$ distribution, optionally obtained with the first or the second correction method, respectively.

5.3 Influence of Coherently Produced ρ^0 Mesons

Coherent production describes processes where the virtual photon interacts with the proton or the deuteron rather than the individual quarks in the nucleon. Therefore, for such types of reactions, the theoretical prediction of the total angular momenta of quarks is not possible with the underlying theory. The highest contribution of these coherently produced events are present in processes with small values of $-t'$ i.e. where the momentum transfer to the target is small.

In the analysis p_T^2, rather than $-t'$, is studied [114]. For exclusive events $p_T^2 \approx |t'|$. For non-exclusive events the minimal kinetically allowed $|t|$ denoted by t_0 is poorly determined, which might distort the $-t'$ distribution if the background in the studied sample is not negligible.

Coherent production is suppressed by the cut $p_T^2 > 0.05\,(\mathrm{GeV}/c)^2$ for the measurement with a NH_3 target and by the cut $p_T^2 > 0.1\,(\mathrm{GeV}/c)^2$ for the measurement with a ^{6}LiD target. At small values of p_T^2 the contribution from coherent production dominates, whereas at large p_T^2 the non-exclusive events contribute significantly as the slope of the p_T^2 distribution for non-exclusive events is more flat than the slopes for coherent and for incoherent exclusive production [114]. Therefore a data based estimation of coherently produced events in the sample is possible via a three-component fit, one component for the coherent, one for the incoherent and one for non-exclusive events:

$$f(p_T^2) = p_0 \cdot e^{-p_1 \cdot p_T^2} + p_2 \cdot e^{-p_3 \cdot p_T^2} + p_4 \cdot e^{-p_5 \cdot p_T^2} \tag{5.5}$$

The results are shown in Fig. 5.13. The coherent contribution is shown with the green dashed line, the non-exclusive contribution with the blue dotted line and

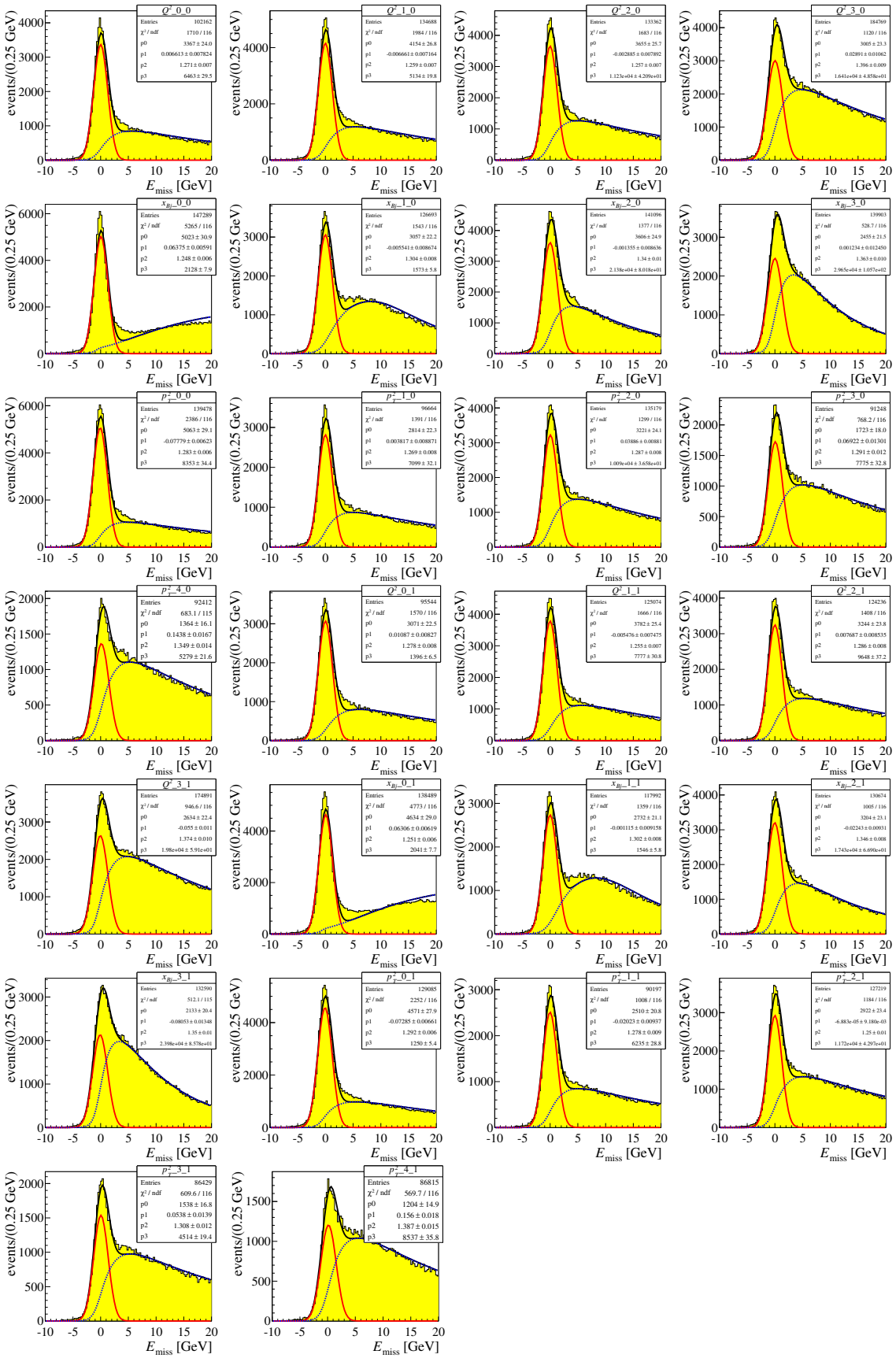

Figure 5.11: The E_{miss} distribution for the 2007&2010 sample together with the signal plus background fits (solid curve). The solid red lines and the dashed blue lines represent the signal and background contributions, respectively. The parameters $p_0 - p_3$ are explained in the text. Here are shown the fits for the $+-+$ configuration for the up plus down (0) and the central (1) target cells.

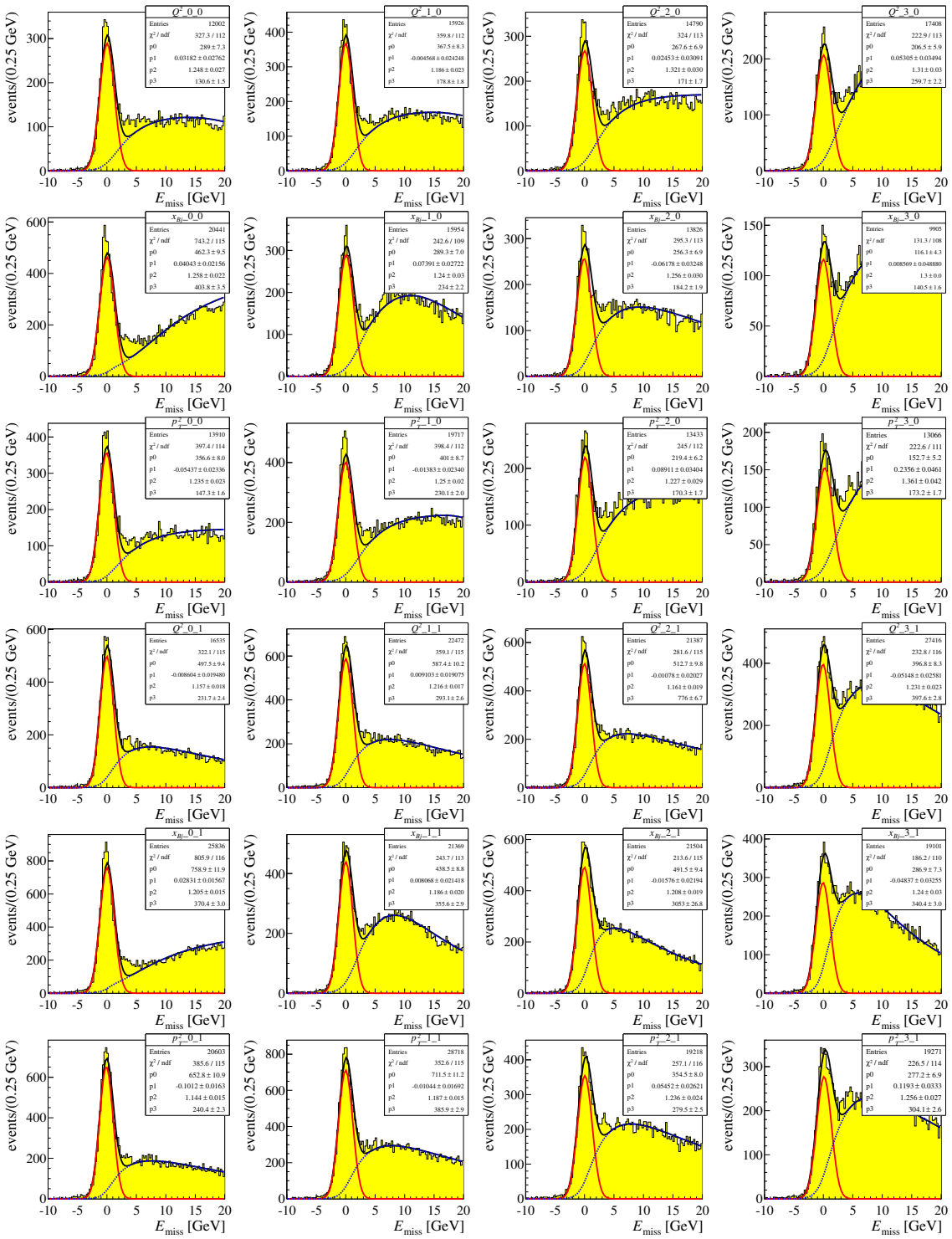

Figure 5.12: The E_{miss} distribution for the 2003&2004 sample together with the signal plus background fits (solid curve). The solid red lines and the dashed blue lines represent the signal and background contributions, respectively. The parameters $p_0 - p_3$ are explained in the text. Here are shown the fits for the $+-$ configuration for the up (0) and the down (1) target cells. The corresponding fits for the $-+$ configuration are presented in the Appendix C.2.

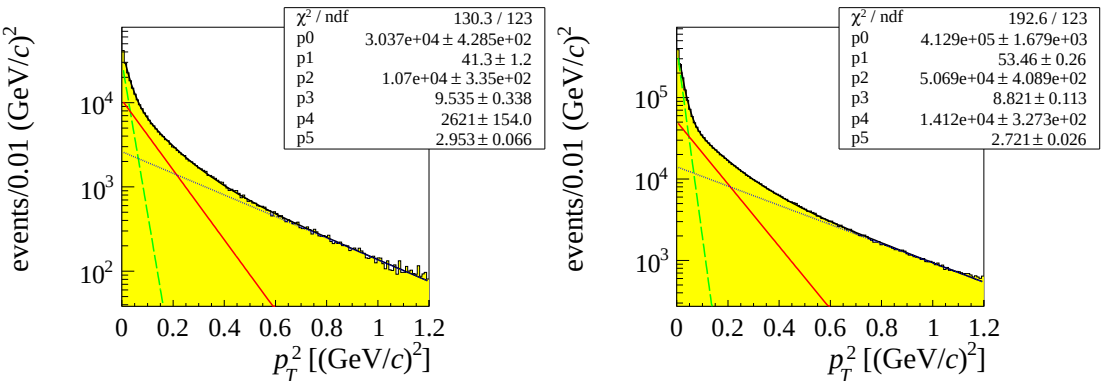

Figure 5.13: Distributions of p_T^2 for the 2003&2004 sample (left) and 2007&2010 sample (right). All cuts indicated in Tab. 4.5 are applied except the cut on p_T^2. The three-component fit defined in Eq. 5.5 is shown with coherent contribution (green dashed line), non-exclusive contribution (blue dotted line) and exclusive contribution (red line).

the exclusive contribution with the red line. Note: This fit provides only a rough data-based estimate of the remaining coherent contribution in the sample; also the background contribution is overestimated.

A model-based estimation is performed in Ref. [115] for the ^{6}LiD target. It is done with a Glauber Model approach and two different mechanisms of meson leptoproduction, the VMD model as well as the color dipole model. Having in mind the outcome of the data-based study as well as the model based study, the remaining coherently produced events is estimated up to 12% for the final proton sample and up to 8% for the final deuteron sample. The influence of the remaining coherent contribution on the extraction of asymmetries is studied in Sec. 7.5.5.

5.4 Additional Contributions to the Background

After the above-mentioned subtraction of semi-inclusive background, the remaining sample still contains non-exclusive events. Important contributions are beside the coherently produced ρ^0 mesons discussed above, the diffractively produced events and the non-resonant $\pi^+\pi^-$-pairs.

Diffractively produced ρ^0 mesons are events in which the target nucleon is excited to a baryonic resonance $N^\star$ or Δ. The resonant state decays into a nucleon and one or several mesons. In this analysis the cut $|E_{\text{miss}}| < E_{\text{miss}}^{\text{limit}} = 2.5\,\text{GeV}$ is used to ensure the exclusivity. Hence diffractively produced ρ^0 mesons can not be distinguished from exclusive produced ρ^0 mesons unless the mass of the baryon resonance M_X is larger than:

$$M_X = \sqrt{2ME_{\text{miss}}^{\text{limit}} + M^2} = 2.4\,\text{GeV}/c^2,$$

The contribution of diffractive dissociation events can be seen in Fig. 4.15 alongside the exclusive peak as a small enhancement over the SIDIS background. In order to estimate the contribution of this type of background the Monte-Carlo generator

HEPGEN [120] is used. It allows to simulate together events originating from the exclusive ρ^0 mesons as well as from diffractively produced ρ^0 mesons. On the Monte-Carlo sample the same cuts are applied as for the real data. The contribution of nucleon-dissociative events to the final sample is found to be 14% [112].

Also non-resonant $\pi^+\pi^-$ production is characterised by $E_{\text{miss}} \sim 0$, but the invariant mass may not necessarily correspond to the mass of the ρ^0 meson. However, these non-resonant $\pi^+\pi^-$ pairs are indistinguishable from the ρ^0 decay products as both final states are produced coherently and hence interfere which each other. The contribution is estimated with the Söding or the Ross-Stodolsky parametrisation to be smaller than 2% [112]. No correction is applied for this contribution.

6. Extraction of the Asymmetries

In this section, the required steps to arrive at the final asymmetries are explained. In Sec. 6.1 the basic concept of asymmetry measurements is introduced, followed by Sec. 6.2 in which the applied extraction methods are presented. The utilisation of these methods result in "raw" asymmetries. The corrections, needed in order to come from the raw asymmetries to the physical asymmetries are explained in Sec. 6.3.

6.1 How to Build the Asymmetries

The transverse part of the cross section in Eq. 2.42 can be expressed as a sum of eight independent transverse spin dependent modulations of ϕ and/or ϕ_S defined in Eq. 2.46. The angles are presented in Fig. 2.11.

To disentangle the polarised part of the cross section from the unpolarised one, the number of ρ^0 candidates in the two opposite states of polarization are counted and compared with each other. Both states are realized at the same time due to the target structure which consists of multiple cells with alternating target polarisation. In the following, the target cells introduced in Sec. 3.2 are denoted, in the direction of the muon beam, with U (UP), C (CENTRAL), and D (DOWN). To suppress acceptance effects in the asymmetry measurement, the polarisation in each cell is changed regularly.

The data taking is organised in periods which are listed for the years 2003&2004 in Tab. 4.3, and for 2007&2010 in Tab. 4.2. To best profit from the available statistics, each period with the same configuration is summed up.

Only if the detector is stable, all unpolarised parts of the cross-section cancel each other out, leaving the spin dependent parts behind. Hence, for this kind of measurement, the stability of the detector is important. It could be shown that changes in the acceptance, which affect the whole target equally, have only a small impact on the extracted asymmetries [102]. This observation enables the performance of a

combined analysis of several periods and years[1]. Thus, two different configurations exist.

For the measurement with the two-cell target, depicted on the left-hand side of Fig. 6.1, the configuration with a positive polarised U cell (negative polarised U cell) and a negative polarised D cell (positive polarised D cell) is denoted by $+-$ $(-+)$. Always two configurations, i.e. four different samples are compared with each other:

2003&2004			2007&2010		
configuration	target	cell	configuration	target	cell
+-	U	D	+-+	U+D	C
-+	U	D	-+-	U+D	C

Here, positive polarisation is depicted in red and negative polarisation in blue. In 2007 and 2010 COMPASS used a transversely polarised three-cell target, depicted on the right-hand side of Fig. 6.1. The two outer cells are polarised in one, the inner cell in the opposite direction. In order to best profit from the statistics available, the events of the two outer cells U and D are summed up.

The number of exclusive ρ^0 mesons as a function of ϕ and ϕ_S can be written for every target cell n ($n \in \{1, 2\}$) and each polarisation state $\pm$ as:

$$N_n^{\pm}(\phi, \phi_S) = a_n^{\pm} \left(1 \pm A(\phi, \phi_S)\right), \tag{6.1}$$

where $a_n^{\pm}$ is the product of the spin-averaged cross section σ_0, the muon flux F, the number of target nucleons N and the acceptance $\alpha_n^{\pm}$:

$$a_n^{\pm} = F \cdot N \cdot \sigma_0 \cdot \alpha_n^{\pm}. \tag{6.2}$$

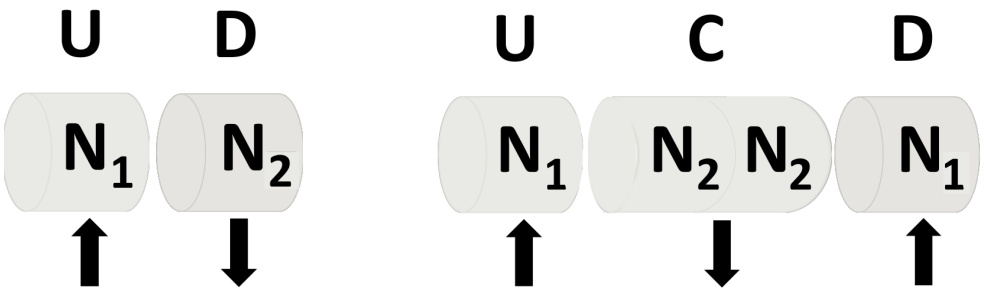

Figure 6.1: Definition of target cells. On the left-hand side the two-cell target used in 2003&2004 is presented whereas on the right-hand side the three-cell target from 2007&2010 is shown.

[1]In SIDIS analysis which do not suffer from limited statistics, it is common to combine the data sets of two consecutive weeks of data samples, grouped in rows on Tab. 4.2 and Tab. 4.3 and extract an asymmetry value for each of them. The final asymmetry is built as the weighted mean of these extractions.

The angular dependence $A(\phi, \phi_S)$ reads:

$$\begin{aligned} A(\phi,\phi_S) &= A_{\mathrm{UT,raw}}^{\sin(\phi-\phi_S)} \sin(\phi-\phi_S) + A_{\mathrm{UT,raw}}^{\sin(\phi+\phi_S)} \sin(\phi+\phi_S) \\ &+ A_{\mathrm{UT,raw}}^{\sin(3\phi-\phi_S)} \sin(3\phi-\phi_S) + A_{\mathrm{UT,raw}}^{\sin(2\phi-\phi_S)} \sin(2\phi-\phi_S) \\ &+ A_{\mathrm{UT,raw}}^{\sin\phi_S} \sin\phi_S + A_{\mathrm{LT,raw}}^{\cos(\phi-\phi_S)} \cos(\phi-\phi_S) \\ &+ A_{\mathrm{LT,raw}}^{\cos\phi_S} \cos\phi_S + A_{\mathrm{LT,raw}}^{\cos(2\phi-\phi_S)} \cos(2\phi-\phi_S). \end{aligned} \tag{6.3}$$

The symbol $A^m_{(\mathrm{UT,LT}),\mathrm{raw}}$ denotes the amplitude for the angular modulation m, and the term "raw" characterises $A^m_{(\mathrm{UT,LT}),\mathrm{raw}}$ as the pure fit result, whereas the correction factor, which will be introduced in Sec. 6.3 is not yet applied. The final goal is to extract these eight angular modulations either with unbinned or one-dimensional and two-dimensional binned fit methods (Sec. 6.2) from the ϕ, ϕ_S distribution of the final sample. For the latter, Eq. 6.1 is evaluated for each of the bins in ϕ and ϕ_S:

$$N^{\pm}_{j,n}(\phi,\phi_S) = a^{\pm}_{j,n}\left(1 \pm A(\phi,\phi_S)\right), \tag{6.4}$$

where the index j denotes the (ϕ, ϕ_S) bin. If a one-dimensional binned extraction method is used every summand in Eq. 6.3 is extracted separately. The binning is provided directly in the azimuthal modulation denoted by Θ. This can be expressed with:

$$N^{\pm}_{j,n}(\Theta) = a^{\pm}_{j,n}\left(1 \pm A_{1D}(\Theta)\right), \tag{6.5}$$

where:

$$\Theta \in \{(\phi-\phi_S), (\phi+\phi_S), (2\phi-\phi_S), (3\phi-\phi_S), \phi_S\}, \tag{6.6}$$

and:

$$\begin{aligned} A(\Theta) \in \{&\sin(\phi-\phi_S), \sin(\phi+\phi_S), \sin(2\phi-\phi_S), \sin(3\phi-\phi_S), \\ &\sin\phi_S, \cos(\phi-\phi_S), \cos(\phi+\phi_S), \cos\phi_S\} \end{aligned} \tag{6.7}$$

Here j denotes the Θ bin.

The angular distributions are presented in Figs. 6.2 and 6.3. They are not flat. Mainly in the ϕ_S distribution acceptance effects are visible. They arise due to the positioning of the trigger hodoscopes which prevent us from triggering on the scattered muons in the whole angular range. The dip in the ϕ_S distribution decreases in the 2007&2010 sample compared to the 2003&2004 sample. The reason is the increase of the angular acceptance to 180 mrad for the upstream target edge due to the renewed target magnet in 2006 (Sec. 3). The angular resolution is limited by the ϕ measurement and is estimated with Monte-Carlo to ≈ 0.16 mrad. However, the resolution of the angle ϕ_S is significantly better with ≈ 0.013 mrad.

6.2 Extraction of the Asymmetries

All asymmetries are extracted using four different methods: the double ratio method (1DDR), the one-dimensional (1DLH) and the two-dimensional binned (2DLH) and the unbinned (UB) maximum likelihood method. In this section the concepts of the different extraction methods are introduced. The advantage and the drawbacks of each of these methods are discussed. A summary of the applied methods and the abbreviation used is listed in Tab. 6.1.

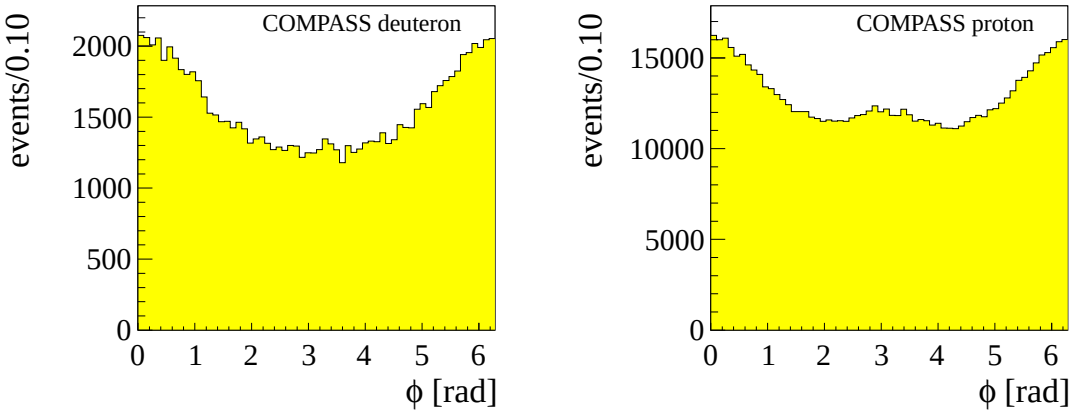

Figure 6.2: The distributions of the angle ϕ defined in Fig. 2.11 for the 2003&2004 sample (left) and 2007&2010 sample (right). All cuts indicated in Tab. 4.5 are applied.

For all binned methods, the fit is performed in the center of each bin. A possible bias effect of the finite bin size has to be considered. A correction of this bias can be calculated analytically [121], and subsequently applied on the fit result. Based on the generalised fit functions:

$$f(\Theta) = a_{k,fit} \sin\Theta(k) + b_{k,fit} \cos\Theta(k), \tag{6.8}$$

$$f(\phi, \phi_S) = a_{k,fit} \sin(k\phi \pm \phi_S) + b_{k,fit} \cos(k\phi \pm \phi_S), \tag{6.9}$$

where $k \in \{0, 1, 2\}$, the number of entries in each bin $\Delta\Theta = \Delta\phi = \Delta\phi_S = \frac{2\pi}{n}$ can be calculated, for instance, via $\frac{1}{\Delta}\int_{\Theta}^{\Theta+\Delta\Theta} f(\Theta)d\Theta$. where Eq. 6.8 is used for one-dimensional and Eq. 6.9 for two-dimensional extractions, respectively. The calculated corrections $\frac{a_{k,fit}}{a_k}$ and $\frac{b_{k,fit}}{b_k}$ are [121]:

$$\frac{a_{k,fit}}{a_k} = \frac{b_{k,fit}}{b_k} = \frac{2\sin\frac{\Delta\Theta}{2}}{\Delta\Theta} \tag{6.10}$$

$$\frac{a_{k,fit}}{a_k} = \frac{b_{k,fit}}{b_k} = \frac{4}{k\Delta\phi\Delta\phi_S} \sin\frac{k\Delta\phi}{2} \sin\frac{\Delta\phi_S}{2}. \tag{6.11}$$

The correction factors for a two-dimensional binned extraction with 12 bins in both ϕ and ϕ_S are listed in Tab. 6.2.

Table 6.1: A summary of the applied methods, the abbreviation used and the number of angular bins. The justification for their choice is given in the text.

method	abbreviation	# of angular bins
double ratio	1DDR	12
one-dimensional likelihood	1DLH	12
two-dimensional likelihood	2DLH	64
unbinned likelihood	UB	-

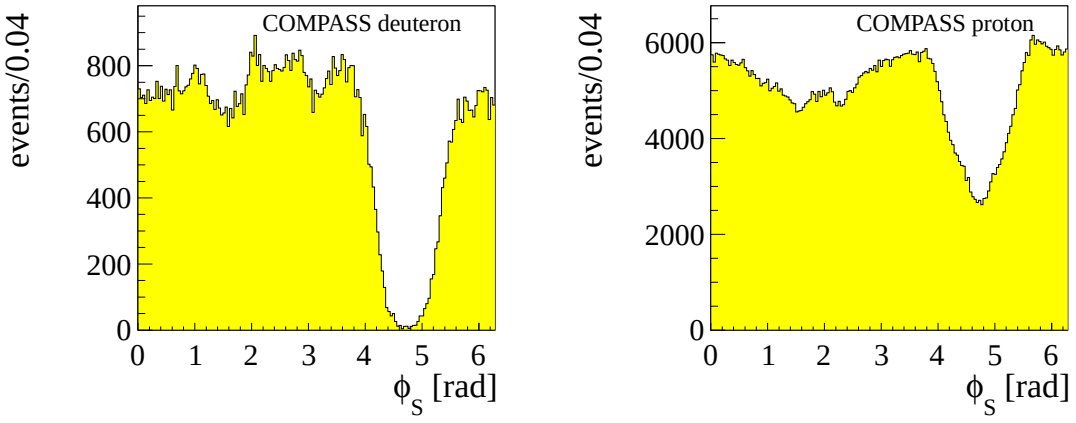

Figure 6.3: The distributions of the angle ϕ_S defined in Fig. 2.11 for the 2003&2004 sample (left) and the 2007&2010 sample (right). All cuts indicated in Tab. 4.5 are applied.

Table 6.2: Finite bin size correction factor for a two-dimensional binned extraction with 12×12 azimuthal bins for the different asymmetries.

$A_{\mathrm{UT}}^{\sin(\phi-\phi_S),\sin(\phi+\phi_S)}, A_{\mathrm{LT}}^{\cos(\phi-\phi_S)}$	$A_{\mathrm{UT}}^{\sin\phi_S}, A_{\mathrm{LT}}^{\cos\phi_S}$	$A_{\mathrm{UT}}^{\sin(2\phi-\phi_S)}, A_{\mathrm{LT}}^{\cos(2\phi-\phi_S)}$	$A_{\mathrm{LT}}^{cos(3\phi-\phi_S)}$
0.9774	0.9886	0.9441	0.8901

In order to investigate possible kinematic dependencies of the asymmetries, all asymmetries are extracted as a function of x_{Bj}, Q^2 and p_T^2, where the variables are binned according to:

$$\begin{array}{lccccccc} x_{Bj}: & & 0.003 & 0.02 & 0.03 & 0.05 & 0.35, & \\ Q^2\ [(\mathrm{GeV}/c)^2]: & & 1.0 & 1.2 & 1.6 & 2.4 & 10.0, & \\ p_T^2\ [(\mathrm{GeV}/c)^2]: & 0.05 & 0.1 & 0.15 & 0.25 & 0.35 & 0.5. & (6.12) \end{array}$$

The first bin in p_T^2 is only used in the analysis of the NH_3 target. The results are plotted against the arithmetic mean of the corresponding kinematic variable in the specified bin.

6.2.1 Double Ratio Method

One of the most intuitive methods to extract asymmetries is know as the Double Ratio Method and is based on:

$$F_j^{\mathrm{DR}} = \frac{N_{1,j}^{\pm} \cdot N_{2,j}^{\pm}}{N_{1,j}^{\mp} \cdot N_{2,j}^{\mp}}, \tag{6.13}$$

where $N_{n,j}^{\pm}$ is the number of events found in the cell/cells labeled with n in Fig. 6.1 in the period $\pm$ and $N_{n,j}^{\mp}$ is the number of events in the corresponding cells found in the coupled period which has the opposite target polarisation. The periods which

belong together can be found in the same row in Tab. 4.2 and Tab. 4.3[2]. The one-dimensional DR is binned in Θ (Eq. 6.6). Inserting Eq. 6.5 in Eq. 6.13 and neglecting second order terms leads to the fit function:

$$f(\Theta) \approx \frac{a_1^{\pm}(\phi,\phi_s)\cdot a_2^{\pm}(\phi,\phi_S)}{a_1^{\mp}(\phi,\phi_s)\cdot a_2^{\mp}(\phi,\phi_S)}\left(1+4A_{1D}(\Theta)\right). \tag{6.14}$$

The extracted values include both the acceptance modulations as well as the pure asymmetry. Therefore, further assumption for the acceptance terms are needed to be able to determine the pure asymmetries. The Double Ratio Method is based on the assumption that the ratio between the acceptance term of the first and that of the second period has the same azimuthal modulation for all the target cells:

$$\frac{\alpha_1^{\pm}(\phi,\phi_s)\cdot\alpha_2^{\mp}(\phi,\phi_S)}{\alpha_1^{\mp}(\phi,\phi_s)\cdot\alpha_2^{\pm}(\phi,\phi_S)} = C = \text{const.} \tag{6.15}$$

Eq. 6.15 is known as reasonable assumption. Since the beam flux across the target cells is equalized by applying appropriate cuts on the phase space of the beam, the number of events in the different cells of the same period cancel out in Eq. 6.14. The Eq. 6.15 is also valid for $a_n^{\pm}$. The statistical error of the double ratio is:

$$\sigma_j^F = F_j^{\mathrm{DR}}\cdot\sqrt{\frac{1}{N_1^{\pm}}+\frac{1}{N_2^{\pm}}+\frac{1}{N_1^{\mp}}+\frac{1}{N_2^{\mp}}}. \tag{6.16}$$

6.2.2 Non-linear Least Squares Fit

Between 1912 and 1922, R.A. Fisher developed the method of maximum likelihood [122]. Nowadays, likelihood methods have become standard. This statistical method allows to estimate unknown model parameters if the underlying data sample is normally distributed. In principle binned and unbinned methods have to be distinguished. In COMPASS they were used in the analysis of azimuthal asymmetries in semi-inclusive deep inelastic scattering off transversely polarised protons [102]. The likelihood method allows fitting the event numbers directly and, hence, makes the fit of event number ratios redundant. They are based on a set of non-linear equations.

6.2.2.1 Binned Fit Method

For a binned maximum likelihood fit the equations are set up according to Eq. 6.1. For four combined samples, it arrives at a system of $4m^2$ of such equations with $4m^2 + n_A$ free parameters, where $j = m \times m$ are the number of bins in ϕ and ϕ_s, respectively, and n_A is the number of fitted physics modulations. The assumption that the acceptance parameters are independent of ϕ and ϕ_S defined in Eq. 6.15

[2]In principle it is also possible to extract the asymmetries out of the single ratio $F_j^{SR} = \frac{N_j^{\pm}}{N_j^{\mp}}$. The drawback of this method is that it gives only unbiased results if there is neither a change in the acceptance nor in the beam flux between the two event samples.

leads to $m^2 - 1$ constraints, so $3m^2 + n_A + 1$ acceptance parameters are needed in total. The expected number of events in the four samples are described by:

$$\begin{aligned} N^+_{j,1} &= C\frac{a^-_{j,1}a^-_{j,2}}{a^+_{j,2}}\left(1 \pm A(\phi, \phi_S)\right), \\ N^-_{j,1} &= a^-_{j,1}\left(1 \pm A(\phi, \phi_S)\right), \\ N^+_{j,2} &= a^+_{j,2}\left(1 \pm A(\phi, \phi_S)\right), \\ N^-_{j,2} &= a^-_{j,2}\left(1 \pm A(\phi, \phi_S)\right). \end{aligned} \tag{6.17}$$

In the following the equations above are labeled with $f_l(\vec{a})$, where $l = \{1, ..., 4m^2\}$ and the $\vec{a}$ denotes the $3m^2 + 1 + n_A$ free parameters. In Eq. 6.17 $A(\phi, \phi_S)$ is defined according to Eq. 6.3 and contains the eight asymmetry amplitudes. The sign depends on the corresponding target cell and period. The fit is solved by minimising $\|\vec{F}(\vec{a})\|^2$ of l target functions $F_l(\vec{a})$, where:

$$\|\vec{F}(\vec{a})\|^2 = \sum_l F_l(\vec{a})^2. \tag{6.18}$$

The structure of the target function depends on the underlying statistics and will be discussed later on. The minimization problem can be solved using the Levenberg-Marquardt (LM) algorithm [123, 124]. This algorithm is included in the GNU Scientific Library (GSL) [125] which provides a collection of numerical routines for scientific computing.

Fit-to-counts Method

If the underlying distribution is not Poisson-like, a direct fit-to-counts method [126] is used. The set of non-linear equations in Eq. 6.17 can be translated to the function $F_l(\vec{a})$:

$$F_l(\vec{a}) = \frac{f_l(\vec{a}) - N_l}{\sigma_l}, \tag{6.19}$$

which allows a weighted least-squares fit of the nonlinear model $f_l(\vec{a})$ and the data N_l to be performed, assuming independent Gaussian errors σ_l. This method is applied for extracting asymmetries using the background corrected ϕ, ϕ_S distribution. The errors σ_l are calculated applying the Gaussian law of error propagation and taking into account the statistical errors on the number of counts and the uncertainties of the number of background events.

Likelihood Method based on Poisson Statistic

If a likelihood fit based on Poisson statistics is used, a probability function is defined as:

$$P_l(\vec{a}) = \frac{e^{-f_l(\vec{a})} f_l(\vec{a})^{N_l}}{N_l!}. \tag{6.20}$$

where N_l is the measured number of counts in bin l and $f_l(\vec{a})$ is the expected number of events, as defined in Eq. 6.17. The non-linear system of Eq. 6.17 can be solved by maximizing the probabilities in Eq. 6.20. This reads:

$$\max_{\vec{a}}(\mathcal{L}) = \max_{\vec{a}}\left(\prod_l P_l(\vec{a})\right). \tag{6.21}$$

Normally it is easier to maximize $\ln(\mathcal{L})$ and this is equivalent to the minimisation of Eq. 6.19 with [19]:

$$F_l(\vec{a}) = \sqrt{2}\sqrt{(f_l(\vec{a}) - N_l) + N_l \ln\left(N_l/f_l(\vec{a})\right)}. \tag{6.22}$$

The likelihood fit based on Poisson statistics is used if asymmetries are extracted on the pure sample, without a background correction.

The two-dimensional likelihood binned method allows for the simultaneously extraction of all eight modulations as shown in Eq. 6.3, and, therefore an evaluation of the covariance matrix:

$$Cov(l,m) = (J^T J)^{-1} \tag{6.23}$$

is possible. Here, J is the Jacobian matrix, which is defined as:

$$J_{lm} = \frac{1}{\sigma_l}\frac{df_l(\vec{a})}{da_m} \tag{6.24}$$

The covariance matrix includes the statistical errors on the best fit parameters calculated from the statistical errors on the data denoted by σ_l. The correlation matrix is:

$$Cor(l,m) = \frac{Cov(l,m)}{\sqrt{Cov(l,l)Cov(m,m)}}. \tag{6.25}$$

When using the two-dimensional binned likelihood method, the correlation between the different modulations is taken into account. Then the bias observed due to the non-flat ϕ_S acceptance is not present. The grid used in both ϕ and ϕ_s avoids the integration over the non-flat ϕ_S distribution. However, the data is binned two-dimensionally and the number of bins have to be chosen with care, in particular for an analysis with limited statistics.

6.2.2.2 Unbinned Likelihood Method

In this method, each event coming from a cell n period $\pm$ with angles (ϕ, ϕ_S) is associated with a probability density function $p_n^{\pm}(\phi, \phi_S)$. This function is proportional to the product of the acceptance of the cell n and the cross section of the physical modulation is parametrised as product of the generalized acceptance function $a_n^{\pm}$ and the physics modulations:

$$\mathrm{P}_n^{\pm}(\phi, \phi_S) = a_n^{\pm}(\phi, \phi_S) \cdot (1 \pm A(\phi, \phi_S))\,. \tag{6.26}$$

For each target cell n (Fig. 6.1), and both polarisation states $\pm$, the functions $a_n^{\pm}$ are different. The assumption of Eq. 6.15 is adapted according to:

$$C_1 = \frac{a_1^+(\phi, \phi_S)}{a_1^-(\phi, \phi_S)}, \qquad C_2 = \frac{a_2^+(\phi, \phi_S)}{a_2^-(\phi, \phi_S)}, \tag{6.27}$$

where the change of acceptance for each target cell can be described by one single constant. This is less strict than Eq. 6.15 but leads to more stable fit results [102]. An extended maximum likelihood fit is performed [102]. In such a fit the probability density function is not normalized to one, but to the theoretically expected number of events μ.

$$\int_0^{2\pi}\int_0^{2\pi} \mathrm{d}\phi \mathrm{d}\phi_S P_n^{\pm}(\phi, \phi_S) = \mu_n^{\pm}. \tag{6.28}$$

The likelihood function $\mathcal{L}(\vec{a})$ to be maximized with respect to the vector of parameters $\vec{a}$ is:

$$\mathcal{L}(\vec{a}) = \prod_{i=1}^{4} \left[\left(e^{\mu_i^+} \prod_{m=1}^{N_i^+} a_i^+(\phi_m, \phi_{S_m})(1 + A(\phi_m, \phi_{S_m})) \right) \cdot \left(e^{\mu_i^-} \prod_{n=1}^{N_i^-} C_i a_i^+(\phi_n, \phi_{S_n})(1 - A(\phi_n, \phi_{S_n})) \right) \right] . \tag{6.29}$$

The fit is performed by minimising $\ln \mathcal{L}$ using the Broyden-Fletcher-Goldfarb-Shanno (BFGS) algorithm from the GNU scientific library.

The advantage of the unbinned method is that it provides stable fit results even with few overall statistics. Therefore, the unbinned likelihood fit is used when evaluating the systematic uncertainties on sub-samples, as done in Sec. 7.5 and Sec. 8.2 where background subtraction is no issue. The chosen background estimation method explained in Sec 7.3 is performed in bins of ϕ, ϕ_S and, therefore, requires a binned fit method. The consideration of the background in an unbinned fit assumes a very good knowledge of the background function.

The result of the estimation methods described above are so called "raw" asymmetries. The dependence on target dilution f, target polarisation P_{T}, the beam polarisation P_ℓ, the depolarisation factor D_{NN} is applied afterwards. This will be described in the next section.

6.3 From Raw to Physical Asymmetries

After the subtraction of semi-inclusive background, the "raw" asymmetries $A^m_{\mathrm{UT,\,raw}}$ and $A^m_{\mathrm{LT,raw}}$ are extracted from the final sample using a two-dimensional binned maximum likelihood fit in ϕ and ϕ_S. They are used to obtain the transverse target single-spin asymmetries A^m_{UT} and double-spin asymmetries A^m_{LT} defined in Eq. (2.46) as:

$$A^m_{\mathrm{UT}}=\frac{A^m_{\mathrm{UT,raw}}}{\langle F_{\mathrm{UT}}\rangle}, \qquad A^m_{\mathrm{LT}}=\frac{A^m_{\mathrm{LT,raw}}}{\langle F_{\mathrm{LT}}\rangle}\,, \tag{6.30}$$

with:

$$F_{\mathrm{UT}}=f\cdot|P_T|\cdot D^m_{NN}(\epsilon), \qquad F_{\mathrm{LT}}=f\cdot|P_T|\cdot P_\ell\cdot D^m_{NN}(\epsilon)\,. \tag{6.31}$$

The mean values are calculated as an arithmetic mean. The denominator consists of the dilution factor f, the target polarisation P_T, the beam polarisation P_ℓ and the depolarisation factor $D^m_{NN}(\epsilon)$ which is specific for the individual asymmetry. Here P_T is used, which in COMPASS kinematics is a good approximation to S_T[3]. The denominator in Eq. 6.30 is calculated in every kinematic bin for each modulation m. The depolarisation and the dilution factor and the beam polarisation are individually quantified for every event, whereas one polarisation value is available for every run for 2007&2010. In 2003&2004 up to three different target polarisation values for one sub-period are used. The correction factors as a function of x_{Bj}, Q^2 and p_T^2 are presented in Fig 6.4. Every factor in the denominator of Eq. 6.30 is discussed individually in the following, taking the 2007&2010 data sample as an example. Only the differences which occur for the 2003&2004 data sample are discussed.

Depolarisation Factor

The depolarisation factors D^m_{NN} describe the fraction of the spin of the lepton which is transferred to the virtual photon. They appear in front of each azimuthal modulation in the cross section in Eq. 2.42. The exact definition is a matter of convention. In Eq. 2.42 the cross section from Ref. [9] is used. The depolarisation factors are given by[4]:

$$\begin{aligned}
D_{NN}^{\sin(\phi-\phi_S)} &= 1,\\
D_{NN}^{\sin(\phi+\phi_S)} = D_{NN}^{\sin(3\phi-\phi_S)} &= \frac{\varepsilon}{2}\\
D_{NN}^{\sin(\phi_S)} = D_{NN}^{\sin(2\phi-\phi_S)} &= \sqrt{\varepsilon(1+\varepsilon)}\\
D_{NN}^{\cos(\phi-\phi_S)} &= \sqrt{1-\varepsilon^2}\\
D_{NN}^{\cos\phi_S} = D_{NN}^{\cos(2\phi-\phi_S)} &= \sqrt{\varepsilon(1-\varepsilon)}
\end{aligned} \tag{6.32}$$

The quantity ϵ is defined in Eq. 2.35. The D^m_{NN} factors[5] as a function of y are shown in Fig. 6.5 as well as the mean values $\langle D^m_{NN}\rangle$ in each kinematic bin, for the 2007&2010 data sample. The factors do not heavily depend on neither p_T^2 nor Q^2. Due to the strong correlation of x_{Bj} and y a dependence on x_{Bj}, especially for the factors associated with the A_{LT} asymmetries, is visible.

[3] The used approximation will be discussed in Sec. 7.4.

[4] In the past often an approximation as a function of y only e.g. in Ref. [12] was used in COMPASS analyses. Here the full expression is implemented. The difference between both is negligible within experimental uncertainties.

[5] Here the approximation as a function of y only is used.

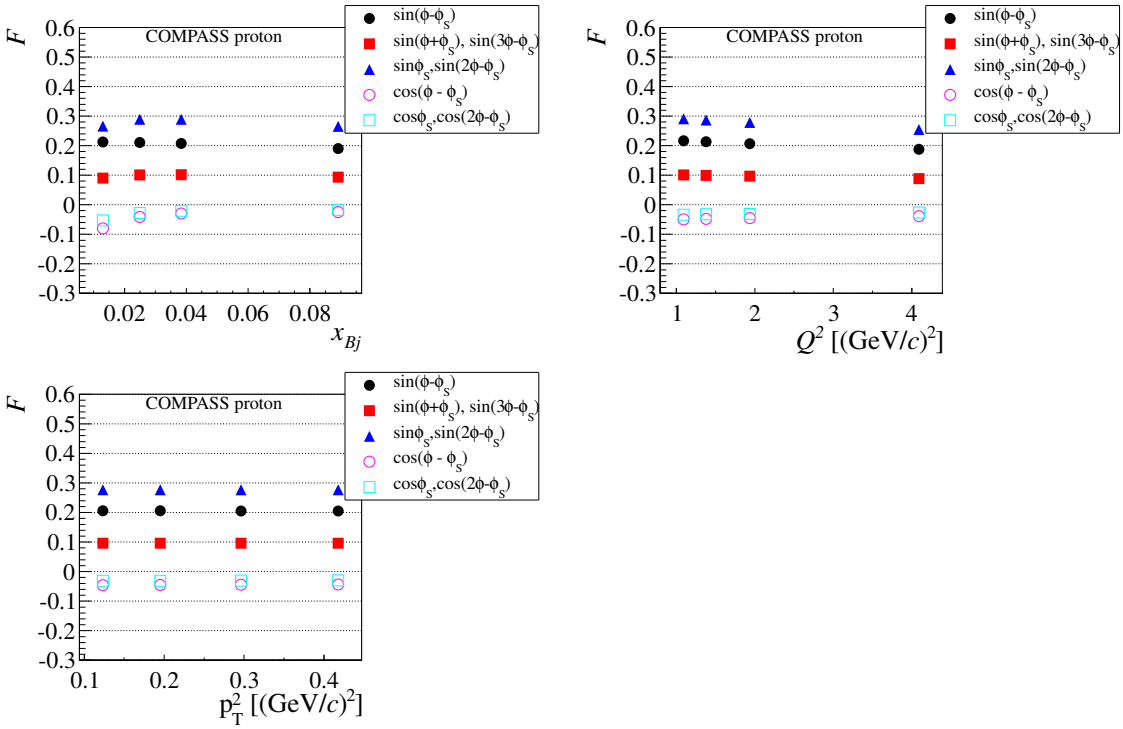

Figure 6.4: Correction factors $F \in \{F_{\mathrm{LT}}^m, F_{\mathrm{UT}}^m\}$ for the different modulations as a function of x_{Bj}, Q^2 and p_T^2. Here the correction factors for the 2007&2010 sample are presented.

Dilution Factor

The dilution factor describes the fraction of polarisable material in the target weighted with the cross section of the reaction studied. Therefore the value is specific for the reaction studied. The dilution factor is parametrised as a function of Q^2 [127]:

$$f^{p/d}(Q^2) = C^{p/d} \frac{n_{p/d}}{n_{p/d} + \sum_A n_A \frac{\sigma_A}{\sigma_{p/d}}}, \tag{6.33}$$

where the measured cross section for a given reaction scattering of a polarisable proton/deuteron or a single nucleon from isotope A is denoted by $\sigma_{p/d}$ and σ_A. In the denominator, the sum over all isotopes present in the target material is built. The correction factor $C^{p/d}$ is calculated in Ref. [128]. The parametrisation of the cross section ratio $\sigma_A/\sigma_{d/p}$ is based on data taken at NMC, E665 and photoproduction experiments and is performed in Ref. [129]. The dilution factor for the 2007&2010 as a function of x_{Bj}, Q^2 and p_T^2 is presented on the right-hand side of Fig. 6.6. The different bands, as seen in the center of this figure, are dedicated to the different target cells and years in the data sample, and appear due to the varying material decomposition of each target cell. The uncertainty is estimated up to 0.02 for both the proton and the deuteron setup [130]. The different target composition is also the reason for the significantly higher dilution factor for the 2003&2004 sample shown on the left-hand side of Fig. 6.6.

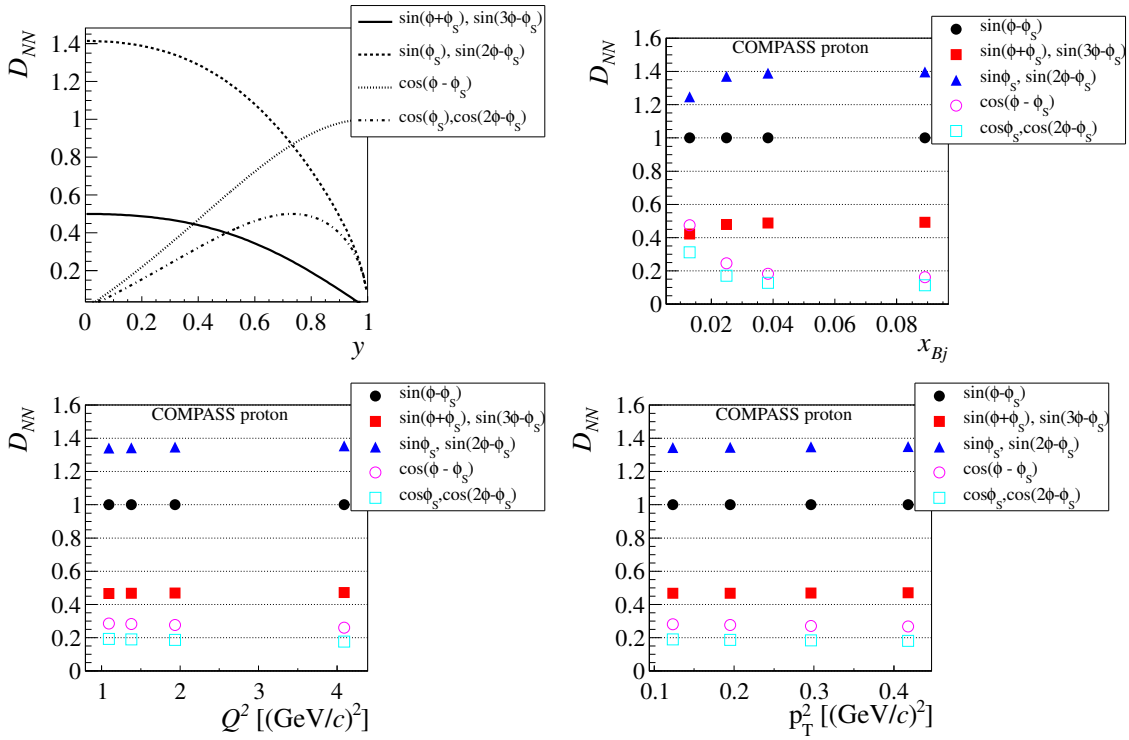

Figure 6.5: Depolarisation factors as a function of y and mean depolarisation factor as a function of x_{Bj}, Q^2 and p_T^2 (moving from top left to bottom right). Every plot includes the factors for the eight different modulations. Here the correction factors for the 2007&2010 sample are presented. Note that for the calculation of the correction factor in Eq. 6.30 the mean of the whole product is used.

Target Polarisation

In the transverse mode, the target polarisation can not be measured. Therefore, the measurement is performed before and after each sub-period in the longitudinal mode. In between, the polarisation values are gained by extrapolation. For the years 2007&2010 the information is available for each run. Here the values stored in the COMPASS offline database are used. As an example the polarisation in % of the D cell as a function of the run number is presented in Fig. 6.7[6]. For 2003&2004 averaged values are taken. They are summarized in Tab. D.1 in the appendix. The error of the polarisation is estimated to be 3% [79, 80] for the proton three-cell setup and 5% [131] for the deuteron two-cell setup.

Beam Polarisation

The beam polarisation depends on the beam momentum as introduced in Sec. 3.1. It is parametrised using a spline function. The result is presented in Fig. 6.8.

[6]The dip of the polarisation value around run number 85800 goes ahead with a failure of the 3He pumps.

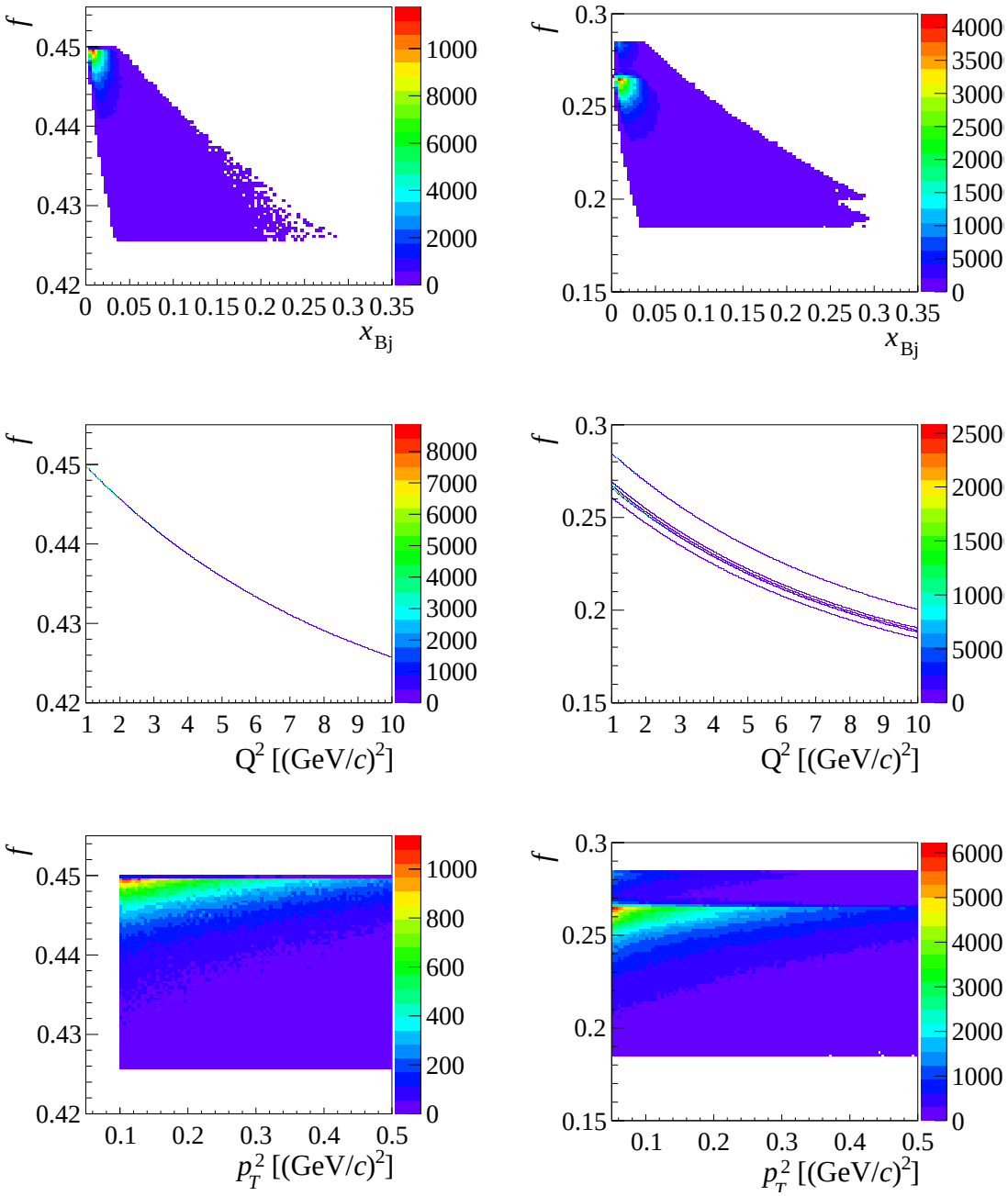

Figure 6.6: Correlation between the dilution factor and x_{Bj} (upper row), Q^2 (middle row) and p_T^2 (lower row) for the 2003&2004 sample (left) and the 2007&2010 sample (right). All cuts indicated in Tab. 4.5 are applied.

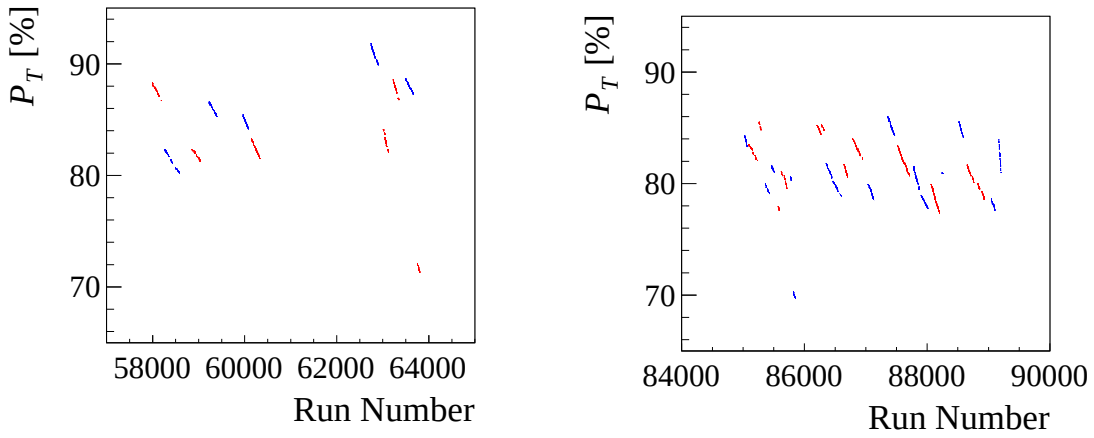

Figure 6.7: Target polarisation in % for the D cell as a function of the run number for the data taking in 2007 (left-hand side) and 2010 (right-hand side). The missing run numbers in 2007 are dedicated to data taking with a longitudinal polarised target.

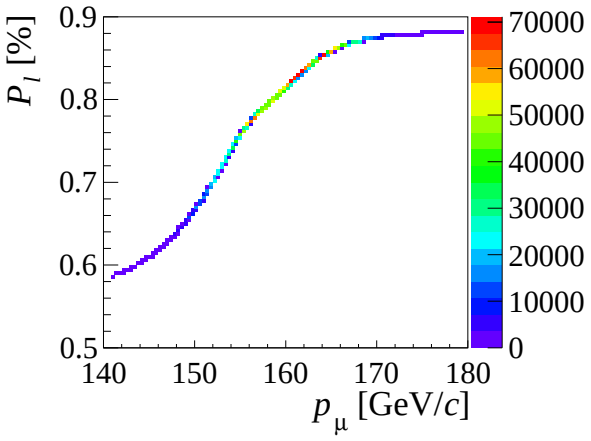

Figure 6.8: Parametrisation of the beam polarisation as a function of the beam momentum.

7. Asymmetries for the NH_3 Target

In Sec. 7.1 the discussion of asymmetries starts, whereas studies based on the data sample before the background correction are shown. In Sec. 7.2, possible influences on the asymmetries due to the presence of non-exclusive events in the final sample are discussed. Finally, the background corrected asymmetries are studied in Sec. 7.3. They are evaluated starting from the background corrected ϕ, ϕ_S distributions $N^{\rm sig}_{k_1}(\phi,\phi_S)$ or $N^{\rm sig}_{k_2}(\phi,\phi_S)$ which were introduced in Sec. 5.2.1. After the discussion of the influence of the S_T to P_T transition in Sec. 7.4 the systematic studies are presented. The chapter is closed with a comparison of $A_{\rm UT}^{\sin(\phi-\phi_S)}$ extracted with one-dimensional and two-dimensional methods.

7.1 Asymmetries before Background Correction

This section is dedicated to the results of the asymmetry extraction. In Fig. 7.1 the physical asymmetries before background correction (background uncorrected asymmetries) are presented. The results from the different extraction methods, as a function x_{Bj}, Q^2 and p_T^2, are shown. The top row shows, the only leading-twist asymmetry $A_{\rm UT}^{\sin(\phi-\phi_S)}$, followed by the four single-spin asymmetries. In the bottom of Fig. 7.1, three double-spin asymmetries are shown. The mean values evaluated in bins of x_{Bj}, Q^2 and p_T^2 for all extracted asymmetries are given. All asymmetries, except $A_{\rm UT}^{\sin\phi_S}$, are compatible with zero within two standard deviations.

7.1.1 Comparison of Extraction Methods

In Fig. 7.1 the asymmetry values obtained with four different extraction methods are presented. The physical asymmetries are shown which are obtained from the pure fit results according to Eq. 6.30.

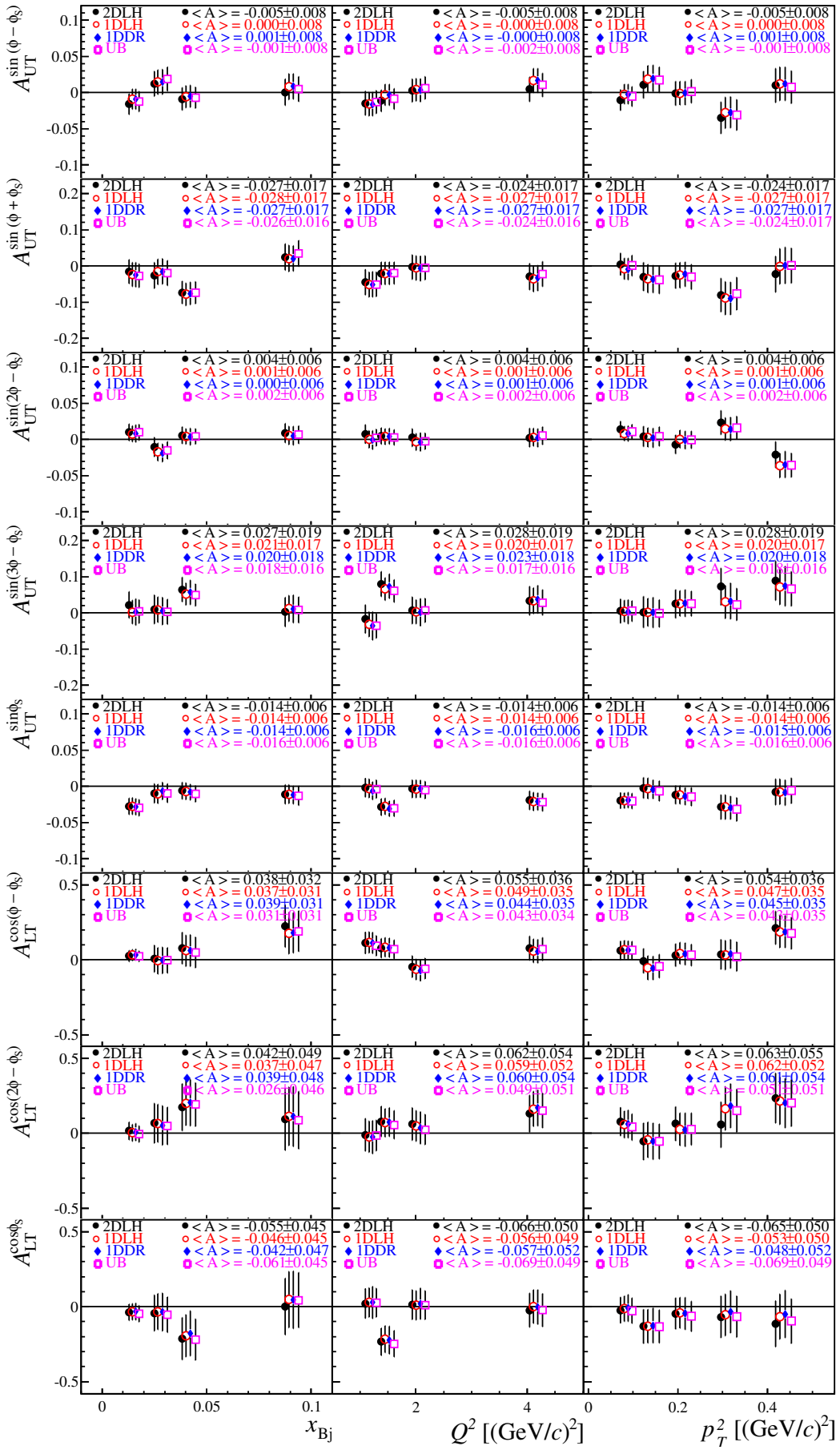

Figure 7.1: Comparison of **background uncorrected asymmetries** extracted with **different methods**. The applied methods are listed in Tab. 6.1 and are explained in the text. Mean values $\langle A \rangle$ and their statistical errors are given.

7.1.1.1 Double Ratio Method

The result of the 1DDR method is shown in Fig. 7.1 with blue diamonds. Ratio Methods were used by the Collaboration in the past [132, 133]. Therefore it was also implemented as part of this work and compared to the results of the other fit methods.

The physical asymmetries in Fig. 7.1 are obtained by dividing the raw asymmetries by the mean of the correction factor evaluated in every bin as shown in Eq. 2.46. For the 1DDR method it is also possible to include the mean correction factor evaluated for every configuration c ($c \in \{1, 2, 3, 4\}$) in the fit function in Eq. 6.14 by replacing $A_{1D}(\phi, \phi_S)$ with:

$$A_{1D}(\phi, \phi_S) \rightarrow \langle f \cdot |P_T| \cdot D^m_{NN}(\epsilon) \rangle_c \cdot A_{1D}(\phi, \phi_S), \tag{7.1}$$

$$A_{1D}(\phi, \phi_S) \rightarrow \langle f \cdot |P_T| \cdot P_\ell \cdot D^m_{NN}(\epsilon) \rangle_c \cdot A_{1D}(\phi, \phi_S), \tag{7.2}$$

where Eq. 7.1 is valid for the single spin asymmetries and Eq. 7.2 has to be used for the double-spin asymmetries. The fit result is then directly the physical asymmetry. Inside the available statistical precision both fit results are comparable.

The result marked with 1DDR is obtained by fitting the function in Eq. 6.14 to the data. The constant parameter C in Eq. 6.15 is a free parameter in every fitted bin. If the acceptance is fully balanced, the parameter should be exactly 1. In Fig. 7.2 the results obtained with a double ratio fit with $C = 1$ and a non-fixed C parameter are compared. The pull distributions contain 13 asymmetry values from the 13 kinematic bins (four in x_{Bj} and Q_2 and five in p_T^2) and are calculated for every asymmetry separately. The pull value in each bin i is calculated via[1]:

$$\text{pull}_i = \frac{A_{1,\text{i}} - A_{2,\text{i}}}{(\sigma_{1,\text{i}} + \sigma_{2,\text{i}})/2}. \tag{7.3}$$

Here, A_1 represents the asymmetry with $C = 1$ and A_2 stands for the asymmetry extraction with the additional parameter C. The statistical uncertainties are denoted by σ_1 and σ_2. For some of the asymmetries a bias is observed. Noticeable is that this bias is negative for the single-spin asymmetries, whereas it is positive for the double spin asymmetries. The values for the parameter C are between 0.998 ± 0.009 and 1.019 ± 0.009, where the distributions are slightly shifted towards positive values but show a comparable shape for all eight asymmetries. The observed bias is a hint to instabilities of the 1DDR method due to the non-uniformed acceptance of the COMPASS spectrometer. Additional drawbacks of the 1DDR method were observed connected to general fit instabilities or the observation of a bias for small statistics or large asymmetries [134, 135, 102]. Hence, today the 1DDR method is usually replaced with likelihood methods.

7.1.1.2 Non-Linear Least Squares Fit

The results of the one-dimensional and two-dimensional likelihood fit are presented in Fig. 7.1 with the black full circle and the open red circle, respectively. The advantage of the one-dimensional binned likelihood method is that the binning is directly performed in the azimuthal modulations Θ in Eq. 6.6. Therefore, a fine

[1] Unless otherwise indicated the Eq. 7.3 is used if a pull distribution is calculated.

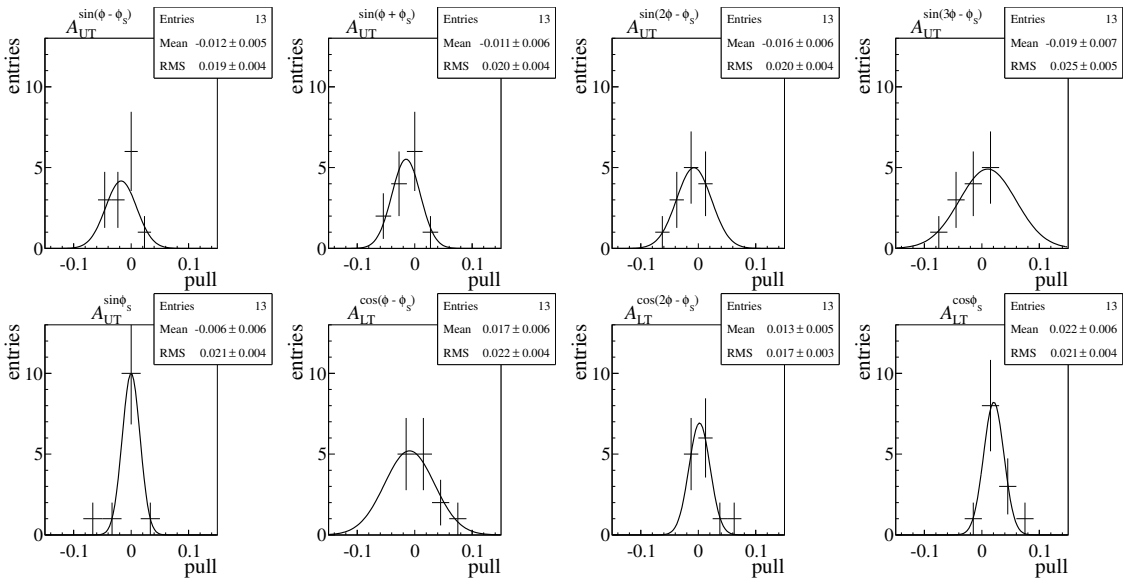

Figure 7.2: Pull distributions demonstrating the compatibility of the results from the double ratio fit, where one value is obtained with a double ratio fit with $C = 1$ and the other with a non-fixed C parameter.

binning with low statistics are even possible. On the other hand every modulation is extracted on its own, consequently the correlation between the different modulations is not taken into account. This is only possible for two-dimensional methods, for instance the two-dimensional likelihood method or the unbinned likelihood fit. In principle, the different modulations are orthogonal to each other which allows the study of each modulation individually by integrating over the others. Although the non-uniform COMPASS acceptance may introduce some instabilities. A possible bias on the asymmetry extraction, due to the non-uniformed acceptance, is studied in Refs. [135, 102]. There, a bias is observed for sizable asymmetries extracted with one-dimensional binned methods, whereas only a negligible effect is observed if two-dimensional binned methods are used. The asymmetry values extracted with an unbinned likelihood fit are presented with violet squares.

The results for the single-spin asymmetries A_{UT}^{m} as a function of the kinematic variables, indicate a reasonable agreement between the different methods. The mean asymmetries are also in good agreement with each other inside the available statistical precision. For the double-spin A_{LT}^{m} asymmetries the results from the unbinned fit deviates compared to the results of the other fit methods. In particular, this is visible if the mean values evaluated in bins of x_{Bj} are compared with those evaluated in bins of Q^2 and p_T^2. Beside the deviation of the values also the statistical error is throughout smaller.

The applied background estimation method, explained in Sec. 5 requires a binned extraction method and only the two-dimensional binned method allows the simultaneously extraction of the eight asymmetries. Therefore, in the following, the default method is the two-dimensional binned likelihood fit with 12 bins in both ϕ and ϕ_S. The motivation for using 12 bins will be discussed later. The other methods are used as internal cross checks and for systematic studies. The difference between the

results obtained with a UB fit and with a 2DLH fit is quantified in Sec. 7.5.2 and is taken into account in the systematic uncertainty.

In the remaining sections several aspects of the asymmetry extraction are discussed in detail. Mainly the 2DLH and the UB fit will be used. Some of the performed tests are done using the physical asymmetry values, others are performed using the pure fit result, the raw asymmetry. Beside the ρ^0 sample a second data sample will be used for some of the test which has a released cut on E_{miss}. The raw asymmetries for the ρ^0 sample and for the enlarged data sample extracted with 2DLH and UB are presented in Fig. D.1 and Fig. D.2, respectively.

7.1.2 Direct Fit of the Physical Asymmetry

Using an unbinned maximum likelihood fit the factors $(f \cdot D_{NN}^m)$ and $(f \cdot P_\ell \cdot D_{NN}^m)$ can be applied as weights on an event-by-event base. Studies done in the past showed, if the target polarisation P_T is included in the weight for every event and varies in time, a bias in the asymmetry extraction is introduced even so the spectrometer is perfectly stable in time [136]. Therefore the mean polarisation $\langle P_T \rangle$ is still applied after the fit. In Fig. 7.3 the comparison of background uncorrected asymmetries extracted with the standard method and with the event-by-event weighting are shown. In the latter case the sizable discrepancy between the mean asymmetry values evaluated in bins of x_{Bj} and those evaluated in Q^2 and p_T^2 observed for the A_{LT} asymmetries in Fig. 7.1 is significantly reduced. On the level of raw asymmetries this incompatibility is not present. Detailed studies show that this incompatibility is due to the correction with the appropriate D_{NN} factors because these factors depend strongly on x_{Bj} for the A_{LT} asymmetries, as depicted in Fig. 6.5. Using a binned method there is no possibility to overcome this problem. The difference is taken into account in the evaluation of the systematic uncertainty in Sec. 7.5.1.

7.1.3 Period-wise vs. Global Analysis

Due to the small cross section of the exclusive ρ^0 production this study suffers from low statistics. Therefore a combined (global) analysis of all data collected by the collaboration with an NH_3 target, is preferred. Beside the study of the stability of the most important variables as a function of time (Sec. 4.3.6) also the stability of the asymmetry values are evaluated as a function of time. A standard normal distribution with RMS ≈ 1 and a mean value ≈ 0 is expected for every modulation. In total, 12 periods in 2007 and 24 periods in 2010 are available as shown in Tab. 4.2. Two consecutive periods always have opposite target polarisations. Therefore, 18 independent asymmetries can be extracted for each of the eight modulations. The extractions are done with the UB, which allows for lower statistics compared to the extractions with binned methods. The test is performed on the level of raw asymmetries.

The differences between the asymmetry value of each period A_i, and the mean asymmetry $\langle A \rangle$ of the entire data taking, are expressed as:

$$\text{pull2}_i = \frac{A_i - \langle A \rangle}{\sqrt{(\sigma_{A_i}^2 - \sigma_{\langle A \rangle}^2)}}. \tag{7.4}$$

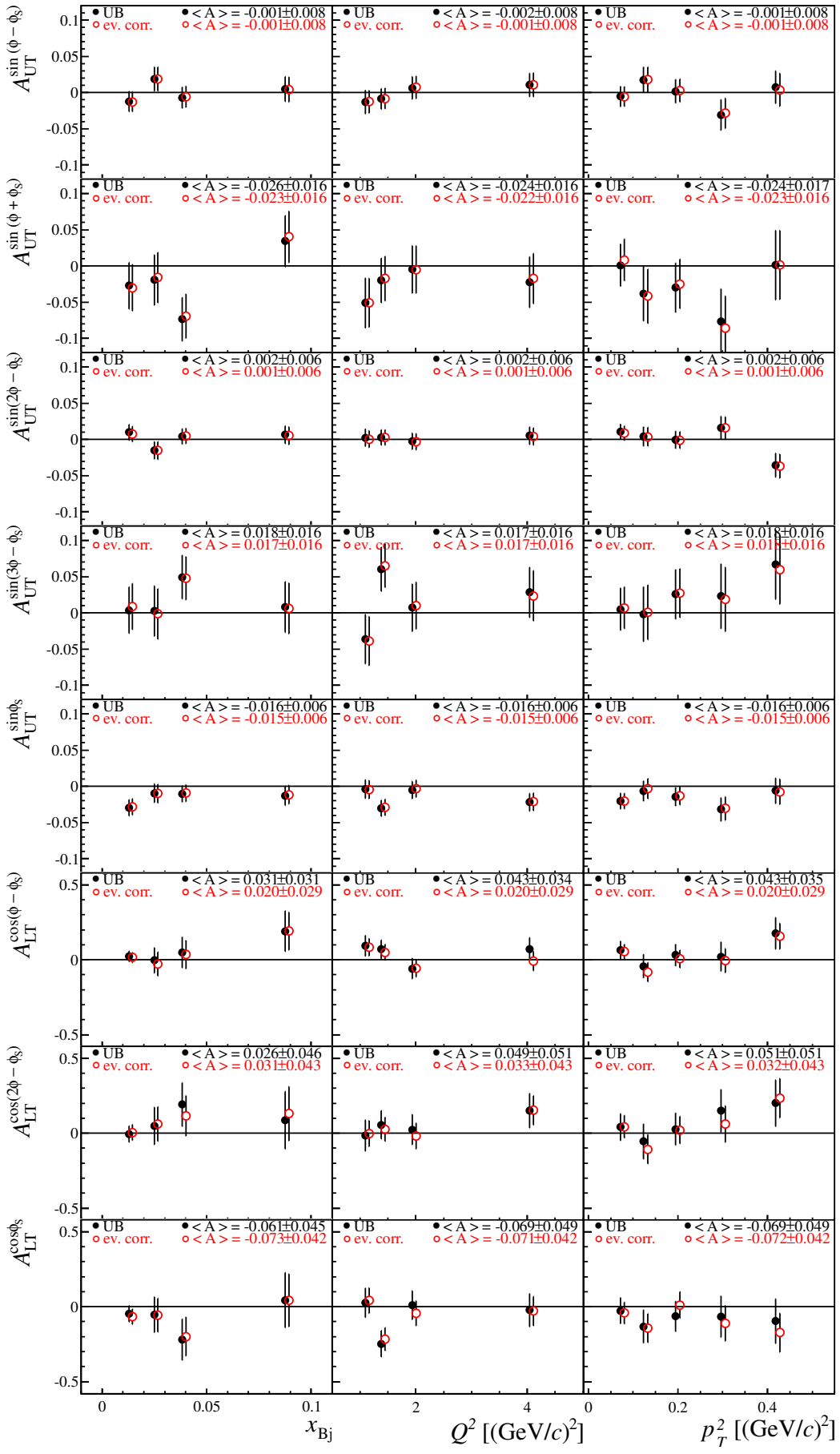

Figure 7.3: **Background uncorrected asymmetries** extracted with **UB**. Here the usage of the correction factor as introduced in Eq. 6.30 (black full circle) is compared with an **event-by-event weighting** (red open circle). Mean values $\langle A \rangle$ and their statistical errors are given.

These studies are done in two different ranges of E_{miss}: 1. In our signal range $-2.5\,\text{GeV} < E_{\text{miss}} < 2.5\,\text{GeV}$; 2. in an extended range $-10\,\text{GeV} < E_{\text{miss}} < 20\,\text{GeV}$, including the range in which the background asymmetries are determined. The latter range contains 2.6 times more events, thereby increases the statistical precision of the performed test. The pull distributions of Eq. 7.4 contain 13 asymmetry values A_i from 13 kinematic bins for each of the 18 independent measurements. The raw asymmetries for $-10\,\text{GeV} < E_{\text{miss}} < 20\,\text{GeV}$, extracted with UB and 2DLH, are depicted in Fig. D.2. They are compatible with zero inside the statistical uncertainty over the entire kinematic range.

Signal Range

The mean values of these 18 independent measurements are shown in Fig. 7.4. In Fig. 7.5, the pull distributions of Eq. 7.4 are depicted for every modulation respectively. The extracted RMS values are between 0.95 and 1.09, except the $\sin(2\phi-\phi_S)$ modulation which has RMS = 1.21. Additionally, the pull distributions are built every year and for every kinematic dependency separately. The results are found to be in-line with Fig. 7.5.

Extended Range

The same studies as in Sec. 7.1.3 are repeated in an extended missing energy range with $-10\,\text{GeV} < E_{\text{miss}} < 20\,\text{GeV}$. Here the statistical precision of the test increases. The higher RMS value of the $\sin(2\phi - \phi_S)$ modulation is not reappearing. The results are depicted in Fig. D.3 and Fig. 7.6. The RMS for every modulation is compatible with one, within the uncertainties, showing the good compatibility of the data samples.

7.1.4 Test of Different Number of Azimuthal Bins

In Fig. 7.1 the asymmetry values are extracted with a 2DLH using 12 bins in both ϕ and ϕ_S. Different numbers of bins for 2DLH are tested and compared with the results from the UB. The test is performed on the level of raw asymmetries to avoid an interplay with the above-mentioned effects, which occur after the correction factor is applied. The results are presented in Fig. 7.7.

For each modulation, the pull distributions defined in Eq. 7.3 between the two asymmetry values, A_1 the result of UB and A_2 the result of 2DLH, is calculated. As an example, the scenario with eight or 12 bins in both ϕ and ϕ_S, are depicted in Fig. 7.8 and Fig. 7.9. The pull distributions contain 13 asymmetry values from the 13 kinematic bins. It is observed that the difference between the UB and the 2DLH results are reduced with higher number of ϕ, ϕ_S bins. This is particularly the case for modulations $(k\phi - \phi_S)$ with $k > 1$. It can easily be seen that a coarse binning does not allow a sufficient resolution of the angular modulations. An upper limit of the number of bins is given by the statistics. Mainly the big dip in the ϕ_S distribution in Fig. 6.3, is due to the asymmetric construction of the trigger system, which prohibits a finer binning.

In Fig. 7.10 the number of events before (left) and after (right)[2] background subtraction (see Sec. 7.3) in each bin appropriate for the asymmetry extraction is shown.

[2]The plot is shown in anticipation of Sec. 7.3, where the background-corrected asymmetries are introduced.

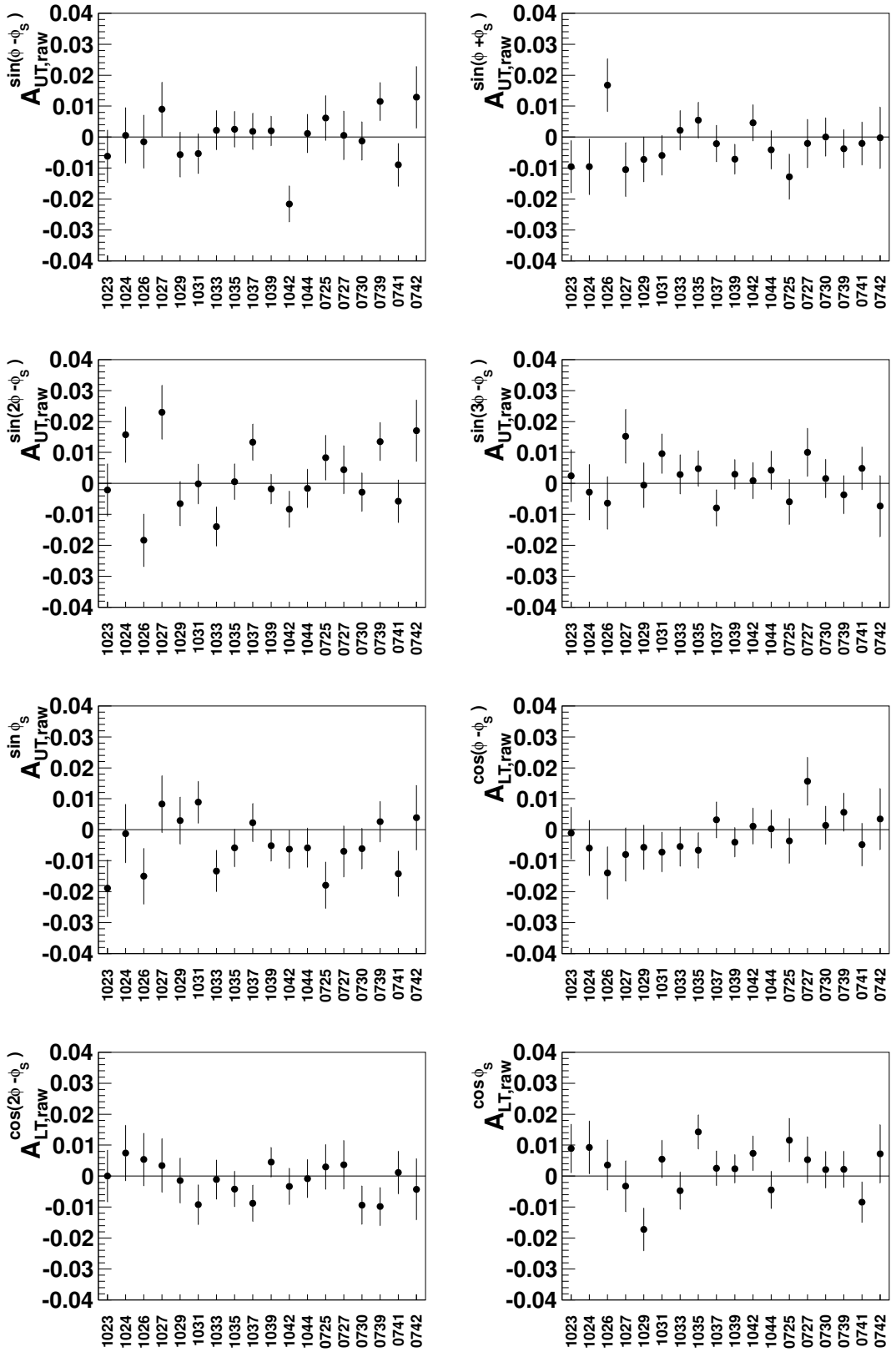

Figure 7.4: **Mean values** of asymmetries for each period in 2007 and 2010. Each abscissa is labeled with four digits, where the first two digits indicate the year and the second two digits indicate the corresponding period. The periods of 2010 are depicted first, followed by 2007. The asymmetry values are extracted for data with $\mathbf{-2.5\,GeV < \boldsymbol{E}_{miss} < 2.5\,GeV}$.

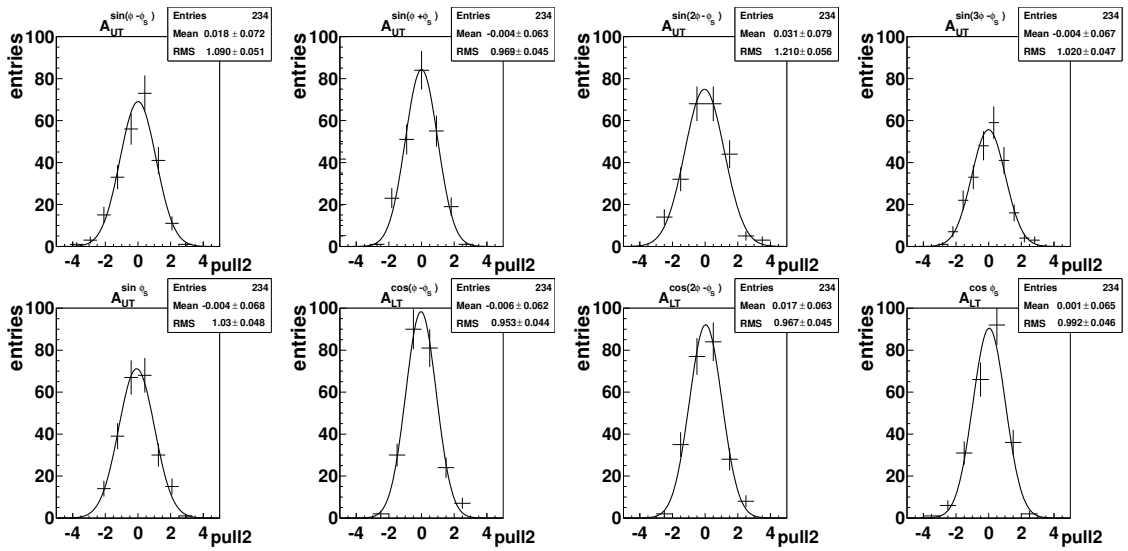

Figure 7.5: Pull distributions demonstrating the compatibility of the results from different periods. The asymmetry values are extracted for data with $\boldsymbol{-2.5\,\mathrm{GeV} < E_{\mathrm{miss}} < 2.5\,\mathrm{GeV}}$.

Here a ϕ, ϕ_S grid with 12×12 bins is used. We do not observe empty bins. The number of events in each bin is sufficiently large enough to perform the fits. The final choice of 12 bins in both ϕ and ϕ_S is a compromise with regard to the statistics available and the observation that the correlation between 2DLH and UB improves with increasing number of bins. The difference of the extracted asymmetry values with UB and 2DLH with 12 bins each in ϕ and ϕ_S is taken into account in the evaluation of the systematic uncertainty in Sec. 7.5.2.

7.1.5 Influence of Particle Identification

A full particle identification of both hadrons as pions in the final state reduces the misidentification of non-pion pairs, but the remaining statistics are not sufficient to perform an asymmetry extraction. In Sec. 4.3.5, the information from the RICH-1 detector is used to exclude events which are identified as kaons, protons or electrons (veto). This cut allows a partial clean-up of the sample. But in the spectrometer just one RICH is present which is situated in the first spectrometer part and allows only the reconstruction of particles in a sub-range of the hadron momentum. Therefore, the kinematic acceptance of the spectrometer and the statistics are significantly reduced and the usage of the RICH information in the analysis is disregarded. Also, the extraction of asymmetries for identified pions and the veto cut allows for systematic studies.

In Fig. 7.11 the asymmetries extracted with 2DLH for the full ρ^0 sample without a background correction and for the sample after the veto cut is compared. The veto cut reduces the statistics between 7% and 12% as a function of x_{Bj}, Q^2 and p_T^2, equally. For most of the data points the asymmetries remain overall unchanged. The differences of the mean values is for all asymmetries up to $0.2{\cdot}\sigma^{stat}$, with respect to the statistical uncertainty of the background uncorrected ρ^0 sample, except for $A_{\mathrm{LT}}^{\cos(\phi-\phi_S)}$, where $0.5 \cdot \sigma^{stat}$ is observed.

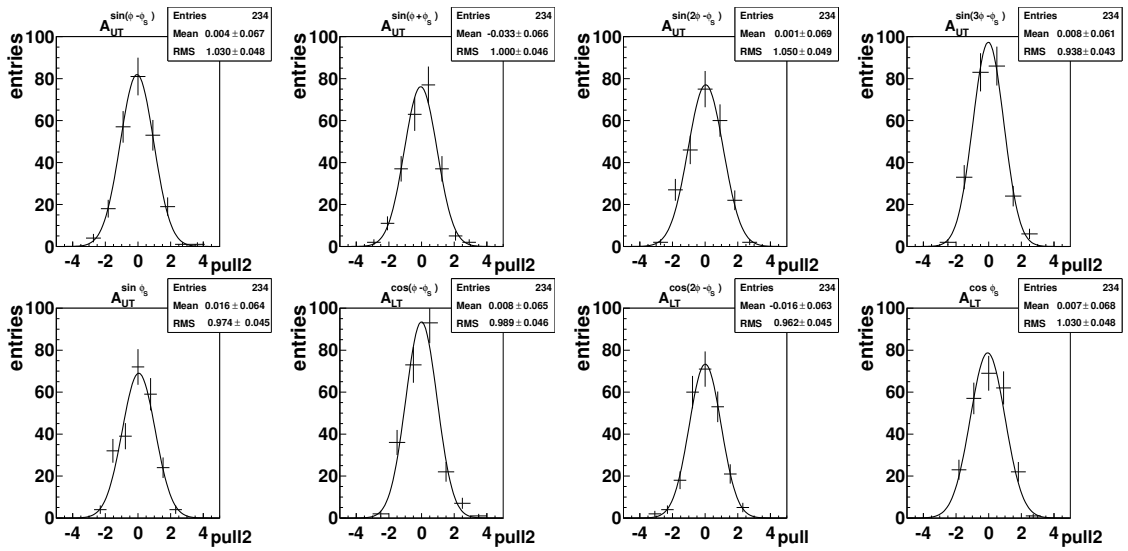

Figure 7.6: Pull distributions demonstrating the compatibility of the results from different periods. The asymmetry values are extracted for data with $\boldsymbol{-10\,\mathrm{GeV} < E_{\mathrm{miss}} < 20\,\mathrm{GeV}}$.

7.1.6 Additional Kinematic Dependencies

Beside the binning in the variables x_{Bj}, Q^2 and p_T^2, which were already introduced, additional kinematic dependencies of the asymmetries are studied. In Fig. 7.12 the asymmetries are shown as a function of E_{miss} , $M_{\pi^+\pi^-}$ and z. Especially the study of the E_{miss} dependence is important as we know that the number of semi-inclusive events is significantly increasing with higher E_{miss} values. All asymmetries are small in the entire kinematic range.

7.2 Background Asymmetries

The ρ^0 meson is reconstructed out of two unlike charged hadrons in the final state. As discussed in Sec. 5, after the application of all cuts a sizable amount of non-exclusive events, mainly semi-inclusive produced ρ^0 mesons are still present in the sample. Beside the determination of the sources and the estimation of the size of the non-exclusive contribution, the influence of these contributions on the asymmetry extraction is crucial. Therefore, first asymmetries extracted for non-exclusive subsamples of the measured data are studied before the background correction of the exclusive asymmetries are discussed in Sec. 7.2.

This section is dedicated to the study of the semi-inclusive background as this is the biggest and most important contribution. The extraction of the asymmetry values for the background is done, following the same path as for the ρ^0 candidates in Sec. 7.1. The same underlying data sample is used although the applied cuts are changed as it is discussed in detail below. Note that the dilution factor changes. Depending on the studied reaction different cross section ratios $\sigma_A/\sigma_{d/p}$ have to be taken into account in Eq. 6.33[3]. The one for semi-inclusive events is shown in

[3]In addition the used parametrisation of $\sigma_A/\sigma_{d/p}$ for semi-inclusive reactions depends on Q^2 and x_{Bj}.

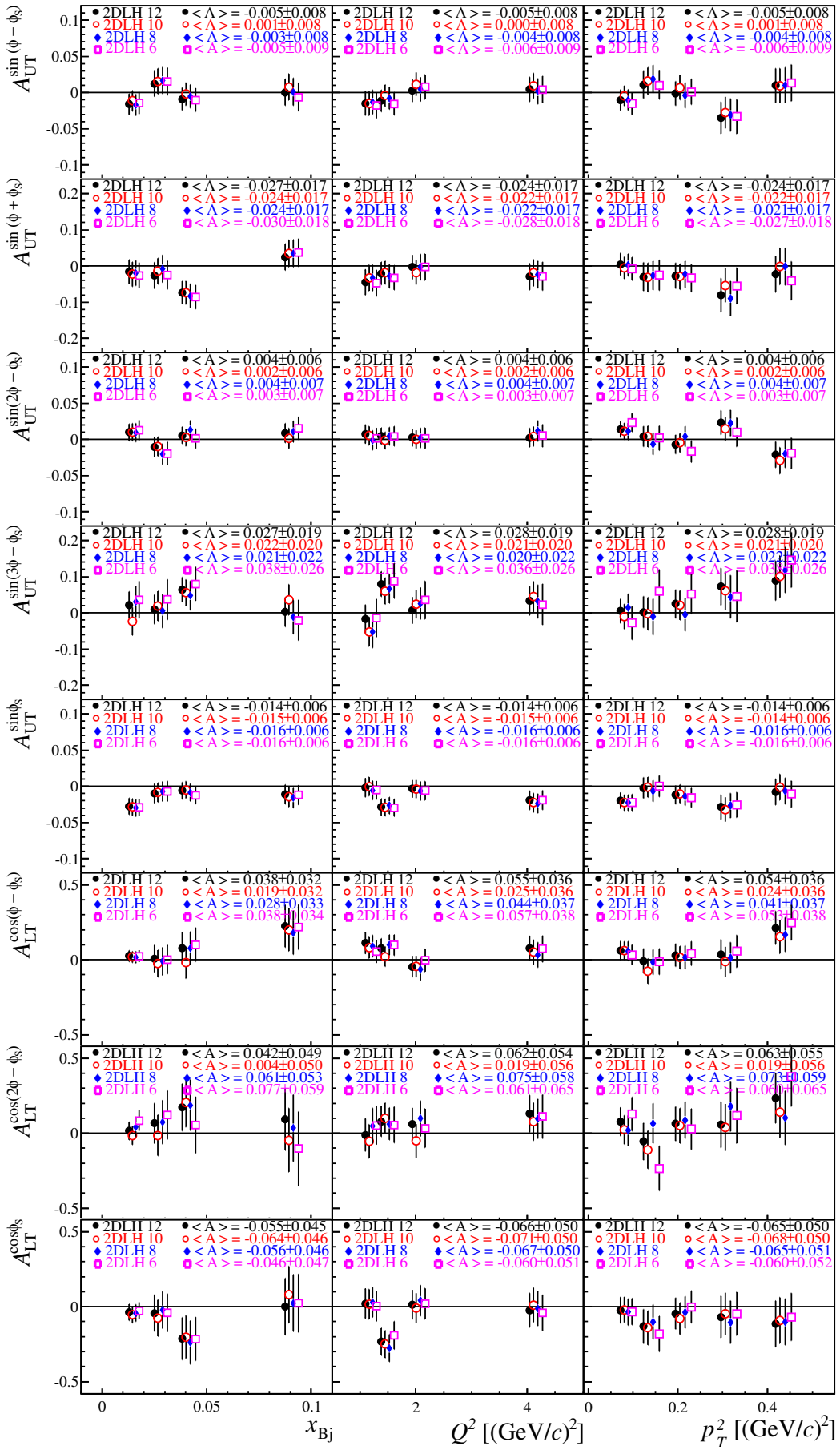

Figure 7.7: Comparison of **background uncorrected asymmetries** extracted with the 2DLH method using **different number of (ϕ, ϕ_S) bins**. Mean values $\langle A \rangle$ and their statistical errors are given.

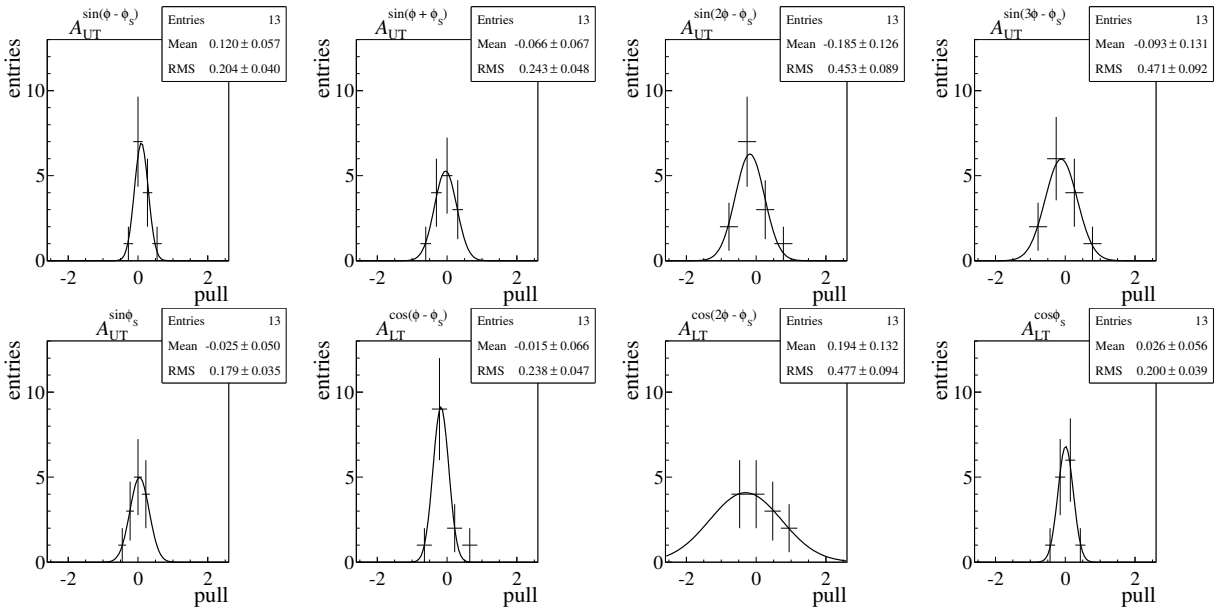

Figure 7.8: Pull distributions demonstrating the compatibility of the results extracted with different estimators. Here the comparison of UB and 2DLH with **eight bins** in ϕ and ϕ_S is shown.

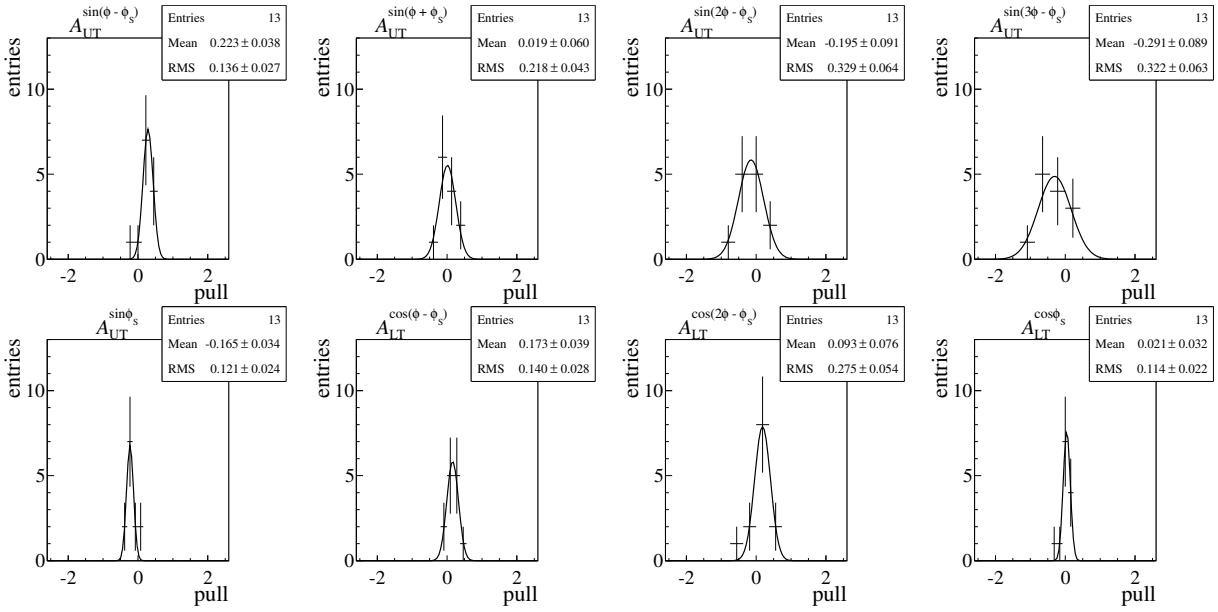

Figure 7.9: Pull distributions demonstrating the compatibility of the results extracted with different estimators. Here the comparison of UB and 2DLH with **12 bins** in ϕ and ϕ_S is shown.

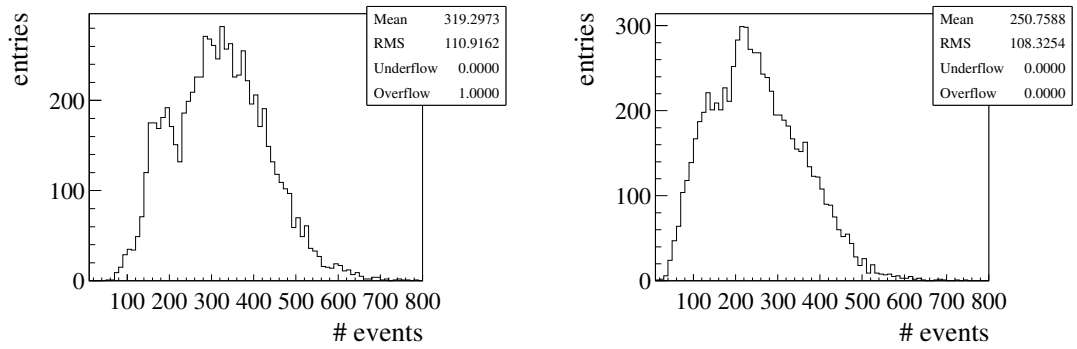

Figure 7.10: Number of events in each bin (appropriate for the asymmetry extraction) before (left) and after (right) subtraction of semi-inclusive background. Note that the abscissa starts at 10.

Fig. 7.13 as a function of x_{Bj}, Q^2 and p_T^2 and is significantly lower as the exclusive one in Fig. 6.6.

The asymmetries extracted in the range $7.0\,\text{GeV} < E_{\text{miss}} < 20.0\,\text{GeV}$ are presented in Fig. 7.15. This range in E_{miss} is well above the exclusive range as well as the area where further background contribution, i.e. diffractive dissociation is present. In this range the statistics are compatible with the one in the exclusive range $-2.5\,\text{GeV} < E_{\text{miss}} < 2.5\,\text{GeV}$. The plots indicate asymmetries compatible with zero inside the statistical uncertainty of the measurement. Additionally, the asymmetries as a function of E_{miss} are presented in Fig. 7.12 for the signal range and in Fig. 7.14 for the background range. While the first contains both the pure exclusive and the semi-inclusive as well as further contributions with unknown interplay between them, the latter only includes semi-inclusive events. Both are compatible with zero within the statistical uncertainty of the measurement.

On the other hand, the measurement of the transverse spin asymmetry $A_{\text{U}}^{\sin(\phi_R+\phi_S-\pi)}$ in semi-inclusive two-hadron production on a NH_3 target at COMPASS results in sizable asymmetry values, rising in strength as a function of x_{Bj} [137, 138][4]. Here, the azimuthal angle ϕ_R is defined as the angle between the two-hadron plane and the scattering plane measured around the direction of the virtual photon [102].

However, the production of ρ^0 mesons is treated as one-single hadron production. This becomes clear if one compares the SIDIS cross section in [11, 10, 12] with the one for exclusive ρ^0 production [9]. They are comparable in contrary to the cross section for the full two-hadron production [139, 140]. Note, that Ref. [12] and Ref. [9] use different conventions for the depolarisation factors. In this thesis, the one of Ref. [9] is consistently applied (see Eq. 6.32). Using the convention of [12], the calculated depolarisation factor for the di-hadron production is smaller. The D_{NN} factor scales reciprocally the asymmetries as well as the statistical errors.

The ρ^0 meson is reconstructed using the two hadron pairs from its decay. The integration over the angles of the hadrons do not introduce any significant bias because the acceptance as a function of these angles is approximately uniform for

[4]Different is the situation for the measurement with the deuterated ^{6}LiD target, where a small asymmetry is observed (Ref. [137]).

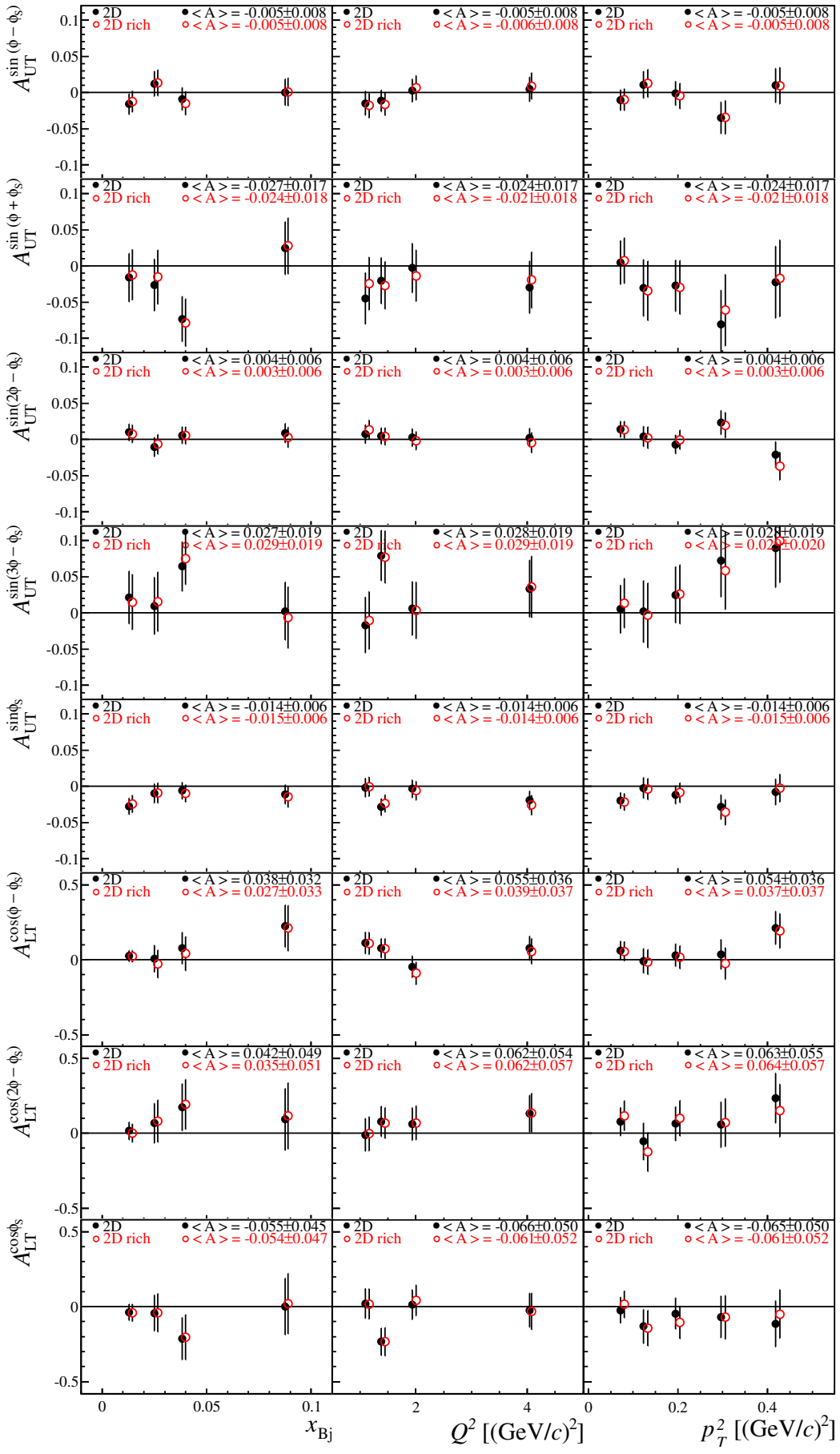

Figure 7.11: Comparison of **background uncorrected asymmetries** extracted with the 2DLH method using the standard ρ^0 sample and a ρ^0 sample where a **veto cut** is applied. Mean values $\langle A \rangle$ and their statistical errors are give.

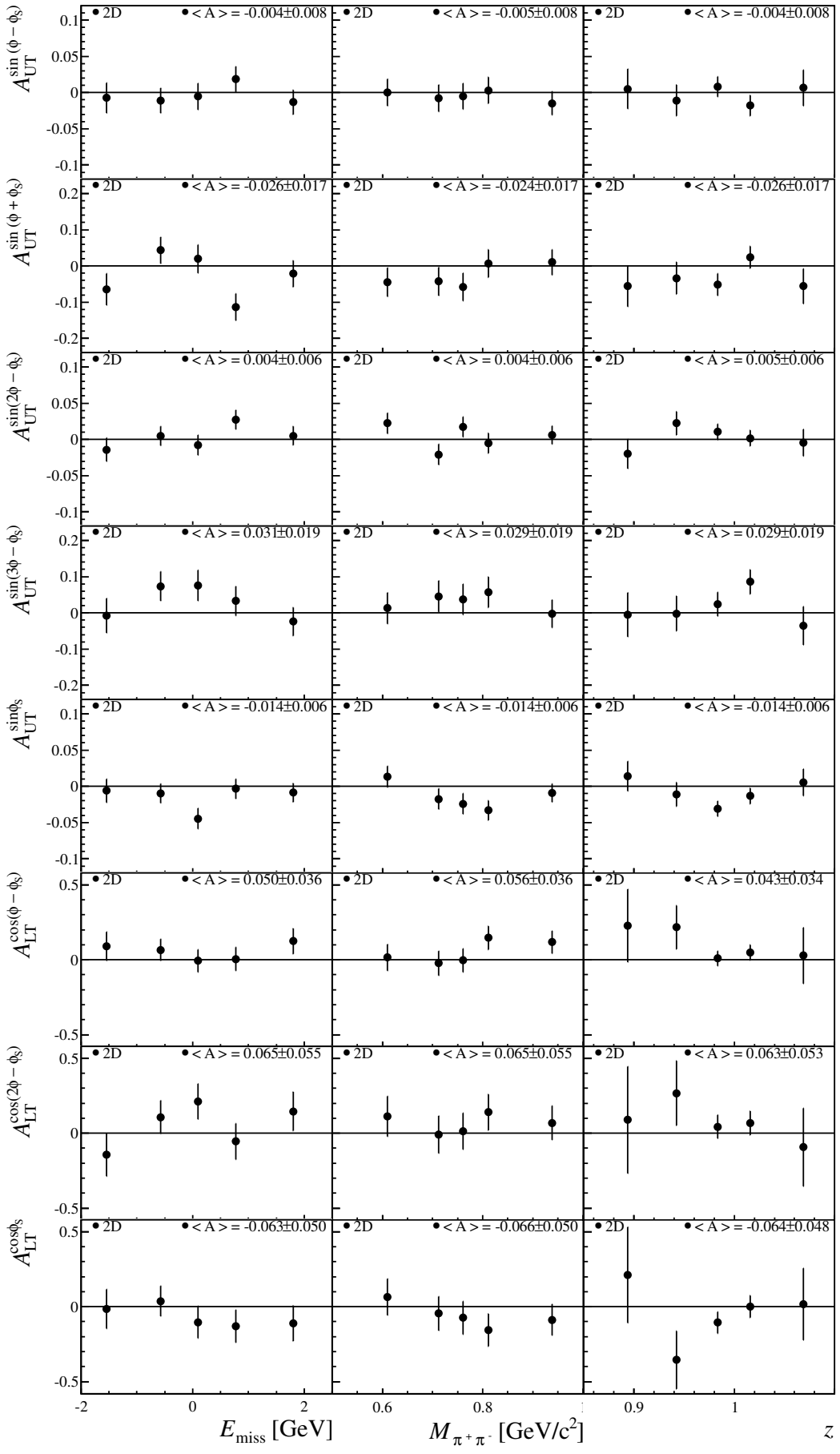

Figure 7.12: Physical asymmetry without background correction as a function of E_{miss}, $M_{\pi^+\pi^-}$ and z. The asymmetry values are extracted with 2DLH. Mean values $\langle A \rangle$ and their statistical errors are given.

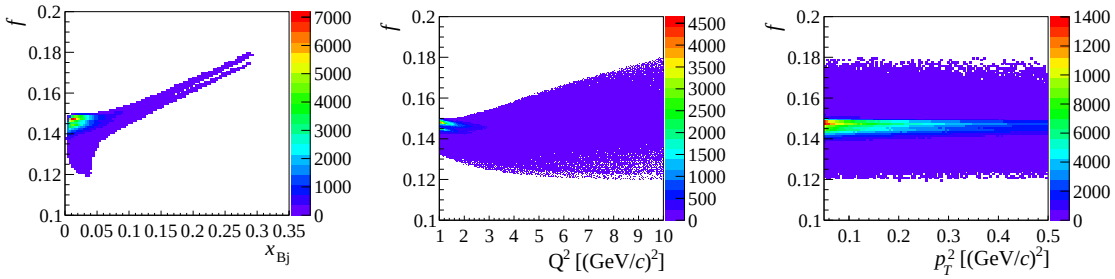

Figure 7.13: Correlation between the semi-inclusive dilution factor and x_{Bj} (left), Q^2 (middle) and p_T^2 (right) for the 2007&2010 sample. All cuts indicated in Tab. 4.5 are applied.

the used sample [141]. The integration over the angles of the hadrons prevents the separation of longitudinal and transverse ρ^0 mesons. The framework of treating the meson production as a two-hadron production in terms of spin density matrix elements, including the decay angular distributions is provided in Ref. [142]. It also allows for a separation of longitudinal and transverse ρ^0 meson. The drawback is that it requires a good knowledge of the experimental acceptance in a multi-dimensional space, including two additional decay angles.

Also semi-inclusive one-hadron production is measured at COMPASS and transverse spin azimuthal asymmetries of charged hadrons are studied for the deuterated ^{6}LiD target [132, 133], as well as the NH_3 target [143, 144, 145]. The Sivers asymmetry [144] and the Collins asymmetry [145] of the proton have been extracted in the range $0.003 < x_{Bj} < 0.7$. The Sivers asymmetry corresponds to the $\sin(\phi - \phi_S)$ modulations, while the Collins asymmetry is defined as $\sin(\phi + \phi_S - \pi)$. The Sivers asymmetry is found to be compatible with zero for negative charged hadrons and positive for positive charged hadrons, whereas a dependence of the asymmetry values as a function of x_{Bj} is observed. Note, that the kinematic range of the analysis differs from the one of the exclusive ρ^0 analysis.

Based on the measured data sample on a NH_3 target in 2007&2010, with the pre-cuts introduced in Sec. 4.1, a pseudo-transversity sample is reconstructed. For this purpose the cuts on the invariant mass and the missing energy of the ρ^0 mesons are released. Moreover, the charged hadron has at least $p_T^2 = 0.1\,(\mathrm{GeV}/c)^2$, where p_T^2 is the transverse momentum with respect to the virtual photon direction. Also the upper limit of Q^2 is released because it is applied to suppress semi-inclusive produced events. In the final state two hadrons are requires. No cut is applied on the charge of these two hadrons. The cuts on the kinematic variables are adapted according to Ref. [144]. The applied cuts are listed in Tab. 7.1. In total around $8 \cdot 10^6$ events with a positive charged hadron and $6 \cdot 10^6$ events with a negative charged hadron in the final states are reconstructed. The asymmetries are extracted for the combined data sample of the years 2007&2010 using an unbinned maximum likelihood fit. After adapting the cuts on the kinematic variables an increasing asymmetry value for $A_{\mathrm{UT}}^{\sin(\phi-\phi_S)}$ as a function of x_{Bj} is observed for positive charged hadrons, as shown in Fig. 7.16, as it is also observed for the asymmetry $A_{\mathrm{UT}}^{\sin(\phi-\phi_S)}$ in semi-inclusive one-hadron production in Ref. [144].

Table 7.1: Summary of all cuts for the pseudo-transversity sample.

topology	Best Primary Vertex reconstructed with 1 incident muon: μ 1 scattered muon: μ'
vertex in the target	PHAST routine PaAlgo::InTarget()
muon identification hadron identification	$X/X_0(\mu') > 30$ $X/X_0(h) < 10$
quality of the tracks	$\chi^2_{red} < 10$ for μ, μ', h $z_{first}(h) < 350$ cm $350 < z_{last}(h) < 3300$ cm h and μ' do not cross SM2 yoke (PHAST routine) h^+ cannot be a muon (PHAST routine)
μ flux through all target cells beam momentum beam back propagation likelihood number of fired BMS planes	PHAST routine $140\,\mathrm{GeV}/c < p_\mu < 180\,\mathrm{GeV}/c$ $0.005 < LH_{\mathrm{back}} < 1$ $N_{BMS} > 2$
domain of analysis	$Q^2 > 1.0(\mathrm{GeV}/c)^2$ $W > 5\,\mathrm{GeV}/c^2$ $0.1 < y < 0.9$ $0.003 < x_{Bj} < 0.7$ $p_T^2 > 0.1\,(\mathrm{GeV}/c)^2$
quality of data	Pure ECAL1 trigger rejected for periods in 2007: W27, W28, W39, W40, W41, W42a

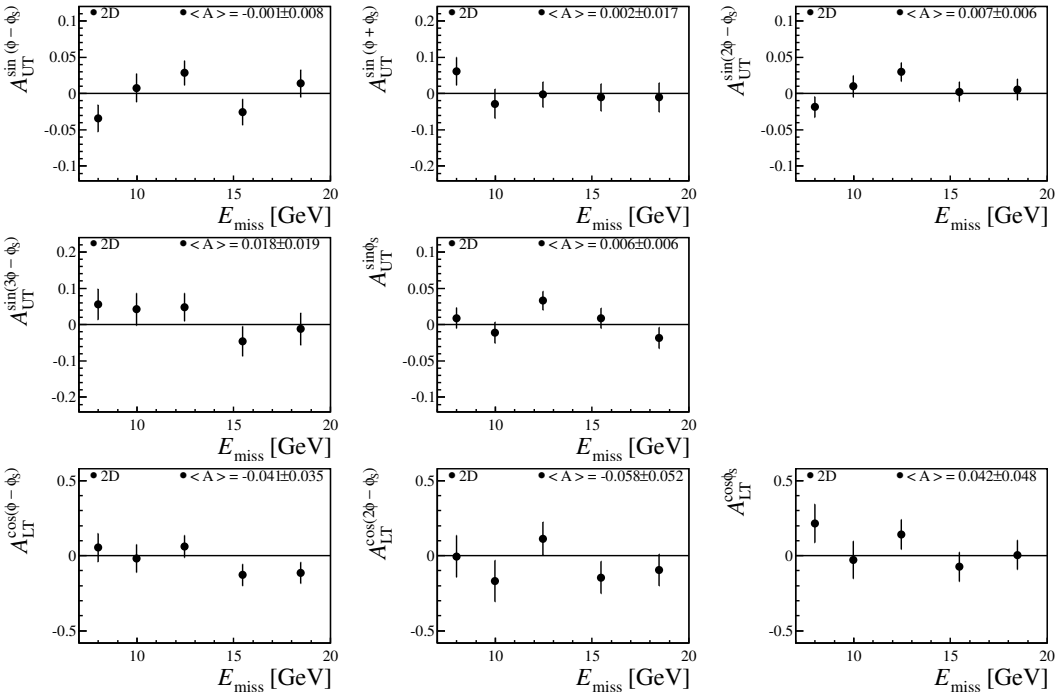

Figure 7.14: Results for background uncorrected asymmetries as a function of E_{miss} for $\mathbf{7.0\,GeV < E_{miss} < 20.0\,GeV}$ are shown.

7.3 Background Corrected Asymmetries

Now let us proceed with background corrected transverse asymmetries for exclusive produced ρ^0 mesons. Three different methods to extract background corrected asymmetries are implemented and compared. They are listed in Tab. 7.2 and can be divided in two different concepts: a correction of the level of the underlying ϕ, ϕ_S or Θ distributions or a correction on the level of asymmetries.

7.3.1 Background Correction on the Level of Azimuthal Distributions

If the estimated number of semi-inclusive events are subtracted from the ϕ, ϕ_S distribution (or Θ distribution), the distribution is not Poisson like any more and a

Table 7.2: A summary of the applied methods to extract background corrected asymmetries.

abbreviation	method
int	scaling of the ϕ, ϕ_S or Θ distribution according to the number of background events
bin	correcting the ϕ, ϕ_S or Θ distribution in every angular bin
UB back	correction on the level of asymmetries

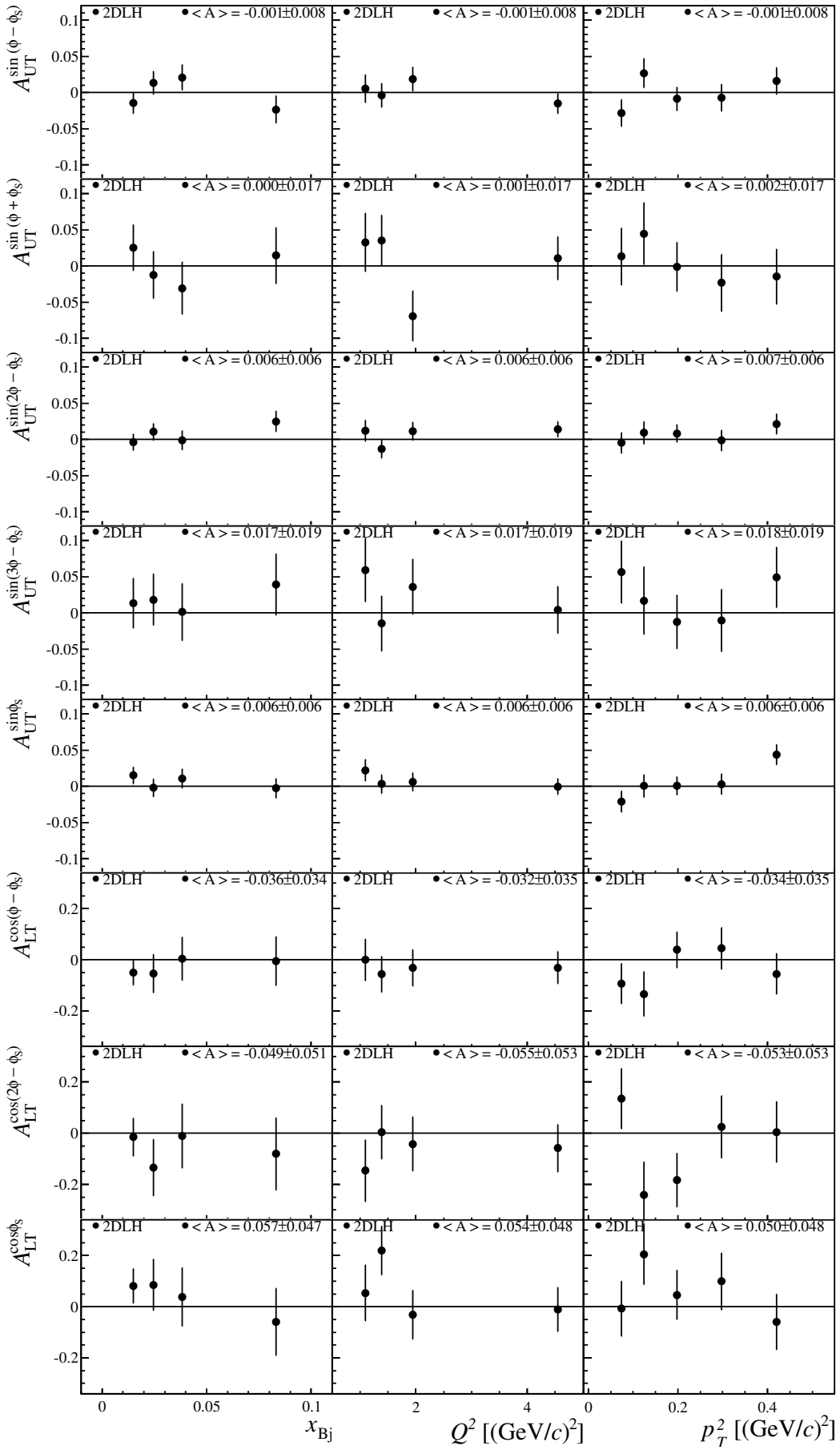

Figure 7.15: Asymmetry for $\mathbf{7.0\,GeV < E_{miss} < 20.0\,GeV}$. The asymmetry values are extracted with 2DLH. Mean values $< A >$ and their statistical errors are given.

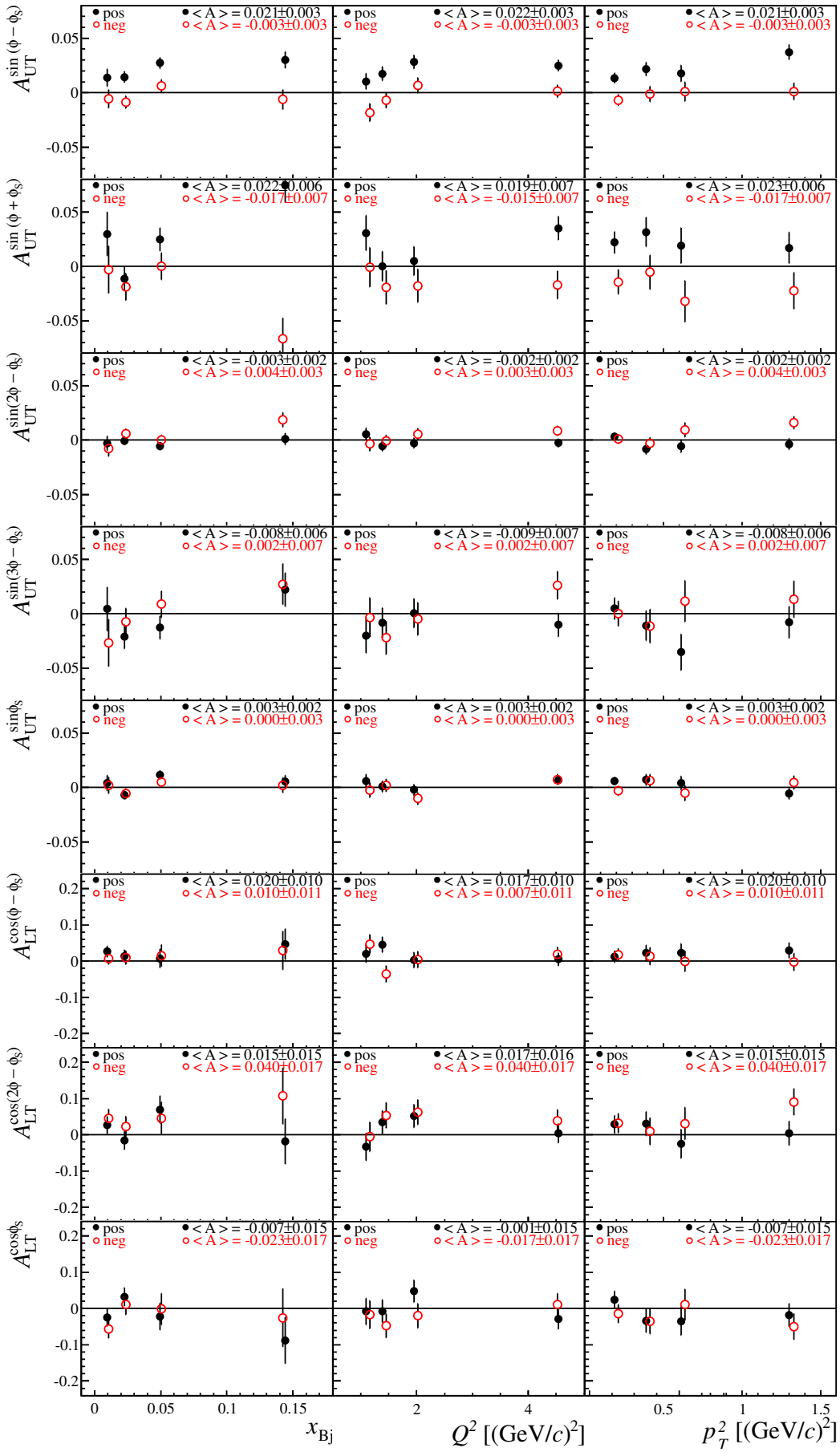

Figure 7.16: Asymmetry for the **pseudo-transversity** sample. The asymmetry values are extracted with UB. Mean values $\langle A \rangle$ and their statistical errors are given.

fit method based on Poisson statistics is no longer applicable. In this case we use a fit-to-counts method and Gauss distributions which has been introduced already in Sec. 6.2.2.1. It has been checked that the statistics is sufficiently large in every (ϕ, ϕ_S) bin to perform the asymmetry extraction. To avoid instabilities, the binning in ϕ and ϕ_S is chosen in order that at least 10 events are present in every bin[5]. The number of entries in each bin for the two-dimensional distribution was already presented in Fig. 7.10.

Here two different approaches are followed, which were explained in Sec. 5.2.1 and are abbreviated in the following with "int" and "bin". In the first case ("int") the background corrected distribution $N^{\text{sig}}_{k_1}(\phi, \phi_S)$ is used. Whereas, the other approach results in the background corrected azimuthal distribution $N^{\text{sig}}_{k_2}(\phi, \phi_S)$. The background corrected raw asymmetries are extracted from the corrected distributions $N^{\text{sig}}_{k_1}(\phi, \phi_S)$ or $N^{\text{sig}}_{k_2}(\phi, \phi_S)$ applying the methods from Sec. 6.2.

Whereas the first approach is used in the extraction of the leading-twist single-spin asymmetry $A_{\text{UT}}^{\sin(\phi-\phi_S)}$ for NH_3 and ^{6}LiD target published in Ref. [146], the second one is used if all eight modulations are studied at once. The attempt to extract the number of semi-inclusive background events bin-by-bin, for a two-dimensional ϕ, ϕ_S grid, suffers from high statistical fluctuations and, therefore, is disregarded for the standard analysis. The results obtained from both methods are shown in Fig. 7.17. Here, 8×8 bins in both ϕ and ϕ_S are used for the two-dimensional binned fit to be less sensitive to statistical fluctuations. The results of both methods are well compatible with each other inside the statistical precision of the measurement. The comparison of both methods is used to estimate a systematical uncertainty due to the background subtraction method in Sec. 7.5.4.2.

In Fig. 7.18 the correlation matrix introduced in Eq. 6.25 is shown. As an example, the first x_{Bj} bin is chosen. All others can be found in the Appendix D.5. Finally, the results for background corrected asymmetries extracted with the standard setup (2DLH, 12 bins in ϕ and ϕ_S, "int" background method) are presented in Fig. 7.19 as a function of x_{Bj}, Q^2 and p_T^2. In the plot two scenarios are shown where the details will be discussed in Sec. 7.5.4.1. Most of the extracted asymmetries seem to be compatible with zero inside $2 \cdot \sigma^{\text{stat}}$. Although the $A_{\text{UT}}^{\sin\phi_S}$ shows a hint towards a slightly negative value.

7.3.2 Background Correction on the Level of Asymmetries

Under the assumption that the asymmetries extracted in the non-exclusive missing energy range $7.0\,\text{GeV} < E_{\text{miss}} < 20.0\,\text{GeV}$ can be extrapolated into the signal range, they can be used to correct the asymmetries extracted for $-2.5\,\text{GeV} < E_{\text{miss}} < 2.5\,\text{GeV}$. The "true" asymmetries are estimated via:

$$A_t^m = \frac{A^m - b \cdot A_b^m}{1 - b}, \tag{7.5}$$

[5]The choice of 12 bins in both ϕ and ϕ_S is a compromise with regards to the statistics available and the observation that the correlation between 2DLH and UB improves with increasing number of bins and is discussed in Sec. 7.1.

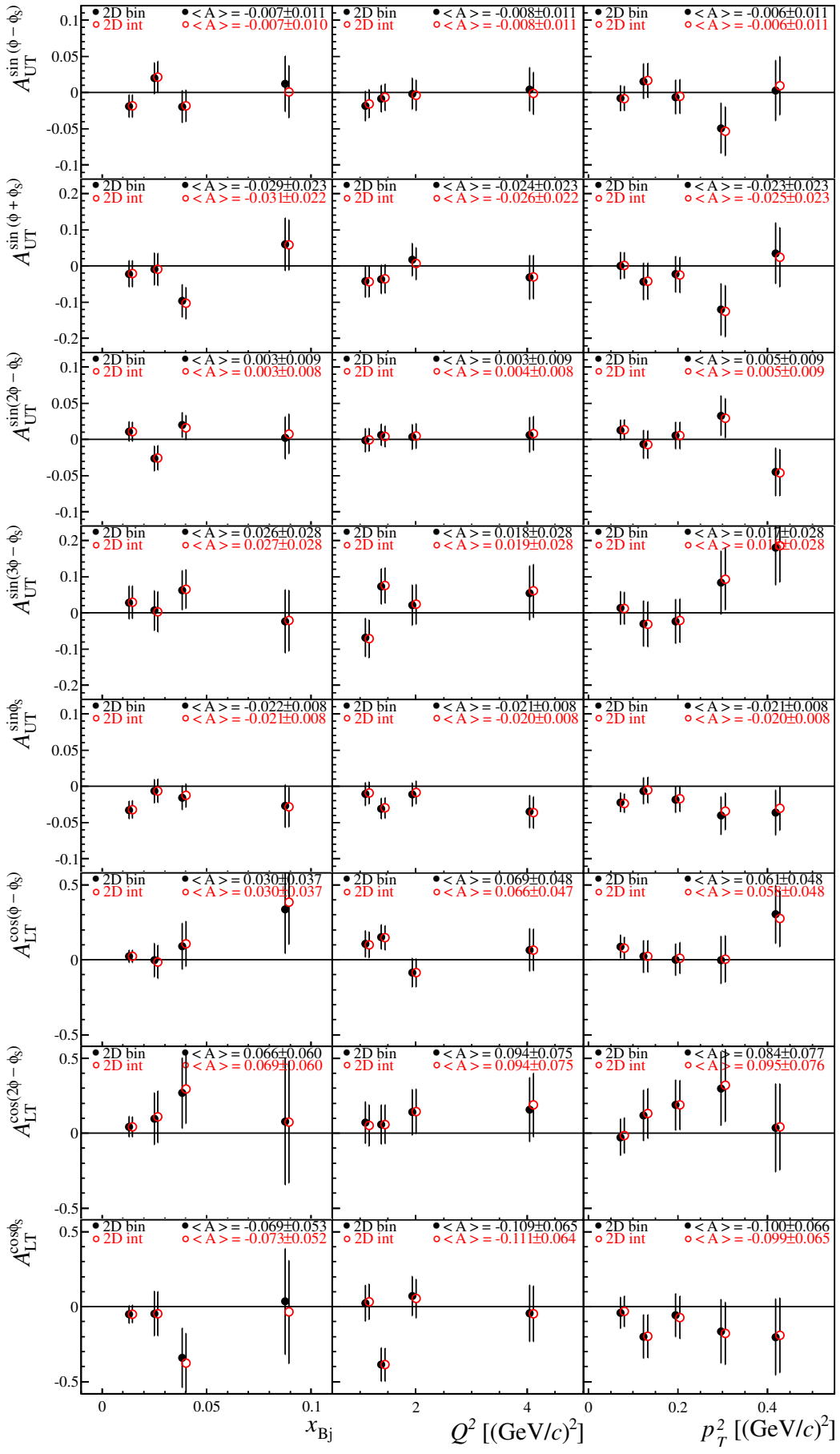

Figure 7.17: Comparison of **background corrected asymmetries** extracted with the 2DLH method using different methods for the background correction. Mean values $\langle A \rangle$ and their statistical errors are given.

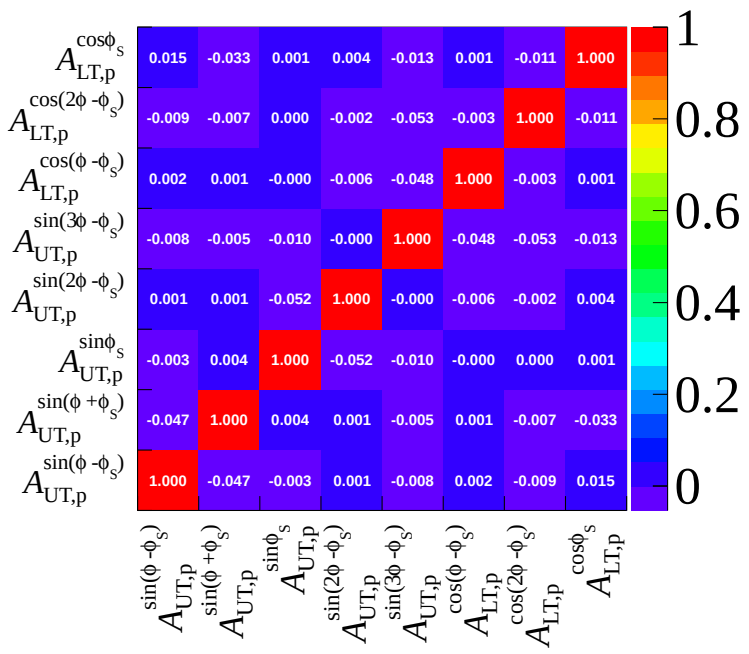

Figure 7.18: Correlation matrix for the 2DLH fit. Here is shown the first bin in x_{Bj} for the 2007&2010 sample.

with A_b^m is the asymmetry m evaluated in the pure background range $7.0\,\text{GeV} < E_{\text{miss}} < 20.0\,\text{GeV}$ and b is the fractional contribution of the background:

$$b = \frac{N_{back}}{N}, \qquad N = N_{back} + N_{sig}, \tag{7.6}$$

which is evaluated according to Sec. 5.2.1. The result is presented in Fig. 7.20 labeled with black full circles. Additionally the asymmetries evaluated in the exclusive range and in the semi-inclusive range are shown with red open circles and blue diamonds, respectively. They are extracted using an unbinned fit. This approach allows the usage of the unbinned likelihood fit. The advantage is that this overcomes the difficulties observed due to the correction of the raw asymmetries with the mean correction factor explained in Sec. 7.1. However the different dilution factors for exclusive and semi-inclusive production (see Fig. 6.6 and Fig. 7.13) lead to a higher statistical uncertainty of the background asymmetries, even when the exclusive and the non-exclusive samples are well balanced. Therefore, the true asymmetry might be disproportionally affected by statistical fluctuations. Nevertheless, a point-by-point comparison of the background corrected asymmetry values in Fig. 7.19 and Fig. 7.20 indicates a reasonable agreement between both methods. For $A^{\sin(3\phi-\phi_S)}$ the mean asymmetry values extracted with the two different methods differs with $0.8 \cdot \sigma^{stat}$, with respect to the statistical uncertainty of the binned extraction. For the other modulations, the differences of the mean asymmetry values are between $0.3 \cdot \sigma^{stat}$ and $0.6 \cdot \sigma^{stat}$.

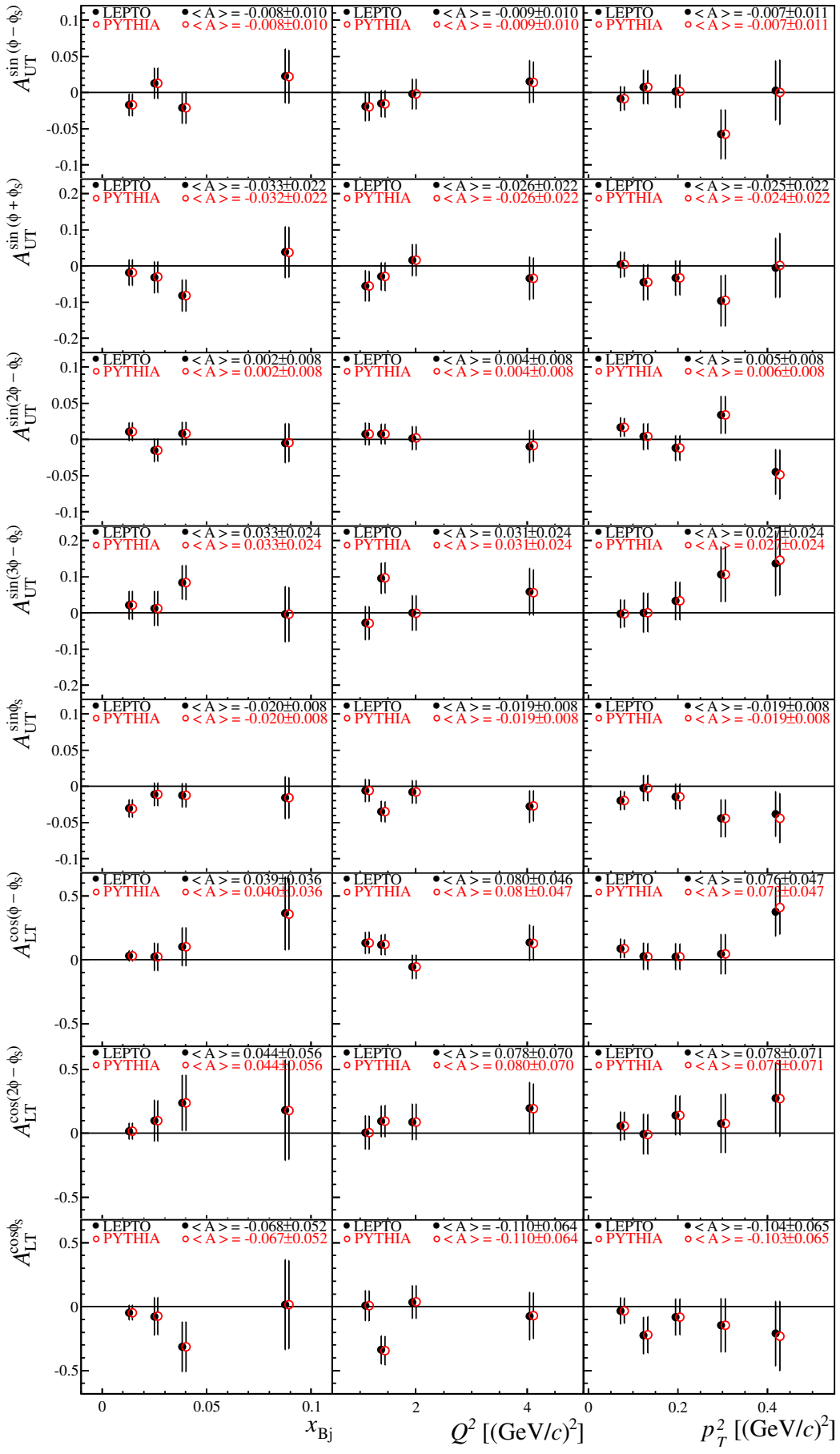

Figure 7.19: Comparison of **background corrected asymmetries** using **weighted PYTHIA** (red open circle) and **weighted LEPTO** (black full circle) for background parametrisation. Mean values $\langle A \rangle$ and their statistical errors are given.

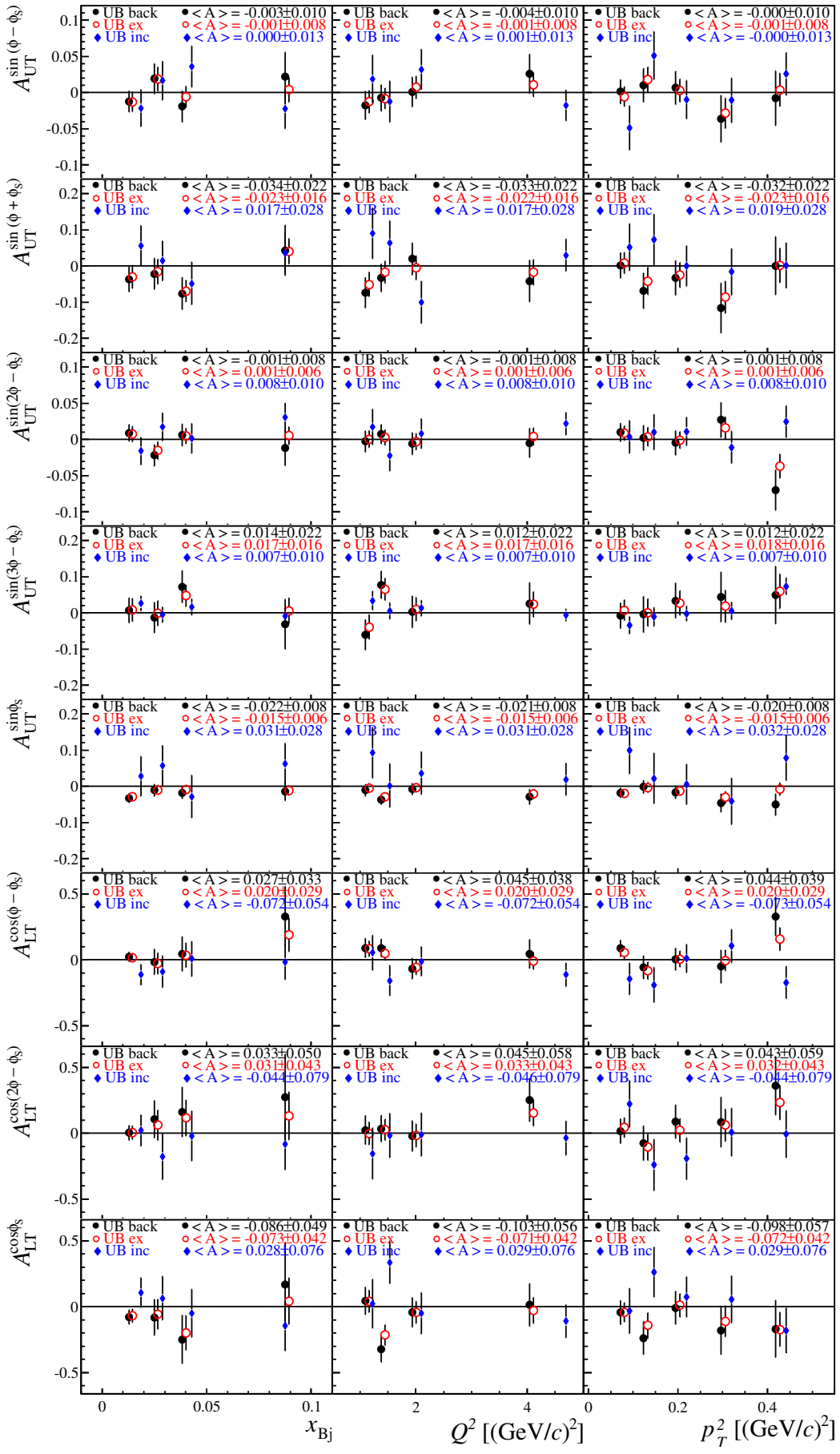

Figure 7.20: Comparison of asymmetries extracted with the **UB** fit. The asymmetries evaluated in the **exclusive range** (red open circles), in the **inclusive range** (blue diamonds) and the **background-corrected** once (black full circle) are shown.

7.4 Influence of the S_T to P_T Transition

Usually, in an experiment, the target is transversely polarised with respect to the direction of the lepton beam and the polarisation value is denoted by P_T. However, in Eq. 2.42, the target polarisation is transversely with respect to the direction of the virtual photon, which is denoted by S_T. In Fig. 7.21 both coordinate systems are shown where the z (z') axis points along q (k). It is possible to transform S_T to P_T by rotating the coordinate system around the $y/(y')$ axis by the angle θ between q and k [9], where:

$$\sin\theta = \gamma \sqrt{\frac{1 - y - \frac{1}{4}y^2\gamma^2}{1+\gamma^2}}, \tag{7.7}$$

and

$$\frac{S_T}{P_T} = \frac{\cos\theta}{\sqrt{1-\sin^2\theta\,\sin^2\phi_S}} \qquad \frac{S_L}{P_T} = \frac{\sin\theta\,\cos\phi_S}{\sqrt{1-\sin^2\theta\,\sin^2\phi_S}}. \tag{7.8}$$

Applying this transformation to Eq. 2.42 results in [9]:

$$\begin{aligned}
&\left[\frac{\alpha_{\rm em}}{4\pi^2}\,\frac{y^2}{1-\varepsilon}\,\frac{1-x_{Bj}}{x_{Bj}}\,\frac{1}{Q^2}\right]^{-1} \frac{d\sigma}{dx_{Bj}\,dQ^2\,d\phi d\phi_S dt}\,\Bigg|_{P_T=0} = \text{terms independent of } P_T \\
&- \frac{P_T}{\sqrt{1-\sin^2\theta\,\sin^2\phi_S}}\Bigg[\sin\phi_S\,\cos\theta\sqrt{\varepsilon(1+\varepsilon)}\,\mathrm{Im}\,\sigma^{+-}_{+0} \\
&+ \sin(\phi-\phi_S)\left(\cos\theta\,\mathrm{Im}\,(\sigma^{+-}_{++}+\varepsilon\sigma^{+-}_{00}) + \frac{1}{2}\sin\theta\sqrt{\varepsilon(1+\varepsilon)}\,\mathrm{Im}\,(\sigma^{++}_{+0}-\sigma^{--}_{+0})\right) \\
&+ \sin(\phi+\phi_S)\left(\cos\theta\,\frac{\varepsilon}{2}\,\mathrm{Im}\,\sigma^{+-}_{+-} + \frac{1}{2}\sin\theta\sqrt{\varepsilon(1+\varepsilon)}\,\mathrm{Im}\,(\sigma^{++}_{+0}-\sigma^{--}_{+0})\right) \\
&+ \sin(2\phi-\phi_S)\left(\cos\theta\sqrt{\varepsilon(1+\varepsilon)}\,\mathrm{Im}\,\sigma^{-+}_{+0} + \frac{1}{2}\sin\theta\,\varepsilon\,\mathrm{Im}\,\sigma^{++}_{+-}\right) \\
&+ \sin(2\phi+\phi_S)\,\frac{1}{2}\sin\theta\,\varepsilon\,\mathrm{Im}\,\sigma^{++}_{+-} + \sin(3\phi-\phi_S)\,\cos\theta\,\frac{\varepsilon}{2}\,\mathrm{Im}\,\sigma^{-+}_{+-}\Bigg] \\
&- \frac{P_T P_\ell}{\sqrt{1-\sin^2\theta\,\sin^2\phi_S}}\Bigg[+\cos(2\phi-\phi_S)\,\cos\theta\,\sqrt{\varepsilon(1-\varepsilon)}\,\mathrm{Re}\,\sigma^{-+}_{+0} \\
&+ \cos\phi_S\left(\cos\theta\sqrt{\varepsilon(1-\varepsilon)}\,\mathrm{Re}\,\sigma^{+-}_{+0} - \sin\theta\sqrt{1-\varepsilon^2}\,\frac{1}{2}(\sigma^{++}_{++}-\sigma^{--}_{++})\right) \\
&- \cos(\phi-\phi_S)\left(\cos\theta\sqrt{1-\varepsilon^2}\,\mathrm{Re}\,\sigma^{+-}_{++} - \frac{1}{2}\sin\theta\sqrt{\varepsilon(1-\varepsilon)}\,\mathrm{Re}\,(\sigma^{++}_{+0}-\sigma^{--}_{+0})\right) \\
&+ \cos(\phi+\phi_S)\,\frac{1}{2}\sin\theta\sqrt{\varepsilon(1-\varepsilon)}\,\mathrm{Re}\,(\sigma^{++}_{+0}-\sigma^{--}_{+0})\Bigg].
\end{aligned} \tag{7.9}$$

The transition from S_T to P_T introduces the term $\cos\theta$ in front of every asymmetry. The additional asymmetries $\sin(2\phi+\phi_S)$ and $\cos(\phi+\phi_S)$ are suppressed by $\sin\theta$. Furthermore some of the $A_{\rm UT,LT}$ asymmetries are supplemented with additional terms which can be connected to an admixture with the longitudinal asymmetries $A_{\rm UL(LL)}$. In the Bjorken limit, θ and γ are small and Eq. 7.9 and Eq. 2.42 fall approximately together. The angle θ between the lepton beam direction and the

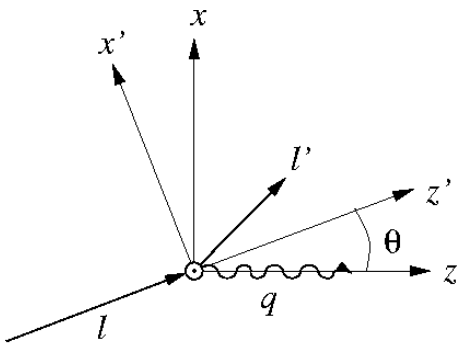

Figure 7.21: The lepton plane in the target rest frame, where z (z') points along q (k). The $y/(y')$ axes point out of the paper plane.

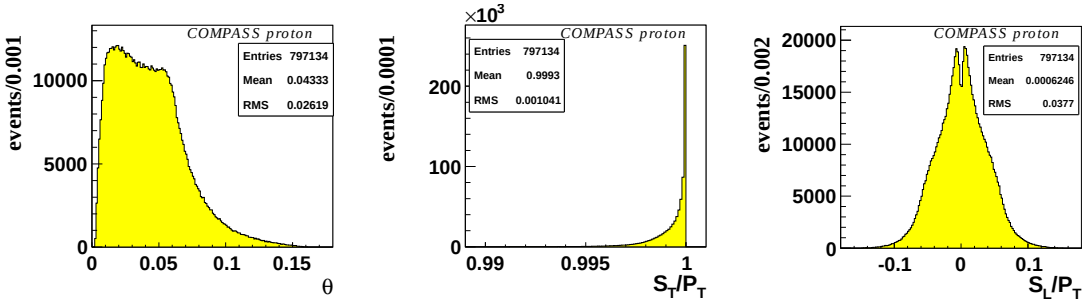

Figure 7.22: On the left-hand side the angle θ between the lepton beam direction and the virtual photon direction as defined in Fig. 7.21 is shown. Additionally, the ratio of the transverse spin vector S_T (middle) or the longitudinal spin vector S_L (right) both with respect to the virtual photon direction and the transverse spin vector with respect to the lepton direction P_T is presented.

virtual photon direction as defined Fig. 7.21 is presented in Fig. 7.22. The mean value is $\langle\theta\rangle \approx 0.04\,\text{rad}$. Additional the distributions from Eq. 7.8 are shown.

In [147] it was shown that the asymmetry $A_{LT}^{\cos\phi_S}$ measured in semi-inclusive deep inelastic scattering of polarised muons off a transversely polarised NH_3 target is biased especially for high x_{Bj} values due to the contribution of the A_{LL} amplitude despite the smallness of $\sin\theta$. The reason is a strong x_{Bj}-dependent A_{LL} asymmetry [148] in semi-inclusive measurement. The formula for correcting $A_{\text{LT}}^{\cos\phi_S}$ in [147] can be adapted to:

$$A_{LT}^{cos\phi'_S} \approx \cos\theta A_{LT}^{cos\phi_S} - \sin\theta \frac{1}{\sqrt{\varepsilon(1-\varepsilon)}} A_{LL}. \tag{7.10}$$

The study of $\langle\sin\theta\rangle$ in bins of Eq. 6.12 indicates an increase as a function of x_{Bj} presented in Fig. 7.23, similar to the situation in semi-inclusive scattering. Therefore, to estimate the bias of $A_{\text{LT}}^{\cos\phi_S}$, the knowledge of A_{LL} measured for exclusive ρ^0 mesons is necessary.

In COMPASS, the A_{LL} asymmetry in exclusive ρ^0 production is only analysed for scattering the longitudinally polarised muon beam on a longitudinally polarised ^{6}LiD target [127]. Here the extracted asymmetry is comparable with zero over the en-

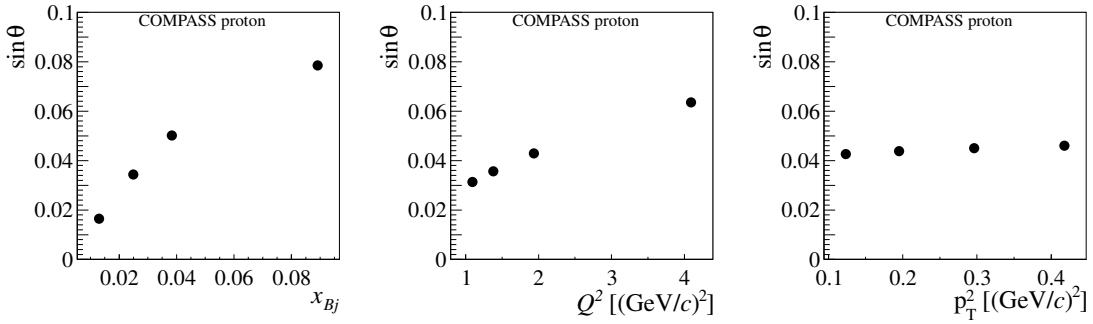

Figure 7.23: Mean values of θ in bins of Eq. 6.12 for the 2007&2010 sample.

tire kinematic range. Additional measurements exist from the SMC as well as the HERMES Collaboration, although these measurements are performed in a different kinematic range compared to COMPASS and suffer from large statistical uncertainties. The measurement of the SMC experiment [129, 149], where a longitudinally polarised muon beam with 190 GeV/c were optionally scattered on an ammonia, butanol or deuterated butanol target indicates a slightly negative value, although the statistics are not sufficient. The HERMES experiment measures a slight increase of A_{LL} with increasing x_{Bj} scattering a 27.5 GeV/c electron (positron) beam on a longitudinally polarised hydrogen or deuterium target [150]. Obviously the present existing data on A_{LL} asymmetry in exclusive ρ^0 production does not allow for a well-founded estimation of possible effects on the $A_{\mathrm{UT,LT}}$ asymmetries.

In Ref. [151] asymmetries for exclusive meson production are related to the corresponding inclusive deep inelastic scattering asymmetries. In this publication the reaction $ep \to ep\rho^0$ as well as $ep \to eX$ is studied and the model dependent relation $A_{\mathrm{LL}}^{\rho^0} = 2 \cdot A_{\mathrm{LL}}^{incl.}$ is derived for forward diffractive ρ^0 production. The $A_{\mathrm{LL}}^{incl.}$ asymmetry was measured at COMPASS [152] based on data taken during the year 2007 with a longitudinally polarised NH_3 target and a longitudinally polarised muon beam with 160 GeV/c. The asymmetry is studied for $3 \cdot 10^{-3}\,(\mathrm{GeV}/c)^2 < Q^2 < 7\,(\mathrm{GeV}/c)^2$ and $5 \cdot 10^{-5} < x_{Bj} < 0.05$ and found to be compatible with zero in the entire kinematic range.

The two additional asymmetries $\sin(2\phi + \phi_S)$ and $\cos(\phi + \phi_S)$ can be added to the function in Eq. 6.3. From a theoretical point of view, all summands in Eq. 6.3 are orthogonal to each other. However, the non-uniform acceptance of the COMPASS detector might lead to a change of the results. Therefore, the fits have been performed also adding the asymmetries $\sin(2\phi + \phi_S)$ and $\cos(\phi + \phi_S)$. In Fig. 7.24 the pulls between both extractions done with 2DLH for the 13 kinematic bins are shown. Here only the pure fit results, i.e. the raw asymmetries are studied. If the additional modulations $k\phi + \phi_S$ are added, the pulls of the standard modulations $k\phi - \phi_S$ and $(k-1)\phi + \phi_S$ are more widely distributed. However, the results are statistically scattered around zero with a RMS of the pulls of up to 0.1. Therefore no systematics are obtained.

After the detailed study, the influence of the θ-related corrections is neglected. For the extraction of the asymmetries Eq. 2.42, is used. To obtain the physical asymmetries the fit results have to be divided by the correction factor which includes the

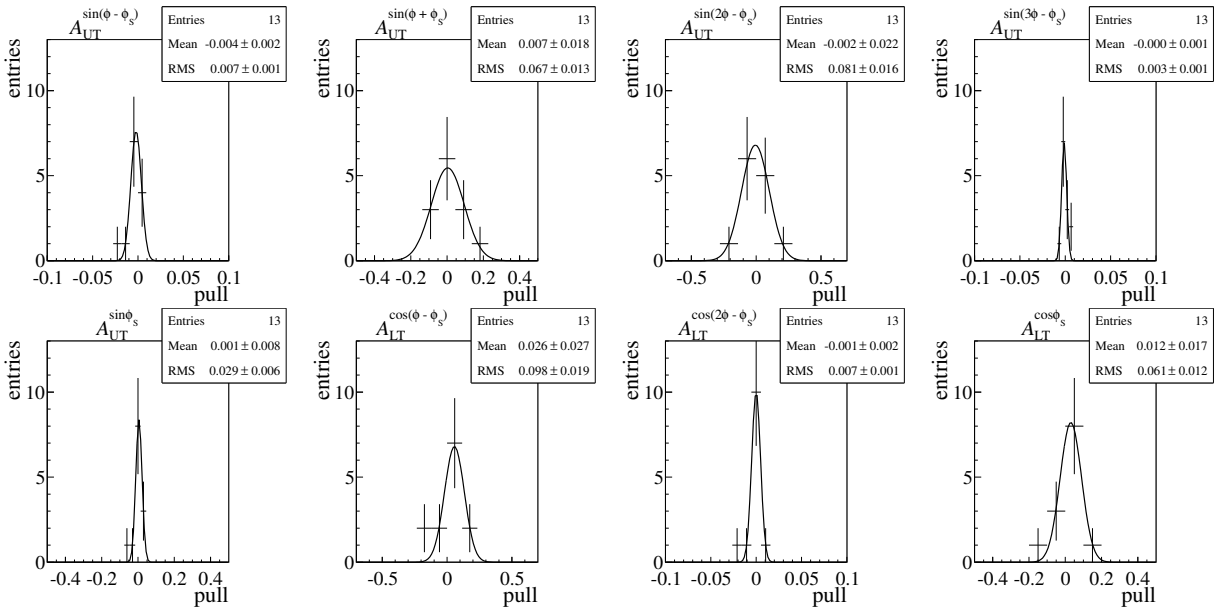

Figure 7.24: Pulls between results obtained by fitting the eight asymmetries studied and all 10 asymmetries, as explained in the text.

dilution factor, the depolarisation factor, the target polarisation and, for the A_{LT} asymmetry, the beam polarisation, and, additionally, the $\sin(\theta)$ term. Since this factor scales the asymmetry value, as well as the statistical uncertainty, the statistics available are not sufficient to draw conclusions on the asymmetries $\sin(2\phi + \phi_S)$ and $\cos(\phi + \phi_S)$.

7.5 Systematic Studies

Several tests to evaluate the systematic uncertainty of the result are discussed in the next two sections. According to the approach in Ref. [153], only substantially contributions which can not be overcome should be included in the final systematic uncertainty.

The stability of the extracted asymmetries is analysed by performing different systematic tests, namely the asymmetry values calculated with different extraction methods are compared (Sec. 7.5.2), the stability of the data sample used over time is studied (Sec. 7.5.3), and the stability of the applied background subtraction method is tested (Sec. 7.5.4). All checks are performed separately for each of the eight modulations. This section is dedicated to the NH_3 target and it includes an introduction of the applied checks as well as the results.

7.5.1 Compatibility of Mean Asymmetries in x_{Bj}, Q^2 and p_T^2

As already mentioned in Sec. 7.1, the mean asymmetry values for the A_{LT} asymmetries evaluated in bins of x_{Bj} differ considerably from those for Q^2 and p_T^2, respectively. This incompatibility is observed equally for the physics asymmetries with and without background correction; although it is not present on the level of raw asymmetries. The differences appear, mainly for $A_{\mathrm{LT}}^{\cos(\phi-\phi_S)}$ and $A_{\mathrm{LT}}^{\cos\phi_S}$, after applying the D_{NN} factor, due to the strong x_{Bj} dependence of the D_{NN} factor as discussed in Sec. 6.3. The differences in the mean asymmetry values, evaluated for x_{Bj}, Q^2 and p_T^2, are taken into account in the systematic uncertainty. Half of the maximum differences expressed in terms of the final statistical error of the background corrected asymmetries are summarized in Tab. 7.3.

Table 7.3: Half of the maximal difference of the mean values of the asymmetries for x_{Bj}, Q^2 and p_T^2, separately for every modulation. The asymmetries in the second column are evaluated with $D_{NN} = 1$, where in the third column the D_{NN} factors according to Eq. 6.32 are used. If no value is given, no difference is observed.

Asymmetry	$\sigma^{sys}/\sigma^{stat}$	
	assuming $D_{NN} = 1$	D_{NN} according Eq. 6.32
$\mathrm{A}_{\mathrm{UT}}^{\sin(\phi-\phi_S)}$	-	-
$\mathrm{A}_{\mathrm{UT}}^{\sin(\phi+\phi_S)}$	0.02	0.07
$\mathrm{A}_{\mathrm{UT}}^{\sin(2\phi-\phi_S)}$	0.06	-
$\mathrm{A}_{\mathrm{UT}}^{\sin(3\phi-\phi_S)}$	-	0.02
$\mathrm{A}_{\mathrm{UT}}^{\sin(\phi_S)}$	0.06	-
$\mathrm{A}_{\mathrm{LT}}^{\cos(\phi-\phi_S)}$	-	0.20
$\mathrm{A}_{\mathrm{LT}}^{\cos(\phi_S)}$	-	0.16
$\mathrm{A}_{\mathrm{LT}}^{\cos(2\phi-\phi_S)}$	0.01	0.08

7.5.2 Comparison of Different Estimators

To avoid double counting, the tests presented here are done on the level of raw asymmetries and before background correction. Systematic effects related to the usage of the correction factor and the background subtraction are addressed in Sec. 7.5.1 and Sec. 7.5.4. The RMS values and half of the shifted means of the pull distributions in Fig. 7.9, correctly expressed in terms of the final statistical errors of the background corrected asymmetries, are taken into account in the systematic uncertainty and are summarized in Tab. 7.4.

7.5.3 Stability of Data Taking

This section is dedicated to the test of the stability of the asymmetries depending on the periods of data taking during the run. To avoid double counting of the systematic uncertainties introduced due to the D_{NN} factor discussed in Sec. 7.5.1,

Table 7.4: Systematic uncertainties related to the choice of estimator expressed in terms of the final statistical error of the background corrected asymmetries, separately for every modulation.

Asymmetry	$\sigma^{\text{sys}}/\sigma^{\text{stat}}$
$A_{UT}^{\sin(\phi-\phi_S)}$	0.14
$A_{UT}^{\sin(\phi+\phi_S)}$	0.16
$A_{UT}^{\sin(2\phi-\phi_S)}$	0.26
$A_{UT}^{\sin(3\phi-\phi_S)}$	0.26
$A_{UT}^{\sin(\phi_S)}$	0.11
$A_{LT}^{\cos(\phi-\phi_S)}$	0.11
$A_{LT}^{\cos(2\phi-\phi_S)}$	0.22
$A_{LT}^{\cos(\phi_S)}$	0.10

raw asymmetries are used[6]. As these studies are not sensitive to the background, they are performed before background correction.

7.5.3.1 Experimental False Asymmetries

For the extraction of the so called false asymmetries, the data samples are combined in such a way that no true asymmetries are present i.e. from the physical point of view no asymmetry is expected. The goal is to estimate the systematic uncertainties due to acceptance variations. The asymmetry values are extracted with a UB.

In Eq. 6.1 the number of exclusive ρ^0 mesons are expressed as a function of ϕ and ϕ_S, assuming an acceptance term $\alpha_n^{\pm}$ independent of ϕ and ϕ_s. In COMPASS the acceptance in ϕ and ϕ_S is not flat, as visible in Fig. 6.2 and Fig. 6.3. Each modulation can be decomposed in its Fourier amplitudes, as shown in Ref. [135]. This study results in the observation that modulations of the acceptance terms exist, which depend on the same angles as the physical asymmetry [154]. Whereas the modulation in the ϕ distribution is mainly due to the contribution of the physical unpolarised asymmetries, the modulation of the ϕ_S distribution is non-physical and depends on the trigger system [154].

Therefore, it is assumed that the acceptance $\alpha_n^{\pm}$ has a ϕ, ϕ_S dependence. Then the number of exclusive ρ^0 mesons as a function of ϕ and ϕ_S can be written for every target cell n as:

$$N_{j,n}^{\pm}(\phi, \phi_S) = c_{j,n}^{\pm}\left(1 + \alpha_{j,n}^{\pm}\Phi^m\right)\left(1 \pm \epsilon^m\Phi^m\right), \tag{7.11}$$

where Φ^m denotes one of the eight azimuthal modulations: $\sin(\phi-\phi_S), \sin(\phi+\phi_S), \sin(2\phi-\phi_S), \sin(3\phi-\phi_S), \sin\phi_S, \cos(\phi-\phi_S), \cos(2\phi-\phi_S), \cos\phi_S$. The different target polarisations are represented by $\pm$ and $c_n^{\pm}$ implies the unpolarised cross

[6]This approach relies on the assumption that the appliance of the correction factor do not introduce an extra asymmetry. This assumption is supported by the observation that the systematic uncertainties evaluated in the signal range based on the physical asymmetries A_{UT}^m differs only within $\pm 0.04 \cdot \sigma^{\text{stat}}$ compared to the systematic uncertainties evaluated using raw asymmetries.

section, the muon flux and the number of target nucleons. The true asymmetry of modulation Φ^m is ϵ^m. It is assumed that the acceptance has the same dependency from the azimuthal angle as the asymmetry.

For this test, data with common target polarisation is combined. According to Fig. 6.1 this can be realised by combining the two outer cells (U and D) of the target or dividing the inner cell (C) in two equally large parts (C_1 and C_2), which are combined with each other. The sub-cells of U, C_1, C_2, D are named with N_1 to N_4 in the direction of the muon beam. We define:

$$r_{14} = \frac{N_1^{\pm} N_4^{\mp}}{N_1^{\mp} N_4^{\pm}} \qquad r_{23} = \frac{N_2^{\pm} N_3^{\mp}}{N_2^{\mp} N_3^{\pm}}. \tag{7.12}$$

In addition, it is possible to combine data with opposite target polarisation from the first half (U and C_1) and the second half (C_2 and D) of the target:

$$r_{12} = \frac{N_1^{\pm} N_2^{\pm}}{N_1^{\mp} N_2^{\mp}} \qquad r_{34} = \frac{N_4^{\pm} N_3^{\pm}}{N_4^{\mp} N_3^{\mp}}. \tag{7.13}$$

Inserting Eq. 7.11 into Eq. 7.12 and Eq. 7.13 the asymmetries:

$$\begin{aligned} A^m_{r_{14}} &\approx \epsilon + (\alpha_1^{\pm} - \alpha_1^{\mp} - \alpha_4^{\pm} + \alpha_4^{\mp})/4, \\ A^m_{r_{23}} &\approx \epsilon + (\alpha_2^{\pm} - \alpha_2^{\mp} - \alpha_3^{\pm} + \alpha_3^{\mp})/4, \\ A^m_{r_{12}} &\approx \epsilon + (\alpha_1^{\pm} - \alpha_1^{\mp} - \alpha_2^{\pm} + \alpha_2^{\mp})/4, \\ A^m_{r_{34}} &\approx \epsilon + (\alpha_4^{\pm} - \alpha_4^{\mp} - \alpha_3^{\pm} + \alpha_3^{\mp})/4, \end{aligned} \tag{7.14}$$

can be build, where $A^m_{r_{14}}$ and $A^m_{r_{23}}$ are false asymmetries so the true asymmetry ϵ of the underlying scattering process is zero. However $A^m_{r_{12}}$ ($A^m_{r_{34}}$) are true asymmetries, extracted from the first (second) half of the target. The true asymmetries are presented in Fig. D.4 whereas the false asymmetries are shown in Fig. D.5. Out of Eq. 7.14 three combinations are built: $A^m_{(r_{14}-r_{23})}$, $A^m_{(r_{14}+r_{23})}$, and $A^m_{(r_{12}-r_{34})}$, all depending on the acceptance terms α_i only. In Fig. D.6 they are shown as a function of x_{Bj}, Q^2 and p_T^2. The mean values for most of the modulations are compatible with zero. As each asymmetry is extracted out of a combination of $\frac{1}{2}$ of the statistics available the study is highly effected by statistical fluctuations. Therefore, in addition, the false asymmetries are evaluated from data in the extended range of the missing energy to increase the statistical precision of the test. In Figs. 7.25, 7.26 and D.7 the results are shown.

The systematic uncertainty is estimated by:

$$\left| A^{i'}_{(r_{14} \pm r_{23})} \right| = \frac{\sum_{i=1}^{13} \frac{\left| A^i_{(r_{14} \pm r_{23})} \right|}{\sigma_i} \frac{1}{\sigma_i^2}}{\sum_i^{13} \frac{1}{\sigma_i^2}}. \tag{7.15}$$

Here we sum up the 13 kinematic bins i. Before this, the quantities are checked for every kinematic dependency separately, indicating a reasonable agreement. According to Ref. [154] the expected statistical fluctuations can be minimised by subtracting in quadrature the statistically expected value 0.68 from the deviation before $\frac{\sigma^{\text{sys}}}{\sigma^{\text{stat}}}$ is evaluated. If $\left| A^{i'}_{(r_{14} \pm r_{23})} \right|$ is smaller then 0.68, σ^{sys} is set to zero. The Eq. 7.15 is also evaluated for $A^m_{(r_{12}-r_{34})}$.

The results for $A_{(r_{14}-r_{23})}$ and for $A_{(r_{14}+r_{23})}$ give an estimate of the bias of the real asymmetry ϵ. The quantity $A_{(r_{14}-r_{23})}$ has the same dependency on the acceptance terms α_i as $A_{(r_{12}-r_{34})}$ which is half the difference of the real asymmetries measured with the two upstream and the two downstream cells. Hence, it is a direct measure of acceptance variations along the target.

The systematic uncertainties are evaluated from the 13 values according to Eq. 7.15. A summary of the extracted systematic uncertainties in the signal range correctly expressed in terms of the final statistical error of the background corrected asymmetries is depicted in Tab. 7.5. Whereas the extracted systematic uncertainties in the extended range correctly expressed in terms of the final statistical error of the background corrected asymmetries is depicted in Tab. 7.6.

Table 7.5: Systematic uncertainties from false (column 2 and 3) and true (column 4) asymmetries expressed in terms of the final statistical error of the background corrected asymmetries separately for every modulation. The asymmetry values are extracted for data with $\mathbf{-2.5\,GeV < E_{miss} < 2.5\,GeV}$.

Asymmetry	$\sigma^{sys}/\sigma^{stat}$		
	(r_{14}-r_{23})	(r_{14}+r_{23})	(r_{12}-r_{34})
$A_{UT}^{\sin(\phi-\phi_S)}$	0.40	0.00	0.40
$A_{UT}^{\sin(\phi+\phi_S)}$	0.00	0.40	0.00
$A_{UT}^{\sin(2\phi-\phi_S)}$	0.00	0.35	0.00
$A_{UT}^{\sin(3\phi-\phi_S)}$	0.17	0.00	0.17
$A_{UT}^{\sin(\phi_S)}$	0.76	0,00	0.74
$A_{LT}^{\cos(\phi-\phi_S)}$	0.52	0.16	0.51
$A_{LT}^{\cos(2\phi-\phi_S)}$	0.14	0.54	0.10
$A_{LT}^{\cos(\phi_S)}$	0.50	0.37	0.48

7.5.4 Stability of Background Subtraction Method

7.5.4.1 Dependence on SIDIS Background Parametrisation

The parametrisation of the background is done with a weighted LEPTO sample, as explained in Sec. 5.1.4. To test the sensitivity of the asymmetry values on the LEPTO generator, a second MC sample is created with the PYTHIA generator. The comparison of the extracted asymmetries, using the background shapes obtained from weighted PYTHIA or from weighted LEPTO as a function of x_{Bj}, Q^2, and p_T^2, is shown in Fig. 7.19. In most of the points the extracted asymmetries are identical and independent of the event generator used. For some modulations there are small differences observed, mostly in the highest p_T^2 bin where the experimental acceptance is limited. On the level of mean asymmetries, no significant deviation between the two results can be observed.

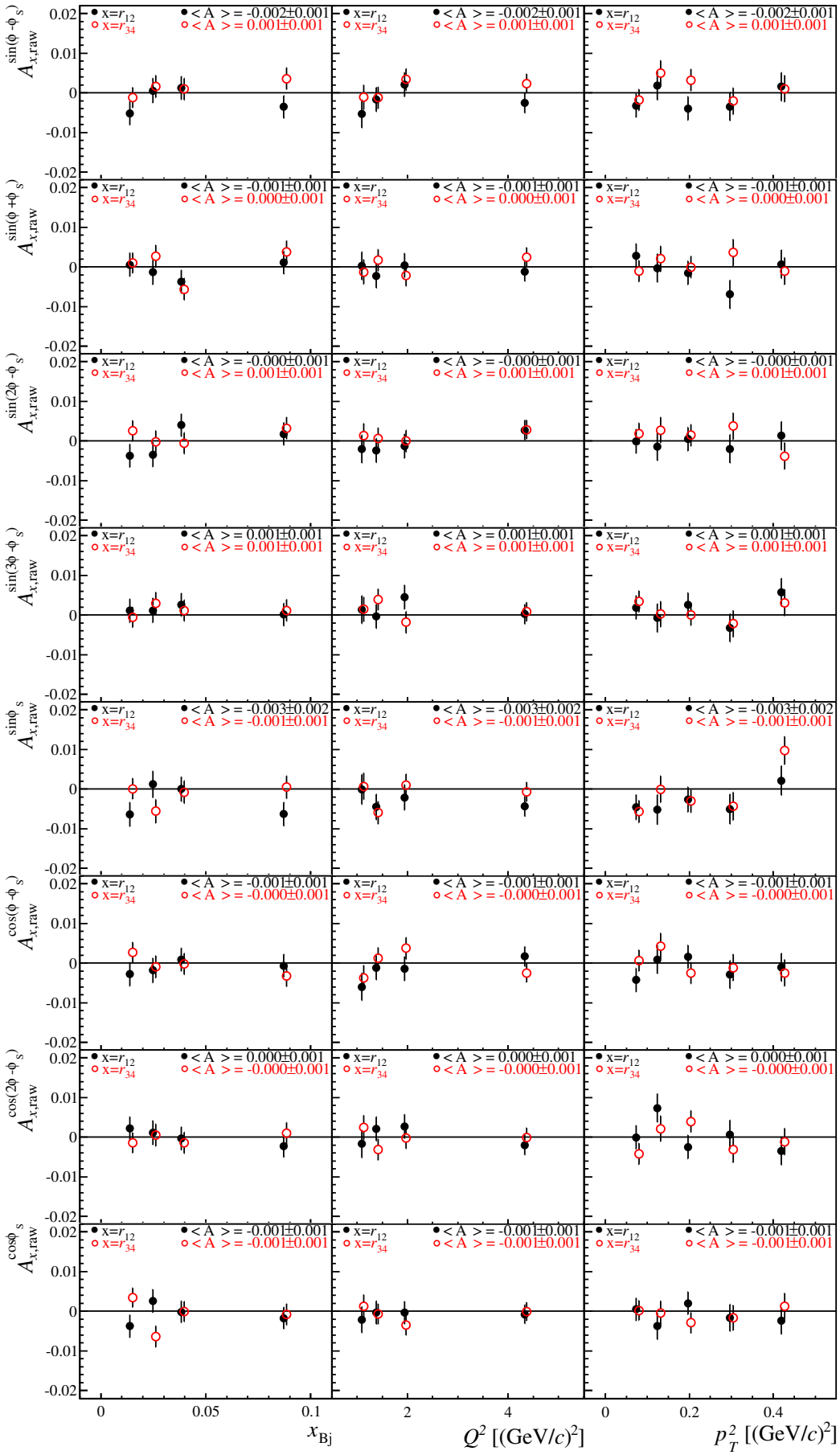

Figure 7.25: $\boldsymbol{A_{r12,\mathrm{raw}}}$ (black full circle), $\boldsymbol{A_{r34,\mathrm{raw}}}$ (red open circle). Mean values $\langle A_{x,\mathrm{raw}} \rangle$ are given. The values are extracted for data with $\boldsymbol{-10.0\,\mathrm{GeV} < E_{\mathrm{miss}} < 20.0\,\mathrm{GeV}}$.

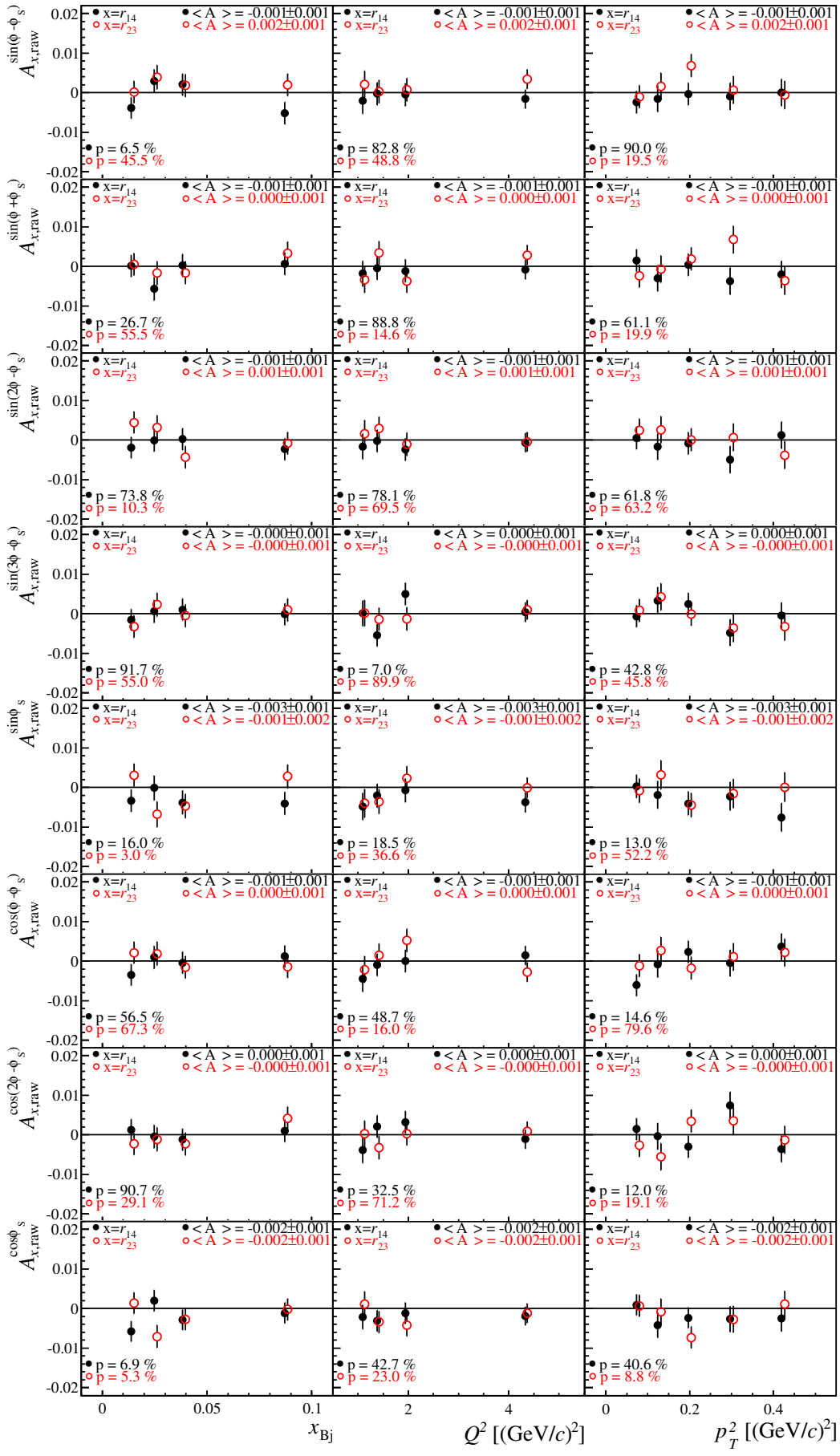

Figure 7.26: Results of $\boldsymbol{A_{r14,\mathrm{raw}}}$ (black full circle), $\boldsymbol{A_{r23,\mathrm{raw}}}$ (red open circle). Mean values $\langle A_{x,\mathrm{raw}} \rangle$ and probabilities p of χ^2 test with respect to $A_{r14,\mathrm{raw}} = 0$ or $A_{r23,\mathrm{raw}} = 0$ are given. The values are extracted for data with $\boldsymbol{-10.0\,\mathrm{GeV} < E_{\mathrm{miss}} < 20.0\,\mathrm{GeV}}$.

Table 7.6: Systematic uncertainties evaluated from false (column 2 and 3) and true (column 4) asymmetries expressed in terms of the final statistical error of the background corrected asymmetries separately for every modulation. The values are extracted for data with $\mathbf{-10\,GeV < E_{miss} < 20\,GeV}$.

Asymmetry	$\sigma^{sys}/\sigma^{stat}$		
	$(r_{14}\text{-}r_{23})$	$(r_{14}+r_{23})$	$(r_{12}\text{-}r_{34})$
$A_{UT}^{\sin(\phi-\phi_S)}$	0.17	0.00	0.17
$A_{UT}^{\sin(\phi+\phi_S)}$	0.11	0.16	0.12
$A_{UT}^{\sin(2\phi-\phi_S)}$	0.10	0.00	0.08
$A_{UT}^{\sin(3\phi-\phi_S)}$	0.00	0.11	0.00
$A_{UT}^{\sin(\phi_S)}$	0.22	0.36	0.22
$A_{LT}^{\cos(\phi-\phi_S)}$	0.23	0.00	0.22
$A_{LT}^{\cos(2\phi-\phi_S)}$	0.22	0.00	0.22
$A_{LT}^{\cos(\phi_S)}$	0.10	0.45	0.09

7.5.4.2 Dependence on SIDIS Background Subtraction Method

We correct for the SIDIS background by subtracting the scaled two-dimensional ϕ, ϕ_S distribution for events in the range $7\,\text{GeV} < E_{\text{miss}} < 20\,\text{GeV}$ ('int' method) as discussed in Sec. 7.3. Using the second method the number of background events are determined in each of the angular bins separately ('bin' method). In Fig. 7.17 the asymmetries extracted with both background subtraction methods are shown. Here a 2DLH with eight bins in ϕ and ϕ_S each is used. A point by point comparison of the asymmetries indicates a reasonable agreement between the two methods. For the integrated method a slightly higher statistical error is observed. The systematic uncertainties related to the choice of the background subtraction method expressed in terms of the final statistical error of the background corrected asymmetries is evaluated as $\sigma_m^{\text{sys}}/\sigma_m^{\text{stat}} = 0.1$ for every asymmetry m.

7.5.4.3 Compatibility of Mean Asymmetries in x, Q^2 and p_T^2

In this section the average of the background corrected asymmetries are compared for x_{Bj}, Q^2 and p_T^2. They are evaluated according to Eq. 6.30. In Sec. 7.5.1 we already discussed that, before the background subtraction, the mean values and its errors evaluated from the bins in x_{Bj} differ from those evaluated from the bins in Q^2 and p_T^2, respectively. This observation is enforced after the background subtraction is done. Half of the maximal differences expressed in terms of the final statistical error of the background corrected asymmetries are taken into account in the systematic uncertainties and are listed in Tab. 7.7.

Table 7.7: Half of the maximal differences of the mean values of the background corrected asymmetries for x_{Bj}, Q^2 and p_T^2, separately for each modulation.

Asymmetry	$\sigma^{sys}/\sigma^{stat}$
$A_{UT}^{\sin(\phi-\phi_S)}$	0.10
$A_{UT}^{\sin(\phi+\phi_S)}$	0.18
$A_{UT}^{\sin(2\phi-\phi_S)}$	0.19
$A_{UT}^{\sin(3\phi-\phi_S)}$	0.13
$A_{UT}^{\sin(\phi_S)}$	0.06
$A_{LT}^{\cos(\phi-\phi_S)}$	0.48
$A_{LT}^{\cos(\phi_S)}$	0.26
$A_{LT}^{\cos(2\phi-\phi_S)}$	0.35

7.5.5 Further Effects

Coherent production is discussed in Sec. 5.3. The amount of the remaining coherently produced events is estimated up to 12% of the final sample. In Fig. 7.27 background uncorrected asymmetries are studied with the 2DLH fit for the small p_T^2 range: $0.01\,(\mathrm{GeV}/c)^2 < p_T^2 < 0.05\,(\mathrm{GeV}/c)^2$. No corrections are applied on the asymmetries for this contribution which is justified by the observation that, in the small p_T^2 range, the asymmetries are either compatible with zero or at least consistent within statistical uncertainty with the asymmetry values for events from the small-p_T^2 range of the standard ρ^0 sample.

Diffractive dissociation of the target nucleon into several particles is another type of background. The contribution from low-mass diffractive dissociation of the nucleon is found to be $\approx 14\,\%$ of the incoherent exclusive ρ^0 signal. Supported by HERA results on ρ^0 production where, for unpolarised protons the angular distributions of proton-dissociative events are found consistent with those of exclusive events [155, 156, 72], this contribution to the background is not removed.

The measurements are performed with a NH_3 and a ^{6}LiD solid state target. Along with the scattering centers, which are protons in NH_3 and deuterons in ^{6}LiD, additional nuclei are present. A summary of the target compositions for 2007 and 2010 are given in Tab. 3.1. For the NH_3 target the highest admixture comes from the ^{14}N nuclei. The correction to the proton asymmetry $A_{UT}^{\sin(\phi-\phi_S)}$, due to the polarisation of ^{14}N nuclei in the ammonia target is estimated according to Refs. [157, 158]. It is proportional to the measured asymmetry for the deuteron and approximately given by:

$$\Delta A_{UT,p}^{\sin(\phi-\phi_S)} = \frac{1}{3}\cdot(-\frac{1}{3})\cdot\frac{1}{6}\cdot\frac{\sigma_d}{\sigma_p}\cdot A_{UT,d}^{\sin(\phi-\phi_S)}\,. \tag{7.16}$$

The factors account for the fraction of polarisable nitrogen nuclei in ammonia, the alignment of proton spin vs. ^{14}N spin, the ratio of ^{14}N to ^{1}H polarisations and the ratio of cross sections, σ_d and σ_p, for exclusive ρ^0 production by scattering muons

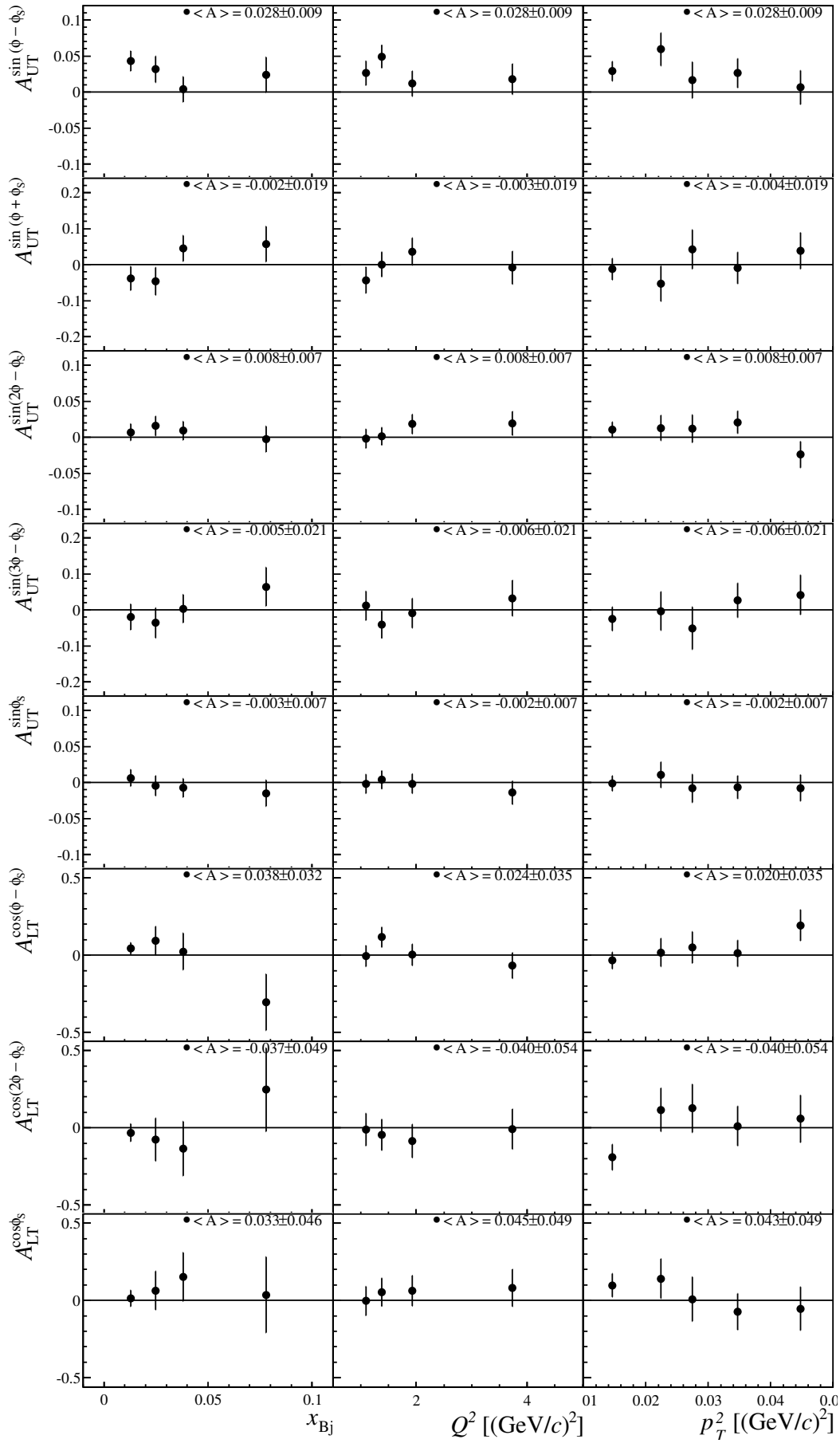

Figure 7.27: Asymmetries extracted with 2DLH in the range $0.01\,(\mathrm{GeV}/c)^2 < p_T^2 < 0.05\,(\mathrm{GeV}/c)^2$.

off unpolarised deuteron and proton targets, respectively. The estimated corrections are very small, typically about 0.1 %, and are neglected.

Radiative corrections are neglected in the present analysis, in particular in the calculation of f. They are expected to be small, mainly because of the exclusivity cuts introduced in Sec. 4.3.4.2 that largely suppress the external photon radiation [159].

7.5.6 Summary of Systematics

A summary for the systematic uncertainties for all modulations is given in Tab. 7.8. For the systematic uncertainties from false asymmetries evaluated over $A_{(r_{14}-r_{23})}$ and $A_{(r_{14}+r_{23})}$, the larger contribution is considered. To account for the systematic uncertainties caused by the background subtraction method and the correction with the appropriate D_{NN} factors, we take the values summarized in Tab. 7.7 into account. For the systematic uncertainties related to the chosen estimator the bias and the RMS of the pull distribution between UB and 2DLH summarized in Tab. 7.4 are used. Additionally, we take the uncertainty of the target dilution factor (2%), the target polarisation (3%) and the beam polarisation (5%) into account. Combined in quadrature, this gives a global systematic normalisation uncertainty of $\sigma^{norm} = 3.6\%$ for the single-spin asymmetries A^m_{UT} and $\sigma^{norm} = 6.2\%$ for the double-spin asymmetries A^m_{LT}. The systematic uncertainty of the asymmetry A^m_i in bin i is calculated as the quadratic sum of all components:

$$\sigma_i^{sys,total} = \sqrt{(\sigma^{sys} \cdot \sigma_i^{stat})^2 + (\sigma^{norm} \cdot |A_i^m|)^2}. \tag{7.17}$$

Table 7.8: Summary of the systematic uncertainties for the results. The values in parentheses are evaluated for data with $-10\,\mathrm{GeV} < E_{\mathrm{miss}} < 20\,\mathrm{GeV}$.

Asymmetry	estimator	false asymmetries	compatibility of mean values	sum
$A_{\mathrm{UT}}^{\sin(\phi-\phi_S)}$	0.14	0.40 (0.17)	0.10	0.44 (0.24)
$A_{\mathrm{UT}}^{\sin(\phi+\phi_S)}$	0.16	0.40 (0.16)	0.18	0.47 (0.29)
$A_{\mathrm{UT}}^{\sin(2\phi-\phi_S)}$	0.26	0.35 (0.10)	0.19	0.48 (0.34)
$A_{\mathrm{UT}}^{\sin(3\phi-\phi_S)}$	0.26	0.17 (0.11)	0.13	0.34 (0.31)
$A_{\mathrm{UT}}^{\sin(\phi_S)}$	0.11	0.76 (0.36)	0.06	0.77 (0.38)
$A_{\mathrm{LT}}^{\cos(\phi-\phi_S)}$	0.11	0.52 (0.23)	0.48	0.72 (0.54)
$A_{\mathrm{LT}}^{\cos(2\phi-\phi_S)}$	0.22	0.54 (0.22)	0.26	0.64 (0.41)
$A_{\mathrm{LT}}^{\cos(\phi_S)}$	0.10	0.50 (0.45)	0.35	0.62 (0.58)

7.6 Comparison of $A_{\mathrm{UT}}^{\sin(\phi-\phi_S)}$ Extracted with 1D and 2D Methods

During the PhD phase two papers have been published containing the asymmetry $A_{\mathrm{UT}}^{\sin(\phi-\phi_S)}$ for exclusive ρ^0 production in high energy muon scattering off transversely polarised protons for the combined 2007 and 2010 COMPASS data [146, 160]. In Fig. 7.28 the two results of $A_{\mathrm{UT}}^{\sin(\phi-\phi_S)}$ are compared with each other. The differences in the extracted values can be explained by changes in the analysis technique. In detail, the estimator used for the extraction and the background subtraction method are changed. In Ref. [146] the analysis is performed with a one-dimensional maximum likelihood fit with 12 bins in $\phi - \phi_S$. In Ref. [146, 160], the asymmetry is extracted with a two-dimensional maximum likelihood fit with 12 bins in ϕ and ϕ_S each. Additionally, now all eight modulations are extracted at once.

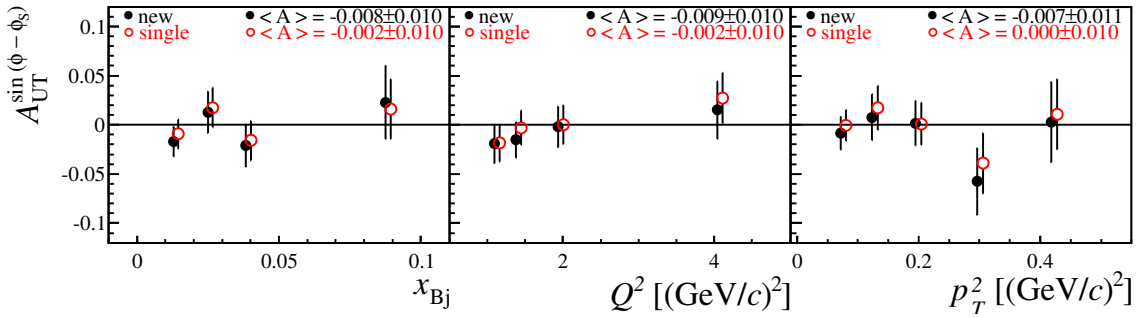

Figure 7.28: Comparison of $A_{\mathrm{UT}}^{\sin(\phi-\phi_S)}$ extracted with one-dimensional (red open circle) and two-dimensional (black full circle) methods. Mean values $\langle A \rangle$ and their statistical errors are given.

In Fig. 7.29 the raw results obtained from three different scenarios are shown: i.) A two-dimensional maximum likelihood fit with 12 bins in ϕ and ϕ_S, where all eight modulations are extracted at once. This is the default method for the new analysis (black full circle); ii.) A single two-dimensional likelihood fit with 12 bins in ϕ and ϕ_S, for every asymmetry (red open circle); iii.) A one-dimensional maximum likelihood fit with 12 bins in Θ (blue diamonds). This is the standard method used in Ref. [146].

The single extraction of the $A_{\mathrm{UT}}^{\sin(\phi-\phi_S)}$ asymmetry with a two-dimensional likelihood fit indicates systematically higher values compared to the ones obtained for the complete extraction. This observation is not confirmed for the other seven asymmetries. The asymmetry values obtained with the different background subtraction methods are compared in Fig. 7.17 for all modulations and agree well with each other. In particular, the differences between both analyses come from the change of the estimator, and the studies related to the dependence on the used estimator can be found in Sec. 7.5.2.

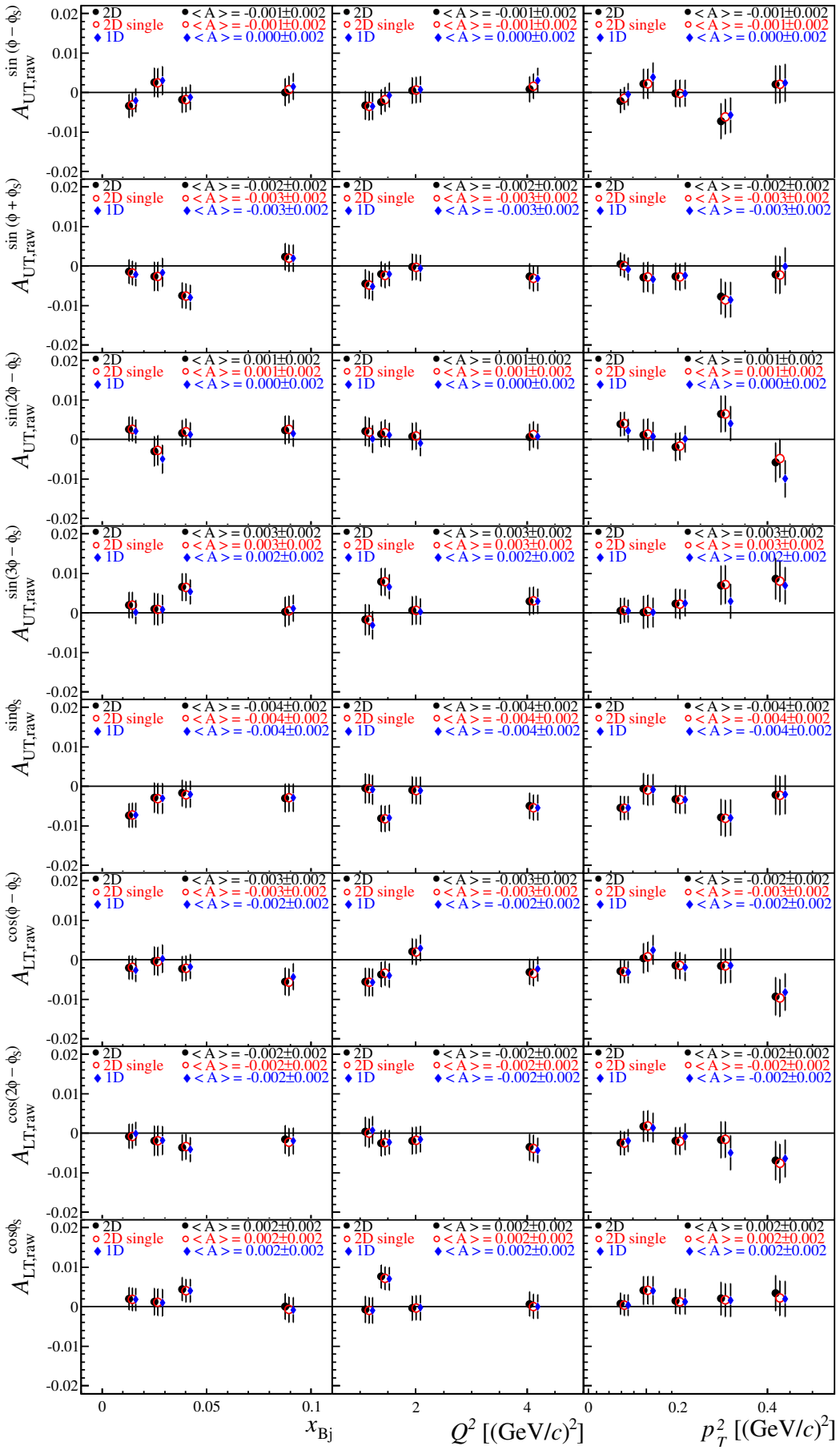

Figure 7.29: Results for background uncorrected raw asymmetries are shown. Explanation of the different results are given in the text.

However, as described in Sec. 7.3, the semi-inclusive background is corrected on the level of the ϕ, ϕ_S distributions. Consequently, this results in different statistical fluctuations after the semi-inclusive background correction and therefore also in different asymmetry terms, even though the data is fully correlated before the background subtraction. An additional uncertainty is introduced due to the semi-inclusive background correction. Thus, comparing both results, for some bins the differences may be larger than the systematic uncertainty of the applied estimator.

8. Asymmetries for the ^{6}LiD Target

This section is dedicated to the extraction of the leading-twist asymmetry $A_{\mathrm{UT}}^{\sin(\phi-\phi_S)}$ from the measurement with a ^{6}LiD target.

8.1 The Leading-twist Asymmetry $A_{\mathbf{UT}}^{\sin(\phi-\phi_S)}$

Due to the limited statistics of the deuteron data and the choice of a binned fit method, only an extraction of the leading-twist asymmetry $A_{\mathrm{UT}}^{\sin(\phi-\phi_S)}$ is performed.

8.1.1 Asymmetry before Background Correction

8.1.1.1 Comparison of Extraction Methods

The physical asymmetry before the background correction is presented in Fig. 8.1. The asymmetry values are obtained using three different extraction methods: the one-dimensional double ratio, the one-dimensional likelihood fit and the unbinned fit. The different methods are introduced in Sec. 6.2. A point-by-point comparison of the different values results in a reasonable agreement inside the statistical uncertainty of the measurements. The results from the one-dimensional methods 1DDR and 1DLH are presented with red open circles and black full circles, respectively. The result of the unbinned method is shown with blue full diamonds.

The standard method used in this analysis is the one-dimensional likelihood method (1DLH). If the asymmetry values are extracted with the one-dimensional binned methods, the mean asymmetry values evaluated in bins of x_{Bj} and Q^2 results in a $0.1{\cdot}\sigma^{stat}$ smaller value in terms of the background uncorrected statistical uncertainty, compared to the results obtained with an unbinned fit. If the asymmetry values are extracted with the 1DLH in bins of p_T^2, the mean asymmetry value differ with $0.1{\cdot}\sigma^{stat}$ from the results evaluated with the two other methods. The difference of the results obtained with the one-dimensional likelihood fit and the unbinned fit is taken into account in the systematic uncertainty. This will be discussed in Sec. 8.2.1.

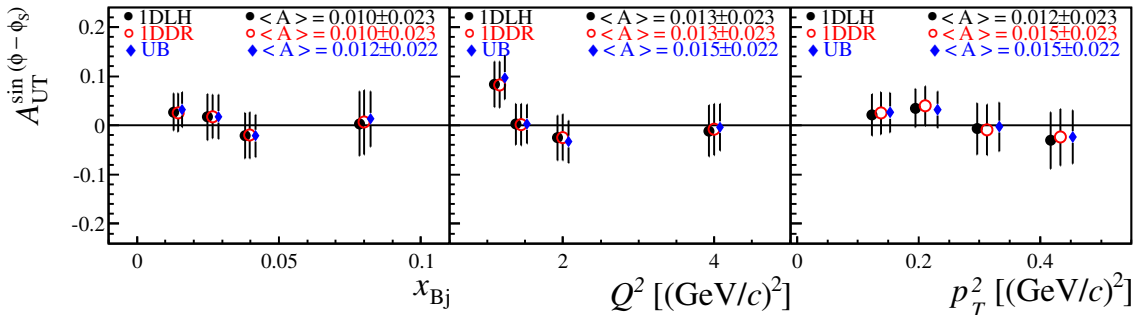

Figure 8.1: Comparison of background uncorrected asymmetry extracted with different methods. The applied methods are listed in Tab. 6.1 and are explained in the text.

8.1.1.2 Period-wise vs. Global Analysis

The data taking is organised in periods. In total, two periods in 2003 and four periods in 2004 are available as shown in Tab. 4.3. Therefore, combining two periods for one asymmetry calculation three independent asymmetries can be extracted for the measurement with a deuterated ^{6}LiD target. The extractions are done with the UB, which allows for lower statistics compared to the extractions with binned methods. The physical asymmetry values for every sub-period are presented in Fig. D.8, whereas the pure fit results, the raw asymmetry values, are shown in Fig. 8.2. They are compatible with each other inside the statistical uncertainty of the measurement. As the stability of the spectrometer do not depend on the exclusive cuts, the compatibility of the three different asymmetry values for $A_{\mathrm{UT}}^{\sin(\phi-\phi_S)}$ is checked for an enlarged event sample with $-10\,\mathrm{GeV} < E_{\mathrm{miss}} < 20\,\mathrm{GeV}$. This range contains 3.3 times more events, thereby increases the statistical precision of the performed test almost by a factor of two. The result is presented in Fig. 8.3.

The differences between the asymmetry values of each period A_i, and the mean asymmetry $\langle A \rangle$ of the entire data taking are expressed in a pull distribution, where each pull value is evaluated according to Eq. 7.4. It contains 36 asymmetry values A_i from 12 kinematic bins (four for every kinematic variable) and three periods. The results are shown in Fig. 8.4, for the exclusive range (left-hand side) and the enlarged missing energy range (right-hand side). Inside the statistical fluctuations the RMS value of both distributions is compatible with 1 and the mean is zero. Therefore, it is not considered in the evaluation of the systematic uncertainty in Sec. 8.2.1.

8.1.1.3 Influence of Additional Asymmetries

The transverse part of the cross section in Eq. 2.42 can be expressed as a sum of eight independent transverse spin dependent modulations of ϕ and/or ϕ_S defined in Eq. 2.46. From a theoretical point of view, all summands in Eq. 6.3 are orthogonal to each other. However, the non-uniform acceptance of the COMPASS detector might lead to a change of the result. Therefore, the unbinned fit has been performed adding the additional seven asymmetries. The result is shown in Fig. 8.5. The pull distribution between the asymmetry values from both kind of extractions are presented in Fig. 8.6 . Here only the pure fit results, i.e. the raw asymmetries are

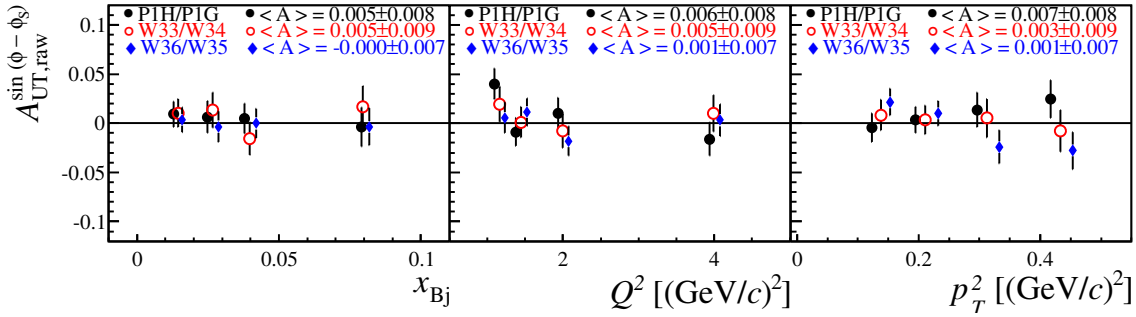

Figure 8.2: Comparison of raw asymmetries extracted in every period in 2003 and 2004. The asymmetry values are extracted for data with $\mathbf{-2.5\,GeV < E_{miss} < 2.5\,GeV}$.

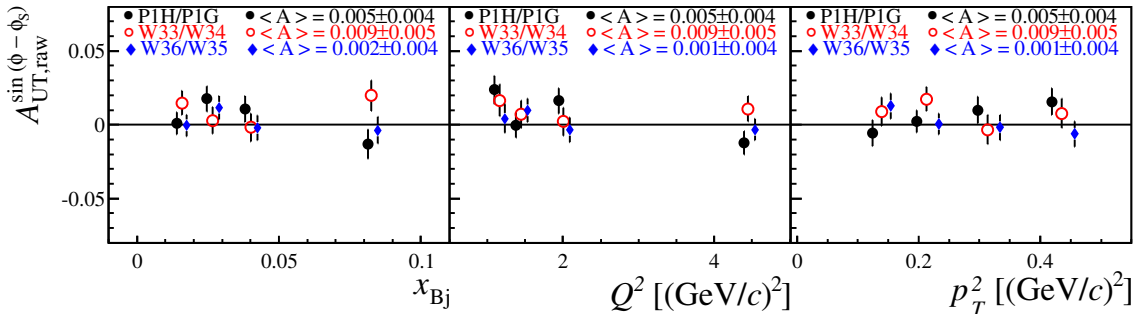

Figure 8.3: Comparison of raw asymmetries extracted in every period in 2003 and 2004. The asymmetry values are extracted for data with $\mathbf{-10\,GeV < E_{miss} < 20\,GeV}$.

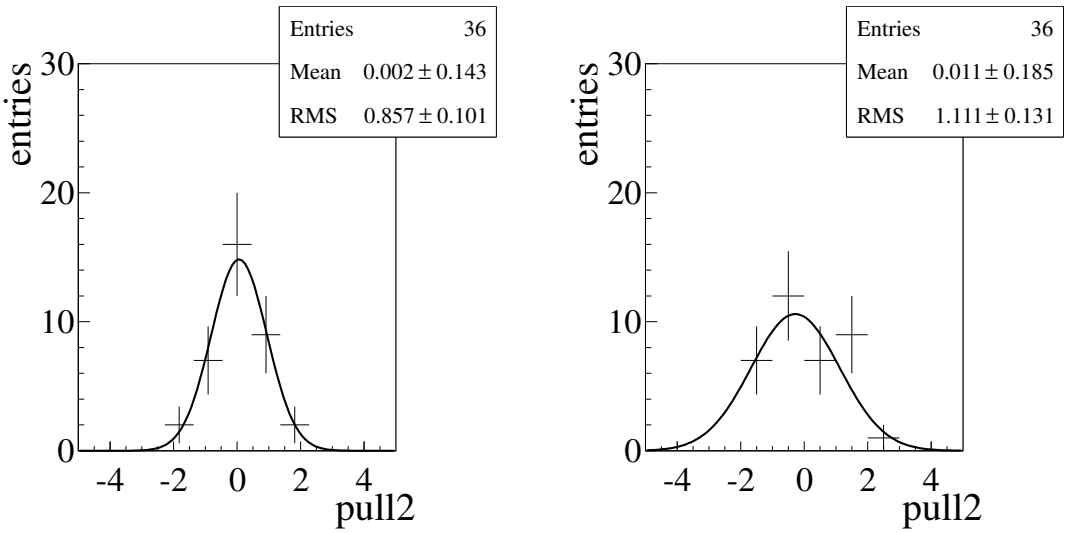

Figure 8.4: Pull distributions demonstrating the compatibility of the results from different periods. The asymmetry values are extracted for data with $\mathbf{-2.5GeV < E_{miss} < 2.5GeV}$ (left-hand side) and $\mathbf{-10GeV < E_{miss} < 20GeV}$ (right-hand side).

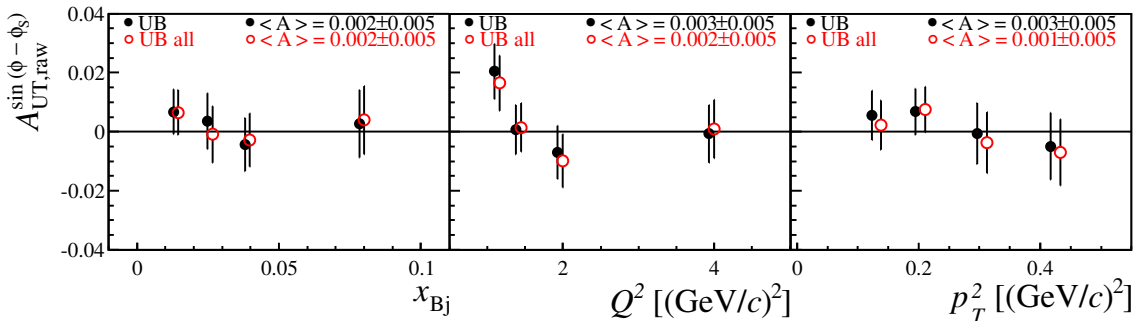

Figure 8.5: Pure fit result for $A_{UT}^{\sin(\phi-\phi_S)}$ fitted alone (black full circle) and together with the other seven asymmetries (red open circle).

studied. The pull distribution has a RMS of 0.24 ± 0.05 and the mean is shifted by $1.8 \cdot \sigma$. The interplay between the asymmetries is taken into account if two-dimensional or unbinned methods are used.

A fit of all eight modulations at once using a 2DLH, as it was done for the proton asymmetries in Sec. 7, is possible if the number of ϕ and ϕ_S bins is reduced to eight and no binning in the kinematic variables is performed. Than no empty bins are observed and the fit is stable. The result of this study is presented in Fig. 8.7. All eight asymmetries are small.

8.1.2 Background Asymmetry

Before the background correction of the exclusive asymmetry has been performed, the asymmetry extracted for the non-exclusive sub-sample of the measured data was studied. Additionally the E_{miss} dependence of the asymmetry for the exclusive data sample as well as the non-exclusive data sample was studied. All asymmetries are small in the entire studied ranges. The $\phi - \phi_S$ distributions are corrected for the remaining semi-inclusive background events in the final sample. The procedure is introduced in Sec. 5.2.1. Both approaches are implemented. The background corrected asymmetry $A_{UT}^{\sin(\phi-\phi_S)}$ evaluated with the "bin" method (black full circle) and the "int" method (red open circle), is shown in Fig. 8.8. In most of the data points the asymmetries are identical. For the "int" method a marginal higher statistical uncertainty is observed. The same observation has also been made for the proton asymmetries in Sec. 7.3. The final results are evaluated using the "bin" method.

8.2 Systematic Studies

In this section the evaluation of systematic uncertainty for the asymmetries measured with a deuterated ^{6}LiD target is presented. Unless otherwise noted identical checks are applied as for the NH_3, hence, the explanation of the studies can be found in Sec. 7.5 and are not repeated here.

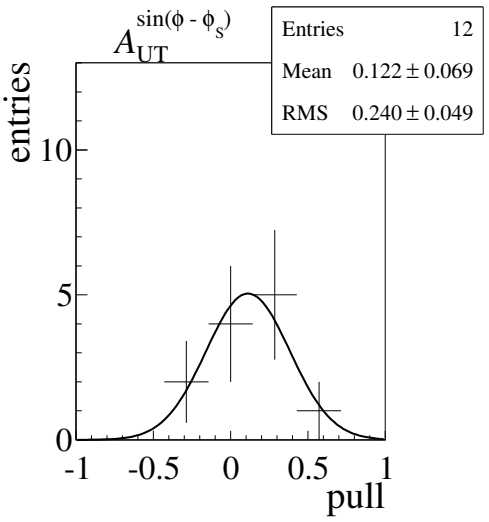

Figure 8.6: Pull between results obtained by fitting only $A_{\mathrm{UT}}^{\sin(\phi-\phi_S)}$ and all eight asymmetries, as explained therein.

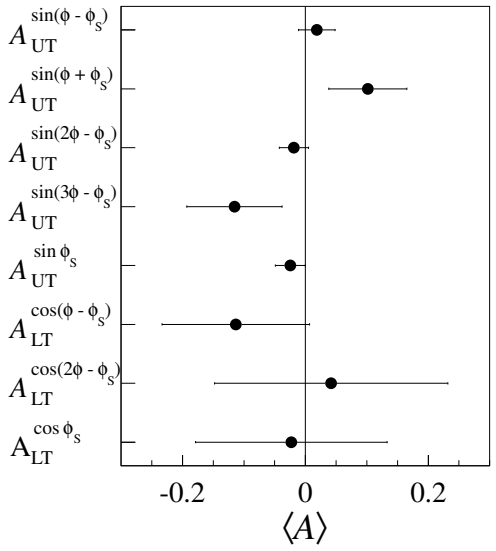

Figure 8.7: Asymmetry and the statistical error for every modulation.

8.2.1 Comparison of Different Estimators

First the systematic uncertainty of the used estimator is investigated. This is done by comparing the results of UB and 1DLH, which are presented in Fig. 8.1. The estimation is performed on the level of asymmetries extracted from background non-corrected data. The RMS value and half of the shifted mean of the pull distribution in Fig. 8.9 correctly expressed in terms of the statistical errors of the background corrected asymmetry are taken into account in the systematic uncertainty.

8.2.2 Stability of Data Taking

The stability of the asymmetries depending on the periods of data taking during the run is checked by studying false asymmetries. Again this is done using raw asymmetries before background correction. The extraction of asymmetries is done using an unbinned fit.

For the two-cell target false asymmetries are build by dividing the U and the D cell in Fig. 6.1 in two equally large parts. The sub-cells of U (D) are named N_1 and N_4 (N_2 and N_3), in the direction of the muon beam. The systematic uncertainty is evaluated according to Sec. 7.5.3.1. The event number ratios are build in the same way as presented in Eq. 7.12. Out of these ratios the two false and two true asymmetries of Eq. 7.14 are constructed. The true asymmetry A_{r12} (A_{r34}) is build using the upper half (lower half) of U and D cell in the direction of the muon beam. They are presented in Fig. D.9 whereas the false asymmetries A_{r14} and A_{r23} are shown in Fig. D.10. The false asymmetries are highly fluctuating around zero. This is reflected in poor probabilities of the χ^2 test with respect to zero for the combination

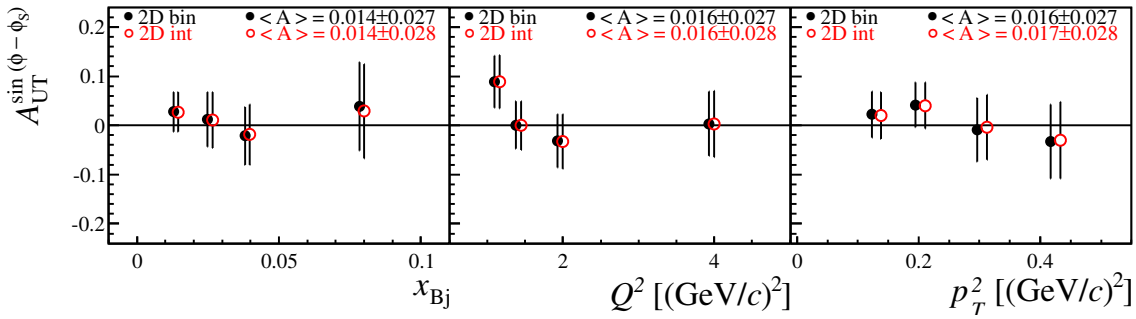

Figure 8.8: Background corrected asymmetry. The applied methods are listed in Tab. 7.2 and are explained Sec. 5.2.1.

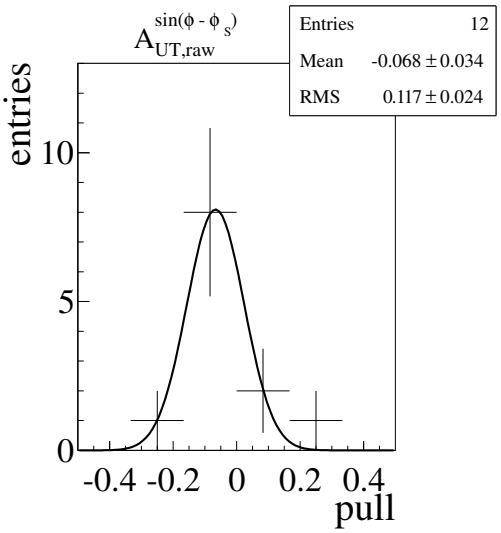

Figure 8.9: Pull distribution demonstrating the compatibility of the results extracted with the methods UB and 2DLH.

$A_{(r14-r23)}$ and $A_{(r12-r34)}$ shown in Fig. D.11. The systematic uncertainty evaluated from the results of $A_{(r14-r23)}$ ($A_{(r12-r34)}$) is quantified to $0.67 \cdot \sigma^{stat}$ ($0.68 \cdot \sigma^{stat}$) in terms of the final statistical error of the background corrected asymmetry. The quantity $\left|A^{i'}_{(r_{14}+r_{23})}\right|$ is smaller then 0.68 and σ^{sys} is set to zero.

To reduce the influence of statistical fluctuations this study is performed additionally in the extended E_{miss} range. The true asymmetries as a function of x_{Bj}, Q^2 and p_T^2 are shown in Fig. 8.10. The false asymmetries are presented in Fig. 8.11. The results for $A_{(r14-r23)}$, $A_{(r14+r23)}$ and $A_{(r12-r34)}$ are shown in Fig. D.12. The results for $A_{(r14+r23)}$ are well compatible with zero. The evaluated systematic uncertainty is $0.09 \cdot \sigma^{stat}$ in terms of the final statistical error of the background corrected asymmetry. The systematic uncertainty evaluated from $A_{(r14+r23)}$ and $A_{(r12-r34)}$ is quantified to $0.56 \cdot \sigma^{stat}$ in terms of the final statistical error of the background corrected asymmetry.

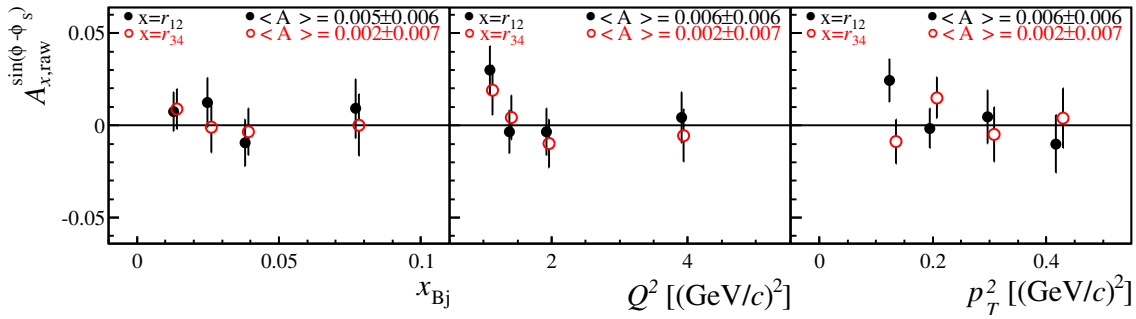

Figure 8.10: $\boldsymbol{A_{r12,\mathrm{raw}}}$ (black full circle), $\boldsymbol{A_{r34,\mathrm{raw}}}$ (red open circle). Mean values $\langle A_{x,\mathrm{raw}} \rangle$ are given. The values are extracted for data with $\boldsymbol{-10.0\,\mathrm{GeV} < E_{\mathrm{miss}} < 20.0\,\mathrm{GeV}}$.

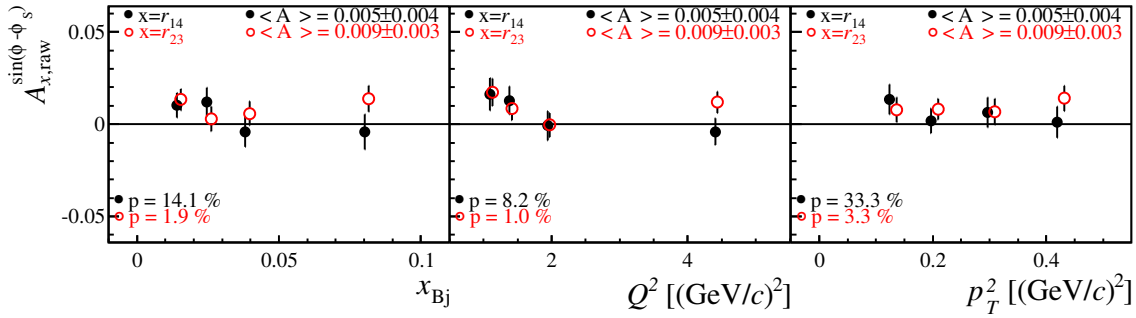

Figure 8.11: $\boldsymbol{A_{r14,\mathrm{raw}}}$ (black full circle), $\boldsymbol{A_{r23,\mathrm{raw}}}$ (red open circle). Mean values $\langle A_{x,\mathrm{raw}} \rangle$ are given. The values are extracted for data with $\boldsymbol{-10.\,\mathrm{GeV} < E_{\mathrm{miss}} < 20.\,\mathrm{GeV}}$.

8.2.3 Stability of Background Subtraction Method

The parametrisation of the shape of the E_{miss} distribution for semi-inclusive background events is done with a weighted LEPTO Monte-Carlo sample, as explained in Sec. 5.1. To test the sensitivity of the asymmetry values on the background parametrisation the values are extracted using the number of background events received from the parametrisation of the non-weighted LEPTO Monte-Carlo. For all bins the amount of semi-inclusive events evaluated with the non-weighted Monte-Carlo is higher compared to the evaluation using a weighted Monte-Carlo. An increase of up to 7% of semi-inclusive events is observed.

The comparison of the extracted asymmetries using the background shapes obtained from weighted LEPTO and non-weighted LEPTO as a function of x_{Bj} , Q^2 and p_T^2 is shown in Fig. 8.12. The higher statistical uncertainty for the latter can be traced back to the higher amount of semi-inclusive events. In most of the data points the asymmetry values are the same. The difference between the mean value of x_{Bj} and Q^2 is not taken into account since it is also present before the background correction (see Fig. 8.1). On the level of mean asymmetries a deviation of $0.04 \cdot \sigma^{stat}$ between the two results can be observed. The same is true if the mean asymmetry evaluated with the two background subtraction methods as a function of p_T^2 is compared (Fig. 8.8).

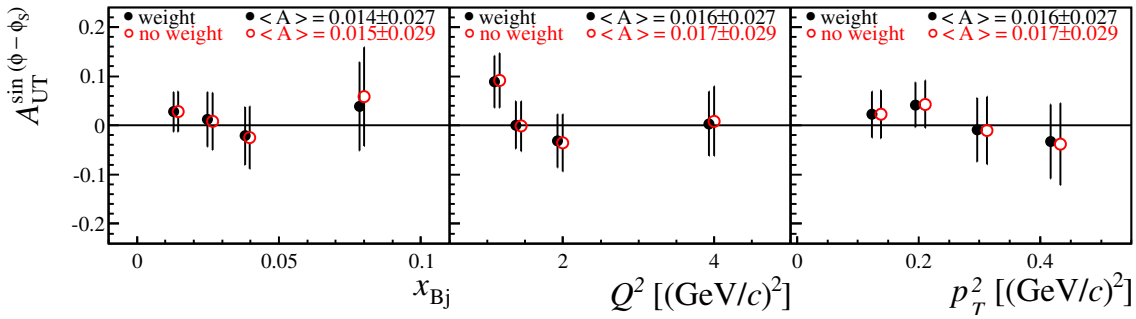

Figure 8.12: Background corrected asymmetry. The background parametrisation is done using the weighted (black full circle) and the non-weighted (red open circle) LEPTO Monte-Carlo sample.

8.2.4 Summary of Systematics

The summary of the systematic uncertainties is given in Tab. 8.1. Three contributions are taken into account: (1) estimator, (2) false asymmetries, and (3) background subtraction method. For the systematic uncertainties related to the chosen estimator, (1), the RMS value and half of the shifted mean of the pull distribution between UB and 2DLH are used. For the systematic uncertainties from false asymmetries, (2), evaluated over $A_{(r_{14}-r_{23})}$ and $A_{(r_{14}+r_{23})}$, the larger contribution is considered[1]. Additionally we take into account the uncertainty of the target dilution factor (2%) and the target polarisation (5%). Combined in quadrature this gives a global systematic multiplicative uncertainty of 5.4%. The total systematic uncertainty of the asymmetry $A_{\mathrm{UT}}^{\sin(\phi-\phi_S)}$ is evaluated in every bin according to Eq. 7.17.

Table 8.1: Summary of the systematic uncertainties for the results. The value in parentheses is evaluated for data with $-10\,\mathrm{GeV} < E_{\mathrm{miss}} < 20\,\mathrm{GeV}$.

Asymmetry	(1)	(2)	(3)	sum
$A_{\mathrm{UT}}^{\sin(\phi-\phi_S)}$	0.10	0.68 (0.56)	0.04	0.69 (0.57)

[1]The procedure to evaluate the systematic uncertainty was updated in Sec. 7.5 compared to the one used in Ref. [146]. Here the updated procedure is used.

9. Asymmetry Results

9.1 Transverse Target Spin Asymmetries

In this thesis transverse target spin azimuthal asymmetries in hard exclusive production of ρ^0 mesons are analysed. The measurement was performed at COMPASS by scattering 160 GeV/c muons off transversely polarised protons and deuterons.

In total, for the measurement with a transversely polarised NH_3 target, eight asymmetries are extracted. The results for the five single-spin asymmetries and the three double-spin asymmetries as a function of x_{Bj}, Q^2 and p_T^2 are shown in Fig. 9.1 and Fig. 9.2, respectively. Error bars show statistical uncertainties σ^{stat}. The systematic uncertainties σ^{sys} are represented by the grey shaded bands. Additionally the mean asymmetry for every modulation is shown in Fig. 9.3. The values are obtained as the arithmetic mean of the mean values evaluated in bins of x_{Bj}, Q^2 and p_T^2 and the highest statistical uncertainty is taken[1]. The numerical values are given in in the Appendix D.4. Note that for $A_{\mathrm{UT}}^{\sin(\phi-\phi_S)}$ as well as for $A_{\mathrm{UT}}^{\sin(2\phi-\phi_S)}$ and $A_{\mathrm{UT}}^{\sin\phi_S}$ the experimental precision is in the order of ± 0.01. The asymmetries are small in the entire kinematic range, within experimental uncertainties.

For the measurement with the ^{6}LiD target the leading-twist single spin asymmetry $A_{\mathrm{UT}}^{\sin(\phi-\phi_S)}$ is extracted. The results are presented in Fig. 9.4. The asymmetry is small in the entire kinematic range. Results for the proton and the deuteron target are obtained for the first time and are unique up to now.

The results of this thesis have been published. The asymmetry $A_{\mathrm{UT}}^{\sin(\phi-\phi_S)}$ for protons and deuterons can be found in Ref. [146], whereas the five single-spin asymmetries and the three double-spin asymmetries are shown in Ref. [160]. The results have been presented at the QNP2012 conference [162], the DIS2013 conference [163] and the PacSpin Symposium.

[1] Additionally the mean asymmetries were calculated from the complete sample. The results of both extraction methods were found to be compatible within $0.38 \cdot \sigma^{\mathrm{stat}}$ for the asymmetry $A_{\mathrm{UT,p}}^{\cos(\phi-\phi_S)}$ and below $0.15 \cdot \sigma^{\mathrm{stat}}$ for the other asymmetries.

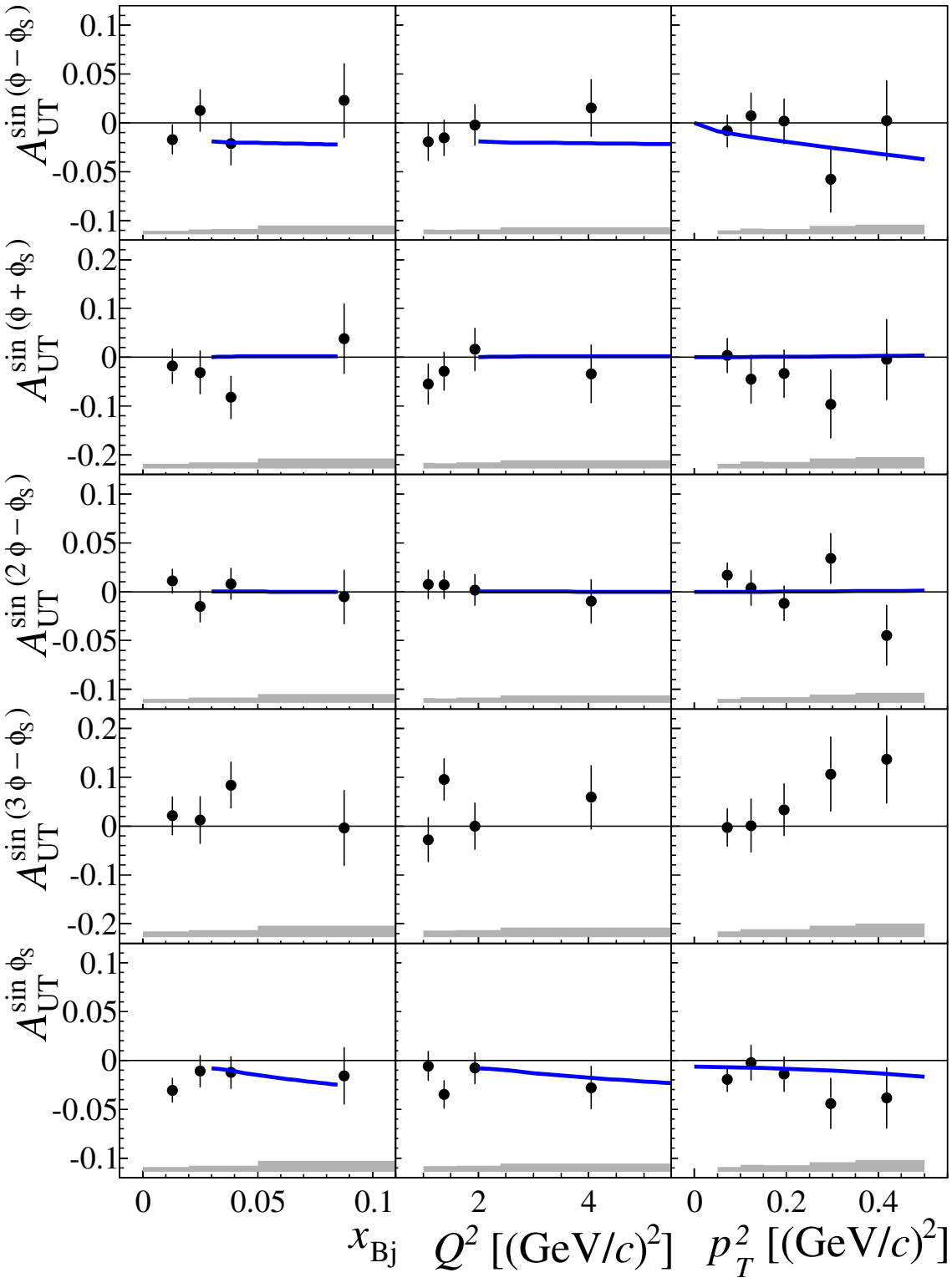

Figure 9.1: Single-spin azimuthal asymmetries for a transversely (T) polarised NH_3 target and unpolarised (U) beam. The error bars (bands) represent the statistical (systematic) uncertainties. The curves show the predictions of the GPD model [161]. They are calculated for the average W, Q^2 and p_T^2 of our data set, $W = 8.1\,\mathrm{GeV}/c^2$ and $p_T^2 = 0.2\,(\mathrm{GeV}/c)^2$ on the left and middle panels, and at $W = 8.1\,\mathrm{GeV}/c^2$ and $Q^2 = 2.2\,(\mathrm{GeV}/c)^2$ on the right. The asymmetry $A_{\mathrm{UT}}^{\sin(3\phi-\phi_S)}$ is assumed to be zero in this model.

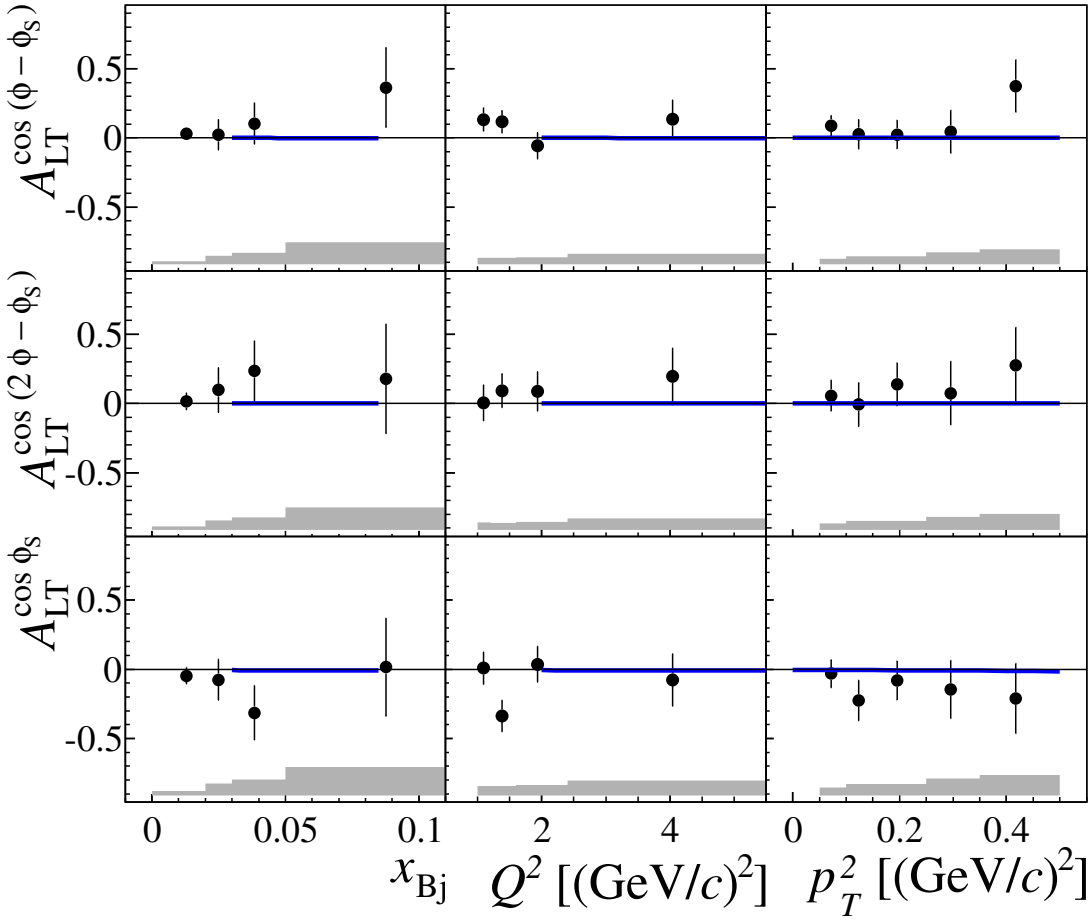

Figure 9.2: Double-spin azimuthal asymmetries for a transversely (T) polarised NH_3 target and a longitudinally (L) polarised beam. The error bars (bands) represent the statistical (systematic) uncertainties. The curves show the predictions of the GPD model [161]. They are calculated for the average W, Q^2 and p_T^2 of our data set, $W = 8.1\,\mathrm{GeV}/c^2$ and $p_T^2 = 0.2\,(\mathrm{GeV}/c)^2$ for the left and middle panels, and at $W = 8.1\,\mathrm{GeV}/c^2$ and $Q^2 = 2.2\,(\mathrm{GeV}/c)^2$ for the right panel.

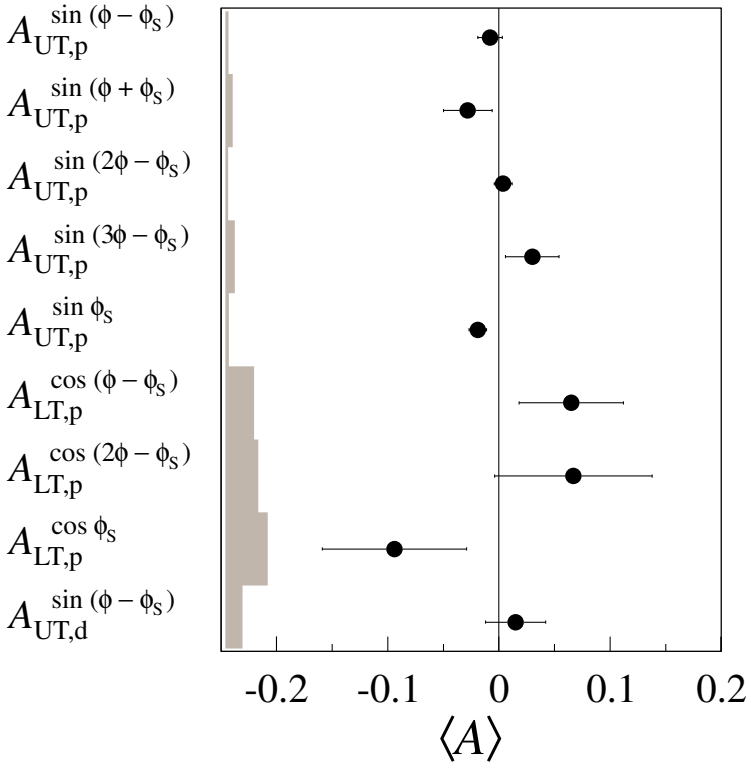

Figure 9.3: Mean value $< A >$ and the statistical error for every modulation. The asymmetries measured with the NH_3 target and the ^{6}LiD target are marked with p and d, respectively. The systematic uncertainty is represented by the band on the left side.

9.2 Comparison with Model Calculations

The calculations are based on the model from Goloskokov and Kroll (GK model). The results for the single spin asymmetries in hard exclusive muoproduction of ρ^0 mesons on transversely polarised protons are given in Fig. 9.1. In Fig 9.2 the corresponding results for the double spin asymmetries are shown. They are presented as blue curves along with the data points. The model calculations include valence quark and sea quark contributions and are done for COMPASS kinematics assuming $W = 8.1\,\mathrm{GeV}/c^2$, $p_T^2 = 0.2\,(\mathrm{GeV}/c)^2$ and $Q^2 = 2.2\,(\mathrm{GeV}/c)^2$. The theoretical calculations and the experimental results are well compatible with each other.

Especially the results involving the transversity GPDs have to be understood as estimates [54]. Hence no uncertainty bands are given in Figs. 9.1 and 9.2. Presently the only available estimates for the transversity GPDs are coming from lattice calculations and the available precision merely allows a rough determination of the transversity GPDs.

The results of the calculations based on the GK model for the single spin asymmetry $A_{\mathrm{UT}}^{\sin(\phi-\phi_S)}$ in hard exclusive muoproduction of ρ^0 mesons on transversely polarised deuterons is shown in Fig. 9.4. This calculation is based on Ref. [113] and do not include the transversity GPDs, but it is observed by the authors that the inclusion of

transversity GPDs have a negligible effect on the asymmetry $A_{\mathrm{UT}}^{\sin(\phi-\phi_S)}$ [161]. Again model calculations and experimental results are well compatible with each other.

Every asymmetry from Eq. 2.46 can be connected to a combination of helicity amplitudes $\mathcal{M}$, defined in Eq. 2.43:

$$\begin{aligned}
A_{\mathrm{UT}}^{\sin(\phi-\phi_S)}\sigma_0 &= -2\mathrm{Im}\Big[\epsilon\mathcal{M}^*_{0-,0+}\mathcal{M}_{0+,0+} + \mathcal{M}^*_{+-,++}\mathcal{M}_{++,++} \\
&\qquad + \frac{1}{2}\mathcal{M}^*_{0-,++}\mathcal{M}_{0+,++}\Big], \\
A_{\mathrm{UT}}^{\sin(\phi+\phi_S)}\sigma_0 &= -\mathrm{Im}\Big[\mathcal{M}^*_{0+,++}\mathcal{M}_{0-,++}\Big], \\
A_{\mathrm{UT}}^{\sin(2\phi-\phi_S)}\sigma_0 &= -\mathrm{Im}\Big[\mathcal{M}^*_{0+,++}\mathcal{M}_{0-,0+}\Big], \\
A_{\mathrm{UT}}^{\sin(3\phi-\phi_S)}\sigma_0 &= 0\ , \\
A_{\mathrm{UT}}^{\sin\phi_S}\sigma_0 &= -\mathrm{Im}\Big[\mathcal{M}^*_{0-,++}\mathcal{M}_{0+,0+} - \mathcal{M}^*_{0+,++}\mathcal{M}_{0-,0+}\Big], \\
A_{\mathrm{LT}}^{\cos(\phi-\phi_S)}\sigma_0 &= \mathrm{Re}\Big[\mathcal{M}^*_{0-,++}\mathcal{M}_{0+,++}\Big], \\
A_{\mathrm{LT}}^{\cos(2\phi-\phi_S)}\sigma_0 &= -\mathrm{Re}\Big[\mathcal{M}^*_{0+,++}\mathcal{M}_{0-0+}\Big], \\
A_{\mathrm{LT}}^{\cos\phi_S}\sigma_0 &= -\mathrm{Re}\Big[\mathcal{M}^*_{0-,++}\mathcal{M}_{0+,0+} - \mathcal{M}^*_{0+,++}\mathcal{M}_{0-,0+}\Big]\,,
\end{aligned} \tag{9.1}$$

According to Tab. 2.4 each of these helicity amplitude can be expressed in terms of a convolution of hard scattering kernels with GPDs, which is labeled by $\mathcal{H}, \mathcal{E}$ ($\mathcal{H}_T, \bar{\mathcal{E}}$):

$$\begin{aligned}
A_{\mathrm{UT}}^{\sin(\phi-\phi_S)} &\propto \mathrm{Im}\,(\mathcal{E}^*\mathcal{H}), \\
A_{\mathrm{UT}}^{\sin(\phi+\phi_S)} &\propto \mathrm{Im}\,(\bar{\mathcal{E}}^*\mathcal{H}_T), \\
A_{\mathrm{UT}}^{\sin(2\phi-\phi_S)} &\propto \mathrm{Im}\,(\bar{\mathcal{E}}^*\mathcal{E}), \\
A_{\mathrm{UT}}^{\sin\phi_S} &\propto \mathrm{Im}\,(\mathcal{H}_T^*\mathcal{H} - \bar{\mathcal{E}}^*\mathcal{E}), \\
A_{\mathrm{LT}}^{\cos(\phi-\phi_S)} &\propto \mathrm{Re}\,(\mathcal{H}_T^*\bar{\mathcal{E}}), \\
A_{\mathrm{LT}}^{\cos(2\phi-\phi_S)} &\propto \mathrm{Re}\,(\bar{\mathcal{E}}^*\mathcal{E}), \\
A_{\mathrm{LT}}^{\cos\phi_S} &\propto \mathrm{Re}\,(\mathcal{H}_T^*\mathcal{H} - \bar{\mathcal{E}}^*\mathcal{E}),
\end{aligned} \tag{9.2}$$

where $\bar{\mathcal{E}}$ is defined in Eq. 2.74. Now we proceed with a discussion of the results. The asymmetry $A_{\mathrm{UT}}^{\sin(\phi-\phi_S)}$ can be connected to a combintion of six helicity amplitudes, where the terms $\epsilon\mathcal{M}^*_{0-,0+}\mathcal{M}_{0+,0+}$ and $\mathcal{M}^*_{+-,++}\mathcal{M}_{++,++}$ represent a combination of $\mathcal{H}$ and $\mathcal{E}$. The inclusion of the transversity GPDs by the third term has a negligible impact on the behaviour of $A_{\mathrm{UT}}^{\sin(\phi-\phi_S)}$. This is confirmed by comparing the calculations of Refs. [113] and [161].

For the measurement with a transversely polarised NH_3 target as well as for the measurement with a transversely polarised ^{6}LiD target small values of the asymmetry $A_{\mathrm{UT}}^{\sin(\phi-\phi_S)}$ are observed in the entire kinematic range. This observation might be explained by an approximate cancellation of two sizable and comparable contributions of opposite signs for the GPDs E^u and E^d, where u and d indicate the active valence quarks.

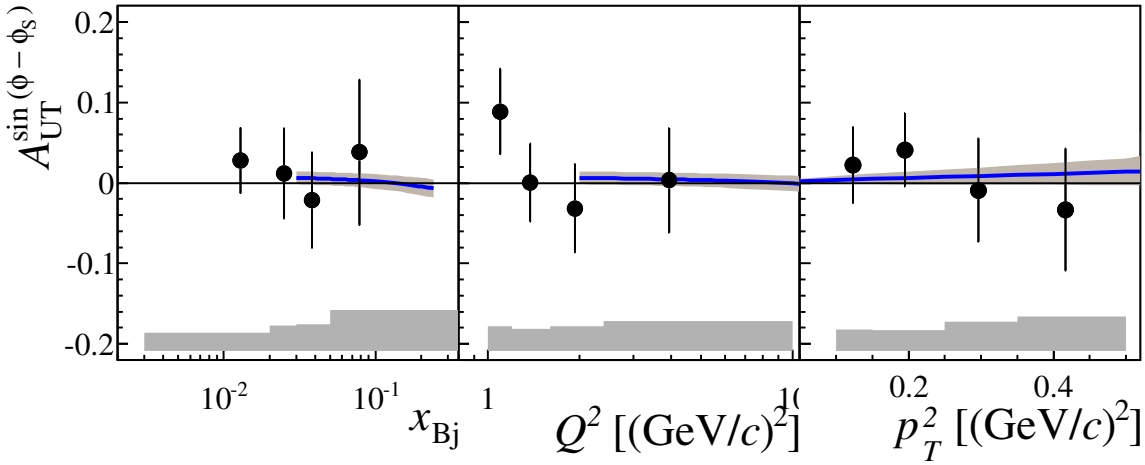

Figure 9.4: Single-spin azimuthal asymmetry $A_{UT}^{\sin(\phi-\phi_S)}$ for a transversely (T) polarised ^{6}LiD target and unpolarised (U) beam as a function of x_{Bj}, Q^2 and p_T^2. Error bars show statistical uncertainties, while the systematic ones are represented by grey bands at the bottom. The curves show the predictions of the GPD model [113, 164] using the set of parameters called 'variant 1'. They are calculated at $W = 8.1\,\mathrm{GeV}/c^2$ and $p_T^2 = 0.2\,(\mathrm{GeV}/c)^2$ for the left and middle panels, and at $W = 8.1\,\mathrm{GeV}/c^2$ and $Q^2 = 2.2\,(\mathrm{GeV}/c)^2$ for the right panels. The theoretical error bands reflect uncertainties of GPD parametrisations.

A small non-vanishing value is measured for the asymmetry $A_{\mathrm{UT}}^{\sin\phi_S}$. This result is in agreement with the model calculations. As shown in Eq. 9.2 the asymmetries $A_{\mathrm{UT}}^{\sin\phi_S}$ and $A_{\mathrm{LT}}^{\cos\phi_S}$ are connected to imaginary and real parts of the same combination: $\mathcal{H}_T^*\mathcal{H} - \bar{\mathcal{E}}^*\mathcal{E}$. In the GK model it is observed that both asymmetries have the same sign and are similar in size [54]. However, presently the experimental precision of the measurement of $A_{\mathrm{LT}}^{\cos\phi_S}$ is not sufficient to draw any conclusions. But a vanishing value is measured for $A_{\mathrm{UT}}^{\sin(2\phi-\phi_S)}$. This asymmetry is represented by the same combination $\bar{\mathcal{E}}_T^*\mathcal{E}$ as the second term in $A_{\mathrm{UT}}^{\sin\phi_S}$. The small negative value of $A_{\mathrm{UT}}^{\sin\phi_S}$ is caused by the first term $\mathcal{H}_T^*\mathcal{H}$ and a substantial contribution might come from $\mathcal{H}_\mathcal{T}$. Therefore, the results may imply the first experimental evidence for the existence of the transverse GPDs H_T in hard exclusive ρ^0 leptoproduction.

10. Conclusion & Outlook

This thesis is dedicated to the analysis of the transverse target spin azimuthal asymmetries in hard exclusive production of ρ^0 mesons. The measurement was performed at the COMPASS experiment at CERN by scattering 160 GeV/c muons off transversely polarised protons and deuterons. For these measurements in the years 2002-2004 data was collected with a ^{6}LiD target, in the years 2007 and 2010 a NH_3 target was used. In this thesis, results for five single-spin and three double-spin azimuthal asymmetries are obtained for protons. Furthermore, the asymmetry $A_{\mathrm{UT}}^{\sin(\phi-\phi_S)}$ is determined for deuterons.

This thesis is the first complete analysis of exclusive ρ^0 mesons of all available data taken with a transversely polarised target at COMPASS. In total, after all selection cuts, 797134 ρ^0 candidates are detected with the NH_3 target and 96646 ρ^0 candidates are measured with the ^{6}LiD target. Of special importance is the understanding of the non-exclusive background, which was studied extensively. The main focus is on the analysis of the dominant semi-inclusive fraction of the background. For this purpose, semi-inclusive Monte-Carlo samples and like-sign data samples are studied. It is found that neither the like-sign data nor the Monte-Carlo events can be used to parametrise the semi-inclusive background directly. To overcome this shortfall the Monte-Carlo sample is weighted, whereby the weights are calculated by comparing the like-sign events from Monte-Carlo and measured data. The number of semi-inclusive events is estimated via a parametrisation of the shape of the missing energy distribution of the weighted Monte-Carlo sample. For the final asymmetries, the subtraction of the semi-inclusive background is done on the level of the azimuthal distributions and the asymmetries are extracted starting from these corrected distributions.

The analysis of asymmetries is performed by combining the data taken in the years 2007&2010 and 2003&2004, respectively. The advantage is that the asymmetry extraction is less sensitive to statistical fluctuations, despite the limited statistics of the measurement. The combined analysis is possible because all important kinematic variables measured in the different periods and years show reasonable agreement between each other. Furthermore, the asymmetries extracted for the different periods and years of data taking are compared with each other and it is checked that no

systematic uncertainties are obtained due to the combined analysis of two different years. Moreover, the false asymmetries are well under control.

Different extraction methods are applied to the data, in particular a one-dimensional double ratio, a one-dimensional likelihood fit, a two-dimensional likelihood fit and an unbinnend likelihood fit. The fit results from these methods are compared and found to be compatible within statistical uncertainties. The applied background estimation method requires a binned extraction method, and it is only the two-dimensional binned method which allows the simultaneous extraction of the eight asymmetries. Hence, this method is chosen to be the default one. The other three methods are used for internal cross checks and to pursue the systematic studies. Three different background correction methods are implemented. The comparison of the results shows a reasonable agreement within the statistical uncertainty of the measurement.

The main asymmetry results are extracted as a function of x_{Bj}, Q^2 and p_T^2 in the range:

$$\begin{gathered} 1.0\,(\mathrm{GeV}/c)^2 < Q^2 < 10.0\,(\mathrm{GeV}/c)^2, \\ 0.003 < x_{Bj} < 0.035 \\ 0.05\,(\mathrm{GeV}/c)^2 < p_T^2 < 0.5\,(\mathrm{GeV}/c)^2 \text{ (protons)}, \\ 0.1\,(\mathrm{GeV}/c)^2 < p_T^2 < 0.5\,(\mathrm{GeV}/c)^2 \text{ (deuterons)}. \end{gathered}$$

Using a NH_3 target the asymmetry $A_{\mathrm{UT}}^{\sin(\phi-\phi_S)}$, as well as $A_{\mathrm{UT}}^{\sin(2\phi-\phi_S)}$ and $A_{\mathrm{UT}}^{\sin\phi_S}$, are measured within the statistical precision of ± 0.01. For all other asymmetries the statistical uncertainties are bigger. Most of the asymmetries are found to be small and compatible with zero in the entire kinematic range. The $\sin\phi_S$ asymmetry is found to be:

$$A_{\mathrm{UT}}^{\sin\phi_S} = -0.019 \pm 0.008(stat.) \pm 0.003(syst.).$$

The extracted asymmetries can be used to constrain GPDs. The results are compared to recent model calculations which are done for COMPASS kinematics. The model calculations agree well with the present results for both proton and deuteron data. The results determined on the proton data are interpreted as evidence for the importance of transverse generalized parton distributions. The small value of the asymmetry $A_{\mathrm{UT}}^{\sin(\phi-\phi_S)}$ for both protons and deuterons can be interpreted by an approximate cancellation of the contributions from the GPDs E^u and E^d.

Next steps in the analysis of exclusive ρ^0 production might be a full acceptance correction and the separation of longitudinally and transversely polarised photons. Varying the photon or meson in the final state will give access to different spin-flavor combinations of GPDs, even with unpolarised beams and targets. At the moment the analysis is limited by the available statistics. The present fixed target experiments do not allow for a sufficient increase of statistics. This might be gained via polarised Collider experiments in the future.

At JLAB [165], RHIC [166] and CERN [83] future programs exist, where HEMP as well as DVCS measurements are planned to be executed. The COMPASS-II program which has already started, is dedicated to the measurement of DVCS. Proposals and ideas also exist for studies using a polarised ep Collider (EIC) [167, 168] in connection with RHIC [169] or JLAB [170], and a high luminosity polarised proton-antiproton Collider at GSI [171]. Additionally, the design and physics program of a future Large Hadron electron Collider (LHeC) is discussed recently [172, 173]. The different experimental programs cover various kinematic ranges. Therefore, future experiments may provide high luminosity measurements over a wide range of kinematics in Q^2, x_{Bj} and t. The enhanced luminosity will allow for the extraction of multi-dimensional maps of the distributions of partons in space and momentum. The enlargement in the kinematic range will also enhance the sensitivity to the gluon distributions. Hence, it will provide a significant contribution towards a complete understanding of the spin structure of the nucleon.

A. Light-Cone-Coordinates

If hadrons and partons move fast in $z-$direction it is natural to introduce light-cone coordinates. A four-momentum-vector $v^\mu = (v^0, v^1, v^2, v^3)$ is given by:

$$v^\mu = v^+ n_+^\mu + v^- n_-^\mu + v_T^\mu, \tag{A.1}$$

where the two light-like four-momentum-vectors n_+ and n_- are:

$$n_+ = \frac{1}{\sqrt{2}}(1,0,0,1) \qquad n_- = \frac{1}{\sqrt{2}}(1,0,0,-1), \tag{A.2}$$

and:

$$\begin{aligned} v^+ = v \cdot n_- = \frac{1}{\sqrt{2}}(v^0 + v^3), \qquad v^- = v \cdot n_+ = \frac{1}{\sqrt{2}} = (v^0 - v^3), \\ \mathbf{v} = (v^1, v^2), \qquad v_T = (0, \mathbf{v}, 0). \end{aligned} \tag{A.3}$$

The invariant product of two four-momentum-vectors is given by:

$$vw = v^+ w^- + v^- w^+ - \vec{v}\vec{w}. \tag{A.4}$$

The light-cone coordinates are defined such that a particle with large momentum in $+v^3$ direction has large n_+ and small n_-.

Dirac matrices

The Dirac gamma matrices are defined as:

$$\gamma^\mu = \begin{pmatrix} 0 & \sigma^\mu \\ -\sigma^\mu & 0 \end{pmatrix} \qquad \gamma^5 = \begin{pmatrix} -1 & 0 \\ 0 & 1 \end{pmatrix} \qquad \mu \in \{1,2,3\} \tag{A.5}$$

with

$$\sigma^1 = \begin{pmatrix} 0 & 1 \\ 1 & 0 \end{pmatrix} \qquad \sigma^2 = \begin{pmatrix} 0 & -i \\ i & 0 \end{pmatrix} \qquad \sigma^3 = \begin{pmatrix} 1 & 0 \\ 0 & -1 \end{pmatrix} \tag{A.6}$$

Additionally it is:

$$\sigma^{\mu\nu} = \frac{i}{2}\left[\gamma^\mu, \gamma^\nu\right] = \frac{i}{2}\left(\gamma^\mu\gamma^\nu - \gamma^\nu\gamma^\mu\right). \tag{A.7}$$

The γ matrices can be formulated in light-cone-coordinates, for instance:

$$\gamma^\pm = \frac{1}{\sqrt{2}}(\gamma^0 \pm \gamma^3), \tag{A.8}$$

B. Structure functions

For completeness the relation of the structure functions with the photoabsorption cross sections is illustrated (Appendix of Ref. [12]). After defining:

$$F^{ij}_{mn}(x,Q^2,z,P^2_{h\perp}) = \frac{Q^2(1-x)}{4\pi^3\alpha}\left(1+\frac{\gamma^2}{2x}\right)^{-1}\frac{d\sigma^{ij}_{mn}}{dzdP^2_{h\perp}} \tag{B.1}$$

the well-known structure functions can be obtained as combinations of the photoabsorption cross sections and interference terms defined in Eq. 2.43:

$$\begin{aligned}
F_{UU,T} &= \frac{1}{2}(F^{++}_{++}+F^{--}_{++}) & F_{UU,L} &= F^{++}_{00}\\
F^{cos\phi}_{UU} &= \frac{1}{\sqrt{2}}(F^{++}_{+0}+F^{--}_{+0}) & F^{cos2\phi}_{UU} &= -ReF^{++}_{+-}\\
F^{sin\phi}_{LU} &= -\frac{1}{\sqrt{2}}(F^{++}_{+0}+F^{--}_{+0}) & F^{sin\phi}_{UL} &= -\frac{1}{\sqrt{2}}(F^{++}_{+0}-F^{--}_{+0})\\
F^{sin2\phi}_{UL} &= -ImF^{++}_{+-} & F_{LL} &= \frac{1}{2}(F^{++}_{++}-F^{--}_{++})\\
F^{cos\phi}_{LL} &= -\frac{1}{2}Re(F^{++}_{+0}-F^{--}_{+0}) & F^{sin(\phi-\phi_S)}_{UT,T} &= -ImF^{+-}_{++}\\
F^{sin(\phi-\phi_S)}_{UT,L} &= -ImF^{+-}_{00} & F^{sin(\phi+\phi_S)}_{UT} &= -\frac{1}{2}F^{+-}_{+-}\\
F^{sin(3\phi-\phi_S)}_{UT} &= -\frac{1}{2}ImF^{-+}_{+-} & F^{sin\phi_S}_{UT} &= -\frac{1}{\sqrt{2}}F^{+-}_{+0}\\
F^{(2\phi-\phi_S)}_{UT} &= -\frac{1}{\sqrt{2}}ImF^{-+}_{+0} & F^{cos(\phi-\phi_S)}_{LT} &= F^{+-}_{++}\\
F^{cos\phi_S}_{LT} &= -\frac{1}{\sqrt{2}}ReF^{+-}_{+0} & F_{LT}cos(2\phi-\phi_S) &= -\frac{1}{\sqrt{2}}ReF^{-+}_{+0}
\end{aligned} \tag{B.2}$$

C. Additional Material - Event Selection & Background Estimation

C.1 Correlation Plots

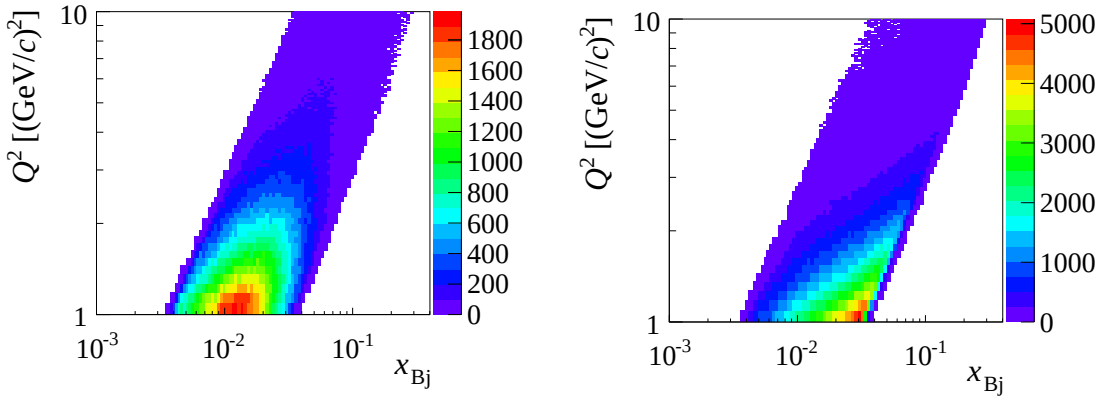

Figure C.1: Correlation between x_{Bj} and Q^2 for the 2003&2004 sample (left) and 2007&2010 sample (right). All cuts indicated in Tab. 4.5 are applied.

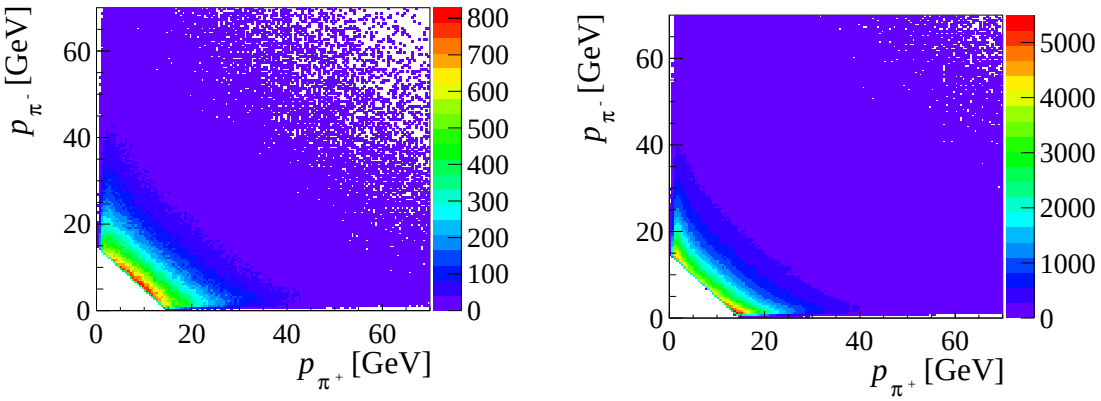

Figure C.2: Correlation between $p_{\pi+}$ and $p_{\pi-}$ for the 2003&2004 sample (left) and 2007&2010 sample (right). All cuts indicated in Tab. 4.5 are applied.

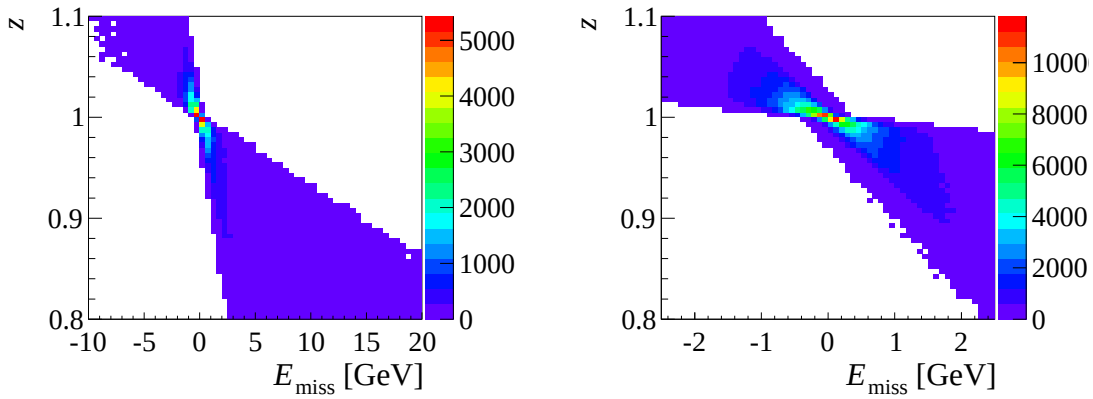

Figure C.3: Correlation between E_{miss} and z for the 2003&2004 sample (left) and 2007&2010 sample (right). All cuts indicated in Tab. 4.5 are applied, except the cut on E_{miss}.

C.2 Background Fits

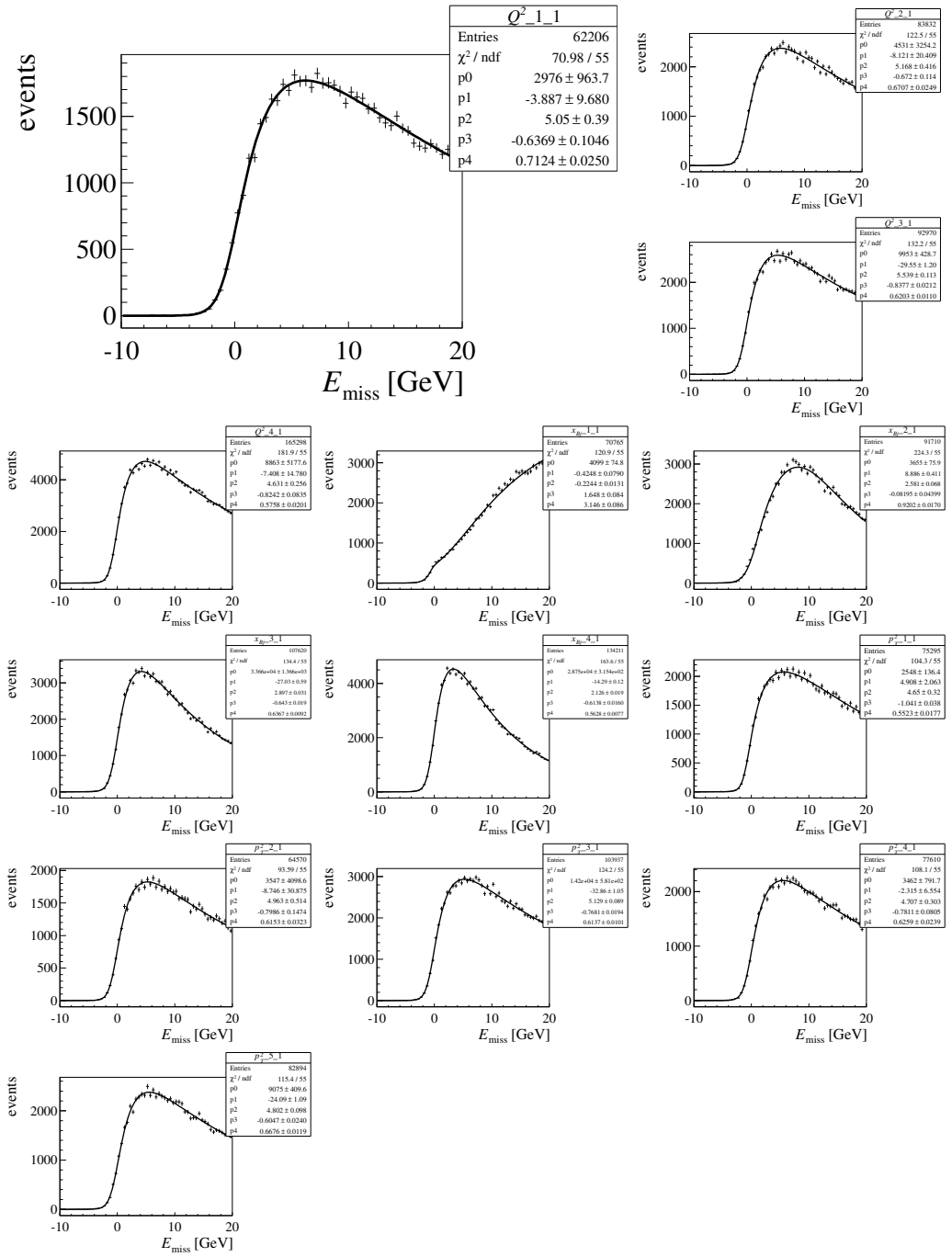

Figure C.4: The E_{miss} distribution from LEPTO Monte-Carlo parametrised with Eq. 5.4 for the 2007&2010 sample. The four bins in Q^2 and x_{Bj} and the five bins in p_T^2 for the central target cell are shown. The bins according to Eq. 6.12 are indicated by the first number in the histogram titles. The corresponding fits for the up plus down target cells are presented in Fig. 5.9.

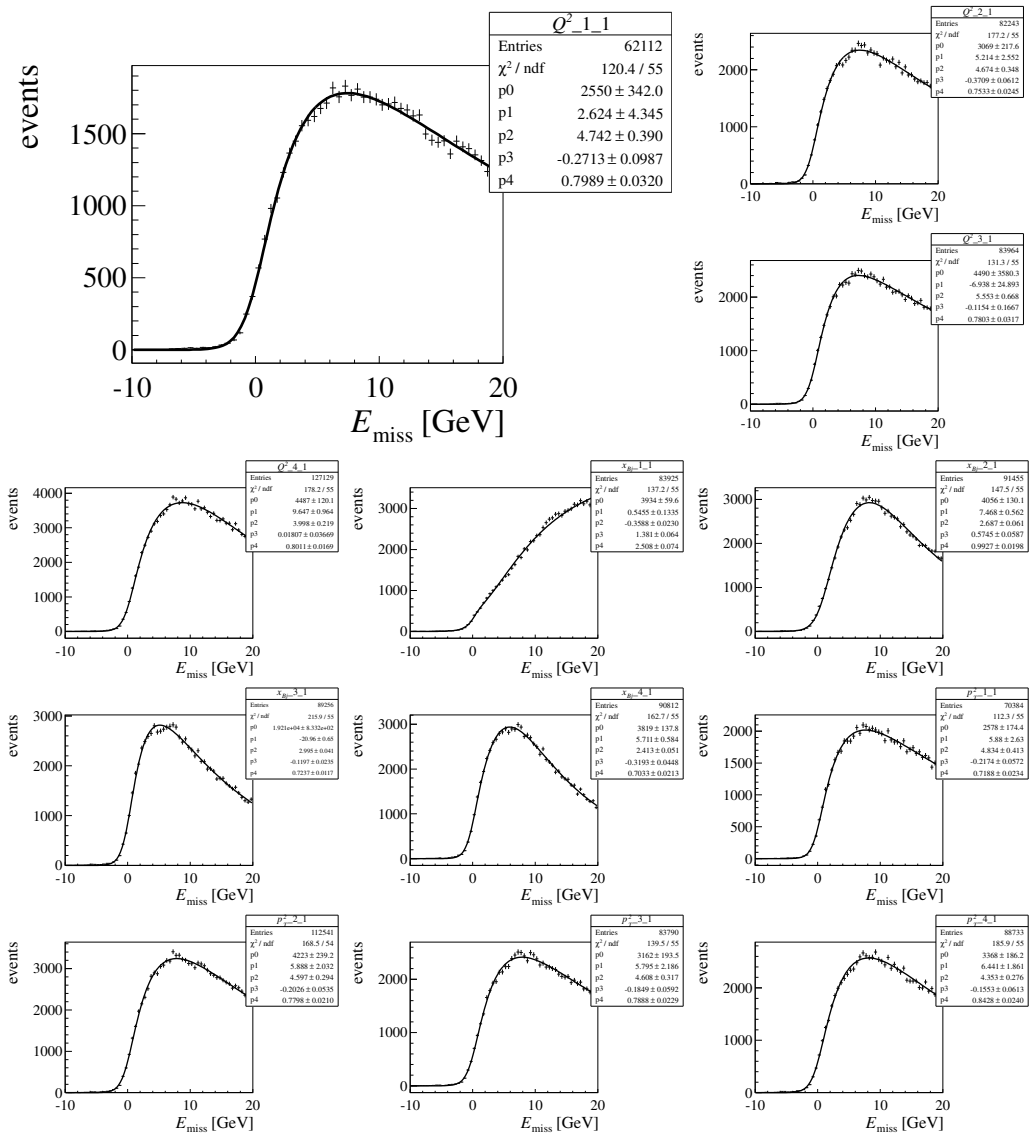

Figure C.5: The E_{miss} distribution from LEPTO Monte-Carlo parametrised with Eq. 5.4 for the 2003&2004 sample. The four bins in Q^2 and x_{Bj} and the five bins in p_T^2 for the down target cell are shown. The bins according to Eq. 6.12 are indicated by the first number in the histogram titles. The corresponding fits for the up target cell are presented in Fig. 5.10.

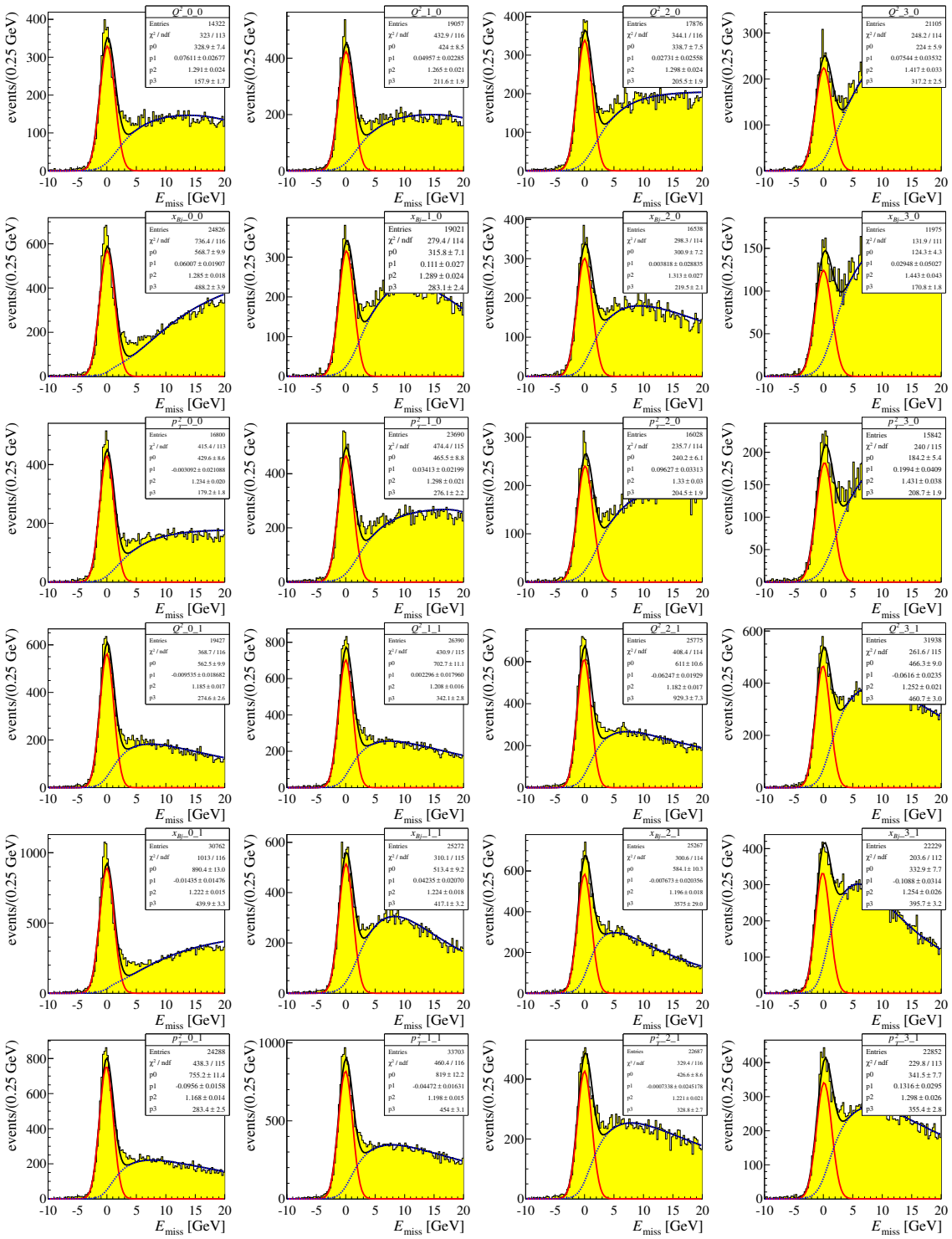

Figure C.6: The E_{miss} distribution for the 2003&2004 sample together with the signal plus background fits (solid curve). The solid red lines and the dashed blue lines represent the signal and background contributions, respectively. The parameters $p_0 - p_3$ are explained in the text in Sec. 5.2.1. Here are shown the fits for the $-+$ configuration for the up plus down (0) and the central (1) target cells. The corresponding fits for the $+-$ configuration are presented in Fig. 5.12.

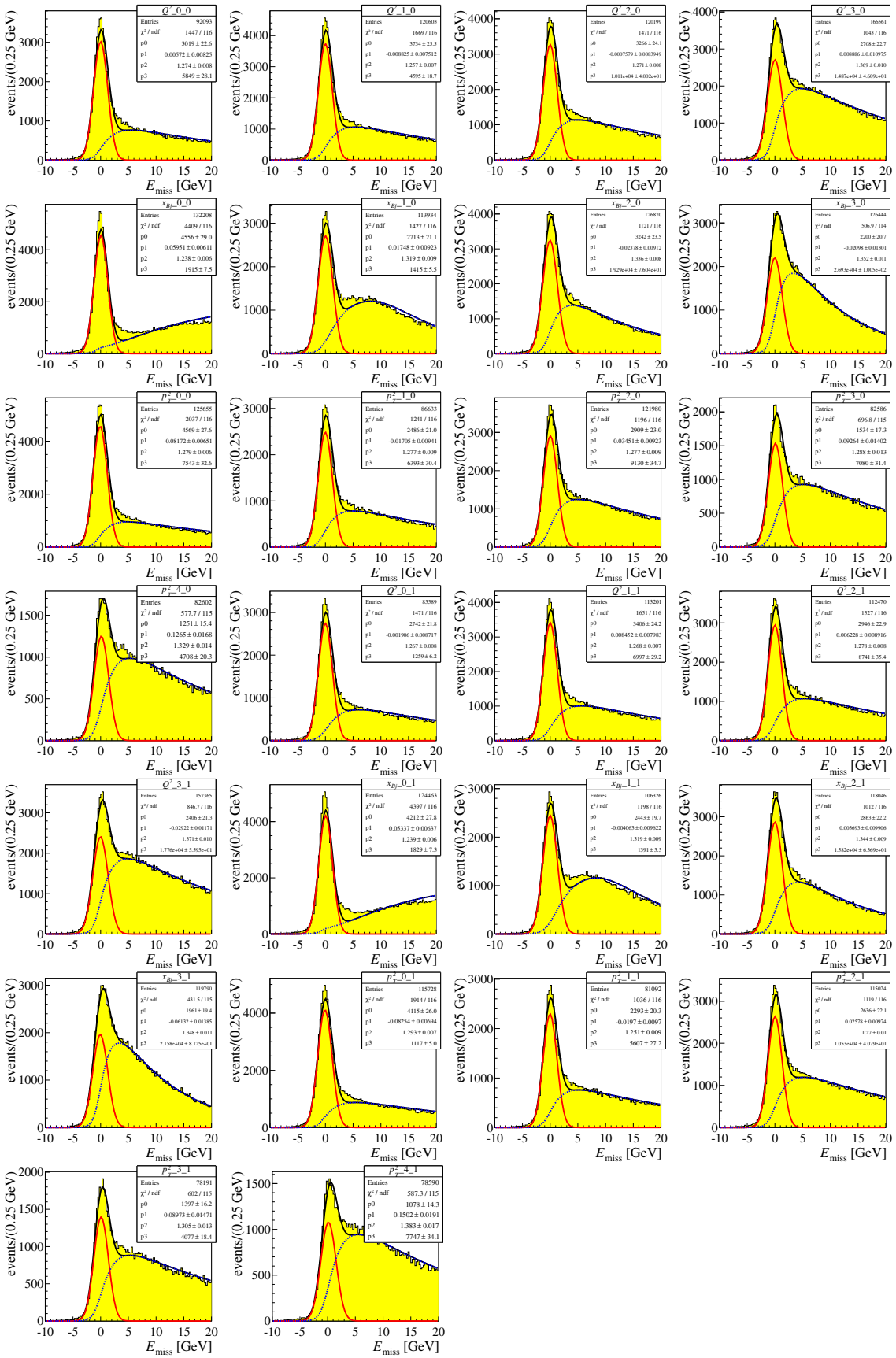

Figure C.7: The E_{miss} distribution for the 2007&2010 sample together with the signal plus background fits (solid curve). The solid red lines and the dashed blue lines represent the signal and background contributions, respectively. The parameters $p_0 - p_3$ are explained in the text in Sec. 5.2.1. Here are shown the fits for the $-+-$ configuration for the up plus down (0) and the central (1) target cells. The corresponding fits for the $+-+$ configuration are presented in Fig. 5.11.

D. Asymmetries

D.1 Target Polarisation Values - ^{6}LiD target

Table D.1: Target polarisation values for 2003 and 2004.

period	first run	last run	U	D
P1G	30773	31123	-0.4970	0.5278
P1H	31192	31247	0.4939	-0.4260
P1H	31277	31524	0.5131	-0.4463
04W33	38991	39168	0.5070	-0.4352
04W34	39283	39289	-0.4480	0.4597
04W34	39326	39429	-0.3860	0.4035
04W34	39481	39545	-0.4614	0.4741
04W35	39548	39780	-0.4644	0.4744
04W36	39850	39987	0.4989	-0.4276

D.2 Asymmetries - NH_3 target

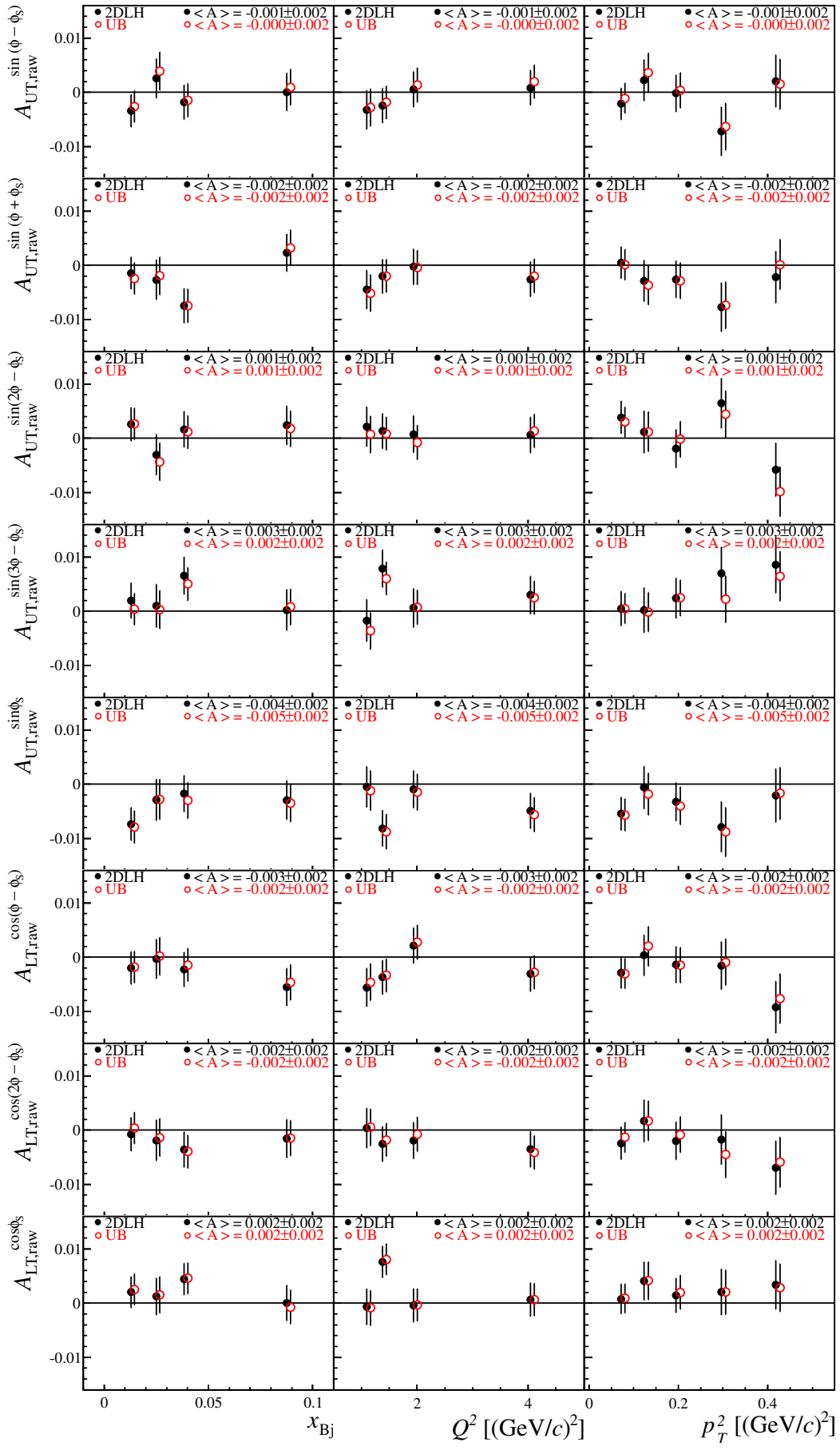

Figure D.1: Comparison of raw asymmetries extracted with an unbinned maximum likelihood fit (red open cricle) and a two-dimensional binned maximum likelihood fit (black open circle). Mean values $< A >$ and their statistical errors are given.

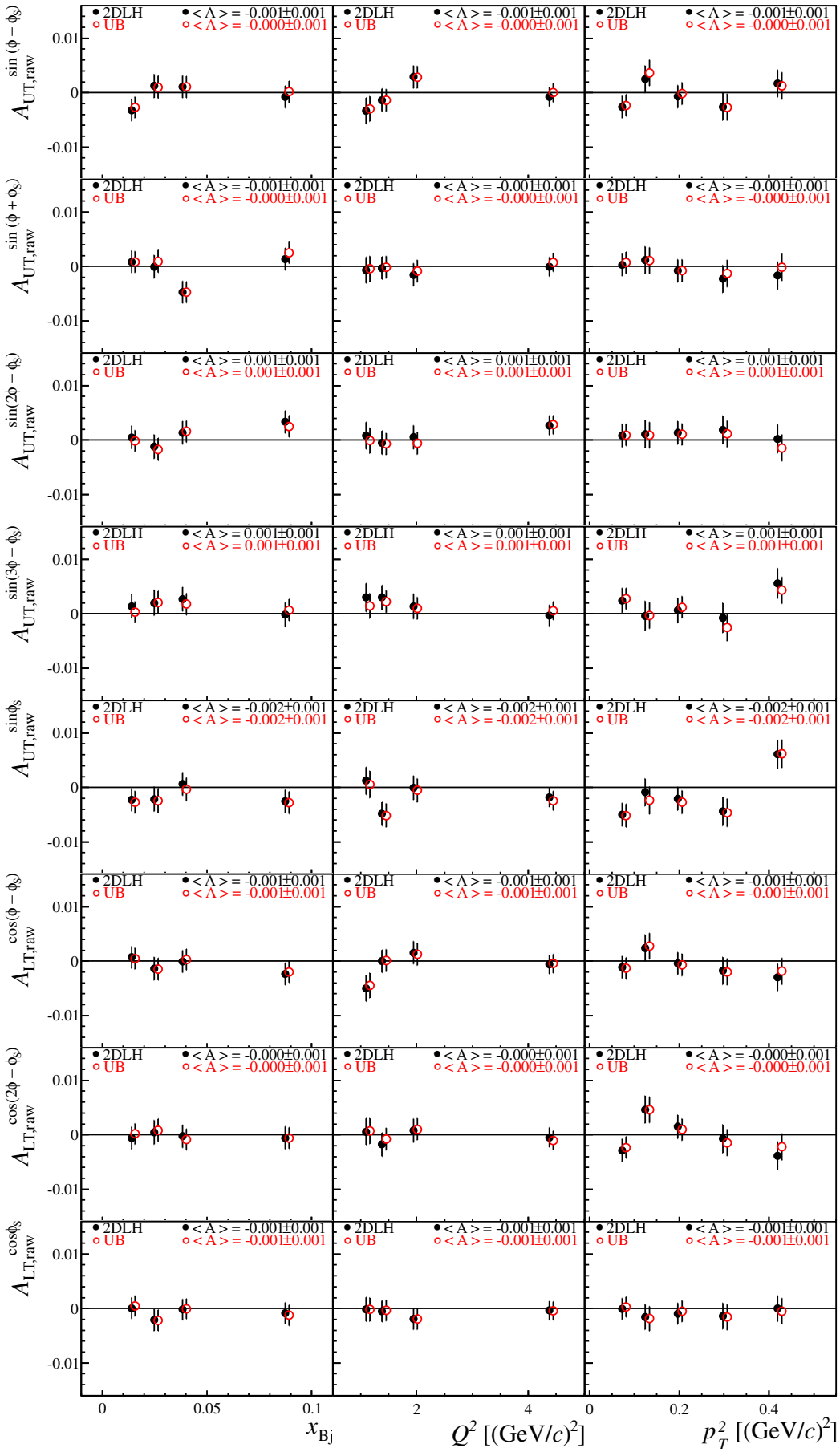

Figure D.2: Comparison of raw asymmetries extracted with an unbinned maximum likelihood fit (red open cricle) and a two-dimensional binned maximum likelihood fit (black open circle). The asymmetry values are extracted for data with $\mathbf{-10\,GeV < E_{miss} < 20\,GeV}$.

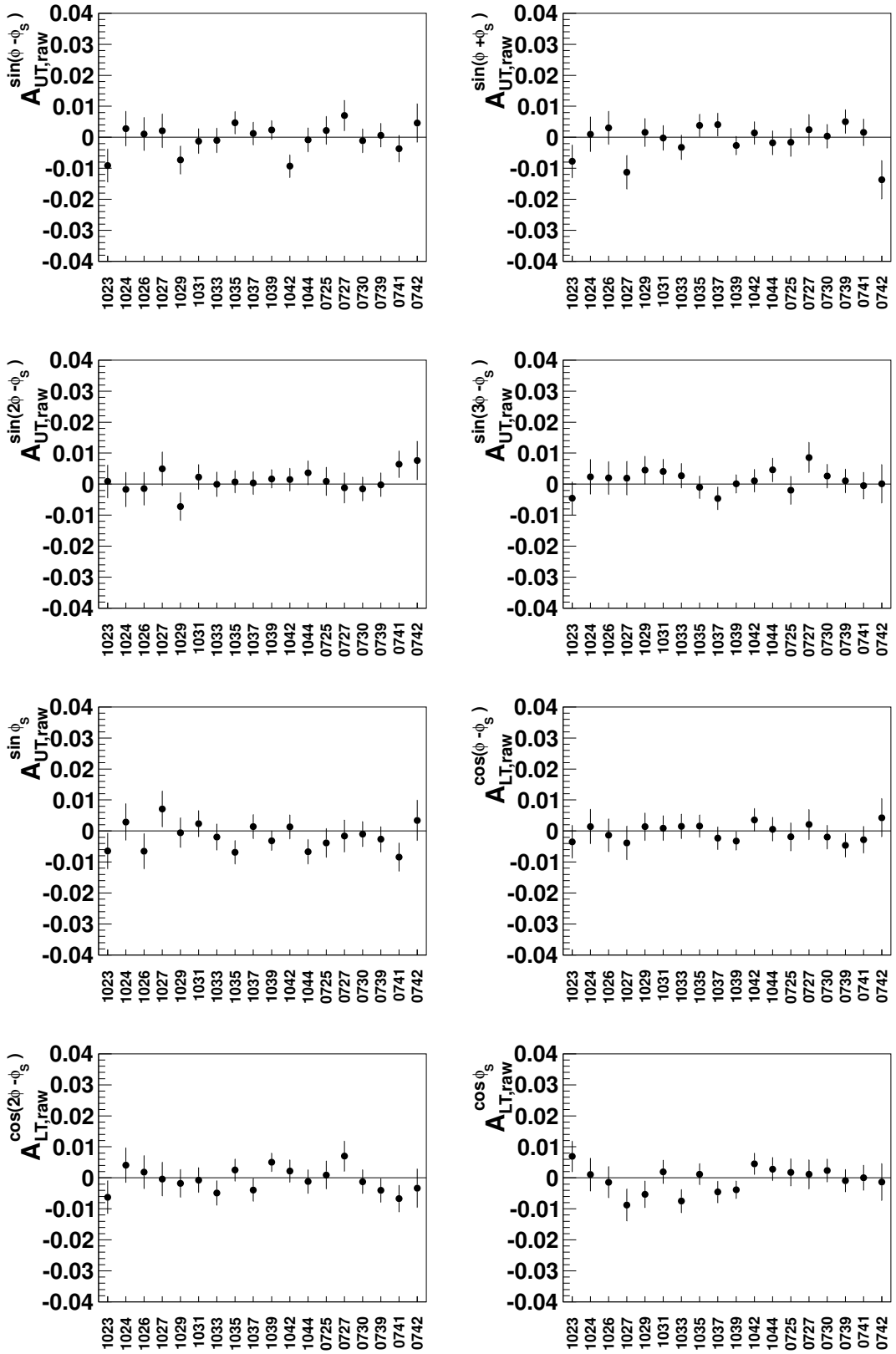

Figure D.3: Mean values of asymmetries for each period in 2007 and 2010. Each abscissa is labeled with four digits, where the first two digits indicate the year and the second two digits indicate the corresponding period. The periods of 2010 are depicted first, followed by 2007. The asymmetry values are extracted for data with $\mathbf{-10\,GeV < E_{miss} < 20\,GeV}$.

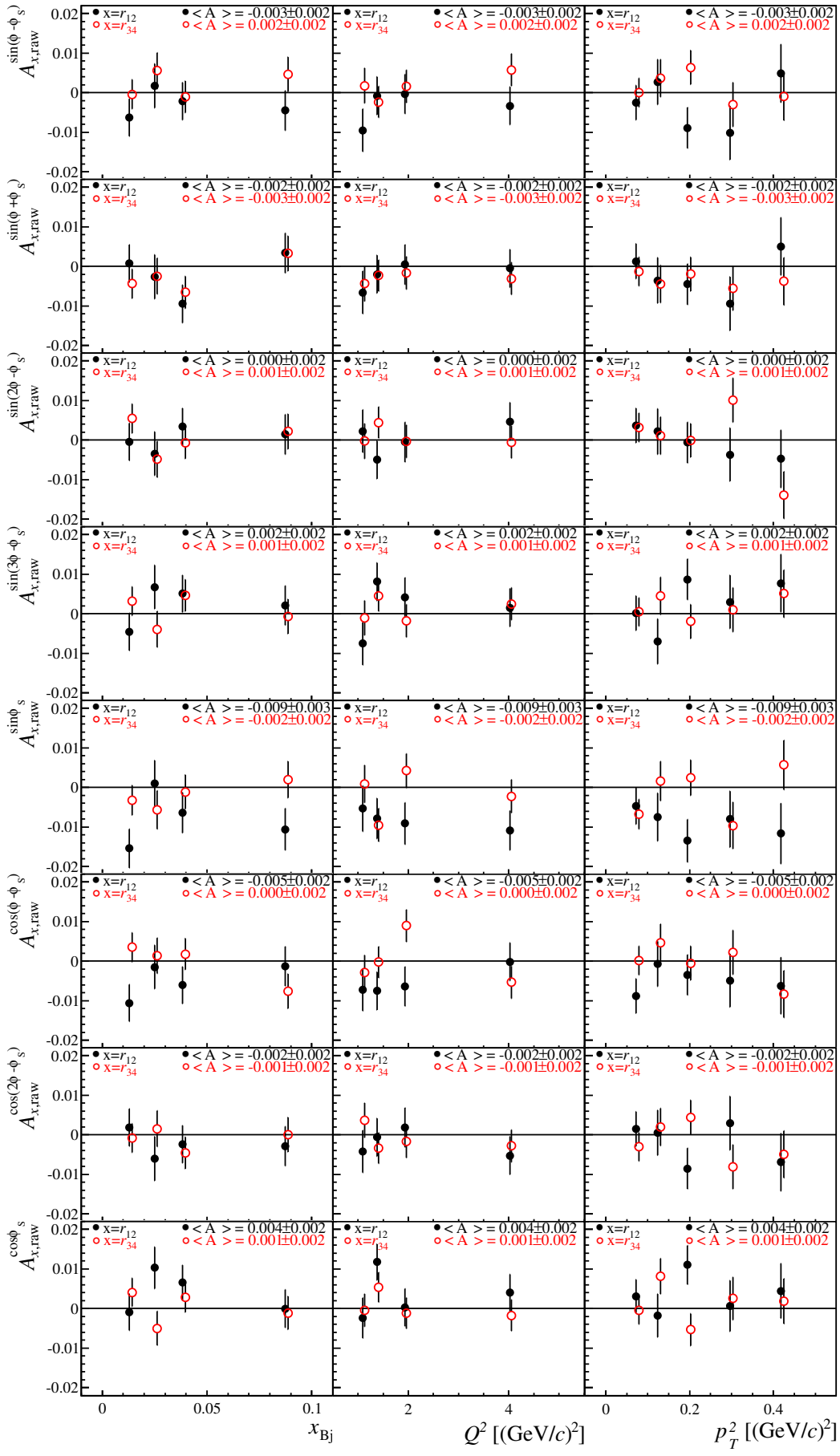

Figure D.4: Results of $\boldsymbol{A_{r12,raw}}$ (black full circle) and $\boldsymbol{A_{r34,raw}}$ (red open circle). Mean values $\langle A_{x,\mathrm{raw}} \rangle$ are given. The values are extracted for data with $\boldsymbol{-2.5\,\mathrm{GeV} < E_{\mathrm{miss}} < 2.5\,\mathrm{GeV}}$.

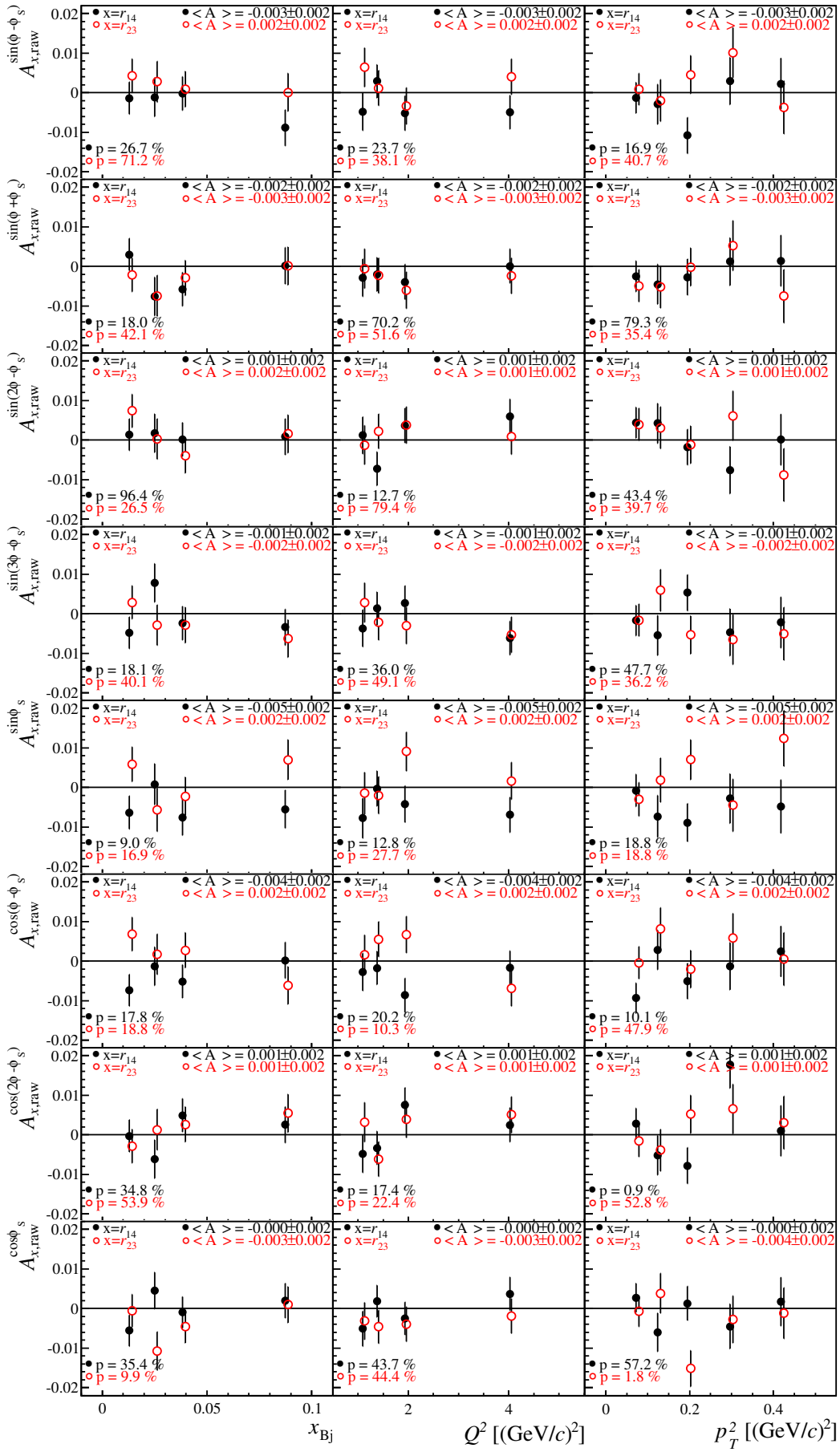

Figure D.5: Results of $\boldsymbol{A_{r14,raw}}$ (black full circle) and $\boldsymbol{A_{r23,raw}}$ (red open circle). Mean values $\langle A_{x,\mathrm{raw}} \rangle$ and probabilities p of χ^2 test with respect to $A_{r14,\mathrm{raw}} = 0$ or $A_{r23,\mathrm{raw}}$ are given. The values are extracted for data with $\boldsymbol{-2.5\,\mathrm{GeV} < E_{\mathrm{miss}} < 2.5\,\mathrm{GeV}}$.

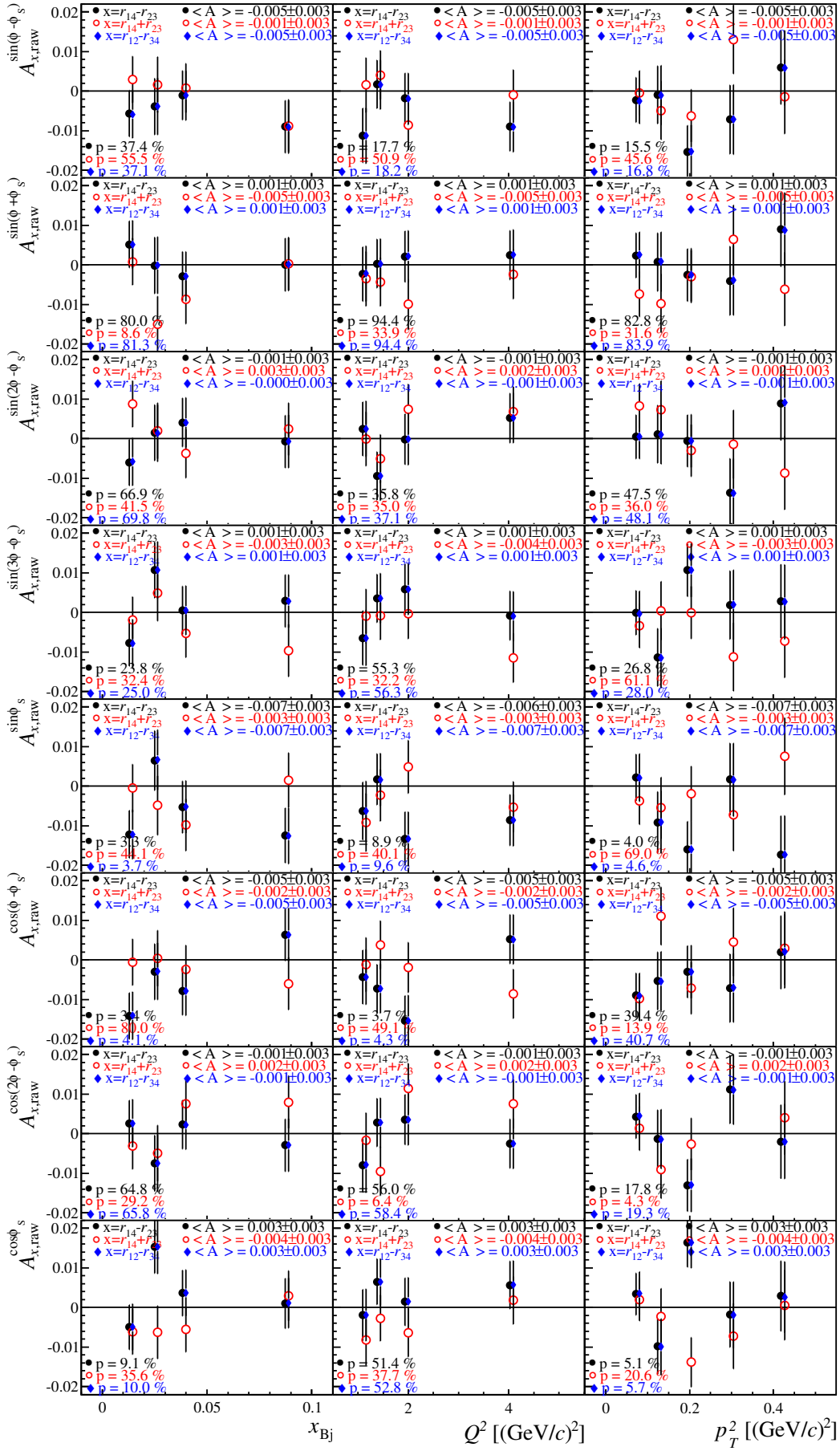

Figure D.6: Results of $\boldsymbol{A_{(r14-r23),\mathrm{raw}}}$ (black full circle) and $\boldsymbol{A_{(r14+r23),\mathrm{raw}}}$ (red open circle), $\boldsymbol{A_{(r12-r34),\mathrm{raw}}}$ (blue diamond). Mean values $< A_{x,\mathrm{raw}} >$ and probabilities p of χ^2 test with respect to $A_{x,\mathrm{raw}} = 0$ are given. The values are extracted for data with $\boldsymbol{-2.5\,\mathrm{GeV} < E_{\mathrm{miss}} < 2.5\,\mathrm{GeV}}$.

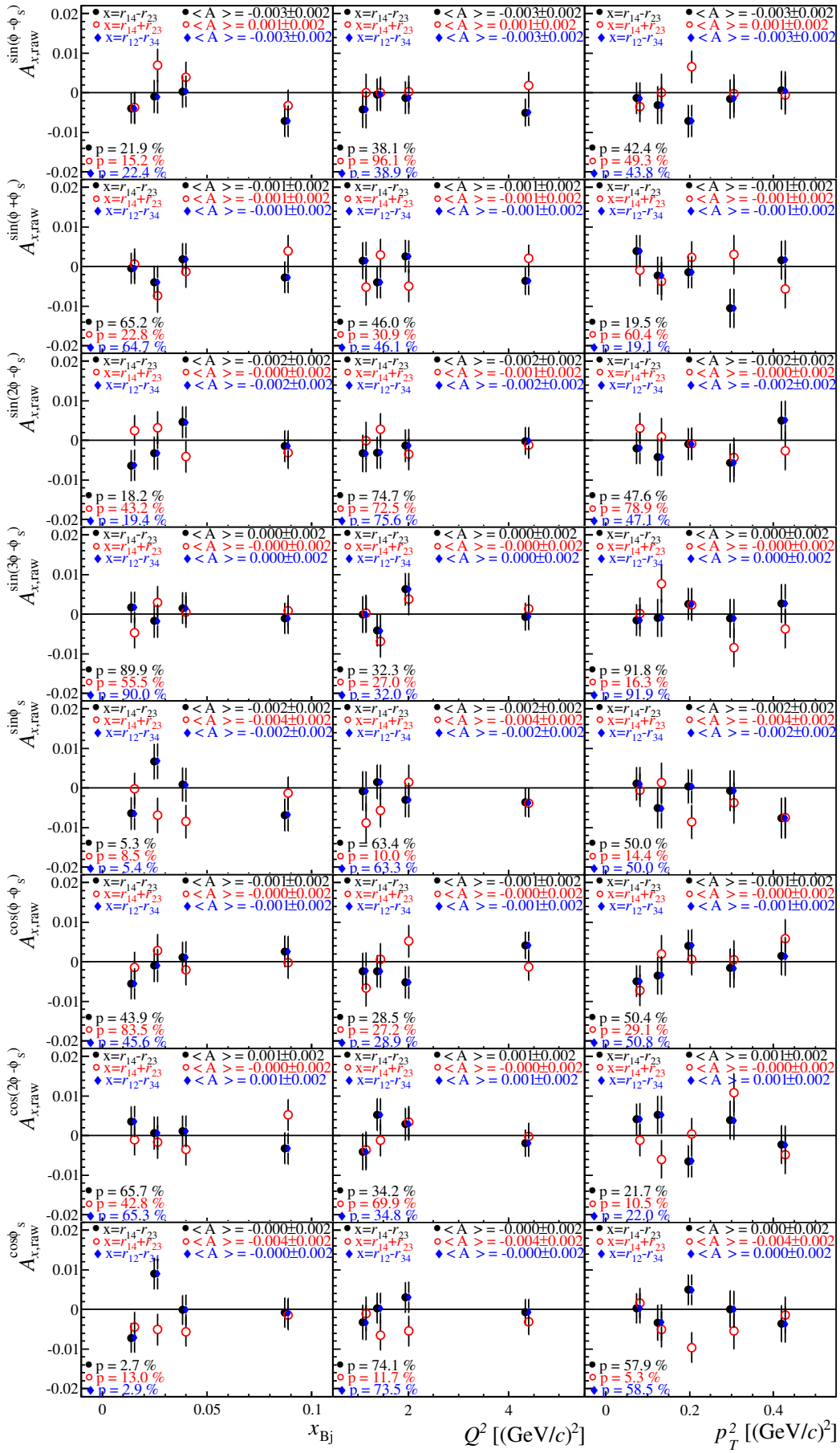

Figure D.7: Results of $\boldsymbol{A_{(r14-r23),\mathrm{raw}}}$ (black full circle) and $\boldsymbol{A_{(r14+r23),\mathrm{raw}}}$ (red open circle), $\boldsymbol{A_{(r12-r34),\mathrm{raw}}}$ (blue diamond). Mean values $< A_{x,\mathrm{raw}} >$ and probabilities p of χ^2 test with respect to $A_{x,\mathrm{raw}} = 0$ are given. The values are extracted for data with $\boldsymbol{-10.\,\mathrm{GeV} < E_{\mathrm{miss}} < 20.\,\mathrm{GeV}}$.

D.3 Asymmetries - ^{6}LiD target

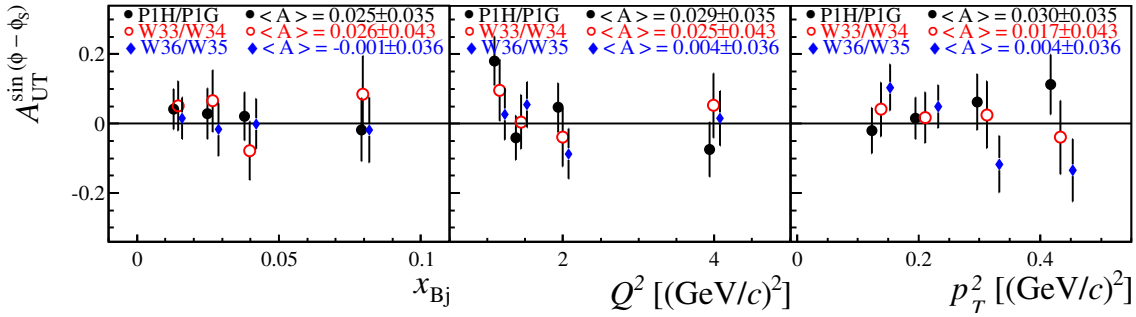

Figure D.8: Comparison of physical asymmetries extracted in every period in 2003 and 2004. The asymmetry values are extracted for data with $\boldsymbol{-2.5\,\mathrm{GeV} < E_{\mathrm{miss}} < 2.5\,\mathrm{GeV}}$.

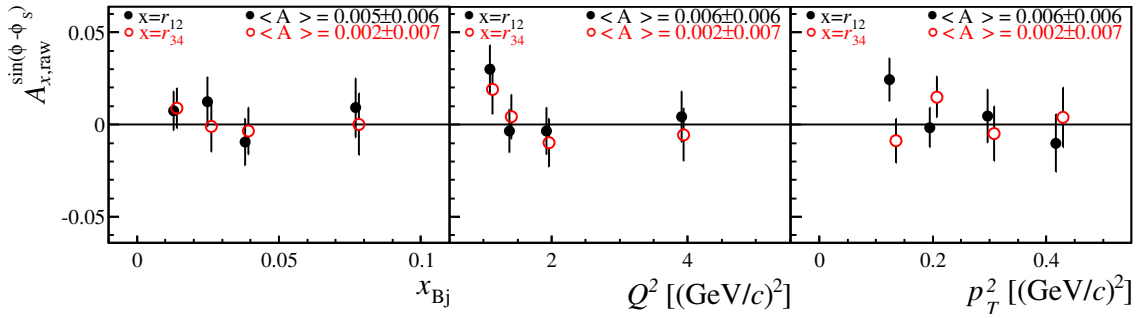

Figure D.9: Results of $\boldsymbol{A_{r12,raw}}$ (black full circle) and $\boldsymbol{A_{r34,raw}}$ (red open circle). Mean values $\langle A_{x,\mathrm{raw}} \rangle$ are given. The values are extracted for data with $\boldsymbol{-2.5\,\mathrm{GeV} < E_{\mathrm{miss}} < 2.5\,\mathrm{GeV}}$.

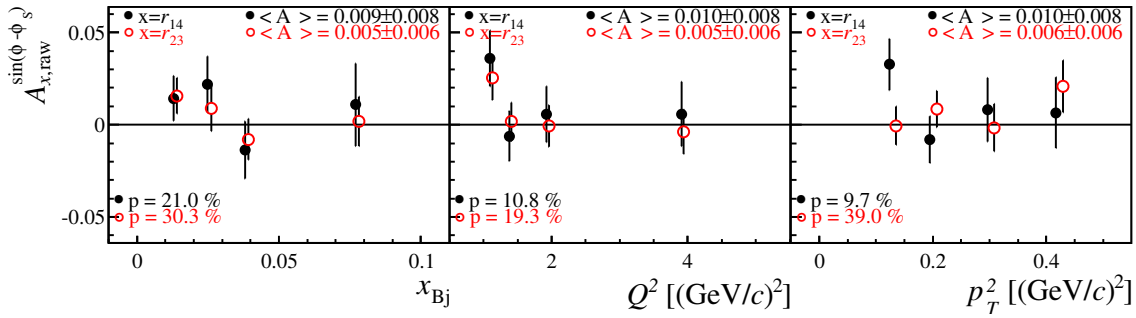

Figure D.10: Results of $\boldsymbol{A_{r14,\mathrm{raw}}}$ (black full circle) and $\boldsymbol{A_{r23,\mathrm{raw}}}$ (red open circle). Mean values $\langle A_{r23,\mathrm{raw}} \rangle$ and probabilities p of χ^2 test with respect to $A_{r23,\mathrm{raw}} = 0$ are given. The values are extracted for data with $\boldsymbol{-2.5\,\mathrm{GeV} < E_{\mathrm{miss}} < 2.5\,\mathrm{GeV}}$.

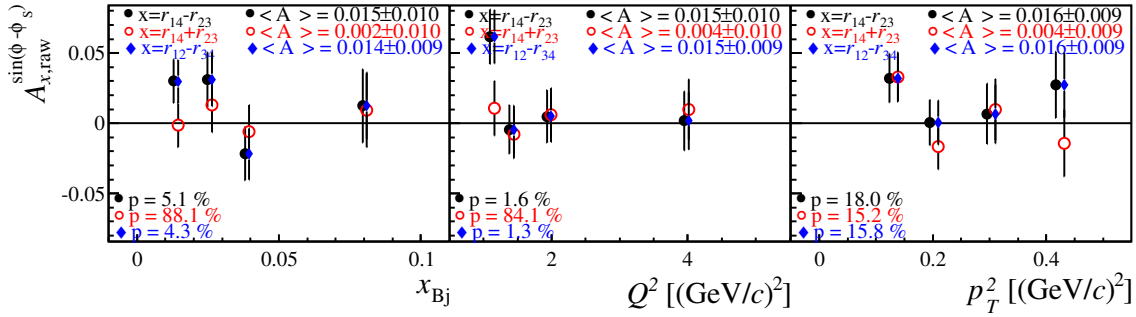

Figure D.11: Results of $\boldsymbol{A_{(r14-r23),\mathrm{raw}}}$ (black full circle) and $\boldsymbol{A_{(r14+r23),\mathrm{raw}}}$ (red open circle), $\boldsymbol{A_{(r12-r34),\mathrm{raw}}}$ (blue diamond). Mean values $\langle A_{x,\mathrm{raw}} \rangle$ and probabilities p of χ^2 test with respect to $A_{x,\mathrm{raw}} = 0$ are given. The values are extracted for data with $\boldsymbol{-2.5\,\mathrm{GeV} < E_{\mathrm{miss}} < 2.5\,\mathrm{GeV}}$.

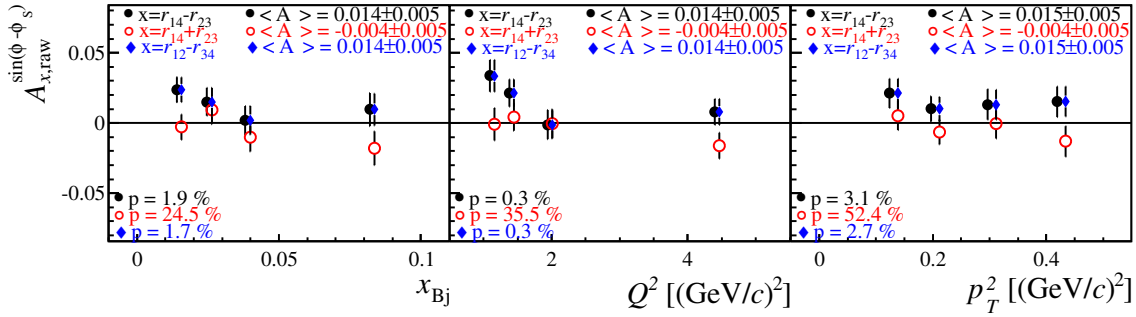

Figure D.12: Results of $\boldsymbol{A_{(r14-r23),\mathrm{raw}}}$ (black full circle) and $\boldsymbol{A_{(r14+r23),\mathrm{raw}}}$ (red open circle), $\boldsymbol{A_{(r12-r34),\mathrm{raw}}}$ (blue diamond). Mean values $\langle A_{x,\mathrm{raw}} \rangle$ and probabilities p of χ^2 test with respect to $A_{x,\mathrm{raw}} = 0$ are given. The values are extracted for data with $\boldsymbol{-10.\,\mathrm{GeV} < E_{\mathrm{miss}} < 20.\,\mathrm{GeV}}$.

D.4 Asymmetry Values

Table D.2: Numerical values for the transverse target spin asymmetry $A_{\mathrm{UT}}^{\sin(\phi-\phi_S)}$ measured on deuterons in bins of Q^2, x_{Bj} and p_T^2. The systematic uncertainties are obtained using the values given in Table 8.1 and a scale uncertainty of 5.4 % accounts for uncertainties in the determination of the target polarisation and target dilution factor for deuteron data.

	$\langle x_{Bj}\rangle$	$\langle Q^2\rangle$ $(\mathrm{GeV}/c)^2$	$\langle p_T^2\rangle$ $(\mathrm{GeV}/c)^2$	$A_{UT,p}^{\sin(\phi-\phi_S)} \pm \sigma^{stat} \pm \sigma^{sys}$
x_{Bj} bin $(\mathrm{GeV}/c)^2$				
$0.003 - 0.02$	0.013	1.4	0.23	$0.03 \pm 0.05 \pm 0.03$
$0.02 - 0.03$	0.025	1.6	0.23	$0.01 \pm 0.06 \pm 0.04$
$0.03 - 0.05$	0.038	2.0	0.23	$-0.02 \pm 0.06 \pm 0.04$
$0.05 - 0.35$	0.078	3.9	0.24	$0.04 \pm 0.10 \pm 0.06$
Q^2 bin				
$1.0 - 1.2$	0.018	1.1	0.23	$0.09 \pm 0.06 \pm 0.04$
$1.2 - 1.6$	0.023	1.4	0.23	$0.00 \pm 0.05 \pm 0.03$
$1.6 - 2.4$	0.031	1.9	0.23	$-0.03 \pm 0.06 \pm 0.04$
$2.4 - 10.0$	0.059	3.9	0.24	$0.00 \pm 0.07 \pm 0.04$
p_T^2 bin $(\mathrm{GeV}/c)^2$				
$0.10 - 0.15$	0.031	1.9	0.12	$0.02 \pm 0.05 \pm 0.03$
$0.15 - 0.25$	0.031	2.0	0.19	$0.04 \pm 0.05 \pm 0.03$
$0.25 - 0.35$	0.032	2.0	0.30	$-0.01 \pm 0.07 \pm 0.04$
$0.35 - 0.50$	0.033	2.1	0.42	$-0.03 \pm 0.08 \pm 0.05$

Table D.3: Numerical values for the transverse target single-spin asymmetries measured on protons in bins of Q^2, x_{Bj} and p_T^2. The systematic uncertainties are obtained using the values given in Table 7.8 and a scale uncertainty of 3.6 % accounts for uncertainties in the determination of the target polarisation and target dilution factor for proton data.

	$\langle x_{Bj} \rangle$	$\langle Q^2 \rangle$ (GeV/c)^2	$\langle p_T^2 \rangle$ (GeV/c)^2	$A_{UT,p}^{\sin(\phi-\phi_S)} \pm \sigma^{stat} \pm \sigma^{sys}$	$A_{UT,p}^{\sin(\phi+\phi_S)} \pm \sigma^{stat} \pm \sigma^{sys}$
x_{Bj} bin (GeV/c)^2					
$0.003 - 0.02$	0.013	1.43	0.17	$-0.017 \pm 0.016 \pm 0.004$	$-0.018 \pm 0.036 \pm 0.011$
$0.02 - 0.03$	0.025	1.62	0.18	$0.013 \pm 0.022 \pm 0.006$	$-0.031 \pm 0.044 \pm 0.013$
$0.03 - 0.05$	0.038	1.91	0.18	$-0.021 \pm 0.022 \pm 0.006$	$-0.082 \pm 0.044 \pm 0.013$
$0.05 - 0.35$	0.088	3.84	0.19	$0.023 \pm 0.038 \pm 0.010$	$0.038 \pm 0.072 \pm 0.021$
Q^2 bin					
$1.0 - 1.2$	0.019	1.10	0.18	$-0.019 \pm 0.020 \pm 0.005$	$-0.055 \pm 0.042 \pm 0.013$
$1.2 - 1.6$	0.025	1.38	0.18	$-0.015 \pm 0.019 \pm 0.005$	$-0.029 \pm 0.039 \pm 0.012$
$1.6 - 2.4$	0.035	1.94	0.18	$-0.002 \pm 0.021 \pm 0.005$	$0.016 \pm 0.044 \pm 0.013$
$2.4 - 10.0$	0.076	4.04	0.19	$0.015 \pm 0.030 \pm 0.008$	$-0.034 \pm 0.060 \pm 0.018$
p_T^2 bin (GeV/c)^2					
$0.05 - 0.10$	0.037	2.07	0.07	$-0.008 \pm 0.017 \pm 0.004$	$0.004 \pm 0.036 \pm 0.011$
$0.10 - 0.15$	0.039	2.13	0.12	$0.007 \pm 0.024 \pm 0.006$	$-0.045 \pm 0.050 \pm 0.015$
$0.15 - 0.25$	0.040	2.18	0.20	$0.002 \pm 0.023 \pm 0.006$	$-0.033 \pm 0.049 \pm 0.015$
$0.25 - 0.35$	0.042	2.24	0.30	$-0.058 \pm 0.035 \pm 0.009$	$-0.096 \pm 0.071 \pm 0.021$
$0.35 - 0.50$	0.043	2.29	0.42	$0.003 \pm 0.041 \pm 0.010$	$-0.005 \pm 0.083 \pm 0.024$

Table D.4: Numerical values for the transverse target single-spin asymmetries measured on protons in bins of Q^2, x_{Bj} and p_T^2. The systematic uncertainties are obtained using the values given in Table 7.8 and a scale uncertainty of 3.6 % accounts for uncertainties in the determination of the target polarisation and target dilution factor for proton data.

	$A_{UT,p}^{\sin(2\phi-\phi_S)} \pm \sigma^{stat} \pm \sigma^{sys}$	$A_{UT,p}^{\sin(3\phi-\phi_S)} \pm \sigma^{stat} \pm \sigma^{sys}$	$A_{UT,p}^{\sin\phi_S} \pm \sigma^{stat} \pm \sigma^{sys}$
x_{Bj} bin			
$0.003 - 0.02$	$0.011 \pm 0.013 \pm 0.005$	$0.021 \pm 0.040 \pm 0.013$	$-0.031 \pm 0.013 \pm 0.005$
$0.02 - 0.03$	$-0.015 \pm 0.016 \pm 0.006$	$0.012 \pm 0.048 \pm 0.015$	$-0.011 \pm 0.016 \pm 0.007$
$0.03 - 0.05$	$0.008 \pm 0.017 \pm 0.006$	$0.084 \pm 0.048 \pm 0.015$	$-0.012 \pm 0.017 \pm 0.007$
$0.05 - 0.35$	$-0.005 \pm 0.028 \pm 0.010$	$-0.004 \pm 0.077 \pm 0.024$	$-0.016 \pm 0.030 \pm 0.012$
Q^2 bin $(\mathrm{GeV}/c)^2$			
$1.0 - 1.2$	$0.008 \pm 0.015 \pm 0.006$	$-0.028 \pm 0.046 \pm 0.015$	$-0.006 \pm 0.016 \pm 0.006$
$1.2 - 1.6$	$0.007 \pm 0.014 \pm 0.005$	$0.096 \pm 0.043 \pm 0.014$	$-0.035 \pm 0.015 \pm 0.006$
$1.6 - 2.4$	$0.002 \pm 0.016 \pm 0.006$	$-0.000 \pm 0.049 \pm 0.015$	$-0.008 \pm 0.017 \pm 0.007$
$2.4 - 10.0$	$-0.010 \pm 0.023 \pm 0.008$	$0.059 \pm 0.065 \pm 0.021$	$-0.028 \pm 0.023 \pm 0.009$
p_T^2 bin $(\mathrm{GeV}/c)^2$			
$0.05 - 0.10$	$0.017 \pm 0.013 \pm 0.005$	$-0.003 \pm 0.039 \pm 0.012$	$-0.019 \pm 0.013 \pm 0.005$
$0.10 - 0.15$	$0.004 \pm 0.019 \pm 0.007$	$0.001 \pm 0.055 \pm 0.017$	$-0.002 \pm 0.019 \pm 0.007$
$0.15 - 0.25$	$-0.012 \pm 0.018 \pm 0.006$	$0.033 \pm 0.053 \pm 0.017$	$-0.014 \pm 0.018 \pm 0.007$
$0.25 - 0.35$	$0.034 \pm 0.026 \pm 0.009$	$0.106 \pm 0.077 \pm 0.024$	$-0.044 \pm 0.026 \pm 0.010$
$0.35 - 0.50$	$-0.045 \pm 0.031 \pm 0.011$	$0.137 \pm 0.090 \pm 0.029$	$-0.038 \pm 0.032 \pm 0.012$

Table D.5: Numerical values for the transverse target double-spin asymmetries measured on protons in bins of Q^2, x_{Bj} and p_T^2. The systematic uncertainties are obtained using the values given in Table 7.8 and a scale uncertainty of 6.2 % accounts for uncertainties in the determination of the target polarisation, beam polarisation and target dilution factor for proton data.

	$A_{LT,p}^{\cos(\phi-\phi_S)} \pm \sigma^{stat} \pm \sigma^{sys}$	$A_{LT,p}^{\cos(2\phi-\phi_S)} \pm \sigma^{stat} \pm \sigma^{sys}$	$A_{LT,p}^{\cos\phi_S} \pm \sigma^{stat} \pm \sigma^{sys}$
x_{Bj} bin			
$0.003 - 0.02$	$0.03 \pm 0.05 \pm 0.03$	$0.02 \pm 0.07 \pm 0.03$	$-0.05 \pm 0.06 \pm 0.04$
$0.02 - 0.03$	$0.02 \pm 0.11 \pm 0.06$	$0.10 \pm 0.17 \pm 0.07$	$-0.08 \pm 0.15 \pm 0.09$
$0.03 - 0.05$	$0.10 \pm 0.16 \pm 0.09$	$0.24 \pm 0.22 \pm 0.10$	$-0.31 \pm 0.20 \pm 0.12$
$0.05 - 0.35$	$0.36 \pm 0.29 \pm 0.16$	$0.18 \pm 0.40 \pm 0.17$	$0.02 \pm 0.36 \pm 0.21$
Q^2 bin $(\mathrm{GeV}/c)^2$			
$1.0 - 1.2$	$0.13 \pm 0.09 \pm 0.05$	$0.01 \pm 0.13 \pm 0.06$	$0.01 \pm 0.12 \pm 0.07$
$1.2 - 1.6$	$0.12 \pm 0.08 \pm 0.06$	$0.09 \pm 0.13 \pm 0.06$	$-0.34 \pm 0.12 \pm 0.07$
$1.6 - 2.4$	$-0.06 \pm 0.10 \pm 0.06$	$0.09 \pm 0.15 \pm 0.06$	$0.04 \pm 0.13 \pm 0.08$
$2.4 - 10.0$	$0.13 \pm 0.14 \pm 0.08$	$0.20 \pm 0.21 \pm 0.09$	$-0.08 \pm 0.19 \pm 0.11$
p_T^2 bin $(\mathrm{GeV}/c)^2$			
$0.05 - 0.10$	$0.09 \pm 0.08 \pm 0.04$	$0.06 \pm 0.12 \pm 0.05$	$-0.03 \pm 0.11 \pm 0.06$
$0.10 - 0.15$	$0.03 \pm 0.11 \pm 0.06$	$-0.01 \pm 0.16 \pm 0.07$	$-0.22 \pm 0.15 \pm 0.09$
$0.15 - 0.25$	$0.02 \pm 0.11 \pm 0.06$	$0.14 \pm 0.16 \pm 0.07$	$-0.08 \pm 0.15 \pm 0.09$
$0.25 - 0.35$	$0.04 \pm 0.16 \pm 0.09$	$0.08 \pm 0.23 \pm 0.10$	$-0.15 \pm 0.22 \pm 0.13$
$0.35 - 0.50$	$0.37 \pm 0.20 \pm 0.11$	$0.28 \pm 0.28 \pm 0.12$	$-0.21 \pm 0.26 \pm 0.15$

D.5 Correlation Matrix

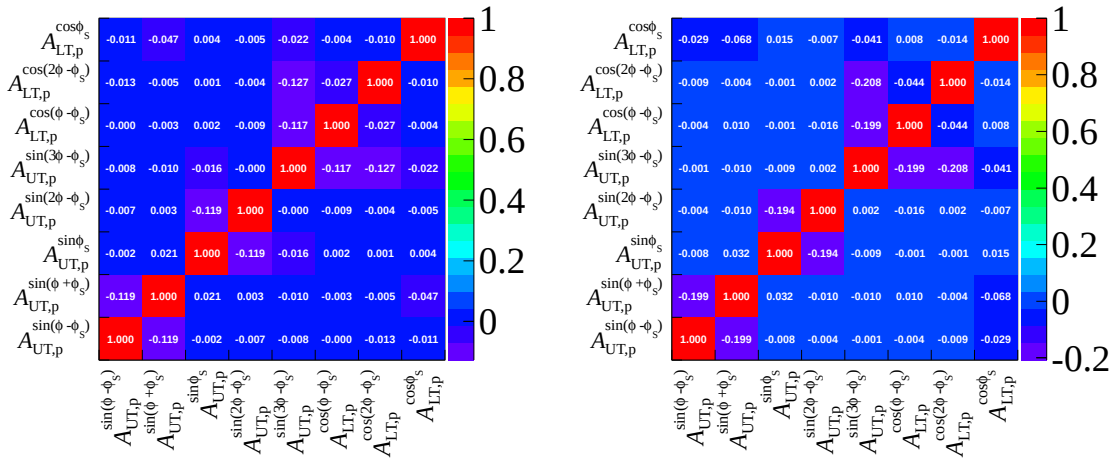

Figure D.13: Correlation matrix for the 2DLH fit. Here is shown the second bin (left) and the third bin (right) in x_{Bj} for the 2007&2010 sample.

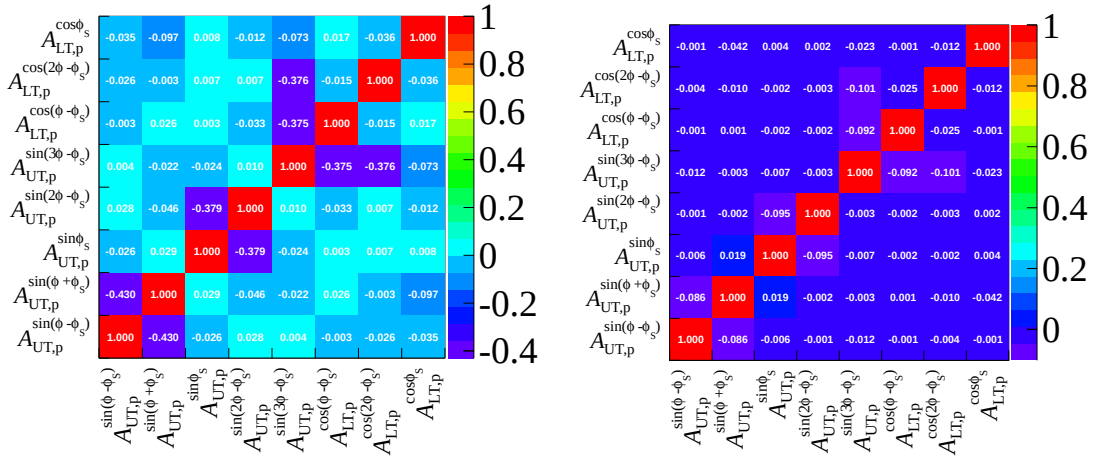

Figure D.14: Correlation matrix for the 2DLH fit. Here is shown the fourth bin in x_{Bj} (left) and the first bin (right) in Q^2 for the 2007&2010 sample.

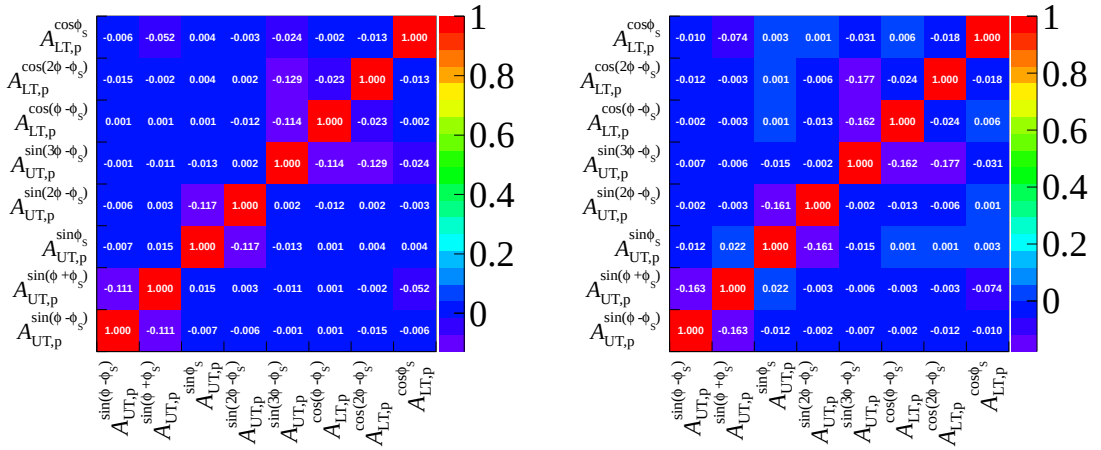

Figure D.15: Correlation matrix for the 2DLH fit. Here is shown the second bin (left) and the third bin (right) in Q^2 for the 2007&2010 sample.

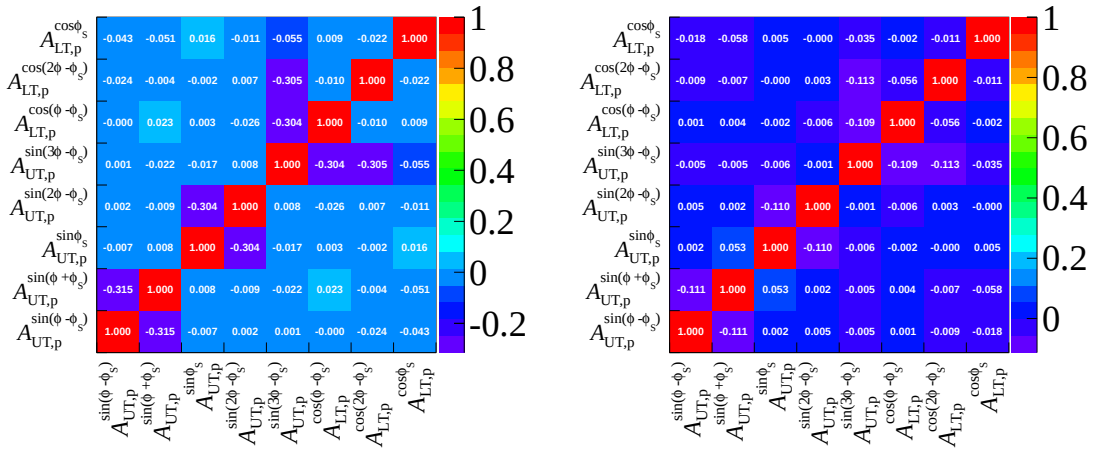

Figure D.16: Correlation matrix for the 2DLH fit. Here is shown the fourth bin in Q^2 (left) and the first bin in p_T^2 (right) for the 2007&2010 sample.

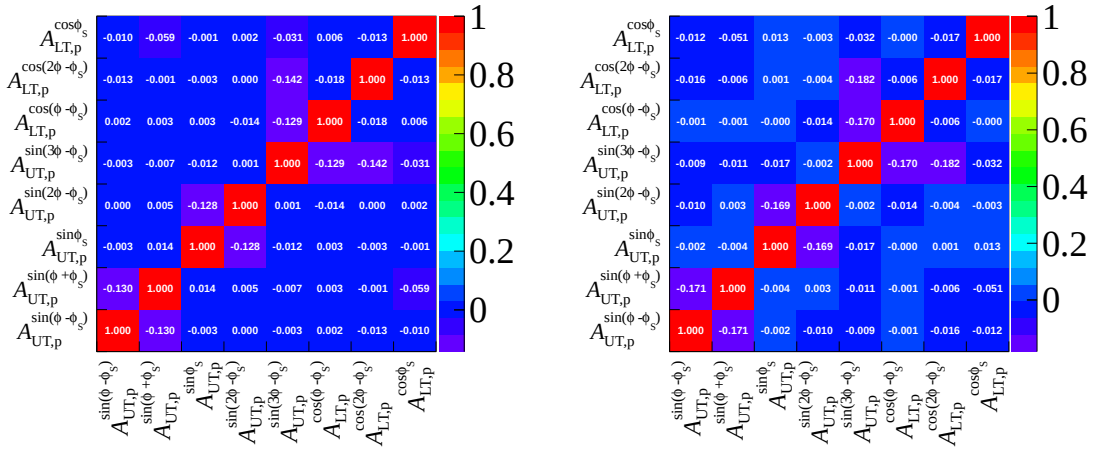

Figure D.17: Correlation matrix for the 2DLH fit. Here is shown the second bin (left) and the third bin (right) in p_T^2 for the 2007&2010 sample.

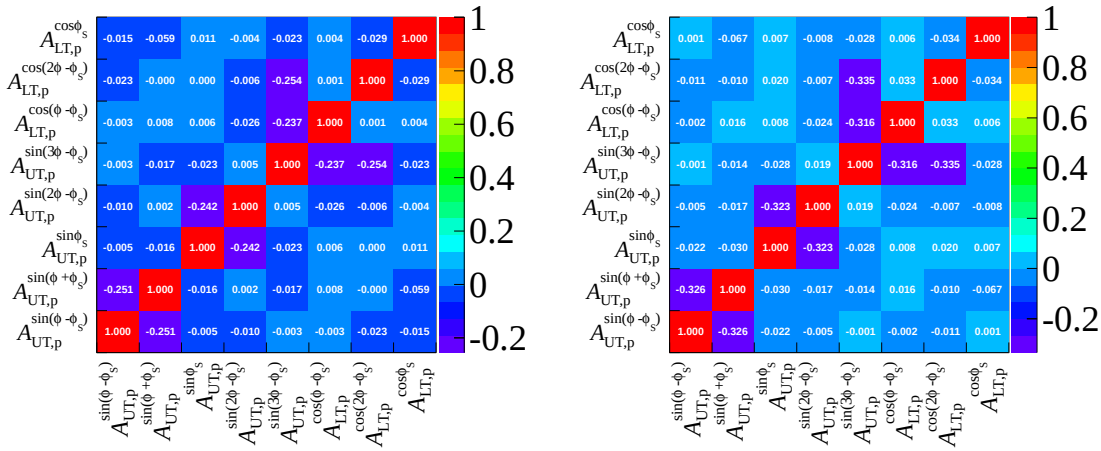

Figure D.18: Correlation matrix for the 2DLH fit. Here is shown the fourth bin (left) and the fifth bin (right) in p_T^2 for the 2007&2010 sample.

Bibliography

[1] E. Rutherford, "The scattering of alpha and beta particles by matter and the structure of the atom", *Phil.Mag.* **21** (1911) 669–688.

[2] E. Leader and M. Anselmino, "A Crisis in the Parton Model: Where, Oh Where Is the Proton's Spin?", *Z.Phys.* **C41** (1988) 239.

[3] R. Jaffe and A. Manohar, "The G(1) Problem: Fact and Fantasy on the Spin of the Proton", *Nucl.Phys.* **B337** (1990) 509–546.

[4] X. Ji, "Gauge-Invariant Decomposition of Nucleon Spin and Its Spin-Off", *Phys. Rev. Lett.* **78** (1997) 610, `arXiv:hep-ph/9603249v1`.

[5] J. C. Collins, L. Frankfurt, and M. Strikman, "Factorization for hard exclusive electroproduction of mesons in QCD", *Phys. Rev. D* **56** (1997) 2982, `arXiv:hep-ph/9611433`.

[6] J. C. Collins, "Factorization for hard exclusive electroproduction", `arXiv:hep-ph/9907513 [hep-ph]`.

[7] M. Burkardt, C. Miller, and W. Nowak, "Spin-polarized high-energy scattering of charged leptons on nucleons", *Rept.Prog.Phys.* **73** (2010) 016201, `arXiv:0812.2208 [hep-ph]`.

[8] C. A. Aidala, S. D. Bass, D. Hasch, *et al.*, "The Spin Structure of the Nucleon", *Rev.Mod.Phys.* **85** (2013) 655–691, `arXiv:1209.2803 [hep-ph]`.

[9] M. Diehl and S. Sapeta, "On the analysis of lepton scattering on longitudinally or transversely polarized protons", *Eur.Phys.J.* **C41** (2005) 515–533, `arXiv:hep-ph/0503023 [hep-ph]`.

[10] T. Arens, O. Nachtmann, M. Diehl, *et al.*, "Some tests for the helicity structure of the pomeron in e p collisions", *Z.Phys.* **C74** (1997) 651–669, `arXiv:hep-ph/9605376 [hep-ph]`.

[11] A. Kotzinian, "New quark distributions and semiinclusive electroproduction on the polarized nucleons", *Nucl.Phys.* **B441** (1995) 234–248, `arXiv:hep-ph/9412283 [hep-ph]`.

[12] A. Bacchetta, M. Diehl, K. Goeke, *et al.*, "Semi-inclusive deep inelastic scattering at small transverse momentum", *JHEP* **0702** (2007) 093, `arXiv:hep-ph/0611265 [hep-ph]`.

[13] C. E. Carlson and M. Vanderhaeghen, "Two-Photon Physics in Hadronic Processes", *Ann.Rev.Nucl.Part.Sci.* **57** (2007) 171–204, arXiv:hep-ph/0701272 [HEP-PH].

[14] A. Metz, M. Schlegel, and K. Goeke, "Transverse single spin asymmetries in inclusive deep-inelastic scattering", *Phys.Lett.* **B643** (2006) 319–324, arXiv:hep-ph/0610112 [hep-ph].

[15] H. Jostlein, I. Kim, K. Konigsmann, *et al.*, "Two Photon Exchange in Deep Inelastic Scattering", *Phys.Lett.* **B52** (1974) 485.

[16] European Muon Collaboration, J. Aubert *et al.*, "A Detailed Study of the Nucleon Structure Functions in Deep Elastic Muon Scattering in Iron", *Nucl.Phys.* **B272** (1986) 158.

[17] HERMES Collaboration, A. Airapetian *et al.*, "Search for a Two-Photon Exchange Contribution to Inclusive Deep-Inelastic Scattering", *Phys.Lett.* **B682** (2010) 351–354, arXiv:0907.5369 [hep-ex].

[18] V. Barone, A. Drago, and P. G. Ratcliffe, "Transverse polarisation of quarks in hadrons", *Phys.Rept.* **359** (2002) 1–168, arXiv:hep-ph/0104283 [hep-ph].

[19] Particle Data Group, J. Beringer *et al.*, "Review of Particle Physics (RPP)", *Phys.Rev.* **D86** (2012) 010001.

[20] J. Bjorken, "Asymptotic Sum Rules at Infinite Momentum", *Phys.Rev.* **179** (1969) 1547–1553.

[21] M. Breidenbach, J. I. Friedman, H. W. Kendall, *et al.*, "Observed Behavior of Highly Inelastic electron-Proton Scattering", *Phys.Rev.Lett.* **23** (1969) 935–939.

[22] On behalf of the COMPASS Collaboration, M. Wilfert, "New COMPASS results on the spin structure function g_1^p and QCD ", *Presentation: XXII. International Workshop on Deep-Inelastic Scattering and Related Subjects* **DIS2014** (2014) .

[23] The HERMES Collaboration, A. Airapetian *et al.*, "Measurement of the virtual-photon asymmetry A_2 and the spin-structure function g_2 of the proton", *Eur.Phys.J.* **C72** (2012) 1921, arXiv:1112.5584 [hep-ex].

[24] R. P. Feynman, "Very high-energy collisions of hadrons", *Phys.Rev.Lett.* **23** (1969) 1415–1417.

[25] P. Jimenez-Delgado, W. Melnitchouk, and J. Owens, "Parton momentum and helicity distributions in the nucleon", *J.Phys.* **G40** (2013) 093102, arXiv:1306.6515 [hep-ph].

[26] D. E. Soper, "Parton distribution functions", *Nucl.Phys.Proc.Suppl.* **53** (1997) 69–80, arXiv:hep-lat/9609018 [hep-lat].

[27] S. Boffi and B. Pasquini, "Generalized parton distributions and the structure of the nucleon", *Riv.Nuovo Cim.* **30** (2007) 387, arXiv:0711.2625 [hep-ph].

[28] A. V. Manohar, "An Introduction to spin dependent deep inelastic scattering", arXiv:hep-ph/9204208 [hep-ph].

[29] G. Baum, M. Bergstrom, P. Bolton, *et al.*, "A New Measurement of Deep Inelastic e p Asymmetries", *Phys.Rev.Lett.* **51** (1983) 1135.

[30] European Muon Collaboration, J. Ashman *et al.*, "An Investigation of the Spin Structure of the Proton in Deep Inelastic Scattering of Polarized Muons on Polarized Protons", *Nucl.Phys.* **B328** (1989) 1.

[31] COMPASS Collaboration, C. Adolph *et al.*, "Leading order determination of the gluon polarisation from DIS events with high-p_T hadron pairs", *Phys.Lett.* **B718** (2013) 922–930, arXiv:1202.4064 [hep-ex].

[32] COMPASS Collaboration, C. Adolph *et al.*, "Leading and Next-to-Leading Order Gluon Polarization in the Nucleon and Longitudinal Double Spin Asymmetries from Open Charm Muoproduction", *Phys.Rev.* **D87** (2013) 052018, arXiv:1211.6849 [hep-ex].

[33] PHENIX Collaboration, A. Adare *et al.*, "Inclusive cross section and double helicity asymmetry for pi^0 production in p^+p collisions at $\sqrt{s} = 62.4$ GeV", *Phys.Rev.* **D79** (2009) 012003, arXiv:0810.0701 [hep-ex].

[34] STAR Collaboration, L. Adamczyk *et al.*, "Longitudinal and transverse spin asymmetries for inclusive jet production at mid-rapidity in polarized $p + p$ collisions at $\sqrt{s} = 200$ GeV", *Phys.Rev.* **D86** (2012) 032006, arXiv:1205.2735 [nucl-ex].

[35] X. Ji, "Deeply virtual Compton scattering", *Phys. Rev. D* **55** (1997) 7114, arXiv:hep-ph/9609381v3.

[36] M. Guidal, H. Moutarde, and M. Vanderhaeghen, "Generalized Parton Distributions in the valence region from Deeply Virtual Compton Scattering", *Rept.Prog.Phys.* **76** (2013) 066202, arXiv:1303.6600 [hep-ph].

[37] S. Goloskokov, "Cross sections and spin asymmetries in vector meson leptoproduction", arXiv:0910.4308 [hep-ph].

[38] X.-D. Ji and J. Osborne, "One loop corrections and all order factorization in deeply virtual Compton scattering", *Phys.Rev.* **D58** (1998) 094018, arXiv:hep-ph/9801260 [hep-ph].

[39] L. Szymanowski, "QCD collinear factorization, its extensions and the partonic distributions", *PoS* **QNP2012** (2012) 015, arXiv:1208.5688 [hep-ph].

[40] A. Bacchetta, U. D'Alesio, M. Diehl, *et al.*, "Single-spin asymmetries: The Trento conventions", *Phys.Rev.* **D70** (2004) 117504, arXiv:hep-ph/0410050 [hep-ph].

[41] M. Diehl and A. Vinnikov, "Quarks vs. gluons in exclusive rho electroproduction", *Phys.Lett.* **B609** (2005) 286–290, arXiv:hep-ph/0412162 [hep-ph].

[42] D. Muller, D. Robaschik, B. Geyer, *et al.*, "Wave Functions, Evolution Equations and Evolution Kernels from Light-Ray Operators of QCD", *Fortsch. Phys.* **42** (1994) 101, arXiv:hep-ph/9812448v1.

[43] A. Belitsky and A. Radyushkin, "Unraveling hadron structure with generalized parton distributions", *Phys.Rept.* **418** (2005) 1–387, arXiv:hep-ph/0504030 [hep-ph].

[44] A. Radyushkin, "Topics in theory of generalized parton distributions", *Phys.Part.Nucl.* **44** (2013) 469–489.

[45] M. Diehl, "Generalized parton distributions", *Phys.Rept.* **388** (2003) 41–277, arXiv:hep-ph/0307382 [hep-ph].

[46] A. V. Radyushkin, "Nonforward Parton Distributions", *Phys. Rev. D* **56** (1997) 5524, arXiv:hep-ph/9704207v7.

[47] K. J. Golec-Biernat and A. D. Martin, "Off diagonal parton distributions and their evolution", *Phys.Rev.* **D59** (1999) 014029, arXiv:hep-ph/9807497 [hep-ph].

[48] K. Goeke, M. V. Polyakov, and M. Vanderhaeghen, "Hard Exclusive Reactions and the Structure of Hadrons", *Prog. Part. Nucl. Phys.* **47** (2001) 401, arXiv:hep-ph/0106012.

[49] S. Goloskokov and P. Kroll, "An Attempt to understand exclusive pi+ electroproduction", *Eur.Phys.J.* **C65** (2010) 137–151, arXiv:0906.0460 [hep-ph].

[50] S. Goloskokov and P. Kroll, "Transversity in hard exclusive electroproduction of pseudoscalar mesons", *Eur.Phys.J.* **A47** (2011) 112, arXiv:1106.4897 [hep-ph].

[51] P. Hoodbhoy and X.-D. Ji, "Helicity flip off forward parton distributions of the nucleon", *Phys.Rev.* **D58** (1998) 054006, arXiv:hep-ph/9801369 [hep-ph].

[52] M. Diehl, "Generalized parton distributions with helicity flip", *Eur.Phys.J.* **C19** (2001) 485–492, arXiv:hep-ph/0101335 [hep-ph].

[53] R. L. Jaffe, "Spin, twist and hadron structure in deep inelastic processes", arXiv:hep-ph/9602236 [hep-ph].

[54] S. Goloskokov and P. Kroll, "Transversity in exclusive vector-meson leptoproduction", *Eur.Phys.J.* **C74** (2014) 2725, arXiv:1310.1472 [hep-ph].

[55] M. Burkardt, "Impact parameter dependent parton distributions and off-forward parton distributions for $\zeta \to 0$", *Phys. Rev. D* **62** (2000) 071503, arXiv:hep-ph/0005108v2.

[56] M. Burkardt, "Erratum: Impact parameter dependent parton distributions and off-forward parton distributions for $\zeta \to 0$ [Phys. Rev. D 62, 071503 (2000)]", *Phys. Rev. D* **66** (2002) 119903.

[57] M. Burkardt, "Impact Parameter Space Interpretation for Generalized Parton Distributions", *Int. J. Mod. Phys A* **18** (2003) 173, arXiv:hep-ph/0207047v3.

[58] J. Arrington, *et al.*, "Conceptual Design Report (CDR) for The Science and Experimental Equipment for The 12 GeV Upgrade of CEBAF", Conceptual Design Report, April, 2005.

[59] E. Leader and C. Lorce, "The angular momentum controversy: What's it all about and does it matter?", *Phys.Rept.* (2013) , arXiv:1309.4235 [hep-ph].

[60] LHPC Collaborations, P. Hagler *et al.*, "Nucleon Generalized Parton Distributions from Full Lattice QCD", *Phys.Rev.* **D77** (2008) 094502, arXiv:0705.4295 [hep-lat].

[61] Jefferson Lab Hall A Collaboration, M. Mazouz *et al.*, "Deeply virtual compton scattering off the neutron", *Phys.Rev.Lett.* **99** (2007) 242501, arXiv:0709.0450 [nucl-ex].

[62] P. Kroll, "A set of generalized parton distributions", arXiv:1303.6433 [hep-ph].

[63] A. Radyushkin, "Double distributions and evolution equations", *Phys.Rev.* **D59** (1999) 014030, arXiv:hep-ph/9805342 [hep-ph].

[64] M. Polyakov and A. Shuvaev, "On'dual' parametrizations of generalized parton distributions", arXiv:hep-ph/0207153 [hep-ph].

[65] V. Guzey and T. Teckentrup, "The Dual parameterization of the proton generalized parton distribution functions H and E and description of the DVCS cross sections and asymmetries", *Phys.Rev.* **D74** (2006) 054027, arXiv:hep-ph/0607099 [hep-ph].

[66] S. Goloskokov and P. Kroll, "The Role of the quark and gluon GPDs in hard vector-meson electroproduction", *Eur.Phys.J.* **C53** (2008) 367–384, arXiv:0708.3569 [hep-ph].

[67] HERMES Collaboration, A. Airapetian *et al.*, "Single-spin azimuthal asymmetry in exclusive electroproduction of pi+ mesons on transversely polarized protons", *Phys.Lett.* **B682** (2010) 345–350, arXiv:0907.2596 [hep-ex].

[68] P. Kroll, "Generalized parton distributions from meson leptoproduction", *Phys.Part.Nucl.* **44** (2013) no. 6, 915–919, arXiv:1211.6857 [hep-ph].

[69] M. V. Polyakov and C. Weiss, "Skewed and double distributions in pion and nucleon", *Phys.Rev.* **D60** (1999) 114017, arXiv:hep-ph/9902451 [hep-ph].

[70] S. V. Goloskokov and P. Kroll, "Vector meson electroproduction at small Bjorken-x and generalized parton distributions", *Eur. Phys. J. C* **42** (2005) 281, arXiv:hep-ph/0501242v2.

[71] HERMES Collaboration, A. Airapetian *et al.*, "Spin Density Matrix Elements in Exclusive rho0 Electroproduction on H-1 and H-2 Targets at 27.5-GeV Beam Energy", *Eur.Phys.J.* **C62** (2009) 659–695, arXiv:0901.0701 [hep-ex].

[72] H1 Collaboration, F. Aaron *et al.*, "Diffractive Electroproduction of rho and phi Mesons at HERA", *JHEP* **1005** (2010) 032, arXiv:0910.5831 [hep-ex].

[73] COMPASS Collaboration, P. Abbon *et al.*, "The COMPASS experiment at CERN", *Nucl.Instrum.Meth.* **A577** (2007) 455–518, arXiv:hep-ex/0703049 [hep-ex].

[74] M. Leberig and L. Gatignon, "The M2 Beam Line", Villar Meeting, CERN, July 2004.

[75] L. Gatignon, "Maximum FLUX in M2 beam", COMPASS technical board, CERN, September 2010.

[76] A. Abragam, "Polarized Targets in High-Energy and Elsewhere", *Proceedings, High Energy Physics With Polarized Beams and Polarized Targets* (1978) .

[77] C. P. T. Group, "COMPASS Polarized Target in 2007", *http://wwwcompass.cern.ch/compass/detector/target/Drawings/NH3target07v01bw.pdf* (2007) .

[78] A. Sandacz, "Dilution factor for exclusive ρ^0 production for COMPASS pol. targets", COMPASS GPD Meeting, October, 2010.

[79] J. Koivuniemi, "Target material in 2007", Electronic Logbook, September 2008.

[80] J. Koivuniemi, "Target material in 2010", Private Communication, March 2012.

[81] N. Doshita *et al.*, "Target material data of run 2003", COMPASS Note 2003-8, January 2004.

[82] J. Koivuniemi, "Target material in 2004", Electronic Logbook, August 2009.

[83] COMPASS Collaboration, F. Gautheron *et al.*, "COMPASS-II Proposal", COMPASS-II Proposal, May 2010.

[84] J. Bisplinghoff, D. Eversheim, W. Eyrich, *et al.*, "A scintillating fibre hodoscope for high rate applications", *Nucl.Instrum.Meth.* **A490** (2002) 101–111.

[85] H. Angerer, R. De Masi, A. Esposito, *et al.*, "Present status of silicon detectors in COMPASS", *Nucl.Instrum.Meth.* **512** (2003) 229–238.

[86] C. Bernet, P. Abbon, J. Ball, *et al.*, "The 40-cm x 40-cm gaseous microstrip detector Micromegas for the high-luminosity COMPASS experiment at CERN", *Nucl.Instrum.Meth.* **A536** (2005) 61–69.

[87] B. Ketzer, J. Ehlers, J. Friedrich, *et al.*, "A fast tracker for COMPASS based on the GEM", *Nucl.Phys.Proc.Suppl.* **125** (2003) 368–373.

[88] V. Bychkov, N. Dedek, W. Dunnweber, *et al.*, "The large size straw drift chambers of the COMPASS experiment", *Nucl.Instrum.Meth.* **A556** (2006) 66–79.

[89] A. Amoroso *et al.*, "The front-end electronics for the COMPASS MWPCs", *Nuclear Instruments and Methods in Physics Research Section A: Accelerators, Spectrometers, Detectors and Associated Equipment* **518** (2004) no. 1-2, 495 – 497.

[90] F. Nerling, "COMPASS Calorimetry in view of future plans", `arXiv:1007.2948 [physics.ins-det]`.

[91] G. Baum *et al.*, "The COMPASS RICH project", *Nuclear Instruments and Methods in Physics Research Section A: Accelerators, Spectrometers, Detectors and Associated Equipment* **433** (1999) no. 1-2, 207 – 211.

[92] P. Abbon, M. Alexeev, H. Angerer, *et al.*, "Particle identification with COMPASS RICH-1", *Nucl.Instrum.Meth.* **A631** (2011) 26–39.

[93] C. Bernet, A. Bravar, J. Hannappel, *et al.*, "The COMPASS trigger system for muon scattering", *Nucl.Instrum.Meth.* **A550** (2005) 217–240.

[94] K. Novotny and E.-M. Kabuss, "Performance of the trigger hodoscopes in 2007 and 2010", COMPASS note 2012-5, November 2012.

[95] F. Herrmann, "Development and Verification of a High Performance Electronic Readout Framework for High Energy Physics", PhD thesis, University of Freiburg, August, 2011.

[96] R. Fruhwirth, "Application of Kalman filtering to track and vertex fitting", *Nucl.Instrum.Meth.* **A262** (1987) 444–450.

[97] PHAST, "PHysics Analysis Software Tools", `http://ges.home.cern.ch/ges/phast`.

[98] ROOT, "A Data Analysis Framework", `http://root.cern.ch/drupal`.

[99] G. Ingelman, A. Edin, and J. Rathsman, "LEPTO 6.5: A Monte Carlo generator for deep inelastic lepton - nucleon scattering", *Comput.Phys.Commun.* **101** (1997) 108–134, `arXiv:hep-ph/9605286 [hep-ph]`.

[100] J.-P. Guillaud, "Miniguide PYTHIA", *CERN-CMS-NOTE-2000-070* (2000) .

[101] GEANT, "Detector Description and Simulation tool", `http://wwwasdoc.web.cern.ch/wwwasdoc/pdfdir/geant.pdf`.

[102] H. Wollny, "Measuring azimuthal asymmetries in semi-inclusive deep-inelastic scattering off transversely polarized protons", PhD thesis, University of Freiburg, April, 2010.

[103] C. Elia, "Measurement of two-hadron transverse spin asymmetries in SIDIS at COMPASS", PhD thesis, University of Triest, March, 2012.

[104] C. Adolph, "One-hadron transverse spin effects on a proton target at COMPASS", PhD thesis, University of Erlangen-Nürnberg, February, 2013.

[105] C. Braun, "Bau und Tests eines sehr dünnen Beam-Counters aus szintillierenden Fasern und Software zur Qualitätsprüfung für das COMPASS Experiment.", Diploma thesis, University of Erlangen-Nürnberg, January, 2010.

[106] The transversity group, "Badspill/badrun lists for new production of 2010 data", http://compassweb.ts.infn.it/transversity/compass/stability/2010/FINAL_-BAD_SPILL_RUN_LISTS.tarz, 2010.

[107] The transversity group, "Badspill/badrun lists for new production of 2007 data", http://compassweb.ts.infn.it/transversity/compass/stability/2007/data/BadrunSpill/badspill_2009_03_04_complete_new_production.tarz, 2009.

[108] P. Sznajder, "Methodical studies of problems in 2004 and 2007 data", COMPASS GPD Meeting, April, 2010.

[109] P. Sznajder, "The new beam reconstruction", COMPASS Analysis Meeting, September, 2011.

[110] K.Schmidt, P. Sznajder, H. Wollny, *et al.*, "Exclusive ρ^0 production using the transversely polarized NH_3 target in 2007 and 2010", COMPASS release note, February, 2012.

[111] J. Bedfer, "Cut on number of radiation lengths", Private Communication, February, 2013.

[112] K.Schmidt, P. Sznajder, H. Wollny, *et al.*, "Exclusive ρ^0 production using transversely polarized ^{6}LiD (2004) and NH_3 (2007) targets", COMPASS note 2011-6, November, 2011.

[113] S. Goloskokov and P. Kroll, "The Target asymmetry in hard vector-meson electroproduction and parton angular momenta", *Eur.Phys.J.* **C59** (2009) 809–819, `arXiv:0809.4126 [hep-ph]`.

[114] E. Burtin, N.d'Hose, H. Fischer, *et al.*, "Exclusive ρ^0 production using transversely polarized ^{6}LiD (2004) and NH_3 (2007) targets", COMPASS note 2009-9, September, 2009.

[115] A. Sandacz, "Separation of coherent and incoherent exclusive processes", COMPASS Analysis Meeting, August, 2007.

[116] C. Adolph, C. Braun, F. Bradamante, *et al.*, "Collins, Sivers and two hadron asymmetries for identied hadrons from the 2010 transversely polarized proton data", COMPASS release note, September, 2012.

[117] C. Adolph, J. Bisplinghoff, C. Braun, *et al.*, "Transverse spin dependent azimuthal asymmetries from 2007 proton data", COMPASS release note, September, 2010.

[118] HERMES Collaboration, A. Airapetian *et al.*, "Beam-helicity asymmetry arising from deeply virtual Compton scattering measured with kinematically complete event reconstruction", *JHEP* **1210** (2012) 042, `arXiv:1206.5683 [hep-ex]`.

[119] H. Wollny, Private Communication, 2011.

[120] A. Sandacz and P. Sznajder, "HEPGEN - generator for hard exclusive leptoproduction", `arXiv:1207.0333 [hep-ph]`.

[121] A. Kotzinian, "Some studies on azimuthal asymmetry extraction", COMPASS Analysis Meeting, May, 2007.

[122] S. M. Stigler, "The Epic Story of Maximum Likelihood",*Statistical Science* **22** (Nov., 2007) 598–620. `http://dx.doi.org/10.1214/07-sts249`.

[123] D. Levenberg, "A Method for the Solution of Certain Problems in Least Squares", Quart. Appl. Math. 2, pages 164-168, 1944.

[124] D. Marquardt, "An Algorithm for Least-Squares Estimation of Nonlinar Parameters", SIAM J. Appl. Math., 11:431-441, 1963.4, 1963.

[125] B. Gough, "GNU Scientific Library Reference Manual", 2nd Edition. Network Theory Ltd., ISBN 0954161734., 1963.4, 2006.

[126] G. Mallot, "Principle of a bias-free "2D" transverse asymmetry fit", COMPASS Analysis Meeting, September, 2007.

[127] COMPASS Collaboration, M. Alekseev *et al.*, "Double spin asymmetry in exclusive ρ^0 muoproduction at COMPASS", *Eur.Phys.J.* **C52** (2007) 255–265, `arXiv:0704.1863 [hep-ex]`.

[128] Gustafsson, K., "Computation of the Dilution Factor for the Year 2002 COMPASS Data", COMPASS note 2003-3, July, 2003.

[129] Spin muon collaboration, A. Tripet, "Exclusive ρ^0 production in polarized DIS at SMC", *Nucl.Phys.Proc.Suppl.* **79** (1999) 529–531, `arXiv:hep-ex/9906008 [hep-ex]`.

[130] P. Sznajder, "Uncertainty of dilution factor", Private Communication, October 2011.

[131] K. Kondo *et al.*, "Polarization measurement in the COMPASS polarized target", *Nuclear Instruments and Methods in Physics Research Section A: Accelerators, Spectrometers, Detectors and Associated Equipment* **526** (2004) 70 – 75.

[132] COMPASS Collaboration, V. Y. Alexakhin *et al.*, "First measurement of the transverse spin asymmetries of the deuteron in semi-inclusive deep inelastic scattering", *Phys.Rev.Lett.* **94** (2005) 202002, arXiv:hep-ex/0503002 [hep-ex].

[133] COMPASS Collaboration, E. Ageev *et al.*, "A New measurement of the Collins and Sivers asymmetries on a transversely polarised deuteron target", *Nucl.Phys.* **B765** (2007) 31–70, arXiv:hep-ex/0610068 [hep-ex].

[134] A. Kotzinian, "MC studies on reconstruction of azimuthal asymmetries", COMPASS Analysis Meeting, Aug, 2007.

[135] A. Kotzinian, "Remarks on acceptance effects in asymmetry extraction", COMPASS note 2007-2, October, 2007.

[136] J. Pretz, "A New Method for Asymmetry Extraction", COMPASS note 2004-11, April, 2004.

[137] COMPASS Collaboration, C. Adolph *et al.*, "Transverse spin effects in hadron-pair production from semi-inclusive deep inelastic scattering", *Phys.Lett.* **B713** (2012) 10–16, arXiv:1202.6150 [hep-ex].

[138] COMPASS Collaboration, C. Adolph *et al.*, "A high-statistics measurement of transverse spin effects in dihadron production from muon-proton semi-inclusive deep-inelastic scattering", arXiv:1401.7873 [hep-ex].

[139] A. Bacchetta and M. Radici, "Partial wave analysis of two hadron fragmentation functions", *Phys.Rev.* **D67** (2003) 094002, arXiv:hep-ph/0212300 [hep-ph].

[140] A. Bacchetta and M. Radici, "Two hadron semiinclusive production including subleading twist", *Phys.Rev.* **D69** (2004) 074026, arXiv:hep-ph/0311173 [hep-ph].

[141] P. Sznajder, "Acceptance studies with MC", Private Communication, November, 2013.

[142] M. Diehl, "Vector meson production from a polarized nucleon", *JHEP* **0709** (2007) 064, arXiv:0704.1565 [hep-ph].

[143] COMPASS Collaboration, M. Alekseev *et al.*, "Measurement of the Collins and Sivers asymmetries on transversely polarised protons", *Phys.Lett.* **B692** (2010) 240–246, arXiv:1005.5609 [hep-ex].

[144] COMPASS Collaboration, C. Adolph *et al.*, "Experimental investigation of transverse spin asymmetries in muon-p SIDIS processes: Sivers asymmetries", *Phys.Lett.* **B717** (2012) 383–389, arXiv:1205.5122 [hep-ex].

[145] COMPASS Collaboration, C. Adolph *et al.*, "Experimental investigation of transverse spin asymmetries in muon-p SIDIS processes: Collins asymmetries", *Phys.Lett.* **B717** (2012) 376–382, arXiv:1205.5121 [hep-ex].

[146] COMPASS Collaboration, C. Adolph *et al.*, "Exclusive ρ^0 muoproduction on transversely polarised protons and deuterons", *Nucl.Phys.* **B865** (2012) 1–20, arXiv:1207.4301 [hep-ex].

[147] C. Adolph, C. Braun, F. Bradamante, *et al.*, "Six beyond Collins and Sivers asymmetries for unidentified hadrons from the 2010 transversely polarized proton data", COMPASS Release Note, September, 2012.

[148] M. Alekseev *et al.*, "Azimuthal asymmetries of charged hadrons produced by high-energy muons scattered off longitudinally polarisd deuterons", *Eur.Phys.J.* **C70** (2010) 39–49, arXiv:1007.1562 [hep-ex].

[149] A. Tripet, "The Exclusive Production of ρ^0 Mesons in Polarized Muon-Nucleon Scattering within the SMC Experiment", PhD thesis, University of Bielefeld, 2002.

[150] HERMES Collaboration, A. Airapetian *et al.*, "Double spin asymmetries in the cross-section of rho0 and phi production at intermediate-energies", *Eur.Phys.J.* **C29** (2003) 171–179, arXiv:hep-ex/0302012 [hep-ex].

[151] H. Fraas, "Cross-Section Asymmetries in Vector Meson Electroproduction and in Inelastic e p Scattering with Polarized Beam and Target", *Nucl.Phys.* **B113** (1976) 532.

[152] COMPASS Collaboration, M. Alekseev *et al.*, "The Spin-dependent Structure Function of the Proton g_1^p and a Test of the Bjorken Sum Rule", *Phys.Lett.* **B690** (2010) 466–472, arXiv:1001.4654 [hep-ex].

[153] R. Barlow, "Systematic errors: Facts and fictions", arXiv:hep-ex/0207026 [hep-ex].

[154] G. Pesaro, "Measurement of COMPASS of transverse spin effects on identified hadrons on a transversely polarised proton target", PhD thesis, University of Trieste, March, 2010.

[155] ZEUS Collaborations, J. Breitweg *et al.*, "Measurement of the spin density matrix elements in exclusive electroproduction of rho0 mesons at HERA", *Eur.Phys.J.* **C12** (2000) 393–410, arXiv:hep-ex/9908026 [hep-ex].

[156] ZEUS Collaboration, S. Chekanov *et al.*, "Exclusive ρ^0 production in deep inelastic scattering at HERA", *PMC Phys.* **A1** (2007) 6, arXiv:0708.1478 [hep-ex].

[157] O. A. Rondon-Aramayo, "Corrections to nucleon spin structure asymmetries measured on nuclear polarized targets", *Phys.Rev.* **C60** (1999) 035201.

[158] COMPASS Collaboration, M. Alekseev *et al.*, "Quark helicity distributions from longitudinal spin asymmetries in muon-proton and muon-deuteron scattering", *Phys.Lett.* **B693** (2010) 227–235, arXiv:1007.4061 [hep-ex].

[159] I. Akushevich, "Radiative effects in processes of diffractive vector meson electroproduction", *Eur.Phys.J.* **C8** (1999) 457–463, arXiv:hep-ph/9808309 [hep-ph].

[160] COMPASS Collaboration, C. Adolph *et al.*, "Transverse target spin asymmetries in exclusive ρ^0 muoproduction", *Phys.Lett.* **B731** (2014) 19, arXiv:1310.1454 [hep-ex].

[161] S. Goloskokov and P. Kroll, "Model calculations", Private Communication, 2013.

[162] K. Schmidt, "Exclusive ρ^0 muoproduction on transversely polarised protons and deuterons", *Proceedings, Sixth International Conference on Quarks and Nuclear Physics, PoS(QNP2012)044* (2012) .

[163] K. Schmidt, "Transverse target spin asymmetries in exclusive ρ^0 muoproduction", *Proceedings, XXI International Workshop on Deep-Inelastic Scattering and Related Subjects, PoS(DIS2013)223* (2013) .

[164] S. Goloskokov, "Model calculations", Private Communication, June 2014.

[165] J. Dudek, R. Ent, R. Essig, *et al.*, "Physics Opportunities with the 12 GeV Upgrade at Jefferson Lab", *Eur.Phys.J.* **A48** (2012) 187, arXiv:1208.1244 [hep-ex].

[166] C. Aidala, N. Ajitanand, Y. Akiba, *et al.*, "sPHENIX: An Upgrade Concept from the PHENIX Collaboration", arXiv:1207.6378 [nucl-ex].

[167] D. Boer, M. Diehl, R. Milner, *et al.*, "Gluons and the quark sea at high energies: Distributions, polarization, tomography", arXiv:1108.1713 [nucl-th].

[168] A. Accardi, J. Albacete, M. Anselmino, *et al.*, "Electron Ion Collider: The Next QCD Frontier - Understanding the glue that binds us all", arXiv:1212.1701 [nucl-ex].

[169] PHENIX Collaboration, A. Adare *et al.*, "Concept for an Electron Ion Collider (EIC) detector built around the BaBar solenoid", arXiv:1402.1209 [nucl-ex].

[170] S. Abeyratne, A. Accardi, S. Ahmed, *et al.*, "Science Requirements and Conceptual Design for a Polarized Medium Energy Electron-Ion Collider at Jefferson Lab", arXiv:1209.0757 [physics.acc-ph].

[171] A. Lehrach, K. Aulenbacher, O. Boldt, *et al.*, "The polarized electron-nucleon collider project ENC at GSI/FAIR", *J.Phys.Conf.Ser.* **295** (2011) 012156.

[172] LHeC Study Group, J. Abelleira Fernandez *et al.*, "A Large Hadron Electron Collider at CERN: Report on the Physics and Design Concepts for Machine and Detector", *J.Phys.* **G39** (2012) 075001, arXiv:1206.2913 [physics.acc-ph].

[173] O. Bruening and M. Klein, "The Large Hadron Electron Collider", *Mod.Phys.Lett.* **A28** (2013) no. 16, 1330011, arXiv:1305.2090 [physics.acc-ph].

Danksagung

Diese Arbeit wurde am Physikalischen Institut der Albert-Ludwigs Universität Freiburg angefertigt. An dieser Stelle möchte ich mich bei denjenigen bedanken, die zum Gelingen dieser Arbeit beigetragen haben.

Ein besonderer Dank geht an Prof. Dr. Horst Fischer, der das interessante Thema stellte und die Betreuung dieser Arbeit übernommen hat, für seine unermüdliche Unterstützung und viele wertvollen Anregungen. Er hatte während der gesamten Zeit der Anfertigung dieser Dissertation immer ein offenes Ohr für mich und meine Arbeit.

Herrn Prof. Dr. Königsmann danke ich für die freundliche Aufnahme in seiner Arbeitsgruppe und die Möglichkeit, diese Dissertation im Rahmen der COMPASS Kollaboration anzufertigen.

Dr. Heiner Wollny danke ich für die gute Teamarbeit, viele wertvollen Anregungen und fruchtbare Diskussionen.

Philipp Jörg, Dr. Wolf-Dieter Nowak, Christopher Regali, Sebastian Schopferer, Stefan Sirtl, Tobias Szameitat und Johannes ter Wolbeek danke ich für das sorgfältige Korrekturlesen dieser Arbeit.

Der gesamten Arbeitsgruppe danke ich für die angenehme Arbeitsatmosphäre, Hilfestellungen bei Software- und Analysefragen und lehrreiche Diskussionen und Anregungen.

Meinen Eltern danke ich dafür, dass sie die ganze Zeit über hinter mir standen und mich unterstützt haben.